2009

Development of Adaptive Mesh Refinement Scheme and Conjugate Heat Transfer Model for Engine Simulations

Qingluan Xue
Iowa State University

Development of adaptive mesh refinement scheme and conjugate heat transfer model for engine simulations

by

Qingluan Xue

A dissertation submitted to the graduate faculty

in partial fulfillment of the requirements for the degree of

DOCTOR OF PHILOSOPHY

Major: Mechanical Engineering

Program of Study Committee:
Song-Charng Kong, Major Professor
Rodney O. Fox
Gap-Yong Kim
Terrence R. Meyer
Xinwei Wang

Iowa State University

Ames, Iowa

2009

TABLE OF CONTENTS

LIST OF TABLES

LIST OF FIGURES

LIST OF ABBREVIATIONS, SYMBOLS AND NOMENCLATURE

Abbreviations:

ALE	arbitrary Lagrangian Eulerian
AMR	adaptive mesh refinement
ATDC	after top dead center
BTDC	before top dead center
CAD	crank angle degree
CDM	continuum droplet model
CFD	computational fluid dynamics
CHT	conjugate heat transfer
DDM	discrete droplet model
DISI	direct injection spark ignition
EE	Eulerian-Eulerian
EGR	exhaust gas recirculation
EVO	exhaust valve open
IC	internal combustion
IVC	intake valve closure
KH	Kelvin-Helmholtz model
LE	Lagrangian-Eulerian
PCCI	premixed charge compression ignition
PDC	partial donor cell differencing
PM	particulate matter (soot)
Pr	Prandtl number
QSOU	quasi-second order upwind differencing
RANS	Reynolds averaged Navier-Stokes equations
Re	Reynolds number

RL	refinement level
RL0, RL1, RL2, RL3	refinement level zero, one, two, and three
RT	Rayleigh-Taylor model
Sc	Schmidt number
Sh	Sherwood number
SI	spark ignition
SMD	Sauter mean diameter
SOI	start of ignition
St	Stokes number
TAB	Taylor-Analogy break-up model
TDC	Top dead center
We	Weber number

Symbols:

a	pressure gradient scaling parameter
A_o	switch (1 or 0) to turn turbulence on or off
A_f	cell face area vector
c_V, c_P	specific heats at constant volume and pressure
D	gas mass diffusion coefficient
F^{spray}	spray momentum transfer term
f	probability distribution function
g	gravity
k	turbulent kinetic energy per unit mass
p	pressure
h	specific enthalpy
I	specific internal energy
K	thermal conductivity
M	mass of cell

M_V	mass of control volume surrounding a vertex
Pr_t	turbulent Prandtl number
$\dot{Q}^{chem}$	chemical source term
$\dot{Q}^{spray}$	spray source term
R_o	universal gas constant
r	radius
$\bar{R} = R_o \sum_m \frac{Y_m^B}{W_m}$	gas constant
Sc_t	turbulent Schmidt number
t	time
T	temperature
$\vec{u}$	velocity
$\tilde{u}$	turbulent gas velocity fluctuation
$\vec{V}_P$	particle velocity
V	volume
$\vec{V}$	velocity
$\dot{W}^{spray}$	spray source term in turbulence equations
W_m	molecular mass of species m
$\vec{x}$	position
Y_m	mass fraction of species m
ϵ	turbulent dissipation rate
ϕ_D	variable implicitness parameter
ϕ_P	variable implicitness parameter for pressure
ρ	density
ρ_m	density of species m
$\dot{\rho}^{spray}$	spray source term
$\dot{\rho}_m^{chem}$	chemical source term for species m
σ	viscous stress tensor
μ	coefficient of viscosity

λ	coefficient of viscosity
Δt	time step

Subscripts:

c	cell
d	droplet
f	face
l	liquid
m	species
P	particle
t	turbulent
v	vertex control volume

Superscripts:

A, B, C	stage A, B, C
n	time level n
$\rightarrow$	vector
$\rightrightarrows$	tensor
$\cdot$	$d()/dt$
$\cdot\cdot$	$d^2()/dt^2$

ACKNOWLEDGMENTS

I wish to express my sincere appreciation to my major professor, Dr. Song-Charng Kong for his understanding, guidance and encouragement throughout this research and the writing of this thesis. I would also like to thank the other members of my committee, Prof. Rodney Fox, Prof. Gap-Yong Kim, Prof. Terrence Meyer, Prof. Alric Rothmayer and Prof. Xinwei Wang for providing insightful suggestions and taking time to serve on my committee.

Special thanks go to Dr. David Torres of Los Alamos National Laboratory for his mentoring and innumerable fruitful discussions that sometimes ran into hours during my visiting term.

Gratitude should also been given to Ford Motor Company for financially supporting this work with Dr. James Yi as the technical monitor.

Thanks also go to Anthony Phan, Matthias Veltman and Prashanth Karra of internal combustion engines laboratory for their help and interesting discussions. I would also like to thank Shiyou Yang from University of Wisconsin at Madison for his help.

A heart felt thanks goes especially to my parents and the rest of my family for their endless love and support, which always have been an essential part of my life. A special thanks to Enruo, for being there with me through every joyful and sad moment. I love you.

ABSTRACT

Spray modeling is a critical component to engine combustion and emissions simulations. Accurate spray modeling often requires a fine computational mesh for better numerical resolutions. This, in turn, will require extensive computer time. A major concern for the successful application of computational methods in an industrial environment is its capability to handle complex configurations with acceptable accuracy at reasonable human and computational costs. To assure the accuracy and reliability of the solution, grid modification and grid refinement studies are often necessary within an iterative process. Adaptive algorithms are a promising approach to realize discretizations that are able to automatically resolve the physically relevant phenomena at reduced costs. The first goal of the dissertation work is to developed a methodology that uses a locally dynamically refined mesh in the spray region for engine spray simulations.

An h-refinement adaptive scheme is developed and implemented into an existing computer code. It is a dynamic process that adapts an initial mesh by employing local cell division and recovery. Adaptation of the cells is composed of isotropic division of one hexahedron into eight sub-cells in three dimensions. The concept of polyhedral elements is implemented to treat any possible hanging node configuration that occurs at the interface between the divided and undivided zones in a natural way. This flexibility of this method was demonstrated to handle successive grid adaptation and efficient data management when it is extended to multi-level refinement process. A special data structure based on octree has been developed for high storage efficiency. The solid-cone and hollow-cone sprays under direct-injection gasoline engine conditions were simulated. Predicted spray characteristics using different mesh densities with various refinement levels were compared. Results show that the present mesh refinement scheme

can accurately predict spray structures with reduced computer times. A significant computational speed-up was achieved by using a relatively coarse mesh with multi-level refinement while maintaining a good level of accuracy.

On the other hand, accurate modeling of the wall heat transfer characteristics within an engine is important for engine design because the amount of heat transfer through the piston, head, and liner surfaces can influence engine efficiency and performance, exhaust emission levels, and engine durability. The surface temperature is a key element for heat transfer, thus an accurate chamber wall surface temperature prediction is crucial for engine heat transfer modeling.

The second part of this study developed a conjugate heat transfer model to predict the combustion chamber surface temperature of an engine. First, the code was modified to account for a non-uniform temperature distribution and was run with the uniform temperature profile specified in the input file. The results were compared with the experimental data. The conduction heat transfer modeling capability was added to the code to predict the heat diffusion inside the solid wall by solving a simplified energy equation with the same numerical method used in fluid region. A fully coupled numerical procedure, which conserved the continuous temperature and heat flux condition, was developed to simultaneously solve the heat transfer in fluid flows and heat conduction in solid. Model validation showed the predicted results agreed well with the analytical solutions. The method was applied to simulate a transient diesel engine with fuel spray. The non-uniform spatial temperature distribution on the piston surface caused by fuel spray was predicted by the conjugate heat transfer model. The present model can be used to predict the temperature of the engine combustion chamber under combustion conditions in future studies.

CHAPTER 1. INTRODUCTION

1.1 Background

Spray processes are widely used in many technical and industrial applications. For example, spray cooling, spray painting, and spray combustion in furnaces, gas turbines, rockets, as well as internal combustion engines. In internal combustion (IC) engines sprays are used to mix the liquid fuel with air and increase its surface area for rapid evaporation and combustion. The spray and mixture formation process, which includes fuel injection, drop break-up and spray atomization, drop collision and coalescence, evaporation of droplets, impingement of droplets on the wall, and air-fuel mixing, is one of the most important factors that control the combustion process. The spray significantly affects the ignition behavior, heat release, and pollutant formation rates and thus fuel consumption and exhaust emissions. Thorough understanding and improvement of the spray and mixture formation is crucial in modern engine design due to the future demands of the restricted emissions and economical fuel consumptions.

Engine heat transfer phenomena have been studied extensively together with the combustion process for many years. It is important to understand the engine heat transfer through the piston, head, and liner components, because heat transfer influences directly engine performance and efficiency, NOx and soot emissions, and engine component thermal stresses. Accurate estimation of local heat fluxes through the combustion chamber is one of the challenges in engine design.

With the enormous increase in computing performance, Computational fluid dynamics (CFD) modeling has played a powerful role to provide valuable insight into spray and combustion processes in engine design over past decades. CFD are becoming a necessity and usually used together with experimental methods in industries. One advantage of numerical simula-

tions is that they are much cheaper and faster in contrast to experiments. In addition, spray and combustion modeling can give much more extensive information for each single variable at any physical location or any time during the complex in-cylinder transient process than experiments could ever provide. Furthermore, numerical modeling can be used to investigate sub-processes (such as the high pressure and high speed flow inside the injection holes) that take place at time or in places that are not accessible and thus can not be studied using experimental techniques. Another capability of numerical modeling is to study a specific sub-process by isolating it from others, which would interact in a real condition.

Lagrangian-Eulerian approach is widely used to model the gas-liquid two-phase flows in the engine spray and combustion simulations. The continuous gas phase is described by the Eulerian formulation. The conservative species mass, continuity, momentum, and energy equations are solved in the three-dimensional flow filed in conjunction with an appropriate turbulent model. Lagrangian formation is used to describe the dispersed liquid phase. Various sub-models are used to describe the change of droplet mass, momentum, and energy. The interaction of both phases is achieved by the exchanges of mass, momentum, and energy as source terms. Although CFD modeling has already reached a very high level in modeling the processes in IC engines, a continuous improvement of existing CFD models is necessary in order to guarantee a detailed and accurate modeling of the relevant sub-process and enhance the predictive quality in the future.

1.2 Motivations

The mixture distribution in internal combustion engines is largely determined by the fuel spray dynamics. A good description of the fuel spray is crucial to achieve an accurate simulation of engine combustion and emissions. An accurate prediction of the spray dynamics in the engine must account for the behavior of the spray at the injector tip, primary and secondary atomization, and droplet collision and coalescence, in addition to the gas-liquid interactions. However, grid dependency is one of the classic and most readily observed problems of numerical accuracy of the Lagrangian-Eulerian approach (Abraham, 1997; Schmidt et al., 2002). The

predicted liquid tip penetration, drop size and vapor distributions by Lagrangian-Eulerian method will change with the grid density and structure. An adequately fine mesh is usually required to predict the spray with sufficient accuracy, which, in turn, necessitates massive computational time and computer resources.

The first objective of this work is to develop an Adaptive Mesh Refinement (AMR) scheme to improve the accuracy and reduce the computational time and resources for the transient engine spray simulations.

On the other hand, Accurate prediction of wall heat flux is necessary for improving the overall accuracy of engine combustion simulations. Heat flux through the combustion chamber walls mainly attributed to convection from gas flow, conduction through impinged fuel film, and radiation of high temperature gas and soot particles. It is apparent that the local wall temperature is a key element to obtain accurate heat flux. Obviously, the commonly used constant wall surface temperature assumption (Amsden et al., 1989) is not sufficient for accurately modeling the combustion chamber wall heat flux.

Therefore, a second objective of this work is to develop a conjugate heat transfer capability into code to predict the distribution of temperature inside the engine components together with the in-cylinder process so that the simulations of engine combustion process can be improved. Also, the temperature profile inside the engine components can help engineer for thermal stress analysis, when the thermal load on the combustion chamber wall is increasing with the increased mean effective pressures (MEP) of new high power density diesel engines.

1.3 Approaches

An adaptive mesh refinement scheme is implemented for engine spray simulation in this work. Mesh adaptation is achieved by dynamically refining or coarsening the local meshes according to the need of spatial resolution, in order to avoid the use of a globally static fine mesh. During cell refinement, the isotropic division of one hexahedron into eight sub-cells was performed in three dimensions. The coarsening process in the inverse of the refinement process, and the coarser mesh are formed by coalescing the sibling cells into their coarser parent cell.

The concept of polyhedral elements was implemented to treat the hanging node configuration that appears at the interface between the divided and undivided zones in a natural way. This approach offers flexibilities in handling successive adaptation for efficient data management. A special data structure based on octree was developed, which offers high storage efficiency.

The fully coupled heat transfer computation (conjugate heat transfer) approach is implemented into the CFD code to predict the distributions of the wall temperature and improve the prediction of wall heat transfer. It calculates the fluid flow and solid temperature simultaneously without the need of using measured heat flux data as the thermal wall boundary conditions. The coupled approach is achieved by maintaining a continuous local heat flux and a common temperature at every locations along the wall surfaces exposed to the high temperature gas.

1.4 Thesis Organization

Figure 1.1 gives an overview of the work in this thesis. In Chapter 2, the survey of mesh dependency of spray modeling and adaptive algorithms is presented. A review of combustion modeling and conjugate heat transfer modeling are then present. The governing equations and numerical methods of the flow solver for this research are described in detail in Chapter 3. The development of adaptive mesh refinement into the collocated KIVA-4 code are described in Chapter 4. The applications of AMR for engine spray are studied in Chapter 5. Chapter 6 presents the diesel spray combustion models. The diesel spray combustion models were integrated into the KIVA-4 code and were validated first. The development and validations of the conjugate heat transfer model into KIVA code are described in Chapter 7 and Chapter 8, respectively. Finally, the conclusions and recommendation are discussed in Chapter 9.

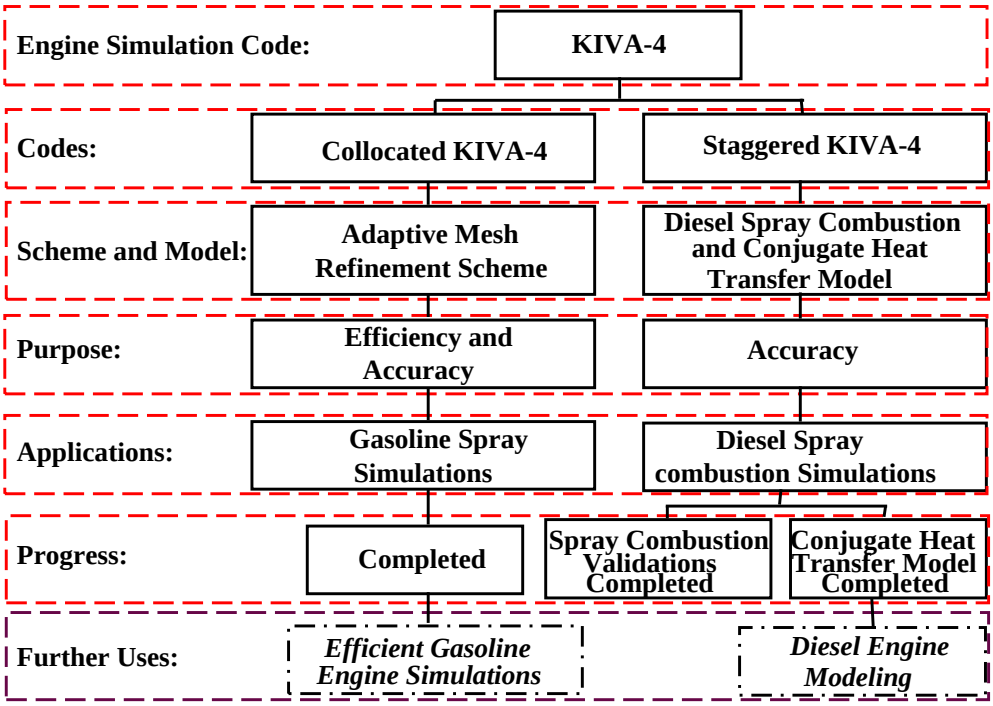

Figure 1.1: The overview of the projects in this study

CHAPTER 2. LITERATURE REVIEW

Basically, two distinct methods are employed to numerically describe multiphase flow system, namely the Lagrangian-Eulerain (LE) approach or discrete droplet model (DDM) (Dukowicz, 1980) and the Eulerian-Eulerian (EE) approach or continuum droplet model (CDM) (Gupta et al., 1978; Heywood, 1988). The LE approach models the spray by calculating the trajectories of the droplets. The EE approach is based on the continuum model and describes the droplet phase in transport equations. Both approaches are characterized by specific advantages and restrictions. Nevertheless, the LE approach is commonly preferred for practical CFD analysis due to the significant advantages regarding complex spray discretization and modeling of flow phenomena such as secondary droplet breakup and drop/wall interactions. The LE approach has been used in KIVA code (Amsden et al., 1989) and other CFD codes such as FIRE, FLUENT, and STAR-CD, etc. for engine spray and combustion simulations. In this chapter, the LE approach is introduced and the grid dependency in modeling spray using LE approach is discussed. The adaptive algorithm and diesel spray combustion models will also be described.

2.1 Grid Dependency in Modeling Sprays in IC Engines

In the Lagrangian-Eulerian model, the continuous phase is solved using Eulerian method on a computational grid, while the dispersed phase is solved using Lagrangian method to track the trajectory of each particle. Monte-Carlo method is applied to describe the spray. The spray droplets are described by stochastic particles, usually referred as parcels. The advantage of LE is the ability to easily track the physical properties associated with individual particles such as size or density and to describe phenomena of relevant sub-processes occuring in the engine sprays. Despite the above advantages, a significant difficulty in modeling sprays using the LE

approach is the strong grid sensitivity.

The mesh dependency can be attributed to two sources: inter-phase coupling and physical sub-models. The values in the center of the host cells are usually used for gas-droplet coupling calculations on a computational grid. The gradients of the variables inside the cells are not considered. A coarse grid will produce poor spatial resolution of the gas phase quantities and thus results in a poor prediction of the gas-liquid interactions. From liquid to gas, the immediate and uniform distribution of the vapor over the cell leads to an unphysically faster diffusion with lower grid resolution. To improve the inter-phase coupling, researchers use interpolation schemes to calculate the gas flow quantities at the location of the droplets. Schmidt et al. (2002) replaced the host node quantities with a weighted average of the gas phase quantities from surrounding nodes. Stalsberg-Zarling et al. (2004) tested the Lagrangian polynomial interpolation and source term distribution methods to improve the grid sensitivity. Hieber (2001) implemented a Void Fraction Compensation method to correct the under-resolved momentum coupling between the liquid and the gas. Lippert et al. (2005) proposed a methodology that can achieve second-order spatial accuracy for the inter-phase coupling between the gas and the liquid. The combination of least-squares fitting for gas-to-liquid coupling and kernel smoothing for liquid-to-gas coupling was shown to eliminate grid artifacts on the spray shape. Beard et al. (2000, 2003) developed a full Lagrangian-Eulerian coupling model to reduce the over-prediction of the exchange rates between gas and liquid due to the effect of the numerical diffusion for insufficient mesh to resolve the steep gradients. The gaseous particles are introduced to retain the fuel vapor and release and transfer to the gas phase gradually. The approach results in an improved prediction of liquid and vapor penetration and in a reduction of grid dependency.

The widely used collision model by O'Rourke (1981) for spray modeling also has the grid sensitive problem (Abraham, 1997). In this algorithm, the gas phase cells serve the calculations of collision probability. The gas phase cells will poorly resolve strong gradient of the number density in dense spray. Therefore this algorithm under-predicts the collision occurrence. Schmidt et al. (2000) developed a new collision method called no-time-counter (NTC). This NTC model uses a separate collision grid from gas phase mesh. They performed a

test on Cartesian mesh in a fixed cylindrical domain and showed a significant reduction of the mesh dependency. Hou et al. (2006) developed an adaptive collision mesh method. The tests showed that the method can achieve high spatial resolution and provide an accurate statistical representation of collision incidence.

The spray regions are dominated by the physical features of both the high velocity and high fuel vapor concentration gradients. The rate of momentum, mass, and heat loss of drops is strongly influenced by the resolution of the velocity, fuel concentration, and temperature in gas field. With an inadequate spatial resolution, the Eulerian field may not be properly resolved in the vicinity of the liquid phase, especially near the nozzle. This can cause an overestimate in momentum diffusion that leads to inaccuracies in modeling the fuel-air mixing. Thus, spray penetration is often under-predicted by using a coarse mesh. Abraham (1997) and Aneja et al. (1998) observed that the penetration of the liquid fuel was sensitive to the spatial resolution in a transient spray. The distribution of the source terms over the gas phase leads to unphysically fast diffusion of the vapor quantities, especially near the nozzle region where the gradients of the velocity and species density are under-resolved due to numerical limit (Abraham, 1997) and modeling assumption (Stiesch, 2003). The standard collision model suffers from the resolution of the collision cells. A sufficiently fine mesh is often required for accurate spray simulations. In fact, mesh resolution is usually lacking in engine simulations, in particular, in the spray regions. However, an overly fine mesh in three-dimensional simulations requires extensive computer time and thus may be prohibitive in engineering design and optimizations. On the other hand, the adaptive mesh refinement (AMR) method can avoid the use of a fine mesh in the entire domain by dynamically refining and coarsening meshes as required.

2.2 Adaptive Mesh Refinement Algorithm

The principal idea of adaptive mesh refinement (AMR) is to enable a higher accuracy solution at lower costs, through a automatically optimal distribution of grid points for the computational region. In essence, AMR is a hierarchical inter-mesh communication scheme. It relies on locally refined mesh or mesh patches to increase the resolution of an underlying

coarse mesh only where needed. It can alleviate some of the complexities of the generation of high quality grid and reduce the number of iterations of " trial-and-error " between the grid generation and solution required for tailoring the grid to the specification of a problem. Thus, It can offer orders of magnitude saving in computational and storage costs over an equivalent uniformly refined mesh. Berger et al. (1984) introduced the concept of AMR on structured grids. In this approach, a nested sequence of locally uniform grid patches is superimposed on an underlying coarse mesh. The grid adaptation methods generally has two categories: r-refinement (grid redistribution) and h-refinement (grid enrichment). r-refinement (see 2.2) is to redistribute the existing grid nodes into an advantageous distribution in the domain, while keeping the total number of grid points constant. This method is especially suited for structured grids involving moving surfaces. Due to the fixed number of grid nodes, the movement of nodes may cause local depletion and thus introduce severe distortion of the grid. So the initial mesh should have sufficient spatial resolution. In the h-refinement technique, more nodes are added to regions where a higher accuracy is desired. This technique relies on the sub-division of mesh elements. This approach results in fine grid elements which are fully nested with their forming coarse grid elements, as well as fine meshes which contain, as a subset of their vertices, all the coarse grid vertices. These properties enable a very accurate and efficient transfer of variables from one grid to another, as well as a simple framework for encoding history effects to determine parent-child relationships between cells. This, in turn, enables efficient use of de-refinement techniques. Efficiency, de-refinement, and accuracy of interpolation make these methods ideal for transient problems. In the meantime, it requires some type of data transfer among the consecutive mesh. The h-refinement method is particularly attractive due to its flexibility, especially when it is used in conjunction with unstructured grids.

A complete adaptive algorithm must include an error estimation indicator, a grid adaptaitive module, and a flow solution module. The basic steps of an adaptive strategy are:

(a) Calculation of the initial solution

(b) Estimation of the local error

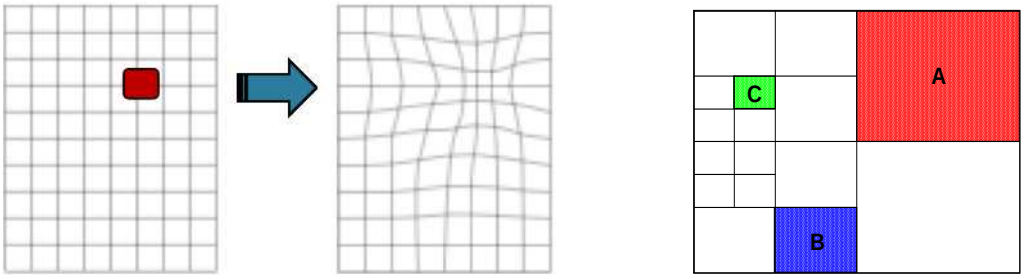

(a) r-refinement (b) h-refinement

Figure 2.1: Grid adaptation on a mesh

(c) Mesh adaptation according to estimated error detector

(d) Initialization of the solution on the adapted mesh

(e) Resumption of the numerical calculations.

AMR was originally developed for inviscid, compressible flow (Berger et al., 1984, 1989). It has been extended to solve Navier-Stokes equations, time dependent problems and more. Several AMR techniques have been developed and applied to compressible flow fields to capture characteristics at the strong gradient or discontinuous regions requiring higher space resolution (such as regions involving shock waves, vortices and wakes). It has been employed on both structured, particularly on Cartesian meshes, and unstructured meshes. Mavriplis (1990) coupled an adaptive grid refinement strategy with an unstructured multigrid algorithm and produced an efficient solver for two-dimensional flow with complex configurations. Pizadeh (1999) combined different grid adaptation techniques and applied to three-dimensional inviscid flow. Wendroff (2005) applied AMR to cell-centered Lagrangian (CCL) coordinates with a high-order method in one-dimensional problems. Anderson et al. (2004) successfully combined AMR with the Arbitrary Lagrangian-Eulerian (ALE) method for applications in inviscid gas dynamics. The advent of adaptive mesh refinement made the Cartesian grid methods practical (Aftosmis, 1997; Aftosmis et al., 2000, 2002). Corrier (1994) implemented adaptively-refined, Cartesian-Cell scheme for Euler and Navier-Stokes Equations. Hunt (2004) conducted an adaptive 3D Cartesian approach for inviscid flow about static and dynamic configurations. Wang

et al. (2002) developed an anisotropic adaptive viscous Cartesian grid method capable of handing complex geometries automatically.

Previous work on engine simulation has shown advantages of local mesh refinement. Nomura et al. (2001) used local grid refinement for the analysis of mixture formation and combustion of the direct injection gasoline engine. However, the local adaptation was limited to a pre-refined region without the capability of dynamical mesh adjustment during the simulation. A dynamic AMR scheme was demonstrated to achieve accurate spray penetration compared to a uniformly fine mesh (Lippert et al., 2005).

2.3 Diesel Engine Modeling

Numerical modeling can provide valuable insights into the physics and chemistry of the combustion processes in diesel engines to improve the engine performance and emission control. Various sub-models have been developed for modeling diesel engine combustion including the wall heat transfer model, spray model, ignition model, combustion model, and NOx and soot emission model. Various models have been developed for diesel combustion simulations based on KIVA3V (Patterson et al., 1994; Kong et al., 1995; Han et al., 1996; Patterson et al., 1998; Kong et al., 1999). These models were successfully applied to model different types of diesel engines under various operating conditions.

The accuracy of any model in a CFD code is dependent on the accuracy of its supporting sub-models. A wall heat transfer model is important because it affects the prediction of engine performance and efficiency, exhaust emissions, and engine component thermal stresses. To avoid the thermal stresses in regions of high heat flux and deterioration of lubricating oil films, proper cooling for the cylinder head, cylinder, and piston is desired. On the other hand, an increase in heat transfer through the combustion chamber walls will lower the gas temperature and pressure in the cylinder, and thus reduce the work per cycle transferred to the piston. Heat lost from the working gas to the cooling system of a conventional diesel engine takes up to 30% of the fuel energy (Liu et al., 1998). Changes of gas temperature due to wall heat transfer also affects the emission formation processes. Because of the importance of heat transfer in engines,

heat transfer models (Han et al., 1997; Tiainen et al., 2004; Schubert et al., 2005) have been studied and incorporated into almost all the computer codes for multidimensional simulation of combustion in engines.

In an internal combustion engine wall heat transfer through the chamber wall consists of gas-phase convection, wall film conduction, and soot radiation. The heat flux depends on the the gas temperature near the wall and the temperature of the combustion chamber wall. Thus, local wall temperature distribution is essential to accurately predict the wall heat transfer in the diesel engine.

Due to the lack of precise wall temperature profile or heat transfer coefficients from measurements, usually models assumes a constant temperature thermal boundary condition on each surface of the cylinder head, liner, and piston. This is not consistent with the real spatial temperature variation on each surface of the combustion chamber.

2.4 Conjugate Heat Transfer Modeling

It is necessary to obtain the temperature distribution on the chamber surfaces. A coupled method, referred to as Conjugate Heat Transfer (CHT) model, can calculate the flow field and heat transfer in the solid regions exposed to the flow simultaneously. Conjugate heat transfer is a useful tool for thermal design and analysis in industrial applications. It has been applied to existing CFD codes for aerothermal analysis (Xue, 2005) and design of microelectronics (Culham et al., 1993). Coupled approach has also been applied for the heat transfer study in IC engines.

Assanis et al. (1987) performed the wall conduction calculation by a combination of zero and one-dimensional energy balances. In the above study, new surface temperatures were determined by performing an energy balance between the cycle averaged gas-to-wall heat transfer rate and the heat rate conducted through the wall at the end of each cycle. This approach is computationally efficient, however, it underestimates the effects of cyclic transient in two-dimensional geometries, such as corners exposed to the combustion gas. Assanis et al. (1988) improved the zero and one-dimensional model to a two-dimensional model and developed a fi-

nite element program to model the transient temperature distributions of the piston, liner, and rings. Liu et al. (1998) developed a two-dimensional axisymmetric transient heat conduction computer program for predicting the temperature of the engine combustion chamber walls. The influence of combustion wall temperature on the engine heat transfer and NOx formation was investigated. Wiedenhoefer et al. (2000) developed a three-dimensional, finite-element-based, transient heat conduction code to calculate the temperature distributions of the components of a heavy-duty diesel engine through an iterative sequence with the KIVA-3V code. Further, Wiedenhoefer et al. (2003) used the code to study the soot deposition in heavy-duty diesel engines with a radiation model accounting for the radiative heat transfer. Xin et al. (2003) developed a methodology of integrating in-cylinder flow and combustion simulations with heat transfer calculations in solid components and cooling passage for practical design applications. Urip (2006) developed a numerical model to solve the temperature distribution inside engine metal components, and performed heat transfer analysis on a V8 FORD engine model. Nuutine et al. (2008) used a conjugate heat transfer model to study the heat transfer and temperature on piston surface with different wall functions.

CHAPTER 3. BASELINE CFD CODES

A family of computational fluid dynamics codes call KIVA have been developed for engine simulations at Los Alamos National Laboratory. These codes integrate the essential underlying physics models such as spray, combustion, and turbulence models with moving boundaries in a CFD code to simulate internal combustion engines. KIVA codes have been used extensively by the universities and industries to serve as a platform for physical sub-model development for engine simulations. In this chapter, the latest version of the KIVA code, KIVA-4 (Torres et al., 2006; Torres, 2007), is introduced, including governing equations and numerical methods.

3.1 Governing Equations

KIVA-4 generalizes the computaional grid from structured to unstructured, which provides an easier route in discretization of physical domains as complicated as internal combustion engines. Its unstructured capability facilitates grid construction for complex geometries and affords a higher degree of flexibility. KIVA-4 solves the conservative equations closed by the $k-\epsilon$ turbulence equations for the gas phase.

The continuity equation for species m is

$$\frac{\partial \rho_m}{\partial t} + \nabla \cdot (\rho_m \vec{u}) = \nabla \cdot [\rho D \nabla (\frac{\rho_m}{\rho})] + \dot{\rho}_m^{chem} + \dot{\rho}_m^{spray} \tag{3.1}$$

where ρ_m is the mass density of species m, ρ is the total mass density, and $\vec{u}$ is the fluid velocity. D is the diffusion coefficient. $\dot{\rho}_m^{chem}$ and $\dot{\rho}_m^{spray}$ are the source terms due to chemistry and spray, respectively. The total fluid density equation is obtained by summing over all species

$$\frac{\partial \rho}{\partial t} + \nabla \cdot (\rho \vec{u}) = \dot{\rho}^{spray} \tag{3.2}$$

The momentum equation for the fluid mixture is

$$\frac{\partial(\rho\vec{u})}{\partial t} + \nabla\cdot(\rho\vec{u}\vec{u}) = -\frac{1}{a^2}\nabla p - A_o\nabla(2/3\rho k) + \nabla\cdot\vec{\vec{\sigma}} + F^{spray} + \rho\vec{g} \tag{3.3}$$

where p is the fluid pressure. The dimensionless quantity a is used in conjunction with the Pressure Gradient Scaling (PGS) (Ramshaw et al., 1985) Method. This is a method for enhancing computational efficiency in low Mach number flows, where the pressure is nearly uniform. The quantity A_o is zero in laminar calculations and unity when one of the turbulence models is used. F^{spray} is the rate of momentum gain per unit volume due to the spray. $\vec{g}$ is the specific body force. The viscous stress tensor is Newtonian in form

$$\vec{\vec{\sigma}} = \mu[\nabla\vec{u} + (\nabla\vec{u})^T] + \lambda\nabla\cdot\vec{u}I \tag{3.4}$$

The internal energy equation is

$$\begin{aligned}\frac{\partial(\rho I)}{\partial t} + \nabla\cdot(\rho\vec{u}I) &= -p\nabla\cdot\vec{u} + (1-A_o)\vec{\vec{\sigma}}:\nabla\vec{u} - \nabla\cdot(-K\nabla T - \rho D\sum_m h_m\nabla(\rho_m/\rho)) \\ &\quad + A_o\rho\epsilon + \dot{Q}^{chem} + \dot{Q}^{spray}\end{aligned} \tag{3.5}$$

where I is the specific internal energy, T is the fluid temperature and h_m the specific enthalpy of species m. $\dot{Q}^{chem}$ and $\dot{Q}^{spray}$ are the source terms from the chemical heat release and spray interactions.

Two transport equations are solved for the turbulent kinetic energy k and its dissipation rate ϵ:

$$\frac{\partial(\rho k)}{\partial t} + \nabla\cdot(\rho\vec{u}k) = -\frac{2}{3}\rho k\nabla\cdot\vec{u} + \vec{\vec{\sigma}}:\nabla\vec{u} + \nabla\cdot[(\frac{\mu}{\mathrm{Pr}_k})\nabla k] - \rho\epsilon + \dot{W}^{spray} \tag{3.6}$$

and

$$\begin{aligned}\frac{\partial(\rho\epsilon)}{\partial t} + \nabla\cdot(\rho\vec{u}\epsilon) &= -(\frac{2}{3}c_{\epsilon_1} - c_{\epsilon_3})\rho\epsilon\nabla\cdot\vec{u} + \nabla\cdot[(\frac{\mu}{\mathrm{Pr}_\epsilon})\nabla\epsilon] + \frac{\epsilon}{k}[c_{\epsilon_1}\vec{\vec{\sigma}}:\nabla\vec{u} \\ &\quad - c_{\epsilon_2}\rho\epsilon + c_s\dot{W}^{spray}]\end{aligned} \tag{3.7}$$

These are standard k-ϵ equations with some added terms. The source term $-(\frac{2}{3}c_{\epsilon_1} - c_{\epsilon_3})\nabla\cdot\vec{u}$ in the ϵ-equation accounts for length scale changes when there is velocity dilatation. Source term involving the quantity $\dot{W}^{spray}$ arise due to interaction with the spray.

The conservation equations are written in the integral form in finite volume frame as follows. Conservation equation of mass for species m:

$$\frac{D}{Dt}\int_V \rho_m dV = \oint_A [\rho D \nabla(\frac{\rho_m}{\rho})]dA + \int_V \dot{\rho}_m^{chem} dV + \int_V \dot{\rho}_m^{spray} dV \tag{3.8}$$

Conservation equation of mass:

$$\frac{D}{Dt}\int_V \rho dV = \int_V \dot{\rho}^{spray} dV \tag{3.9}$$

Conservation equation of momentum:

$$\frac{D}{Dt}\int_V \rho\vec{u}dV = -\oint_S [\frac{1}{a^2}P + A_o\frac{2}{3}\rho k]dA + \oint_S \vec{\vec{\sigma}}\cdot dA + \int_V F^{spray}dV + \int_V \rho\vec{g}dV \tag{3.10}$$

Conservation equation of energy:

$$\begin{aligned}\frac{D}{Dt}\int_V \rho I dV &= \int_V -P\nabla\cdot\vec{u}dV + \int_V (1-A_o)\vec{\vec{\sigma}}:\nabla\vec{u}dV + \oint_A [K\nabla T + \rho D\sum_m h_m \\ &\quad \nabla(\frac{\rho_m}{\rho})]dA + \int_V A_o\rho\epsilon dV + \int_V \dot{Q}^{spray}dV + \int_V \dot{Q}^{chem}dV \end{aligned}\tag{3.11}$$

and the $k-\epsilon$ turbulence equations

$$\begin{aligned}\frac{D}{Dt}\int_V \rho k dV &= -\int_V \frac{2}{3}\rho k\nabla\cdot\vec{u}dV + \int_V \vec{\vec{\sigma}}:\nabla\vec{u}dV + \oint_A [(\frac{\mu}{Pr_k})\nabla k]dA - \int_V \rho\epsilon dV \\ &\quad + \int_V \dot{W}^{spray}dV \end{aligned}\tag{3.12}$$

$$\begin{aligned}\frac{D}{Dt}\int_V \rho\epsilon dV &= -\int_V (\frac{2}{3}c_{\epsilon_1} - c_{\epsilon_3})\rho\epsilon\nabla\cdot\vec{u}dV + \oint_A [(\frac{\mu}{Pr_\epsilon})\nabla\epsilon]\cdot dA + \int_V \frac{\epsilon}{k}[c_{\epsilon_1}\vec{\vec{\sigma}}:\nabla\vec{u} \\ &\quad -c_{\epsilon_2}\rho\epsilon + c_s\dot{W}^{spray}]dV \end{aligned}\tag{3.13}$$

where Pr_k, Pr_ϵ, c_{ϵ_1}, c_{ϵ_2}, $c_{\epsilon_3}$and c_s are turbulence constants defined in Table 3.1 (Launder et al., 1974; Yakhot et al., 1992). The state relations are assumed to be those of an ideal gas mixture as described below.

$$P = R_0 T\sum_m (\frac{\rho_m}{W_m}) \tag{3.14}$$

$$I(T) = \sum_m (\frac{\rho_m}{\rho})I_m(T) \tag{3.15}$$

Constants	Standard $k-\epsilon$	RNG $k-\epsilon$
c_{ϵ_1}	1.44	1.42
c_{ϵ_2}	1.92	1.68
c_{ϵ_3}	-1.0	Eq.(3.55)
Pr_ϵ	1.3	0.72
Pr_k	1.0	0.72
c_μ	0.09	0.085
c_s	1.5	1.5

Table 3.1: Turbulence constants

$$c_p(T) = \sum_m (\frac{\rho_m}{\rho}) c_{pm}(T) \tag{3.16}$$

$$h_m(T) = I_m(T) + \frac{R_0 T}{W_m} \tag{3.17}$$

A stochastic method for Lagrangian particle dynamics is used to solve the spray droplet phase (Amsden et al., 1989). The spray equation formulation is used to represent the complex physical processes, drop collisions and coalescences and breakup, in engine sprays. In the spray equation a droplet probability distribution function f is solved. f has eleven independent variables, and they are the three droplet position components $\vec{X}$, three velocity components $\vec{V}$, equilibrium radius r, temperature T_d, distortion from sphericity y, the time rate of change $\dot{y}$, and time t. The temporal and spatial evolution of the distribution function is described by a conservation equation. It is commonly referred to as the spray equation and can be written as:

$$\begin{aligned} \frac{\partial f}{\partial t} &= -\nabla_{\vec{X}} \cdot (f\vec{V}) - \nabla_{\vec{V}} \cdot (f\vec{F}) - \frac{\partial}{\partial r}(fR) - \frac{\partial}{\partial T_d}(f\dot{T}_d) - \frac{\partial}{\partial y}(f\dot{y}) - \frac{\partial}{\partial \dot{y}}(f\ddot{y}) \\ &\quad + \dot{f}_{collision} + \dot{f}_{breakup} \end{aligned} \tag{3.18}$$

$\vec{F}$ denotes the force per unit mass, i.e. an acceleration. R, $\dot{T}_d$, and $\ddot{y}$ are the time rates of change of radius r, temperature T_d, and oscillation velocity $\dot{y}$, respectively, for an individual drop. The source terms $\dot{f}_{collision}$ and $\dot{f}_{breakup}$ account for changes in the distribution function due to droplet collision and breakups, respectively. The collision source term $\dot{f}_{collision}$ is given

by

$$\begin{aligned}
\dot{f}_{collision} &= \frac{1}{2}\int\int f(\vec{x},\vec{v_1},r_1,T_{d_1},y_1,\dot{y}_1,t)f(\vec{x},\vec{v_2},r_2,T_{d_2},y_2,\dot{y}_2,t)\pi(r_1+r_2)^2|\vec{v}_1-\vec{v}_2| \\
&\{\sigma(\vec{v},r,T_d,y,\dot{y},\vec{v}_1,r_1,T_{d_1},y_1,\dot{y}_1,\vec{v}_2,r_2,T_{d_2},y_2,\dot{y}_2) \\
&-\delta(\vec{v}-\vec{v}_1)\delta(r-r_1)\delta(T_d-T_{d_1})\delta(y-y_1)\delta(\dot{y}-\dot{y}_1)\} \\
&-\delta(\vec{v}-\vec{v}_2)\delta(r-r_2)\delta(T_d-T_{d_2})\delta(y-y_2)\delta(\dot{y}-\dot{y}_2) \\
&d\vec{v}_1dr_1dT_{d_1}dy_1d\dot{y}_1d\vec{v}_2dr_2dT_{d_2}dy_2d\dot{y}_2 \qquad (3.19)
\end{aligned}$$

The collision transition probability function σ is defined so that $\sigma d\vec{v}drdT_d dydy\dot{}$ is the probable number of drops with properties in the implied intervals that result from a collision between a droplet with subscript 1 properties and one with subscript 2 properties. Two types of collisions are accounted for. If the collision impact parameter b is less than a critical value b_{cr} the droplets coalesce, and if b exceeds b_{cr} the droplets maintain their sizes and temperatures but undergo velocity changes. The critical impact parameter b_{cr} is given by

$$\begin{aligned}
b_{cr}^2 &= (r_1+r_2)^2 min(1.0, 2.4f(\gamma)/We_L) \\
f(\gamma) &= \gamma^3 - 2.4\gamma^2 + 2.7\gamma \\
\gamma &= r_2/r_1 \qquad where \quad r_1 \le r_2 \\
We_L &= \rho_d|\vec{v}_1-\vec{v}_2|r_1/a(\overline{T}_d) \qquad with \quad \overline{T}_d = \frac{r_1^3T_{d_1}+r_2^3T_{d_2}}{r_1^3+r_2^3}
\end{aligned}$$

The quantity a is the liquid surface tension coefficient, which is assumed to vary linearly between reference value a_0 at reference temperature T_0 and zero at the fuel species critical temperature T_{cr}. The σ is

$$\begin{aligned}
\sigma &= \frac{b_{cr}^2}{(r_1+r_2)^2}\delta[r-(r_1^3+r_2^3)^{1/3}]\delta[\vec{v}-\frac{r_1^3\vec{v}_1+r_2^3\vec{v}_2}{r_1^3+r_2^3}]\delta[T_d-\frac{r_1^3T_{d_1}+r_2^3T_{d_2}}{r_1^3+r_2^3}]\delta(y-y_2)\delta(\dot{y}-\dot{y}_2) \\
&+\frac{2}{(r_1+r_2)^2}\int_{b_{cr}}^{r_1+r_2}[\delta(r-r_1)\delta(\vec{v}-\vec{v}')\delta(T_d-T_{d_2})\delta(y-y_1)\delta(\dot{y}-\dot{y}_1) \\
&+\delta(r-r_2)\delta(\vec{v}-\vec{v}_2')\delta(T_d-T_{d_2})\delta(y-y_2)\delta(\dot{y}-\dot{y}_2)]bdb \qquad (3.20)
\end{aligned}$$

where

$$\vec{v_1'} = \frac{r_1^3\vec{v}_1 + r_2^3\vec{v}_2 + r_2^3(\vec{v}_1 - \vec{v}_2)\frac{b-b_{cr}}{r_1+r_2-b_{cr}}}{r_1^3 + r_2^3}$$
$$\vec{v_1'} = \frac{r_1^3\vec{v}_1 + r_2^3\vec{v}_2 + r_1^3(\vec{v}_2 - \vec{v}_1)\frac{b-b_{cr}}{r_1+r_2-b_{cr}}}{r_1^3 + r_2^3}$$

The breakup source term $\dot{f}_{breakup}$ is given by

$$\dot{f}_{breakup} = \int f(\vec{x}, \vec{v}_1, r_1, T_{d_1}, 1, \dot{y}_1, t)\dot{y}_1 B(\vec{v}, r, T_d, y, \dot{y}, \vec{v}_1, r_1, T_{d_1}, \dot{y}_1, \vec{x}, t)d\vec{v}_1 dr_1 dT_{d_1} d\dot{y}_1 \quad (3.21)$$

The breakup transition probability function B is defined so that $Bd\vec{v}drdT_d dyd\dot{y}$ is the probable number of droplets with properties in the implied intervals that are produced by the breakup of a droplet with subscript 1 properties. The meaning of Eq.(3.21) is the following: when a droplet's distortion y exceeds unity, it break up into a distribution of smaller drops given by B. We obtain the total source to f by multiplying the local flux of droplets through the surface $y \equiv 1$ by B and integrating over the entire surface $y \equiv 1$.

After breakup we assume the droplet radii follow a χ-squared distribution:

$$g(r) = \frac{1}{\bar{r}} e^{-r/\bar{r}} \quad (3.22)$$

where the Sauter Mean Radius r_{32} is given by

$$r_{32} = 3\bar{r} = \frac{r_1}{\frac{7}{3} + \frac{1}{8}\frac{\rho_d r_1^3}{a(T_{d_1})}\dot{y}_1^2} \quad (3.23)$$

The product droplet velocities also differ from that of the parent droplet by a velocity with magnitude w and with direction randomly distributed in a plane normal to the relative velocity vector between the parent drop and gas. The quantity w is given by

$$w = \frac{1}{2} r_1 \dot{y}_1 \quad (3.24)$$

The precise form for B is

$$B = g(r)\delta(T_d - T_{d_1})\delta(y)\delta(\dot{y})\frac{1}{2\pi}\int \delta[\vec{v} - (\vec{v}_1 + w\vec{n})]\vec{n} \quad (3.25)$$

where the integral is over normal directions to the relative velocity vector. We now define the functions F, R, $\dot{T}_d$, and $\ddot{y}$ that determine the trajectories of individual droplets. The droplet

acceleration F has contribution due to aerodynamic drag and gravitation force:

$$F = \frac{3}{8}\frac{\rho}{\rho_d}\frac{|\vec{u}+\vec{u}^{'}-\vec{v}|}{r}(\vec{u}+\vec{u}^{'}-\vec{v})C_D + \vec{g} \tag{3.26}$$

The drag coefficient C_D is given by

$$\begin{cases} \frac{24}{Re_d}(1+\frac{1}{6}Re_d^{2/3}) & Re_d \leq 1000 \\ 0.424 & Re_d > 1000 \end{cases} \tag{3.27}$$

where $Re_d = \frac{2\rho|\vec{u}+\vec{u}^{'}-\vec{v}|r}{\mu_{air}(\hat{T})}$, and $\hat{T} = \frac{T+2T_d}{3}$. The gas turbulent velocity $\vec{u}^{'}$ is added to the local mean gas velocity when calculating a droplet's drag and vaporization rate. It is assumed that each component $\vec{u}^{'}$ follows a Gaussian distribution with mean square deviation $2/3k$. Thus we assume

$$G(\vec{u}^{'}) = (4/3\pi k)^{-3/2} exp(-3|\vec{u}^{'}|^2/4k) \tag{3.28}$$

The value of $\vec{u}^{'}$ is chosen once every turbulence correlation time t_{turb} and is otherwise held constant. The droplet correlation time is given by

$$t_{turb} = min(k/\epsilon, c_{ps}, \frac{k^{3/2}}{\epsilon}\frac{1}{|\vec{u}+\vec{u}^{'}-\vec{v}|}) \tag{3.29}$$

where c_{ps} is an empirical constant with value 0.16432. Thus t_{turb} is the minimum of an eddy breakup time and a time for the droplet to traverse an eddy.

The rate of droplet radius change R is given by the Frossling correlation,

$$R = -\frac{(\rho D)_{air}(\hat{T})}{2\rho_d r}\frac{Y_1^* - Y_1}{1-Y_1^*}Sh_d \tag{3.30}$$

where Sh_d is the Sherwood number for mass transfer, Y_1^* is the fuel vapor mass fraction at the droplet's surface, $Y_1 = \rho_1/\rho$, and $(\rho D)_{air}(\hat{T})$ is the fuel vapor diffusivity in air. The Sherwood number is given by

$$Sh_d = (2.0 + 0.6Re_d^{1/2}Sc_d^{1/3})\frac{\ell n(1+B_d)}{B_d} \tag{3.31}$$

where $Sc_d = \frac{\mu_{air}(\hat{T})}{\rho D_{air}(\hat{T})}$ and $B_d = \frac{Y_1^* - Y_1}{1 - Y_1^*}$. The surface mass fraction Y_1^* is obtained from

$$Y_1^*(T_d) = \frac{W_1}{W_1 + W_0(\frac{p}{p_v(T_d)} - 1)} \tag{3.32}$$

where W_0 is the local average molecular weight of all species exclusive of fuel vapor and $p_v(T_d)$ is the equilibrium fuel vapor pressure at the temperature T_d. To obtain Eq (3.32), we have assumed that the droplet temperature is uniform and that the partial pressure of fuel vapor at the droplet's surface equals the equilibrium vapor pressure. For the vapor diffusivity in air we use the empirical correlation

$$(\rho D)_{air}(T) = D_1 T^{D_2} \tag{3.33}$$

where, D_1 and D_2 are constants.

The rate of droplet temperature change is determined by the energy balance equation

$$\rho_d \frac{4}{3}\pi r^3 c_\ell \dot{T}_d - \rho_d 4\pi r^2 R L(T_d) = 4\pi r^2 Q_d \tag{3.34}$$

where c_ℓ is the liquid specific heat, $L(T_d)$ is the latent heat of vaporization, and Q_d is the rate of heat conduction to the droplet surface per unit area. Equation (3.28) is a statement that the energy conducted to the droplet either heats up the droplet or supplies heat for vaporization. The heat conduction rate Q_d is given by the Ranz-Marshall correlation

$$Q_d = \frac{K_{air}(\hat{T})(T - T_d)}{2r} Nu_d \tag{3.35}$$

where

$$\begin{aligned} Nu_d &= (2.0 + 0.6 Re_d^{1/2} Pr_d^{1/3}) \frac{\ell n(1 + B_d)}{B_d} \\ Pr_d &= \frac{\mu_{air}(\hat{T}) c_p(\hat{T})}{K_{air}(\hat{T})} \\ K_{air}(\hat{T}) &= \frac{K_1 \hat{T}^{3/2}}{\hat{T} + K_2} \end{aligned}$$

Here, c_p is the local specific heat at constant pressure and at temperature $\dot{T} = (T + 2T_d)/3$, and K_1 and K_2 are constants.

Consistent with the approximation that the liquid density is constant, we also assume its internal energy I_ℓ is a function of temperature alone. Thus the liquid enthalpy will have a small pressure dependence,

$$h_\ell(T_d, p) = I_\ell(T_d) + p/\rho_d \tag{3.36}$$

Since the latent heat of vaporization L is the energy required to convert a unit mass of liquid to vapor at constant pressure equal to the equilibrium vapor pressure, the liquid and vapor enthalpies and internal energies and L are related by

$$L(T_d) = h_1(T_d) - h_\ell(T_d, p_v(T_d)) = I_1(T_d) + RT_d/W_1 - I_\ell(T_d) - p_v(T_d)/\rho_d \tag{3.37}$$

The equation for the acceleration of the droplet distortion parameter is

$$\ddot{y} = \frac{2}{3}\frac{\rho}{\rho_d}\frac{(\vec{u} + \vec{u}^{'} - \vec{v})^2}{r^2} - \frac{8a(T_d)}{\rho_d r^3}y - \frac{5\mu_\ell(T_d)}{\rho_d r^2}\dot{y} \tag{3.38}$$

where $\mu_\ell(T_d)$ is the viscosity of the liquid. Equation (3.38), which is based on the analogy between an oscillating droplet and a spring-mass system, is the equation of a forced, damped harmonic oscillator. The external forces is supplied by the gas aerodynamic forces on the droplet. The restoring force is supplied by surface tension forces. Damping is supplied by liquid viscosity. A detailed discussion of Eq. (3.38) may be found in (O'Rourke et al., 1987).

The exchange functions $\dot{\rho}^{spray}$, F^{spray}, $\dot{Q}^{spray}$, and $\dot{W}^{spray}$ are obtained by summing the rates of change of mass, momentum, and energy of all droplets at position $\vec{x}$ and time t.

$$\begin{aligned}
\dot{\rho}^{spray} &= -\int f\rho_d 4\pi r^2 R d\vec{v} dr dT_d dy d\dot{y} \\
F^{spray} &= -\int f\rho_d (4/3\pi r^3 F^{'} + 4\pi r^2 R\vec{v}) d\vec{v} dr dT d dy d\dot{y} \\
\dot{Q}^{spray} &= -\int f\rho_d 4\pi r^2 R[I_\ell(T_d) + \frac{1}{2}(\vec{v} - \vec{u})^2] \\
&\quad +4/3\pi r^3[c_\ell \dot{T}_d + F^{'} \cdot (\vec{v} - \vec{u} - \vec{u}^{'})] d\vec{v} dr dT_d dy d\dot{y} \\
\dot{W}^{spray} &= -\int f\rho_d 4/3\pi r^3 F^{'} \cdot \vec{u}^{'} d\vec{v} dr dT_d dy d\dot{y}
\end{aligned}$$

where $F^{'} = F - g$. Physically, $\dot{W}^{spray}$ is the negative of the rate at which the turbulent eddies are doing work in dispersing the spray droplets. Since $\vec{u}^{'}$ follows the Gaussian distribution

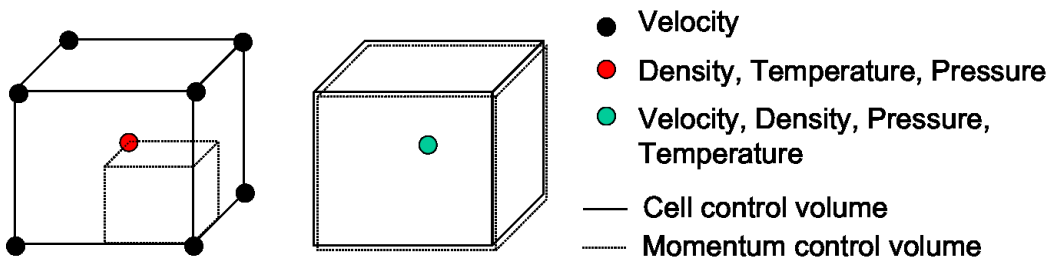

Figure 3.1: The variable placement in a staggered mesh (left) and a collocated mesh (right)

(Eq.3.28) it can be shown that $\dot{W} < 0$, and thus this term always depletes turbulent kinetic energy.

By solving the spray equation, the exchange terms can be obtained so that the interactions between the liquid and gas phases. In order to assure conservation of mass, momentum and energy of the total system (liquid and gas), these terms need to be added to the gas phase conservation equations above.

3.2 Numerical Schemes

KIVA-4 solves the conservation equations in three stages using an Arbitrary Lagrangian-Eulerian (ALE) method. Stage A computes the influence of the spray and chemical reactions on the gas phase. Stage B solves the governing equations in Lagrangian form using a finite volume scheme. Stage C is the Eulerian stage in which the grid is moved to new locations and the corresponding fluxes of mass, momentum, energy, and turbulence are exchanged.

KIVA-4 staggers its variables. Variables including density, temperature, and pressure, are located at cell center, and the corresponding control volume coincides with the cell volume (see Fig. 3.1). On the other hand, velocity is located at the vertices, and the corresponding control volume (vertex control volume) consists of portions of computational cells that share a given vertex (see Fig. 3.1). The numerical method for the governing equations are summarized in the solution sequence of stages A, B, and C.

3.2.1 Stage A

The density of species is solved at a constant volume. Contributions from spray evaporation and chemical reactions are included.

$$\frac{\rho_m^A - \rho_m^n}{\Delta t} = \dot{\rho}_m^{chem} + \dot{\rho}_m^{spray} \tag{3.39}$$

The momentum transfer due to spray and gravity force is computed over each momentum control volume.

$$\begin{aligned} \frac{(M_V^A + S_V)\vec{u}^A - M_V^n \vec{u}^n}{\Delta t} &= -\sum_V N_p \frac{4}{3}\pi\rho_p[(r_p^B)^3(\frac{\vec{v}_p' + \Delta t D_p \tilde{u}}{1 + \Delta t D_p}) - (r_p')^3 \vec{v}_p'] \\ &\quad + \vec{g} M_V^n \end{aligned} \tag{3.40}$$

$$S_V = \Delta t \sum_v N_P \frac{4}{3}\pi\rho_P (r_P^B)^3 \frac{\Delta t D_P}{1 + \Delta D_P} \tag{3.41}$$

The energy calculation is conducted in a constant volume where only the spray and chemical reaction sources are accounted.

$$\frac{M^A I A - M^n I^n}{\Delta t} = V^n(\dot{Q}^{chem} + \dot{Q}^{spray}) \tag{3.42}$$

3.2.2 Stage B

In the Lagrangian stage B, the density of species are computed due to the diffusion.

$$M^B(Y_m^B - Y_B^A) - \frac{\Delta t}{Sc_t}[\sum_f (\mu_t^n)_f (\nabla Y_m^A)_f \cdot A_f^n + \sum_f (\mu_t^n)_f \nabla[\phi_D (Y_m^B - Y_m^A)]_f \cdot A_f^n] = 0 \tag{3.43}$$

The turbulent Schmidt number $Sc_t = \frac{\mu_t}{\rho D}$. The viscosity $\mu_t = \mu_{air} + A_o c_\mu \rho \frac{k^2}{\epsilon}$. Here, μ_{air} is the laminar air viscosity.

The momentum transfer is computed for the diffusion terms and the viscous stress terms.

$$\begin{aligned} &(M_V^B + S_V)\frac{\vec{u}^B - \vec{u}^A}{\Delta t} - \sum_c [\frac{1}{(a^n)^2}(\phi_p P^p + (1 - \phi_p)P^p) + A_0 \frac{2}{3}\rho^A k^A]_c \sum_f \chi_{f_c} A_{f_c}^n \\ &+ \sum_c [\phi_D \vec{\vec{\sigma}}(\vec{u}^B) + (1 - \phi_D)\vec{\vec{\sigma}}(\vec{u}^A)]_c \cdot \sum_f \chi_{f_c} A_{f_c}^n = 0 \end{aligned} \tag{3.44}$$

First the internal energy is updated to intermediate t-stage accounting for turbulence dissipation and enthalpy diffusion.

$$M^B \frac{I^t - IA}{\Delta t} = A_0 M^B \epsilon^A + \sum_f (\rho D)_f^n \{\sum_m h_m(T_f^n) \nabla[\phi_D Y_m^B + (1 - \phi_D) Y_m^A]_f\} \cdot A_f^n \tag{3.45}$$

Then, the viscous dissipation terms and diffusion terms are included to compute the internal energy at this stage to obtain the temperature,

$$\begin{aligned} T^B &= \{T^t + \frac{P^p + P^n}{2c_V^t}\frac{V^n}{M^B} + \frac{\Delta t}{M^B c_V^t}[\frac{1}{Pr_t}\sum_f (c_p\mu_t)_f \nabla(\phi_D T^B + (1-\phi_D)\tilde{T})_f \cdot A_f^n \\ &\quad +(1-A_0)(\phi_D \vec{\vec{\sigma}}(\vec{u}^B) : \nabla\vec{u}^B + (1-\phi_D)\vec{\vec{\sigma}}(\vec{u}^A) : \nabla\vec{u}^A)V^B]\}\{\frac{1}{1+\frac{P^p+P^n}{2c_V^t P^p}\bar{R}}\} \end{aligned} \quad (3.46)$$

The pressure p^B is solved so that the volume V^B from the ideal equation of state and the Lagrangian volume V^{LAG} computed from the movement of the cell faces agree. The volume approximation from equation of state at p^B is given as,

$$V_c^B = V^B - \frac{1}{\gamma^t}\frac{V^B}{P^p}(P^B - P^p) \quad (3.47)$$

and the Lagrangian volume is calculated by

$$\begin{aligned} V^{LAG} &= V^n + \Delta t\sum_f [(\vec{u}\cdot A)_f^t + \Delta t\frac{dA_f}{dt}\cdot\vec{u}_f^n - \frac{\Delta t}{\rho_f^B}\nabla[\frac{\phi_p}{(a^n)^2}P^B + \frac{1-\phi_p}{(a^n)^2}P^n \\ &\quad +(\frac{2}{3}A_0\rho^A k^A)]_f \cdot A_f^n] \end{aligned} \quad (3.48)$$

A pressure P^B is sought so that V_c^B and V^{LAG} agree to some tolerance.

$$|V_c^B - V^{LAG}| < tol \quad (3.49)$$

The SIMPLE method is used to solve the velocity from Eq. (3.44), temperature from Eq. (3.46) and pressure from Eq (3.49) iteratively for stage B. Once the pressure criteria is satisfied, the pressure, temperature, and velocity are obtained at stage B. The density and internal energy are also updated. The individual equations (3.43), (3.44), (3.46), (3.49), (3.52), and (3.53) are solved by the conjugate residual method (O'Rourke et al., 1986).

3.2.3 Stage C

The turbulence equations are solved after the kinematic quantities in phase B are computed. The turbulent kinetic energy and turbulence dissipation rate are first updated with the spray contributions,

$$\frac{M^B k^A - M^n k^n}{\Delta t} = \dot{W}^{spray} V^n \quad (3.50)$$

$$\frac{M^B \epsilon^A - M^n \epsilon^n}{\Delta t} = c_s \dot{W}^{spray} V^n \frac{\epsilon^A}{k^n} \quad (3.51)$$

and then the diffusion terms in k and ϵ equations are solved using

$$\begin{aligned}\frac{M^B k^B - M^B k^A}{\Delta t} &= -\frac{2}{3}\rho^B \frac{V^B - V^n}{\Delta t}[(1-f)k^n + fk^B] + V^n[\phi_D \vec{\vec{\sigma}}(\vec{u}^B) : \nabla u^B + (1-\phi_D)\vec{\vec{\sigma}} \\ &\quad (\vec{u}^A) : \nabla \vec{u}^A] + \sum_f \frac{(\mu_t^n)_f}{Pr_k} \nabla[\phi_D k^B + (1-\phi_D)k^A]_f \cdot A_f^n \\ &\quad -M^B \frac{\epsilon^n}{k^n} k^B \qquad (3.52)\end{aligned}$$

$$\begin{aligned}\frac{M^B \epsilon^B - M^B \epsilon^A}{\Delta t} &= -(\frac{2}{3}c_{\epsilon_1} - c_{\epsilon_3})\rho^B \frac{V^B - V^n}{\Delta t}[(1-f)\epsilon^n + f\epsilon^B] + c_{\epsilon_1}\frac{\epsilon^n}{k^n} V^n[\phi_D \vec{\vec{\sigma}}(\vec{u}^B) : \nabla \vec{u}^B \\ &\quad +(1-\phi_D)\vec{\vec{\sigma}}(\vec{u}^A) : \nabla \vec{u}^A] + \sum_f \frac{(\mu_t^n)_f}{Pr_\epsilon} \nabla[\phi_D \epsilon^B + (1-\phi_D)\epsilon^A]_f \cdot A_f^n \\ &\quad -c_{\epsilon_2} M^B \frac{\epsilon^n}{k^n} \epsilon^B \qquad (3.53)\end{aligned}$$

In the RNG (ReNormalization Group) $k-\epsilon$ equations, the equation (3.53) is replaced by

$$\begin{aligned}\frac{M^B \epsilon^B - M^B \epsilon^A}{\Delta t} &= -(\frac{2}{3}c_{\epsilon_1} - c_{\epsilon_3})\rho^B \frac{V^B - V^n}{\Delta t}[(1-f)\epsilon^n + f\epsilon^B] + (c_{\epsilon_1} - \tilde{\tau})\frac{\epsilon^n}{k^n} V^n[\phi_D \vec{\vec{\sigma}}(\vec{u}^B) : \\ &\quad \nabla \vec{u}^B + (1-\phi_D)\vec{\vec{\sigma}}(\vec{u}^A) : \nabla \vec{u}^A] + \sum_f \frac{(\mu_t^n)_f}{Pr_\epsilon} \nabla[\phi_D \epsilon^B + (1-\phi_D)\epsilon^A]_f \cdot A_f^n \\ &\quad -c_{\epsilon_2} M^B \frac{\epsilon^n}{k^n} \epsilon^B \qquad (3.54)\end{aligned}$$

where $\tilde{\tau} = \frac{(1-\frac{\tau}{4.38})}{(1+0.012\tau^3)}$, and $\tau = \frac{k^n}{\epsilon^n}\sqrt{\frac{1}{\mu_t^n}[\phi_D \vec{\vec{\sigma}}(\vec{u}^B) : \nabla \vec{u}^B + (1-\phi_D)\vec{\vec{\sigma}}(\vec{u}^A) : \nabla \vec{u}^A] + \frac{2}{3}(\nabla \cdot \vec{u}^B)^2}$. In addition c_{ϵ_3} is replaced by

$$c_{\epsilon_3} = \begin{cases} 0.41333 + 0.06899\tau\tilde{\tau} - \frac{2}{3}c_\mu \tilde{\tau} \nabla \cdot \vec{u}^B \frac{k^n}{\epsilon^n} & (\text{if } \nabla \cdot \vec{u}^B \geq 0) \\ 0.41333 - 0.06899\tau\tilde{\tau} - \frac{2}{3}c_\mu \tilde{\tau} \nabla \cdot \vec{u}^B \frac{k^n}{\epsilon^n} & (\text{if } \nabla \cdot \vec{u}^B < 0) \end{cases} \qquad (3.55)$$

Pr_k, Pr_ϵ, c_{ϵ_1}, c_{ϵ_2}, and c_s are turbulence constants of RNG defined in Table 3.1. Wall functions are used to set velocities and modify the cell internal energy for cells adjacent to a wall.

In stage C, vertices are moved from their stage B locations to their new locations before the next global time step, $n+1$. When cell faces move with the vertices, the fluxes of mass, internal energy and turbulence quantities are computed at the cell faces. The faces of the vertex control volume also change and the momentum flux is computed between the vertex control volume. There are two types of convection scheme in KIVA-4: partial donor cell differencing (PDC) and quasi-second-order upwind (QSOU) differencing (Amsden et al., 1989). The flux equations are

solved by sub-cycling at a small time step Δt_c that satisfies the Courant stability condition. The time step is defined by,

$$\Delta t_c \leq f_{con} \Delta t^n \mathbf{min}_f(|\frac{V_c}{\delta V_f}|) \tag{3.56}$$

Here $f_{con} = 0.2$ and the minimum is a minimum over all faces. Thus, the number of sub-cycling of the flux calculation $n_{subcycle}$ is given by,

$$n_{subcycle} = \frac{\Delta t^n}{\Delta t_c}$$

3.2.4 Stochastic Particle Method

A Monte Carlo method is used for solving for the spray dynamics. This method samples randomly from assumed probability distributions that govern droplet properties at the injection and droplet behavior subsequent to injection, droplet collision and droplet breakup.

3.3 Collocated Version of KIVA-4

The collocated version of KIVA-4 has also been developed (Torres, 2007). In this version, the velocity is co-located at the cell-center along with density, temperature, and pressure (see Fig. 3.1). One advantage of the relocation of the velocity to the cell-center is that the velocity boundary conditions do not need to be prescribed at nodes but rather faces. Another advantage is that it become easier to incorporate other numerical schemes into the KIVA-4 code.

The primary equation which needs to be modified is the conservation equation of momentum equation (3.10). Basically, the viscous stress tensor term $\oint_A \sigma \cdot dA$ is needed to compute over all the faces of the cell instead of the vertex control volume as in staggered KIVA-4.

The collocation of pressure and velocity can cause unphysical pressure oscillations (Tsui et al., 2006). This is known as "checker-board" problem, which is a consequence of the linear interpolation for pressure difference in a co-located arrangement. Rhie et al. (1983) suggest that a higher-order term should be included to prevent this effect. Rhie-Chow interpolation method is used for computing face velocities to mitigate the unphysical pressure oscillations (Torres, 2007) in co-located arrangement. The term $(\vec{u} \cdot A)_f^B$ that is used for pressure solution Eq.(3.49)

and for flux calculations is computed by (Torres et al., 2006):

$$
\begin{aligned}
(\vec{u}\cdot A)_f^B &= (\vec{u}\cdot A)_f^t + \Delta t \frac{dA}{dt}\cdot \vec{u}_f^n - \frac{\Delta t}{\rho_f^B}\nabla[\frac{\phi_p}{(a^n)^2}P^B + \frac{1-\phi_p}{(a^n)^2}P^n(\frac{2}{3}A_o\rho^A k^A)]\cdot A_f^n \\
&\quad -\frac{\Delta t}{\frac{1}{2}(\rho_c+\rho_{cn})}[(\nabla P)_f - \frac{1}{2}[(\nabla P)_c + (\nabla P)_{cn}]]\cdot A_f^n \qquad (3.57)
\end{aligned}
$$

The flux of momentum is computed using the cell-centered-based scheme used for mass and internal energy fluxing. In addition, particles are coupled with gas using the cell-centered velocity of gas in the spray term $\int_V F^{spray} dV$.

CHAPTER 4. IMPLEMENTATION OF ADAPTIVE MESH REFINEMENT SCHEME

This chapter presents the implementation of the adaptive mesh refinement scheme for three-dimensional hexahedral meshes. First the cell division and deletion processes will be described in detail. The adaptive data structure and overall procedure of the adaptation integrated into collocated KIVA-4 are then presented. Here the collocated version of KIVA-4 is used, due to its advantages of efficient successive adaptation (Torres et al, 2006).

4.1 Refinement Strategy and Data Structure

The adaptive algorithm basically includes three elements: (1) adaptive data structure, (2) adaptive criterion, and (3) solution re-mapping procedure. The h-refinement approach was used in this study. This grid enrichment method starts from an initial coarse mesh, and the node insertion/deletion is performed during the simulation. A tree-based algorithm is applied to store the hierarchical grid structure as shown in Fig. 4.1. When a cell is tagged for refinement, the cell becomes the parent cell (root) and is isotropically split into eight child cells (leaves) that are siblings. Further refinements will introduce members of the next generation cells. The coarsening process is the recovery of the parent cell from its child cells by combining the original child cells.

The key decision in implementing the multilevel scheme is the design of an effective mesh adaptation strategy. The adaptation should be done on the fly on any level of the refined grid or the original grid. The procedure is intended to adequately represent the solution on the coarse mesh while still adapting fast enough to reduce the computational effort. This section will first describe the steps in performing the cell refinement and coarsening. The procedure

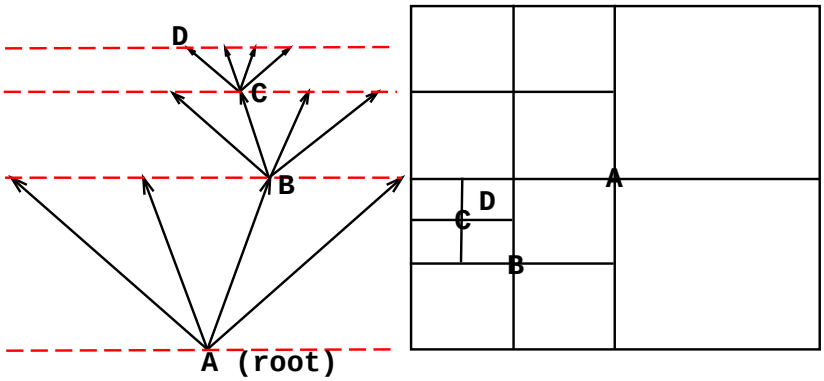

Figure 4.1: Logical relationship between cells for a two-dimensional tree. Each cell is represented by a square. Cell A is the root cell of the tree. Arrows indicate the relation of parent and children. Dashed lines indicate the relation of siblings

and adaptive data structure specific to the present CFD code will follow.

4.1.1 Cell Refinement

Refinement is achieved by recursive subdivisions of an initial coarse mesh (referred to as refinement level 0 or RL0 mesh), as shown in Figure 4.2. Figure 4.3 shows the cell indexing convention of a parent cell and its child cells. Any cell can be traced to the initial parent cell on the refinement level 0 mesh. Further, if a cell is refined N times, it will be the refinement level N mesh and have parent cells at level 0 through level (N-1). If a cell has never been divided, the refinement process starts from tagging the cells for division. Successive refinements to a cell will occur depending on the criteria. However, the difference in the refinement levels of the neighboring cells cannot exceed one in order to prevent interface cells from high skewness for mesh quality control. This will result in a gradual decrease in the size of the cells for the regions with high flow gradients. After the cells are tagged for refinement, the following steps are implemented:

(1) Sweep through all the cells tagged for division, and these cells will become parent cells. If a new parent cell has never been refined, the new nodes, edges, and faces will be

introduced to the interior of the cell. If a new parent cell was previously refined, then the previous subdivided nodes, sibling edges, and faces will be reactivated.

(2) If the faces of the parent cell are not divided, they will be subdivided, thus resulting in the generation of child edges, faces, and cells. Simultaneously its child cells on the new mesh will replace the parent cell. Appropriate arrays will be updated, and the relationship of the parent cell and its child cells will be recorded for future coarsening.

(3) If the neighboring cells have the same level as the original parent cell, AMR faces with hanging nodes will occur. If the neighboring cells have a higher level than the original parent cell, then original AMR faces will no longer exist because the new child cells have the same refinement level as the neighboring cells at this point. Connectivity information will be updated accordingly.

(4) If there are liquid drops in the parent cell, the drops will be distributed to the child cells according to their physical locations.

(5) If the parent cell is an injector cell, one of the child cells will become the injector cell according to the physical locations.

4.1.2 Cell Coarsening

In principle, the coarsening process is the inverse of the refinement process. Cells that have been tagged for deletion are eliminated with their sibling cells, resulting in the deletion of the corresponding child nodes, edges, and faces. The coarser meshes are formed by coalescing the sibling cells into their coarser parent cell. Only one level of coarsening is allowed in each coarsening activity. The parent cells are recovered by employing a special array. This array gives the identity of the parent cell for each child cell. Similar arrays give the parent faces and edges. Thus, expensive searches through the data structure can be avoided. The memory penalty for storing these data for the parents is not significant.

The coarsening process starts at the finest mesh level and then sweeps through the cells tagged for deletion recursively in the decreasing order of their refinement levels. All the sibling

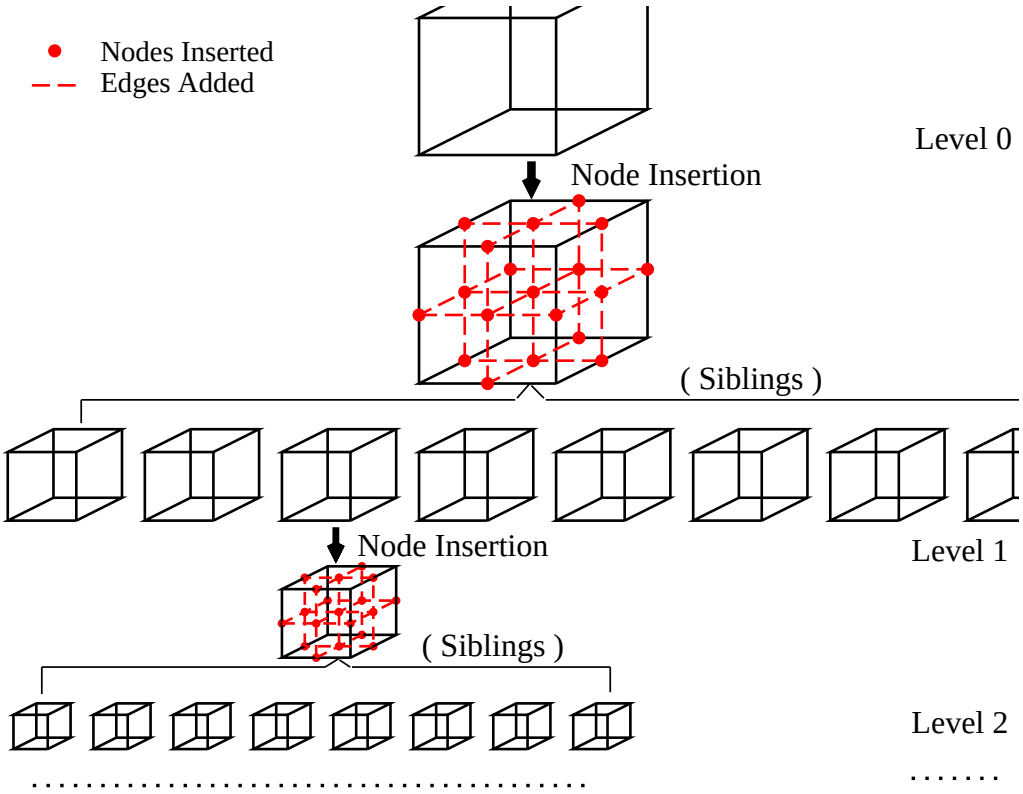

Figure 4.2: The isotropic node-insertion for a hex mesh. New nodes are inserted, sub-edges, sub-faces, and child cells are generated.

cells need to meet the coarsening criteria before the restoration of their parent cell. If one or more of the siblings has children of its own, then coarsening is suspended until those child cells have been coarsened. The grid cells will not be coarsened beyond their initial sizes. After all the sibling cells are tagged for coarsening, the following steps are implemented:

(1) Sweep through all of the cells tagged for coarsening, and trace the relationship between the parent and child cells.

(2) Sweep through all the parent cells to be restored. The child cells, and their faces, edges, and nodes that were previously embedded to the interior of each parent cell, are now deleted.

(3) The above deletion may leave some of the faces and edges of the parent cell divided. If

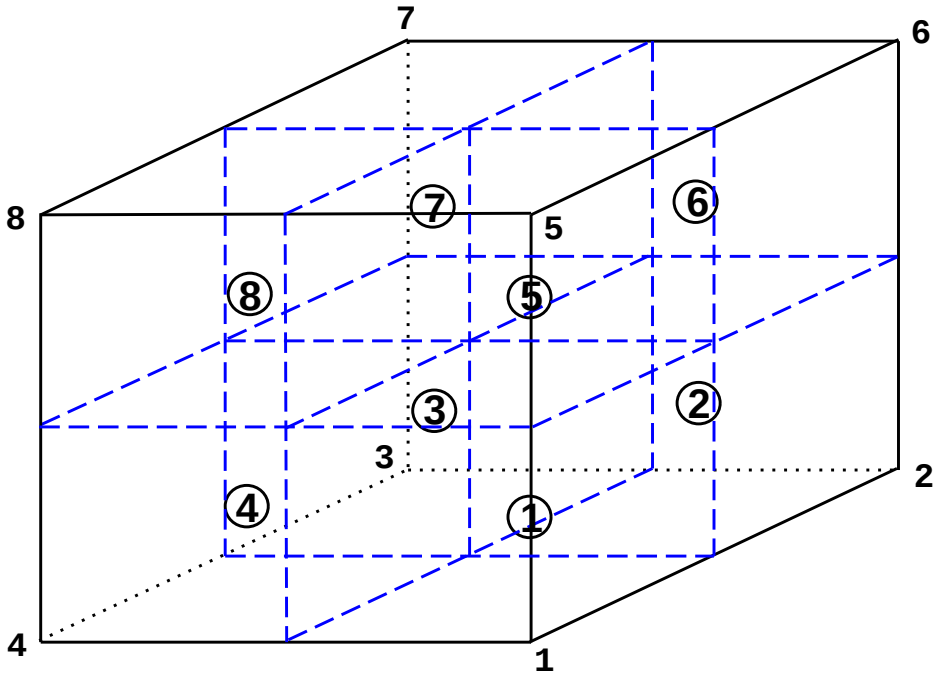

Figure 4.3: Illustration of the indices and relations of the child cells inside a parent cell. **1**-**8** indicate the cell indexing convention in KIVA-4 code. ①-⑧ indicate the children cells of a split cell

the adjacent cells have the same level as the parent cell, these sibling faces and edges are coarsened to restore the parent cell.

(4) If the adjacent cells have different refinement levels from the parent cell, the faces and edges are not deleted after coarsening, and thus the AMR face with hanging nodes will exist. Connectivity information will be updated accordingly.

(5) If there are liquid drops inside any of the sibling cells, they will be assigned to the parent cell.

(6) If the injector cell is one of the sibling cells, the parent cell will be identified as the injector cell.

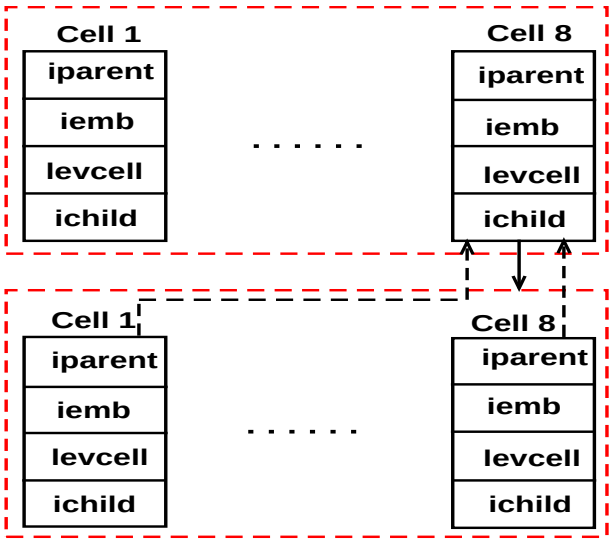

Figure 4.4: Relationship between the child cells and the parent cell and related data structure. The dashed box indicates a group of sibling cells, the dashed line with arrow indicates the relation from children to parent, and the solid line with arrow indicates the relation from the parent to the children

4.1.3 Adaptive Data Structure

The implementation of data structures for a dynamic adaptive algorithm is a relatively complicated task. The complexity and efficiency of the implementation strongly depend on the available mesh information from the flow solver and on the amount of the mesh information available from the previous adaptation step. This information is contained in the data that provide the connectivities between nodes, edges, faces, and cells. In the present work, a new set of cell-based data structures for the adaptation was developed and was well suited for the flow solver to achieve high storage efficiency. Appropriate attention to programming is needed for achieving an efficient access to the neighboring cells and cell level, as well as efficient traversal of all child cells and parent cells. The tree structure implemented is illustrated in Fig. 4.4. The essential arrays and trees are included in the data structures that conform to the convention of KIVA-4 as described in the following.

The level of the adapted mesh is indicated by the refinement level array LEVCELL(i), i=1,ncells:

LEVCELL(i) = 0 for the initial grid

LEVCELL(i) = n for the grid of Nth refinement level

The adaptive algorithm flags a local cell for refinement or coarsening with its siblings using the values of the cell flag array IEMB(i), i=1,,ncells:

IEMB(i) = 0: the cell i is tagged for neither refinement nor coarsening

IEMB(i) = 1: the cell i is tagged for refinement

IEMB(i) = -1: the cell i is tagged for coarsening

Eight child cells are formed after the isotropic division during the refinement. A tree structure is used to store the sibling cells sequentially. The tree is indicated by the array ICHILD(i,cell) for i=1,8. The parent of the sibling cells is marked by the array IPARENT(i) for i=1,ncells. An illustration of the tree corresponding to an adapted mesh is shown in Figure 1.

After an edge is divided, it is marked as a parent edge, and the set of two sibling edges are assigned to the edge array E2E(i,edge) for i=1,2. Similarly, after a face is divided and marked as a coarse face, the four sibling faces are assigned to the face array F2F(i,face) for i=1,4. Nodes are inserted into the faces, and sub-edges are formed. The four sub-edges are marked by the array F2E(i,iface) for i=1,4.

The storage penalty for storing these data for the parents is not significant since the number of the parent cells is one-eighth of the number of the child cells for each refinement level.

4.2 Adaptive Refinement Criteria

A successful adaptive strategy should be able to obtain solutions with controlled accuracy in a cost-effective manner. The suitable adaptation criterion, which represents the dominant physical features in the flow field, is critical to detect the cells/regions where a high resolution is needed. A popular indicator is to use the gradients of the solutions to detect the significant flow features in engineering applications (Aftosmis, 1994; Kallinderis and Baron, 1989). Chang and Haworth (1997) demonstrated a kinetic-energy-imbalance-based locally adaptive refinement for a shear-driven flow and a pressure-driven flow. The criterion used in the present study is based on the sum of the mass of fuel vapor and liquid, since many complex physical phenomena such as high velocities and species gradients, gas-liquid momentum transport, and liquid source re-

distributions take place along with the spray region (Nomura et al., 2001; Beard et al., 2003; Lippert et al., 2005). The gradient-based error estimator was also studied in this work.

4.3 Refinement/Coarsening Procedures

Figure 4.5 shows the procedure for the adaptive mesh refinement scheme on the unstructured mesh. The adaptive process begins with the calculation of using a baseline mesh with an initial solution. The refinement/coarsening estimation is conducted to decide if an adaptation is needed. The overall procedure can be summarized as follows.

1. Start from the baseline mesh, build all connectivities for unstructured mesh, and obtain solutions from the flow solver.

2. Tag the cells for refinement according to the prescribed refinement criteria. If the refinement is not needed, by-pass the refinement activity steps.

3. During refinement, insert nodes into the edges, faces, and cell centers to isotropically split the cells that require refinement as shown in Fig. 4.2.

4. Recount the number of nodes, edges, faces, and cells due to node insertion. Update all the node, edge, face, and cell mapping arrays corresponding to the newly inserted nodes. Note that the node numbers of the original mesh after the refinement are still kept the same.

5. Build the connectivity data for all the new child cells. The tree-based storage is built and updated. The node type, face type, and cell type are assigned and updated for new cells.

6. Update the cell neighbor-related arrays at the interface between the refined and unrefined cells based on the information from the previous step.

7. After mesh adaptation, the solution variables are mapped onto the new child cells or parent cells, and the host cell of particles are reassigned.

8. Determine if the next level refinement is required. If yes, return to step (2), otherwise, proceed to next time-step calculation.

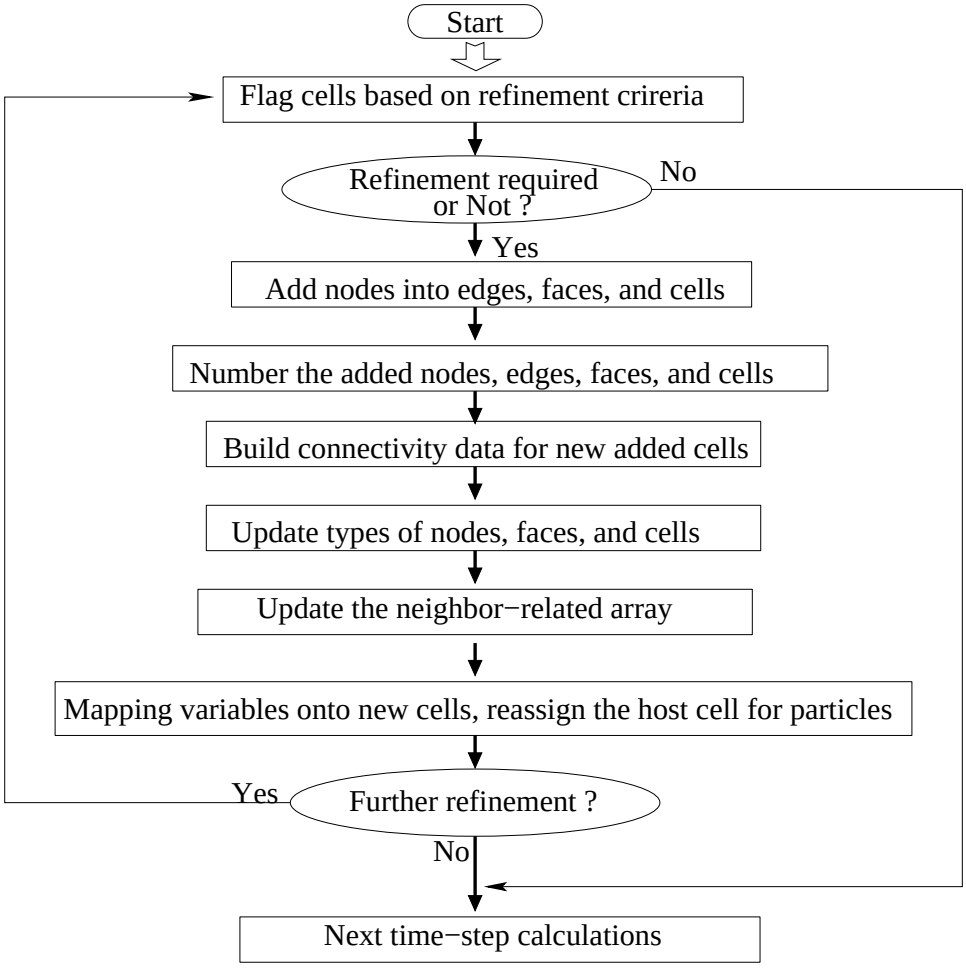

Figure 4.5: The schematic of adaptive mesh refinement for the unstructured mesh

4.4 Solution Remapping

When a cell is tagged for refinement, the cell division is performed. New nodes, edges, faces and cells are added. The relationship of the new generation cells is created and added, and the connectivity of the computational mesh is updated. Once the grid alterations are made, a mapping procedure is used to interpolate the solutions computed on the baseline grid onto the new finer grid. All the flow variables are interpolated and spray particles are also re-assigned to the newly refined cells. The conservation laws are observed during solution mapping procedure. In the framework of the finite-volume scheme, the value of Φ_c at the center X_c of

a cell is integrated over the control volume,

$$\Phi_c = \frac{1}{V}\int_{V_c} \Phi dV \tag{4.1}$$

where V_c is the volume of the cell. A second-order accurate finite volume discretization is used, assuming that the flow variables vary linearly over the control volume,

$$\Phi(X) = \Phi_c + (\nabla\Phi_c)\cdot(X - X_c) \tag{4.2}$$

According to the above scheme, the linear interpolation of a flow variable (ϕ_c) at the parent cell center (X_c) onto a new grid (X_{child}) is applied by using the known value and the gradient ($\nabla\phi_c$) of the parent cell. The values of the variable for new cells are obtained as,

$$\Phi(X_{child}) = \Phi_c + (\nabla\Phi_c)\cdot(X_{child} - X_c) \tag{4.3}$$

The estimates of second-order gradients within each cell are provided by a least-squares procedure in the solution mapping. The least-squares formation is shown to give more accurate estimations in calculating the vertex/cell gradient compared to other methods (Anderson et al., 1994; Hyams, 2000; Wang, 2000). Figure 4.6 shows the stencil reconstruction for the center cell by the least-squares formulation on an unstructured grid in two dimensions. This procedure takes data from face neighbors in the connectivity graph as shown in Fig. 4.6. The full three-dimensional coefficients for the least-squares formulations are rewritten as (Hyams, 2000; Wang, 2000),

$$\Phi_{child}(x,y,z) = \Phi_c + \Phi_x(x_{child} - x_c) + \Phi_y(y_{child} - y_c) + \Phi_z(z_{child} - z_c) \tag{4.4}$$

$$\begin{bmatrix} \Phi_x \\ \Phi_y \\ \Phi_z \end{bmatrix} = W \begin{bmatrix} \sum_n (\Phi_n - \Phi_c)(x_n - x_c) \\ \sum_n (\Phi_n - \Phi_c)(y_n - y_c) \\ \sum_n (\Phi_n - \Phi_c)(z_n - z_c) \end{bmatrix} \tag{4.5}$$

$$W = \frac{1}{\Delta}\begin{bmatrix} I_{yy}I_{zz} - I_{yz}^2 & I_{xz}I_{yz} - I_{xy}I_{zz} & I_{xy}I_{yz} - I_{xz}I_{yy} \\ I_{xz}I_{yz} - I_{xy}I_{zz} & I_{xx}I_{zz} - I_{xz}^2 & I_{xy}I_{xz} - I_{xx}I_{yz} \\ I_{xy}I_{yz} - I_{xz}I_{yy} & I_{xy}I_{xz} - I_{xx}I_{yz} & I_{xx}I_{yy} - I_{xy}^2 \end{bmatrix} \tag{4.6}$$

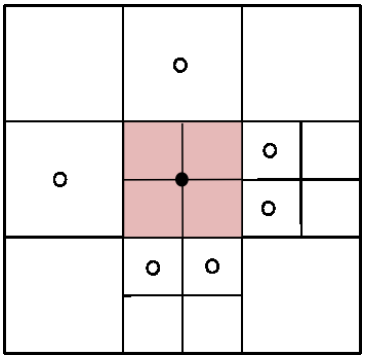

Figure 4.6: Diagram of least-squares reconstruction stencil in two-dimensional space

$$
\begin{aligned}
\Delta &= I_{xx}(I_{yy}I_{zz} - I_{yz}^2) + I_{xy}(2I_{xz}I_{yz} - I_{xy}I_{zz}) + I_{xz}^2 I_{yy} \\
I_{xx} &= \sum_n (x_n - x_c)^2; \quad I_{yy} = \sum_n (y_n - y_c)^2; \quad I_{zz} = \sum_n (z_n - z_c)^2 \\
I_{xy} &= \sum_n (x_n - x_c)(y_n - y_c) \\
I_{xz} &= \sum_n (x_n - x_c)(z_n - z_c) \\
I_{yz} &= \sum_n (y_n - y_c)(z_n - z_c)
\end{aligned}
$$

(Φ_x,Φ_y,Φ_z) is the gradient $\nabla\Phi_c$. The formula will guarantee local conservations.

When a parent cell is recovered from its child cells, the volume-weighted average value over the child cells is computed to obtain the value at the parent cell center,

$$\Phi_c = \frac{1}{V}\int\int_{V_s} \Phi_s dV = \frac{1}{V}\sum_{s=1}^{n} \Phi_s V_s \tag{4.7}$$

The solution-mapping procedure is applied to all the flow variables. During refinement, the spray particles are assigned to one of the child cells based on their physical locations. During coarsening, all the particles associated with the child cells are assigned to the parent cell.

4.5 Fluxing Calculation

A refined cell adjacent to a non-refined neighbor gives rise to the occurrence of the so-called "hanging node," which could cause problems in numerical interpolation and local conserva-

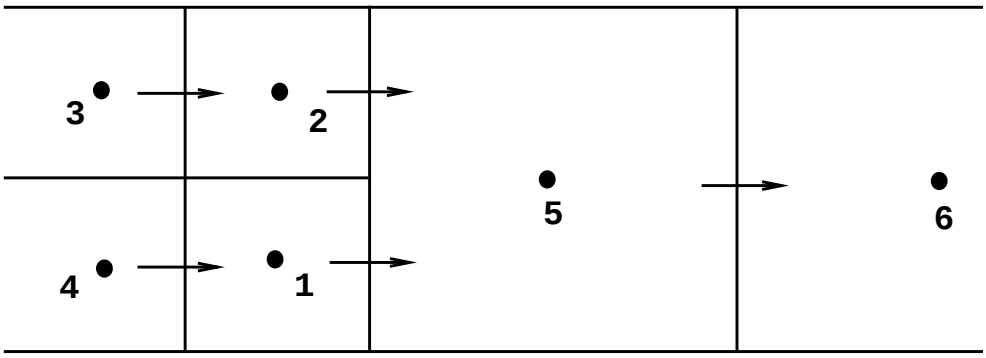

Figure 4.7: Contributions of fluxes for polygonal control volume of an arbitrary topology (2D). For cell 5, the flux from left is the sum of the flux from cell 1 to cell 5 and the flux from cell 2 to cell 5

tion. Some studies created the transition elements or buffer zones to eliminate the hanging nodes (Aftosmis, 1994; Mavriplis, 2000), or used values on the coarse mesh and performed interpolation to obtain values on the hanging nodes (Kallinderis and Baron, 1989). The major drawback of the above approaches is that buffer zones require nontrivial cell bookkeeping and can introduce considerable restrictions for successive mesh refinements. In the present study, the use of polyhedral cells of arbitrary topology, which is widely used in unstructured flow solvers, can mitigate numerical difficulties in diffusion and convection calculations. This face-based approach can avoid the traditional limitations on the number of faces bounding a cell (Muzaferija and Gosman, 1997). A face with hanging nodes is simply treated as several subfaces and thus does not require any special numerical treatment. The calculation of fluxes and their contribution to the cells can be efficiently handled by face-based loops (see Figure 4.7). This method provides more freedom to efficiently manage the grid system.

CHAPTER 5. VALIDATIONS AND APPLICATIONS OF ADAPTIVE MESH REFINEMENT TO ENGINE SPRAY MODELING

This chapter presents the validation and application of AMR for engine spray simulation. The spray parameters, including spray penetration and global Sauter Mean Diameter (SMD), are investigated, as well as the computational performance of AMR code. The sensitivity investigation of AMR method was also described.

5.1 Engine Spray Simulations

5.1.1 Computational Conditions

A constant-volume chamber with a dimension of 10 cm in diameter and 10 cm in height was considered in the present study as shown in Fig. 5.1. Two O-type grids were used in the simulations. The spatial resolutions of the grids are $20\times20\times20$ and $40\times40\times40$, respectively. In this study both the solid-cone and hollow-cone sprays are simulated. The liquid fuel is injected from the center of the top surface into the chamber. The injection velocity is 135 m/s, and the injection duration is 1.22 ms with a total of 3.6 mg of fuel. The nozzle diameter and initial drop size are 200 μm. A fixed time-step of 1 μs is used to isolate the effect of the time-step sensitivity (Abani et al., 2006).

The initial temperature and pressure in the chamber are 300 K and 1 bar, respectively. Physical sub-models accounting for drop collision, coalescence, vaporization, and breakup are the standard models of KIVA (Amsden, 1997) (Torres, 2007). The RNG k-ϵ turbulence model (Han et al., 1998) was used for turbulence simulation. The refinement and coarsening criterion used is the sum of the mass of liquid drops and fuel vapor in each cell with a threshold of 1.0 mg. A cell will be refined isotropically into eight child cells when the threshold value is

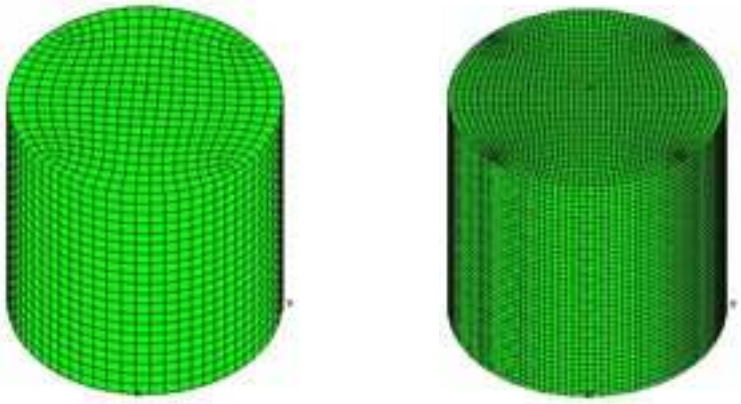

(a) (b)

Figure 5.1: Computational domain with baseline coarse mesh (left) and fine mesh (right)

exceeded.

5.1.2 Spray Structure and Penetrations

An ideal AMR implementation can provide identical solutions to those predicted by the globally fine mesh at a reduced computational cost. This section will describe the validation and performance of the AMR scheme for engine spray simulations.

5.1.2.1 Solid-Cone Spray

The penetration and distribution of the liquid drops will be presented and compared. Figures 5.2, 5.3 and 5.4 show the predicted drop distributions at different times after fuel injection. Results are obtained using three different meshes, namely, the coarse mesh, the fine mesh, and the AMR mesh. The drops are colored based on their radii. It is shown that the spray penetration on the coarse mesh is much shorter than that on the other two meshes due to poor momentum coupling between the liquid and gas phases (Abraham, 1997) (Beard et al., 2000). However, results of using AMR show very similar spray patterns to those on the fine mesh shown at three different times of 1.2 ms, 2.0 ms, and 3.0 ms.

Figure 5.5 shows the computed liquid penetration versus time after the start of injection. The liquid penetration is the distance between the nozzle exit and the location of the leading

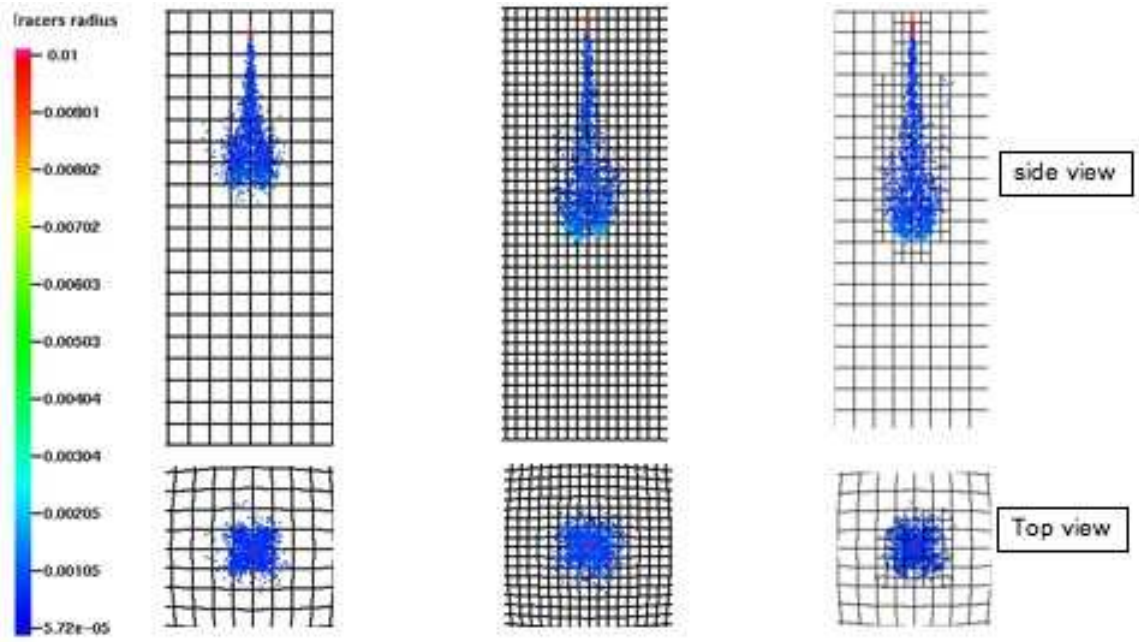

Figure 5.2: Spray structure at 1.2 ms after start of injection. The scale is based on drop radius (cm). (solid-cone spray)

group of the drops (98% of total liquid mass). It can be seen that the spray penetration in the coarse mesh is much shorter than the others. The liquid penetrations of the fine mesh and the AMR mesh agree very well. The penetration predicted by using the AMR mesh is slightly higher than that predicted by the fine mesh by 0.5% at 3.0 ms. The size distributions of the predicted drops are also very similar between the fine mesh and the AMR mesh judged by the distributions of color.

5.1.2.2 Hollow-Cone Spray

The model was also used to simulate a hollow-cone spray that is often used in direct-injection spark ignition (DISI) engines. The spray cone angle is 45 $degree$ and the thickness is 15 $degree$. Figures 5.6, 5.7 and 5.8 show the distributions of the liquid drops predicted by using three different meshes. It is found that the spray penetration on the coarse mesh is more limited than the other two meshes. The spray patterns obtained using the globally fine mesh and the AMR mesh are very similar to each other.

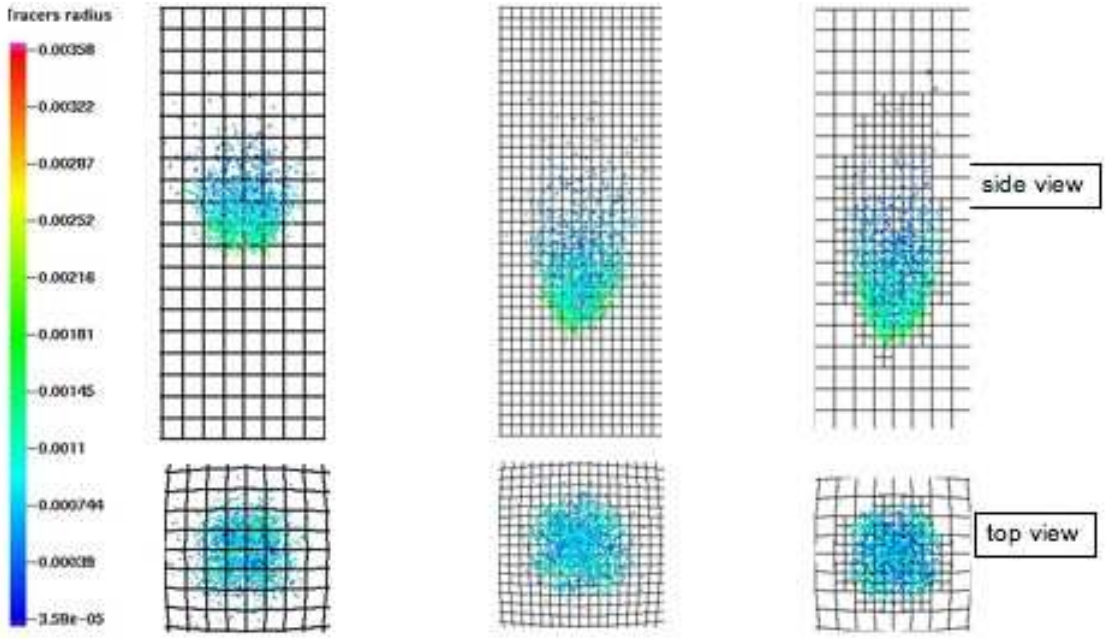

Figure 5.3: Spray structure at 2.0 ms after start of injection (solid-cone spray).

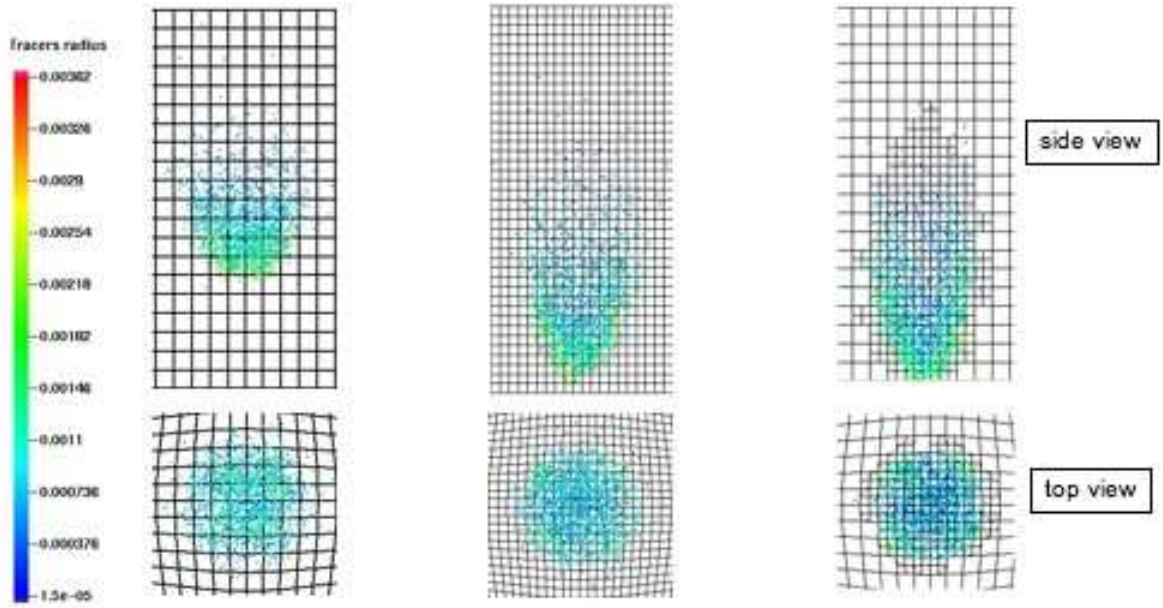

Figure 5.4: Spray structure at 3.0 ms after start of injection (solid-cone spray).

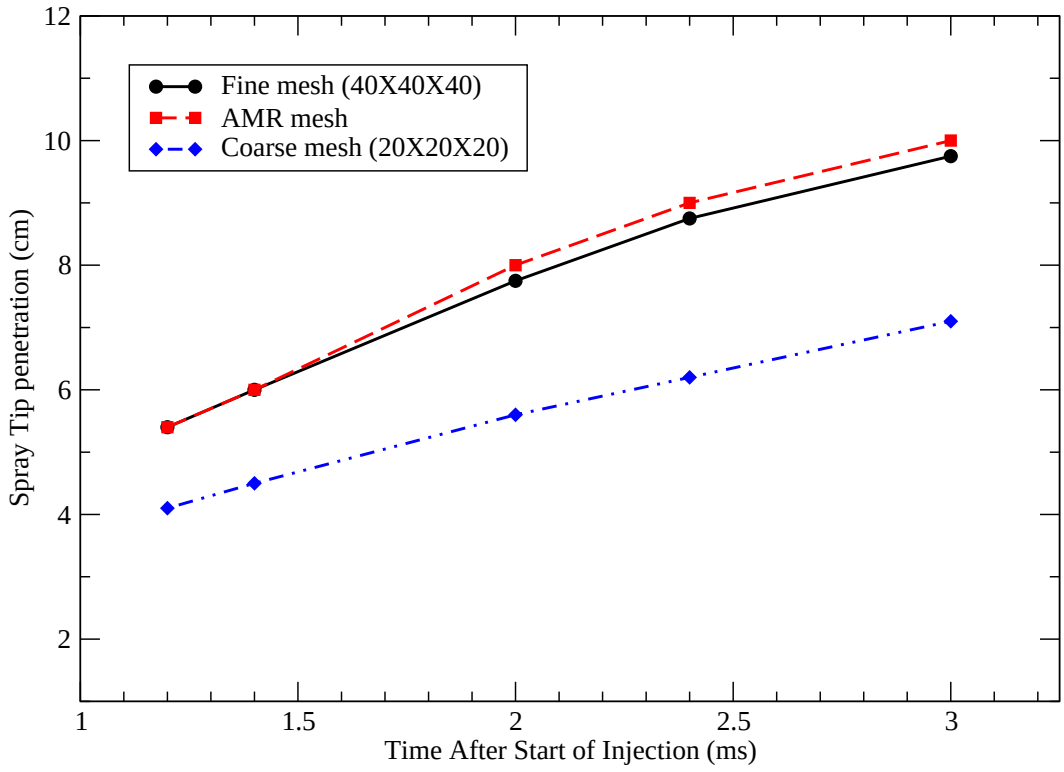

Figure 5.5: Comparison of the liquid penetrations of using different meshes versus time (solid-cone spray).

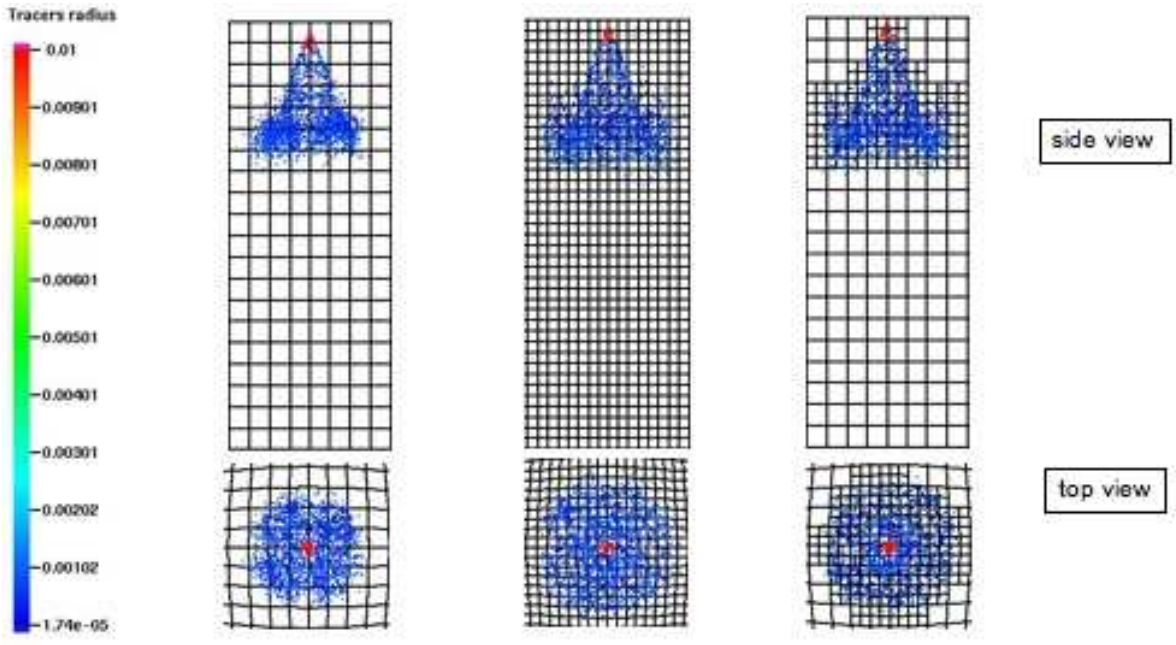

Figure 5.6: Spray structure at 1.2 ms after start of injection (hollow-cone spray)

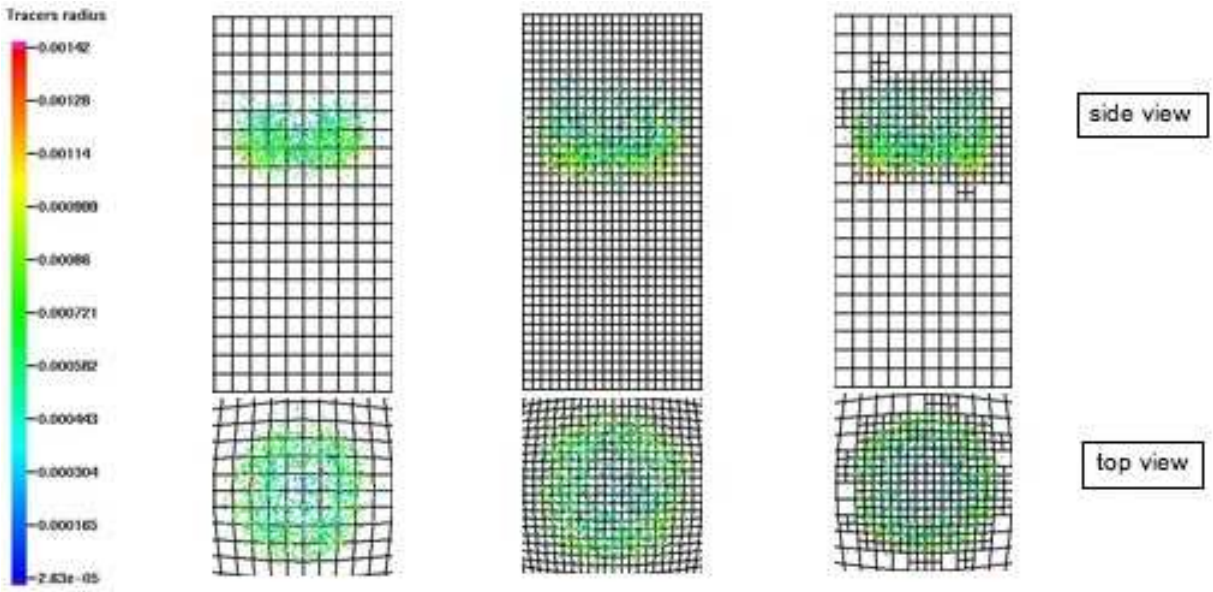

Figure 5.7: Spray structure at 2.0 ms after start of injection (hollow-cone spray)

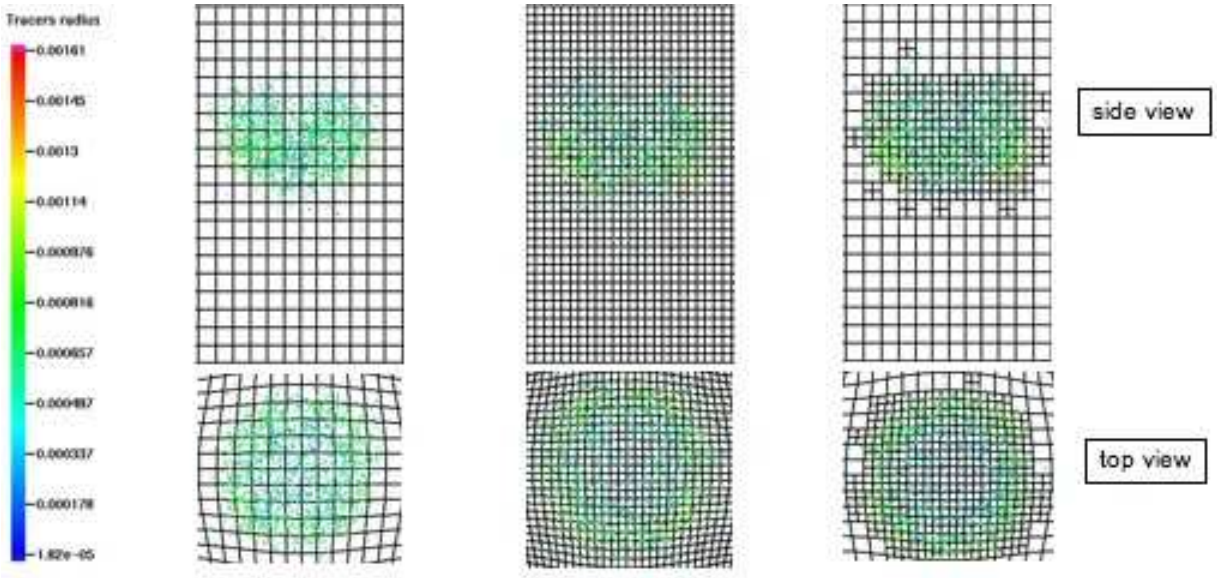

Figure 5.8: Spray structure at 3.0 ms after start of injection (hollow-cone spray)

5.1.2.3 Fuel Vapor and Temperature Distributions of Solid-Cone Spray

The predicted fuel vapor and temperature distributions are given and compared between different meshes at different times after start of injection of fuel. Figures 5.9, 5.10, 5.11 gives the fuel vapor distributions at 1.2 ms, 2.0 ms, and 3.0 ms after start of fuel injection, respectively. AMR compares well to the fine mesh. The poor resolution of coarse mesh causes the over-diffusion as shown in figures. The temperature contours are shown in 5.12, 5.13, 5.14. Predictions using AMR are similar to those using fine mesh. The shorter penetration and faster diffusion result in the difference in temperature distribution with coarse mesh.

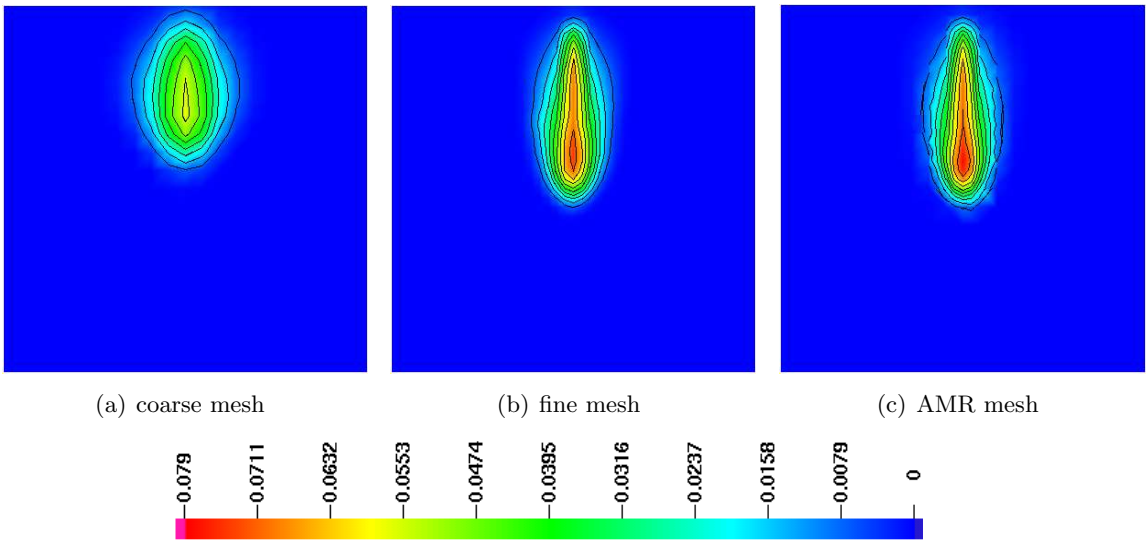

(a) coarse mesh (b) fine mesh (c) AMR mesh

(d) mass fraction

Figure 5.9: Fuel vapor distributions predicted using different meshes at 1.2 ms after start of injection of fuel (solid-cone spray)

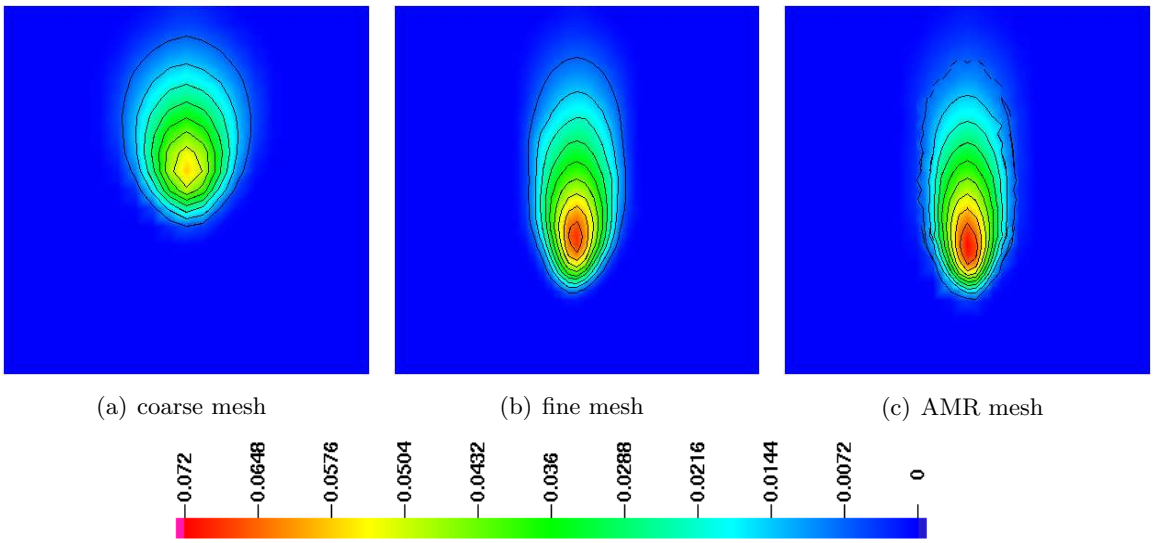

(a) coarse mesh (b) fine mesh (c) AMR mesh

(d) mass fraction

Figure 5.10: Fuel vapor distributions predicted using different meshes at 2.0 ms after start of injection of fuel (solid-cone spray)

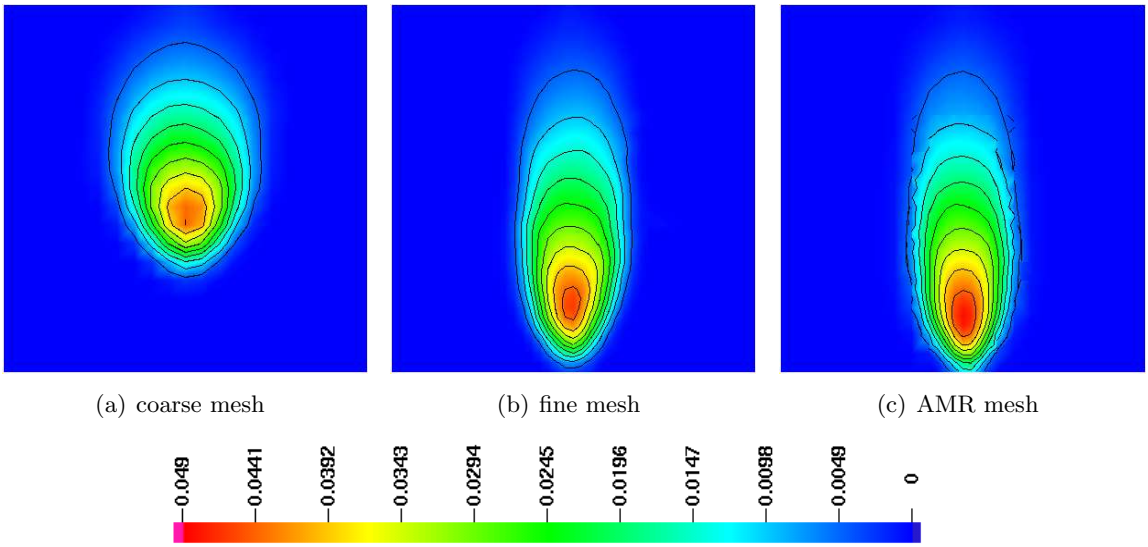

(a) coarse mesh (b) fine mesh (c) AMR mesh

(d) mass fraction

Figure 5.11: Fuel vapor distributions predicted using different meshes at 3.0 ms after start of injection of fuel (solid-cone spray)

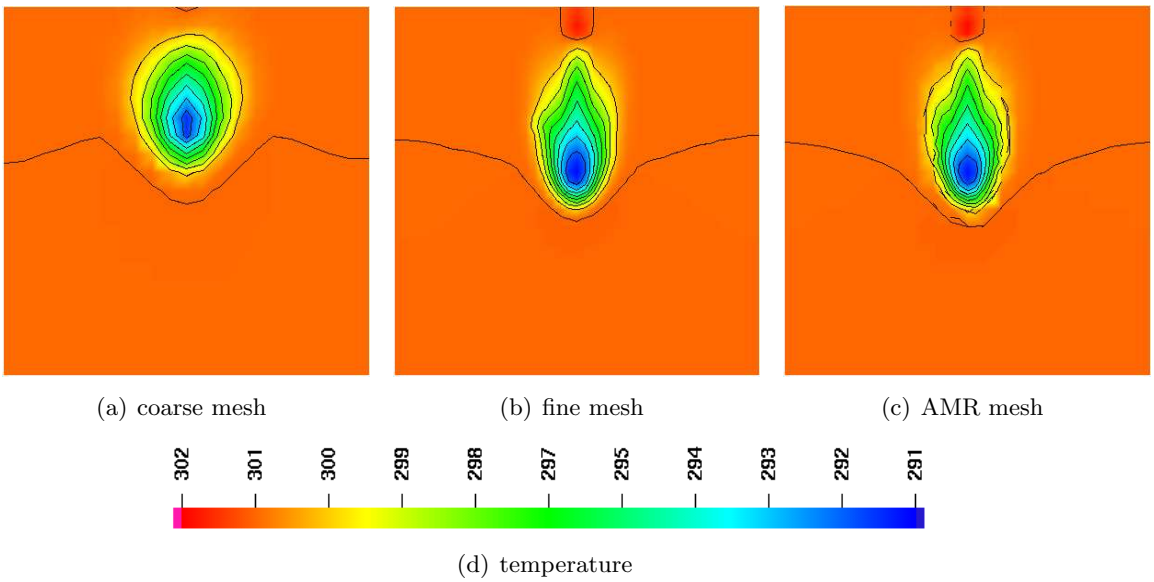

(a) coarse mesh (b) fine mesh (c) AMR mesh

(d) temperature

Figure 5.12: Temperature contours predicted using different meshes at 1.2 ms after start of injection of fuel (solid-cone spray)

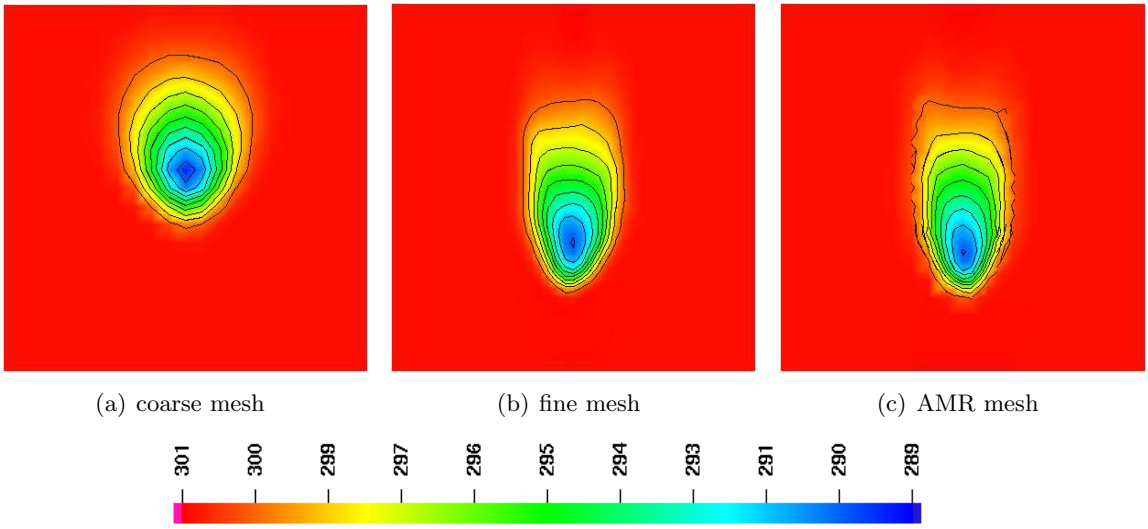

(a) coarse mesh (b) fine mesh (c) AMR mesh

(d) temperature

Figure 5.13: Temperature contours predicted using different meshes at 2.0 ms after start of injection of fuel (solid-cone spray)

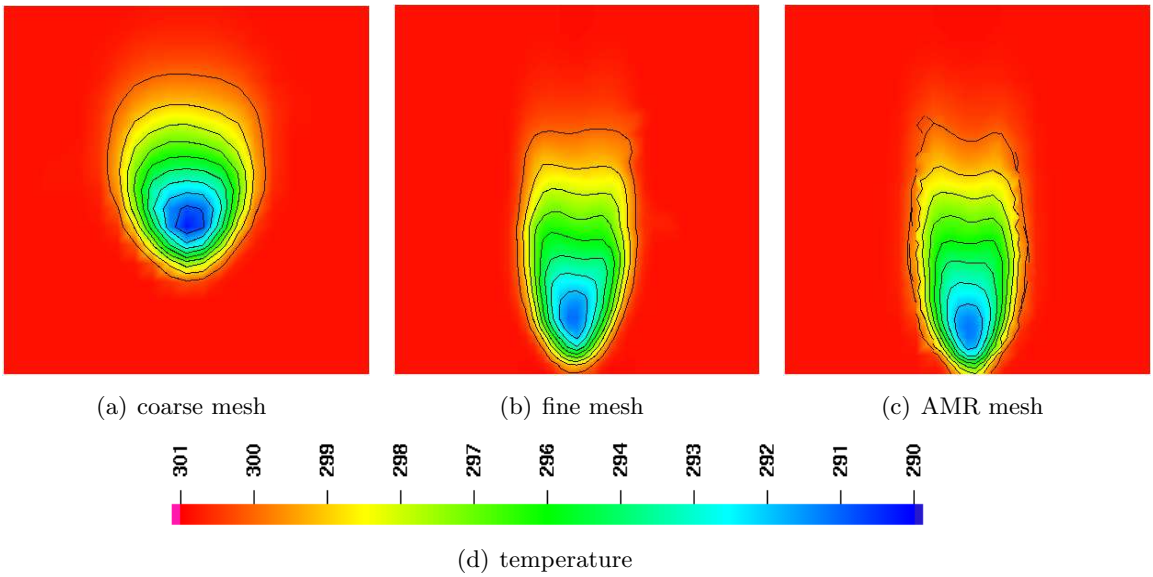

(a) coarse mesh (b) fine mesh (c) AMR mesh

(d) temperature

Figure 5.14: Temperature contours predicted using different meshes at 3.0 ms after start of injection of fuel (solid-cone spray)

5.1.3 Combustion Chamber with Moving Boundary

One of the challenges for engine simulations is the moving boundary. One case with moving boundary is conducted. The chamber has a bore of 10 cm and a stroke of 8.5 cm (see Fig. 5.1). Two O-type grids were used in the simulations. The spatial resolutions of the grids are $20 \times 20 \times 20$ and $40 \times 40 \times 40$, respectively. In this study, a solid-cone injector was simulated. The injection velocity was 135 m/s, and the injection started at 190 degrees after top-dead-center (ATDC). The injection duration was 10 crank angle degrees (CAD) with a total of 3.6 mg of fuel. The nozzle hole diameter and initial drop size were both 200 μm. The engine speed was 1000 rpm. The computation started at 180 ATDC with an initial temperature and pressure in the chamber of 300 K and 1 bar, respectively. Physical sub-models accounting for droplet collision, coalescence, vaporization and breakup are models described in KIVA (Amsden et al., 1989). The RNG k-ϵ turbulence model (Han et al., 1997) was used for turbulent simulation. A cell will be refined if the mass of liquid fuel exceeds 10^{-6} g.

The predicted spray structures, fuel vapor distributions, temperature contours, and w-component of velocity are compared on three different meshes at 200, 240, and 300 ATDC, respectively. Overall the predictions using AMR agree well with those using fine mesh. On the other hand, the results using coarse mesh under-predict the spray penetrations and over-predict the diffusion in the radial direction as shown in Figures 5.15 at 200 ATDC, and 5.16 at 240 ATDC. Figures 5.17, 5.18, and 5.19 show the fuel vapor distributions at 200, 240 and 300 ATDC, respectively. It can be seen that AMR gives similar distributions as the fine mesh. Coarse mesh causes the faster diffusion due to the poor grid resolution. Similar results occur for the temperature contours as shown in Figures 5.20, 5.21, and 5.22. Figures 5.23, 5.24, and 5.25 give the w-component of velocity for three different meshes. Again the AMR gives good agreement with the fine mesh. The coarse mesh over-predicts the diffusion of velocity over the large computational cells, and thus leads to small penetration velocity of fuel drops.

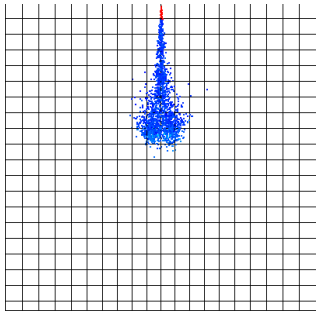

(a) coarse mesh (side view)

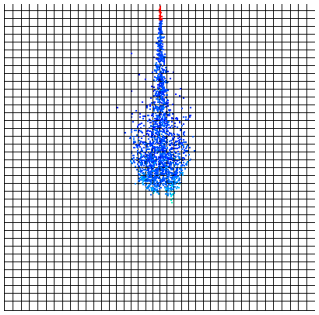

(b) fine mesh (side view)

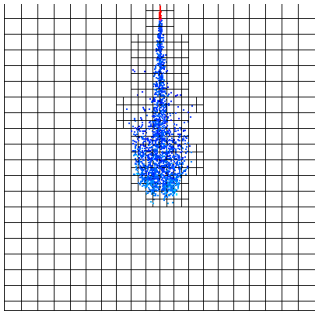

(c) AMR mesh (side view)

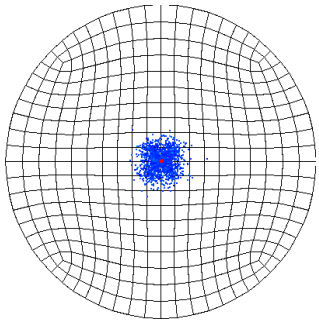

(d) coarse mesh (top view)

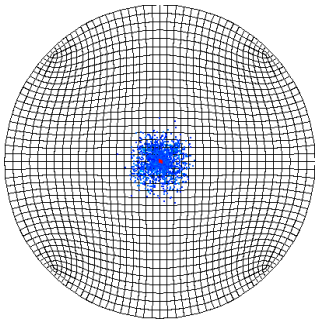

(e) fine mesh (top view)

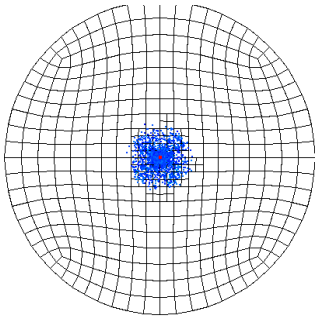

(f) AMR mesh (top view)

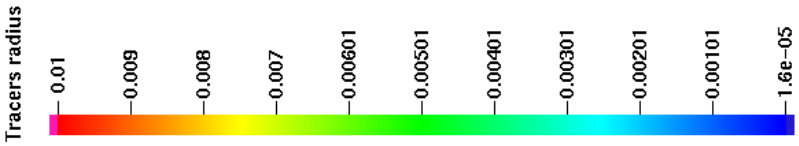

(g) tracers radius

Figure 5.15: Spray structure predited using different meshes at 200 ATDC

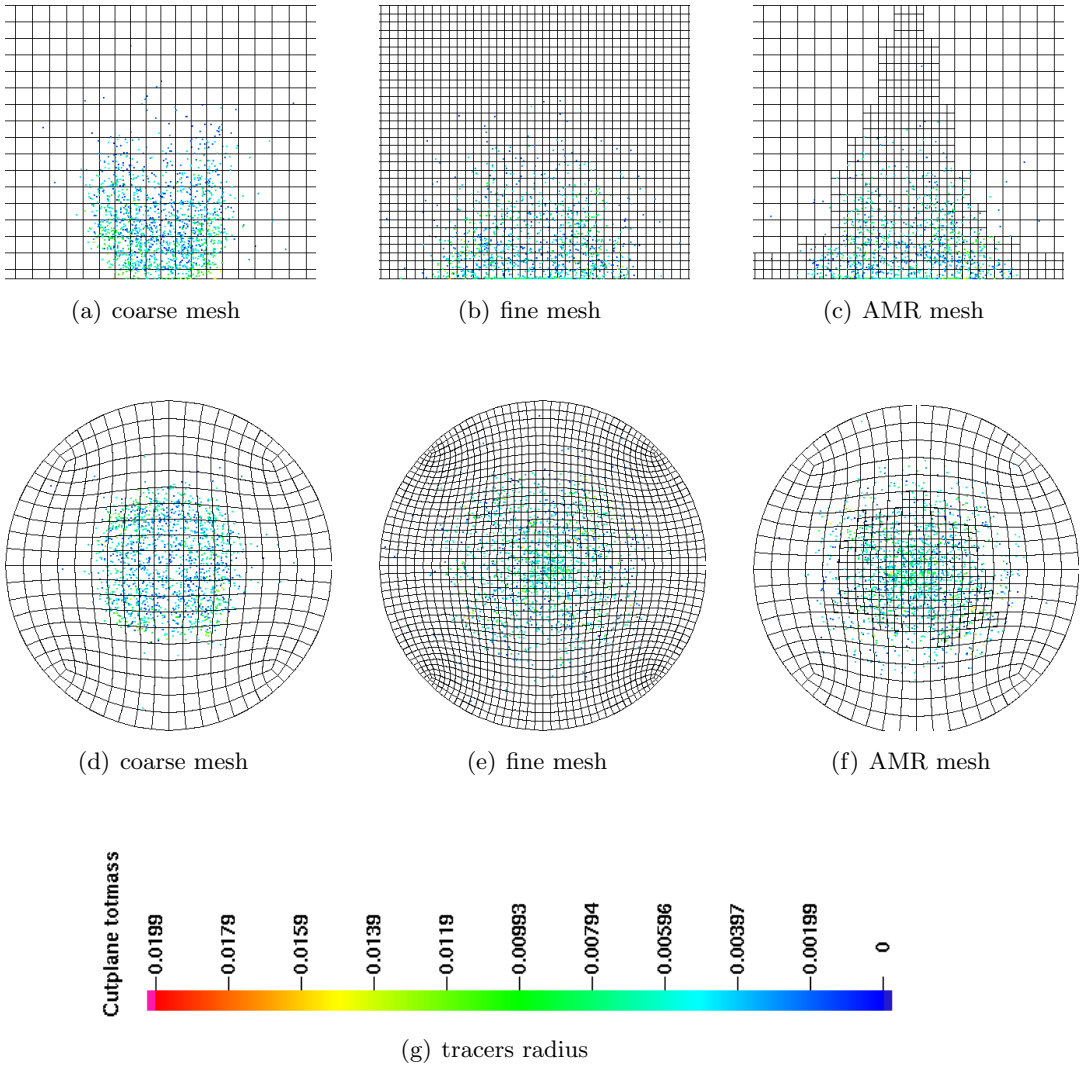

(a) coarse mesh (b) fine mesh (c) AMR mesh

(d) coarse mesh (e) fine mesh (f) AMR mesh

(g) tracers radius

Figure 5.16: Spray structure predicted using different meshes at 240 ATDC

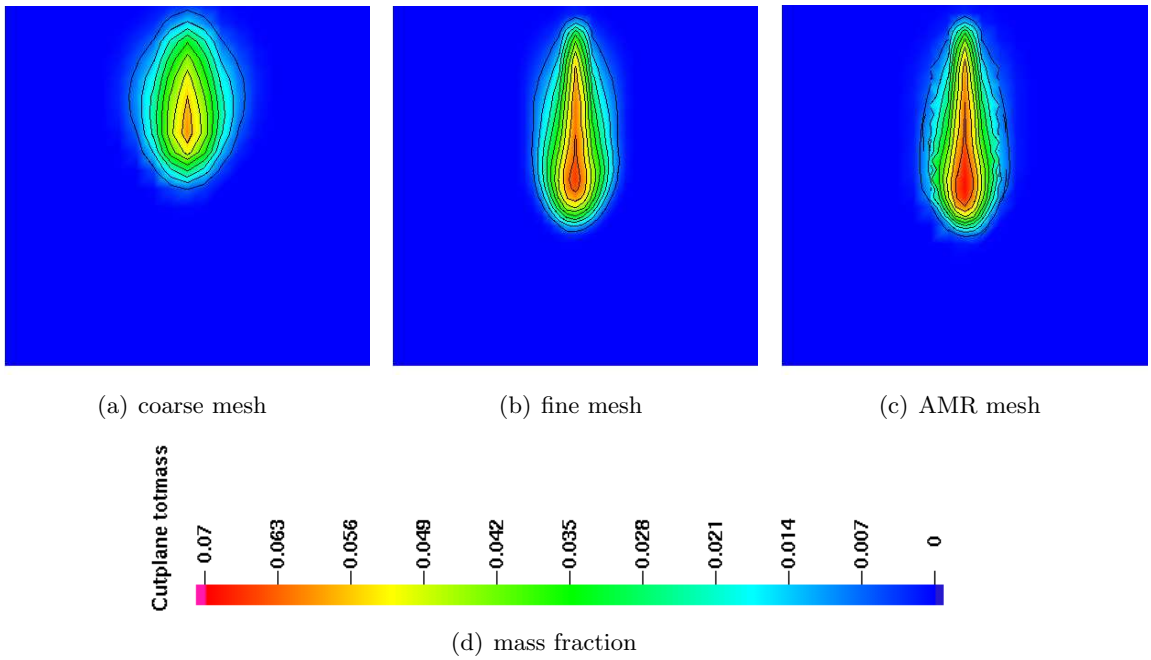

(a) coarse mesh (b) fine mesh (c) AMR mesh

(d) mass fraction

Figure 5.17: Fuel vapor distributions predicted using different meshes at 200 ATDC

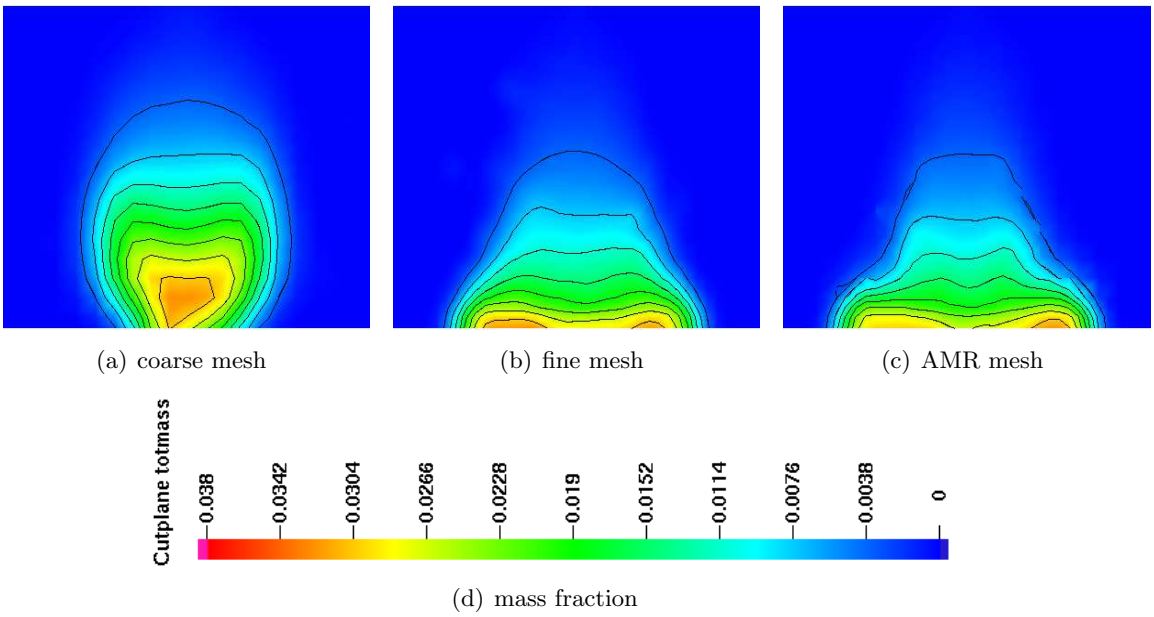

(a) coarse mesh (b) fine mesh (c) AMR mesh

(d) mass fraction

Figure 5.18: Fuel vapor distributions predicted by different meshes at 240 ATDC

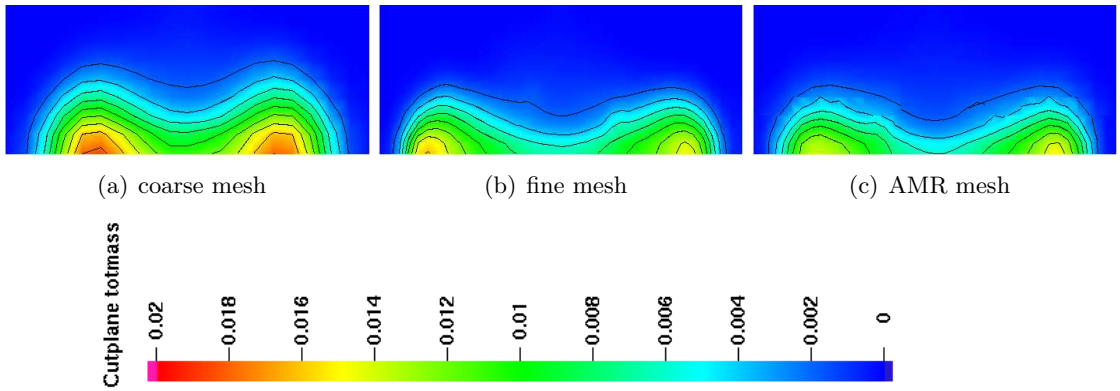

(a) coarse mesh (b) fine mesh (c) AMR mesh

(d) mass fraction

Figure 5.19: Fuel vapor distributions predicted by different meshes at 300 ATDC

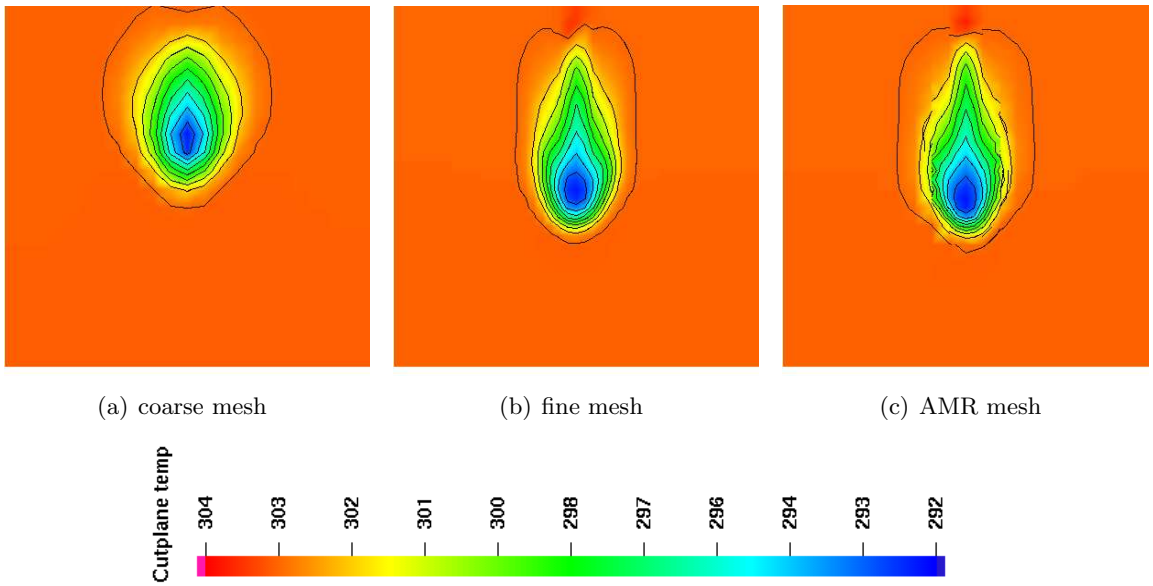

(a) coarse mesh (b) fine mesh (c) AMR mesh

(d) temperature

Figure 5.20: Temperature contours predicted using different meshes at 200 ATDC

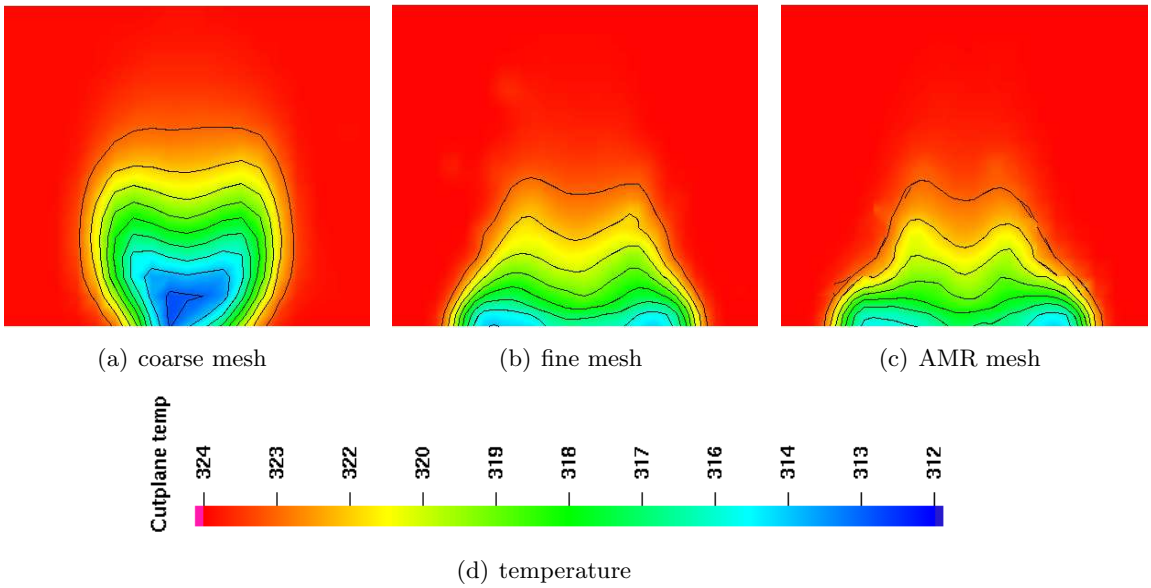

(a) coarse mesh (b) fine mesh (c) AMR mesh

(d) temperature

Figure 5.21: Comparison of temperature contour predicted using different meshes at 240 ATDC

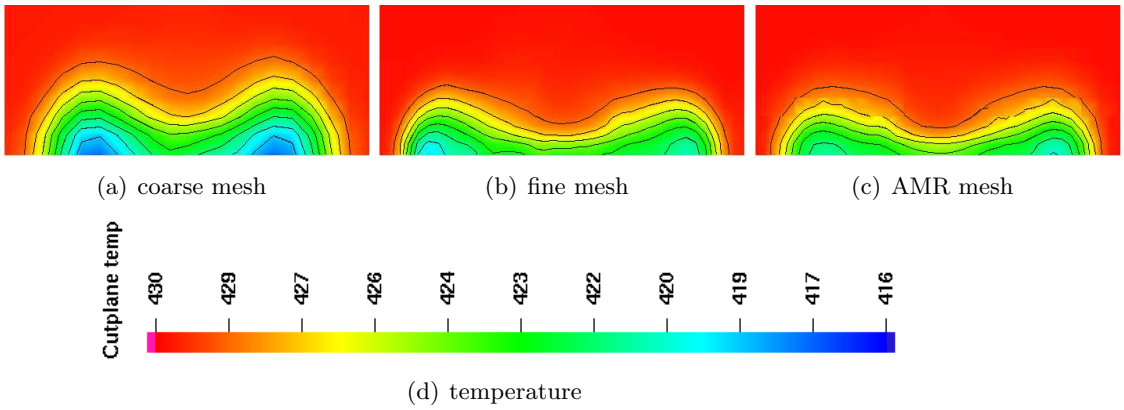

(a) coarse mesh (b) fine mesh (c) AMR mesh

(d) temperature

Figure 5.22: Temperature contour predicted using different meshes at 300 ATDC

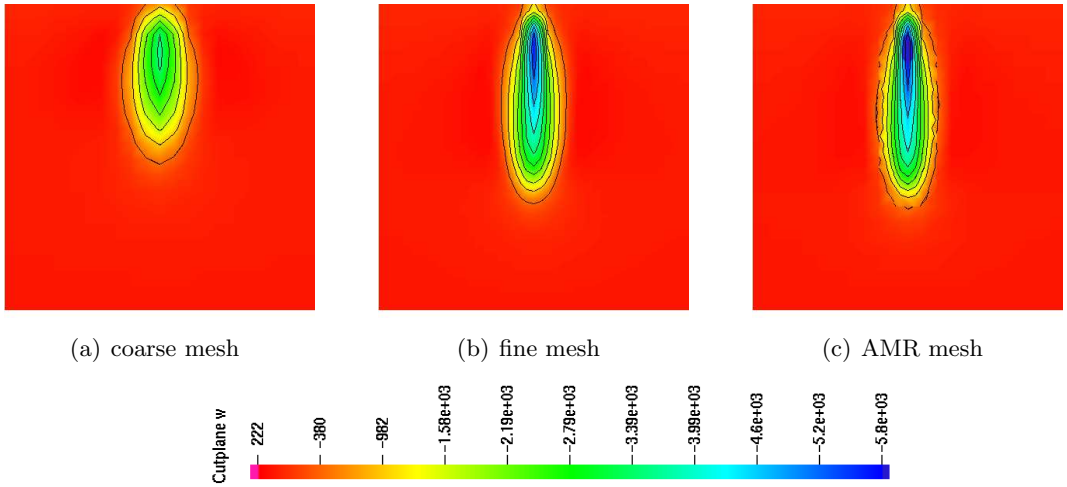

(a) coarse mesh (b) fine mesh (c) AMR mesh

(d) w-velocity

Figure 5.23: W-component of velocity contours predicted using different meshes at 200 ATDC

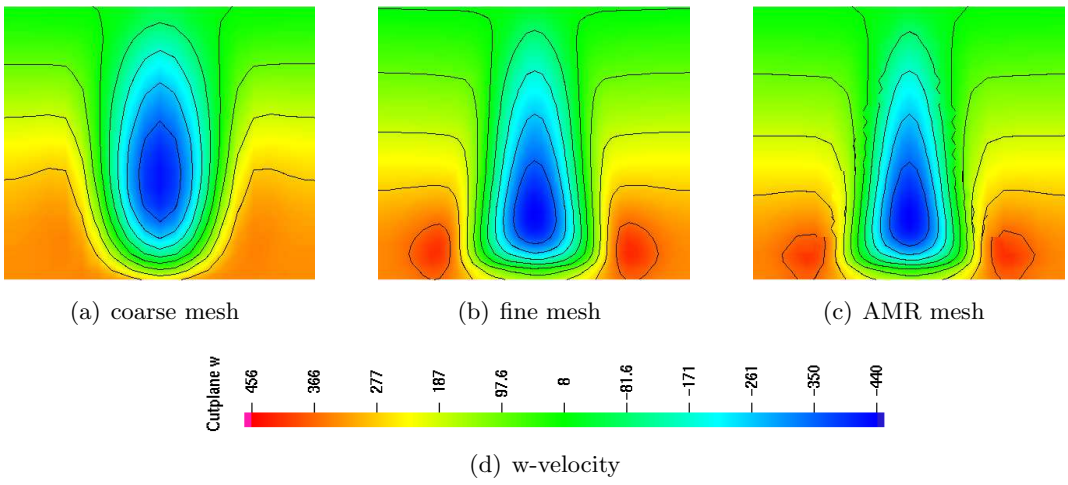

(a) coarse mesh (b) fine mesh (c) AMR mesh

(d) w-velocity

Figure 5.24: W-component of velocity contours predicted using different meshes at 240 ATDC

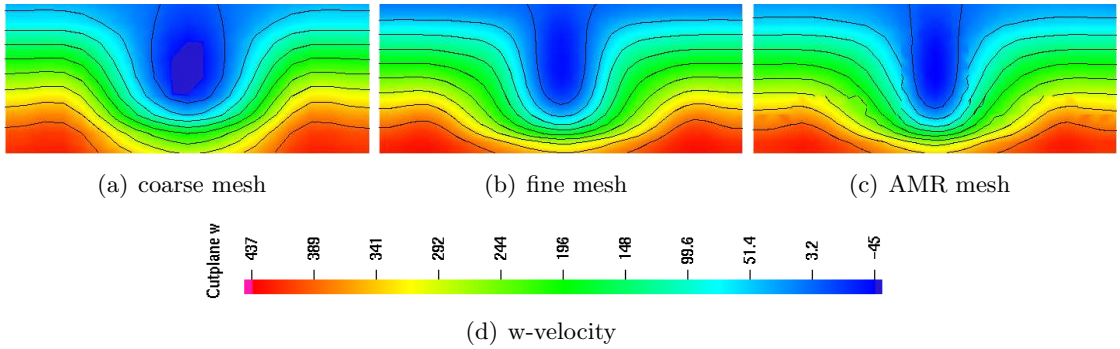

(a) coarse mesh (b) fine mesh (c) AMR mesh

(d) w-velocity

Figure 5.25: W-component of velocity contours predicted using different meshes at 300 ATDC

5.1.4 Computational Efficiency

The computer time from the start of injection to 3.0 ms and the speed-up are given in Tab. 5.1 and 5.2. The speed-up is based on the computer time of using the finest grid and is defined as the following,

$$Speedup\ (S) = \frac{Computer\ time\ for\ globally\ fine\ mesh\ (t_{fine})}{Computer\ time\ (t)} \tag{5.1}$$

Simulations using the AMR mesh shows a significant speed-up while maintaining an accurate prediction of the spray structure. As can be seen, the AMR calculation achieves nearly 5 times of the speed-up for the solid-cone spray and 3 times of the speed-up for the hollow-cone spray.

The AMR calculation achieves a speed-up of 2 over the fine mesh for the moving piston case. A particular manner associated with the snapping is implemented to achieve efficient refinement and keep good mesh quality at the moving face.

Table 5.1: Computer time and speed up of the solid-cone spray simulation

Mesh	Effective mesh resolution	Computer time (s)	Speed up
Coarse mesh	$20 \times 20 \times 20$	14.4	5
Fine mesh	$40 \times 40 \times 40$	72	1
AMR mesh	$40 \times 40 \times 40$	15	4.8

Table 5.2: Computer time and speed up of the hollow-cone spray simulation

Mesh	Effective mesh resolution	Computer time (s)	Speed up
Coarse mesh	$20 \times 20 \times 20$	15.2	5
Fine mesh	$40 \times 40 \times 40$	76	1
AMR mesh	$40 \times 40 \times 40$	25	3.04

5.2 Multi-Level Dynamically Refinement

5.2.1 Computational Conditions

A constant-volume chamber with a dimension of 10 cm in diameter and 10 cm in height was considered in the validation case as shown in Figure 5.26. Four O-type grids were used. The spatial resolutions of the grids were $80 \times 80 \times 80$, $40 \times 40 \times 40$, $20 \times 20 \times 20$, and $10 \times 10 \times 10$, which were used for zero-level (RL0), one-level (RL1), two-level (RL2), and three-level (RL3) refinement calculations, respectively. Both the solid-cone and hollow-cone sprays were simulated. The liquid fuel (iso-octane) was injected from the center of the top surface into the chamber. The injection velocity was 135 m/s and the injection duration was 1.22 ms with a total of 3.6 mg of fuel. The nozzle size and initial drop size were 200 μm in diameter. A fixed time-step of 1 μs was used to isolate the effect of the time-step sensitivity.

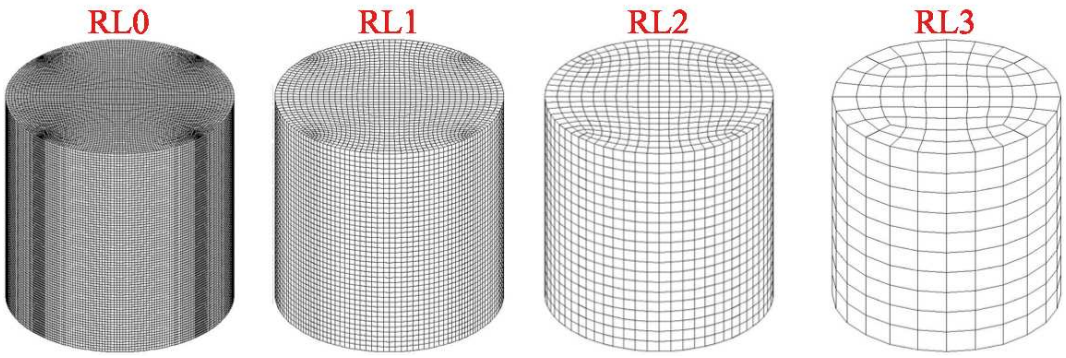

Figure 5.26: Computational domains with meshes for different levels of adaptation

The initial temperature and pressure in the chamber were 300 K and 1 bar, respectively. The physical sub-models accounting for the drop collision, coalescence, vaporization, and break-up were the standard models of KIVA-4 (Torres and Trujillo, 2006). The RNG $k-\epsilon$ turbulence model was used for turbulence simulation (Han and Reitz, 1995). The refinement and coarsening criteria used were the sum of the mass of liquid drops and fuel vapor in each cell with thresholds of 10^{-7} g for one-level, 10^{-6} g for two-level, and 10^{-5} g for three-level refinement,

respectively. To validate the accuracy of the adaptive algorithm, the liquid spray structure, the global Sauter Mean Diameter (SMD), and the spray tip penetrations are compared.

5.2.2 Spray Structures and Penetrations

5.2.2.1 Solid-Cone Spray

The penetration and distribution of the liquid drops will be presented and compared. Figures 5.27(a) and 5.27(b) show snapshots of the predicted drop distributions at different times after fuel injection. Results are obtained using different adaptive levels on four different meshes. The drops are colored based on their radii. Results show that the fine mesh and coarse meshes with appropriate refinement levels produce very similar spray penetrations. On the other hand, the drop distributions shown in the top views are somewhat different. The results predicted by the three-level refinement show a pronounced cross-shaped structure. One possible cause is that the adaptive threshold makes the refinement lag behind the occurrence of the spray events (such as collision, breakup). However, The overall size distributions of the predicted drops are very similar between the finest mesh and adaptive meshes as will be discussed later.

Figures 5.28 and 5.29 show the computed liquid tip penetrations after the start of injection without AMR and with AMR, respectively. The liquid penetration is the distance between the nozzle exit and the location of the leading group of the drops (98% of the total liquid mass). Figure 5.28 shows that the spray penetrations on the coarse meshes are much shorter than those on the fine meshes due to poor momentum coupling between the liquid and gas phases. However, the predictions of the penetrations were significantly improved by using AMR in the coarse meshes as seen in Figure 5.29 It can be seen that the liquid penetrations on the fine mesh and the coarse meshes using AMR agree very well, especially for the one-level and two-level adaptation cases. The spray tip penetration on the three-level adaptive mesh shows a nearly constant discrepancy against the fine meshes shortly after the fuel injection. One probable cause is that the mesh around the nozzle exit was too coarse initially. The poor spatial resolution of the dense spray next to the nozzle not only can under-resolve the strong gradient but can also cause fast diffusion, thus resulting in a shorter penetration.

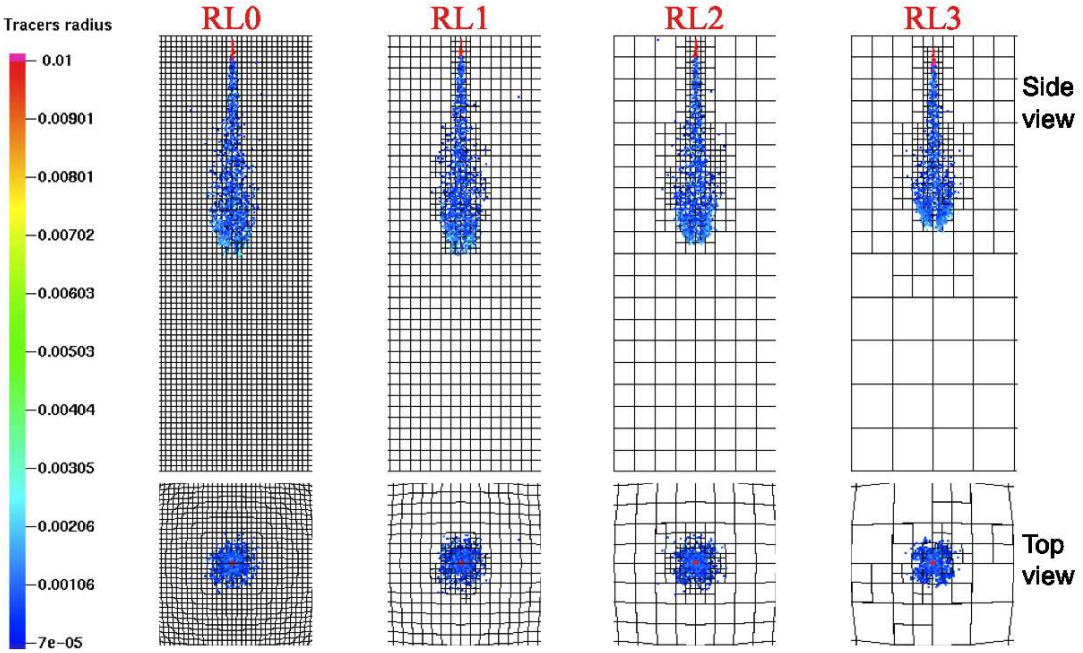

(a) Spray structure at 0.8 ms

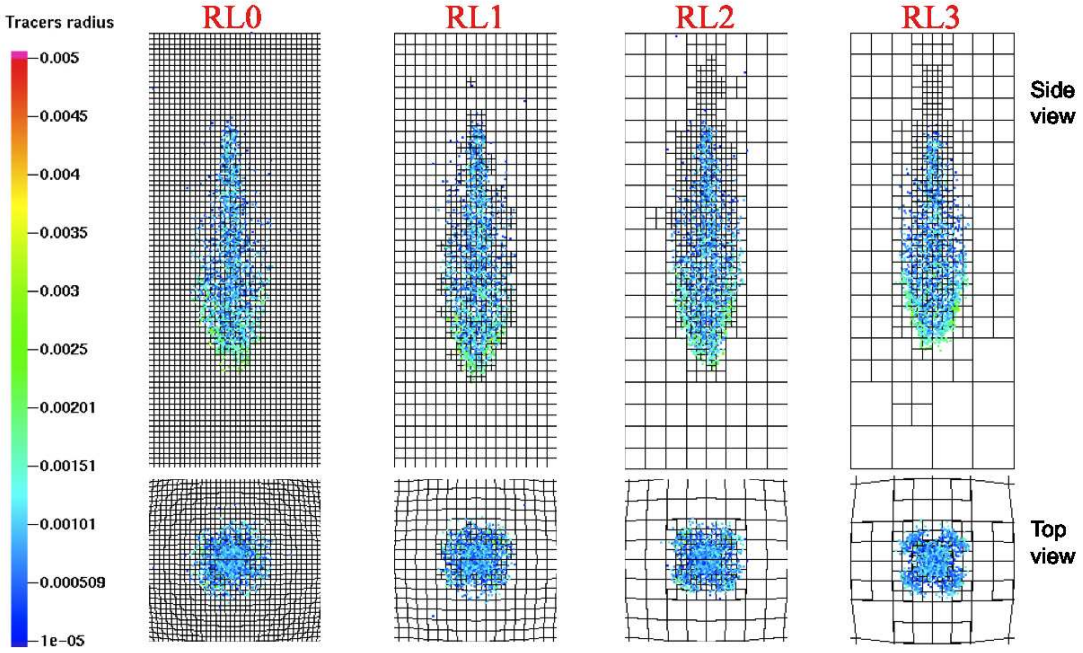

(b) Spray structure at 1.4 ms

Figure 5.27: Spray structure at 0.8 ms and 1.4 ms after start of injection (solid-cone spray)

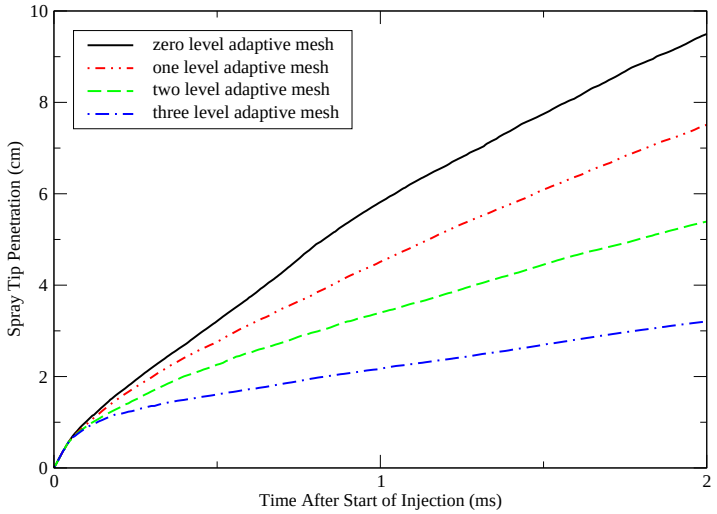

Figure 5.28: Comparison of the liquid spray tip penetrations predicted using different meshes without using AMR (solid-cone spray).

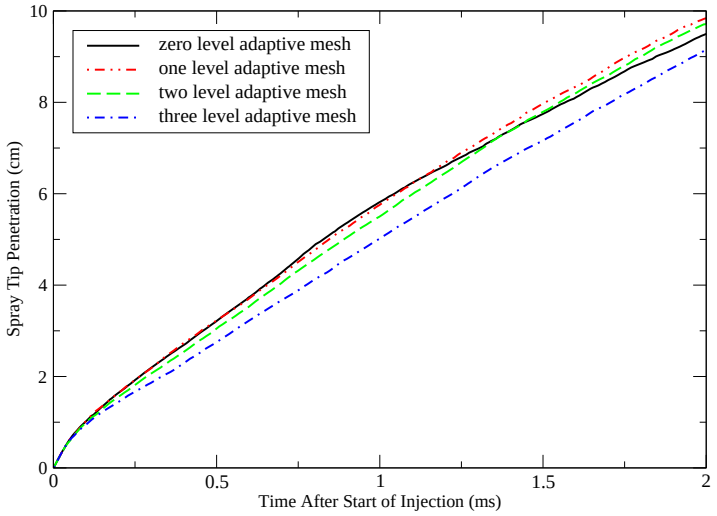

Figure 5.29: Comparison of the liquid spray tip penetrations predicted using different adaptive meshes (solid-cone spray)

5.2.2.2 Hollow-Cone Spray

The present model was also used to simulate a hollow-cone spray that is also used in direct-injection gasoline engines. Figure 5.30 and 5.31 show the distributions of the liquid drops predicted by using four different meshes with appropriate refinement levels. The spray patterns on all the meshes are very similar. From the top-view results, one can see that the radial penetration is shorter on the three-level adaptive mesh compared to the other meshes. The initial coarse mesh near the nozzle can cause fast diffusion of the radial momentum and result in short penetrations. It was found that the spray tip penetrations (on the side view) for all the meshes are very similar as shown in Figure 5.32. For the three-level adaptive mesh, the spray tip penetration is predicted better than that of the solid-cone spray. That is because for the hollow-cone spray, the poor spatial resolution near the nozzle only partially influences the axial momentum exchange as compared to the solid-cone spray case. The other part of the influence affects the radial momentum exchange leading to a shorter radial penetration.

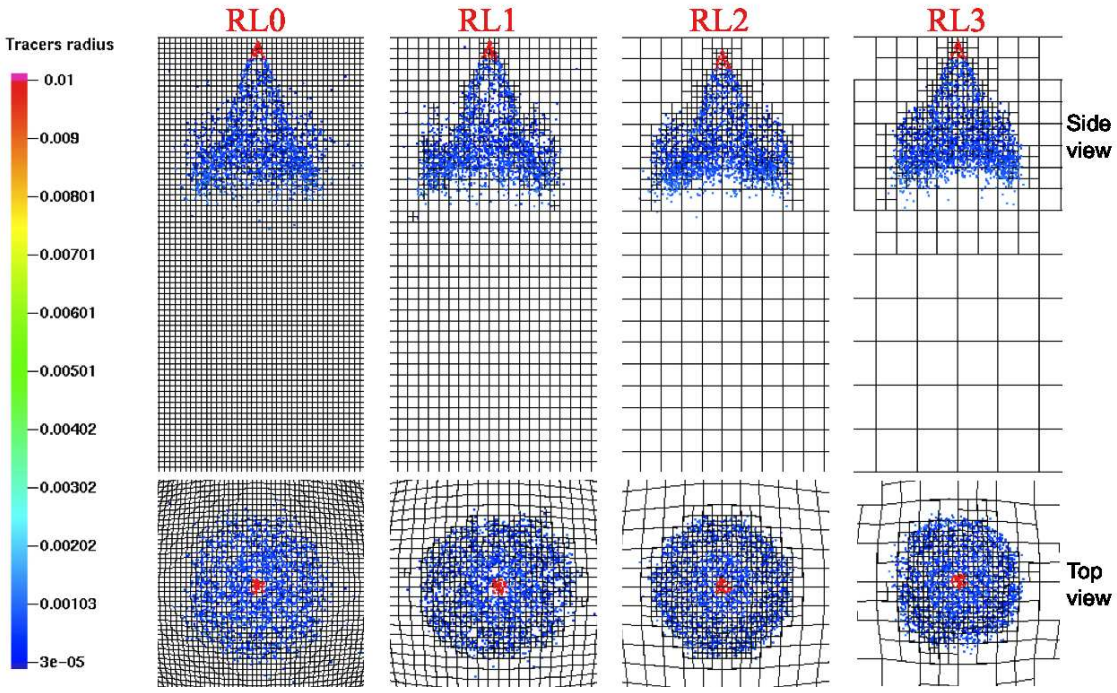

Figure 5.30: Spray structure at 1.2 ms after start of fuel injection (hollow-cone spray)

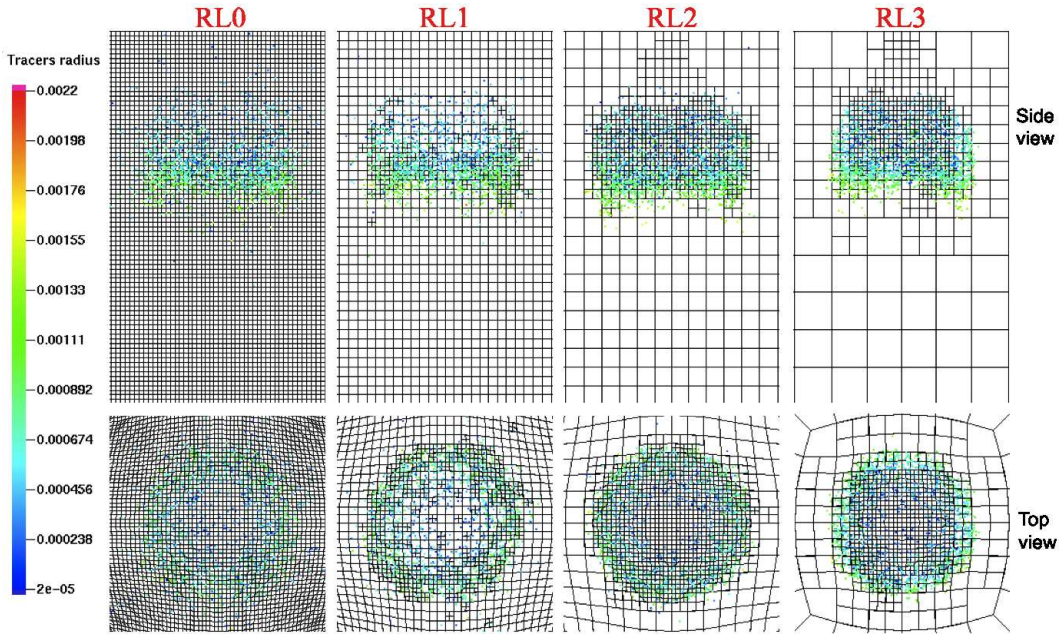

Figure 5.31: Spray structure at 2.0 ms after start of injection (hollow-cone spray)

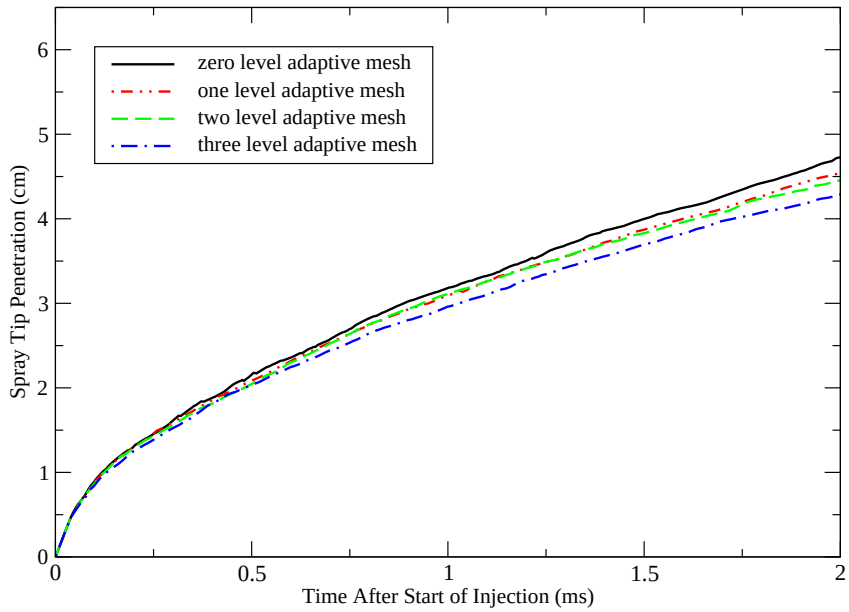

Figure 5.32: Comparison of the liquid spray tip penetrations predicted using different adaptive meshes (hollow-cone spray)

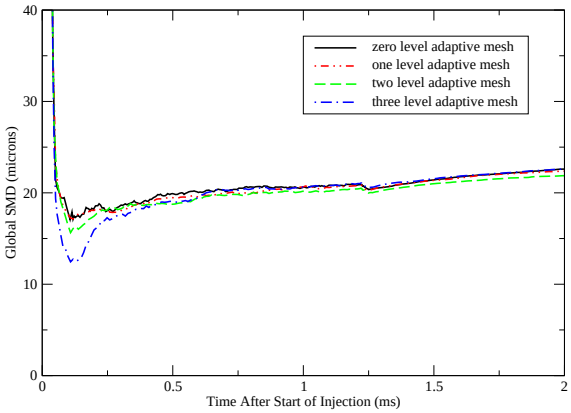

Figure 5.33: Comparison of the global SMD predicted using different adaptive meshes (solid-cone spray)

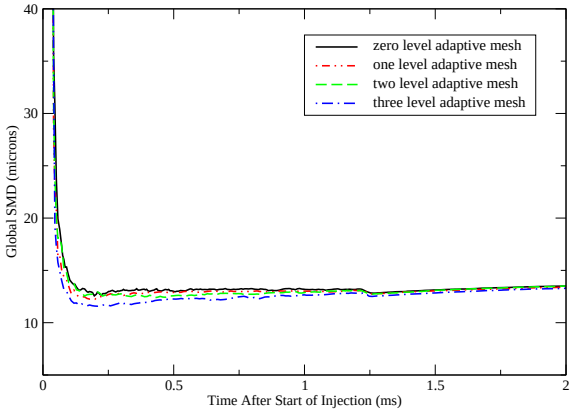

Figure 5.34: Comparison of the global SMD predicted using different adaptive meshes (hollow-cone spray)

5.2.3 Sauter Mean Diameter

The predicted global Sauter Mean Diameters using the adaptive meshes are compared for both the solid-cone and hollow-cone sprays. The SMD is a quantity characterizing the average droplet size of spray and the success of spray break-up. The SMD is the diameter of a model drop whose volume-to-surface-area ratio is equal to the ratio of the sum of all droplet volumes in the spray to the sum of all droplet surface areas and defined by

$$SMD = \sum_{i=1}^{n} d_i^3 / \sum_{i=1}^{n} d_i^2 \tag{5.2}$$

Results of the solid-cone spray simulations show good agreement after 0.5 ms between different meshes as shown in Figure 5.33. The three-level refinement mesh results in a large difference in SMD at the beginning. The present collision model uses the gas phase cell as the collision cell. The initial coarse grid near the nozzle may not adequately resolve the spatial gradient of the number density of drops, and hence under-predict the collision incidences, thus reducing the probability of drop coalescence to form bigger drops. Figure 5.34 shows that the predicted SMD agrees very well between different meshes with different levels of adaptation for the hollow-cone spray. The three-level adaptive mesh also gives a reasonably good prediction. The reason can be attributed to the configuration of the hollow-cone spray in which drops are penetrating into more cells initially.

5.2.4 Fuel Vapor and Temperature Distributions

Figures 5.35 and 5.36 show the predicted fuel vapor distribution at 0.8 ms and 1.4 ms after start of fuel injection, respectively. The fuel vapor distribution compares reasonably well. Figures 5.37 and 5.38 show the predicted temperature distribution at 0.8 ms and 1.4 ms, respectively. The temperature contours agree well with each other. Both the fuel and temperature contours predicted using three-level adaptive mesh shows a discrepancy against the fine mesh, which is caused by the shorter fuel spray penetration shortly after the fuel injection due to the initially coarse mesh around the nozzle exit as discussed above.

Quantitative comparisons are also made for mass fraction and temperature at the center of the chamber in the axial direction. Figures 5.39 and 5.40 show the values of mass fraction at 0.8 ms and 1.4 ms after start of fuel injection, respectively. It can be seen that the trend was captured by the one-level refinement and two-level refinement, although the values were slightly overproduced. The same is true for gas temperature as shown in Figures 5.41 and 5.42. Overall, Results predicted using one-level and two-level refinement agree well with those using the fine mesh. Because of under-predicted spray tip penetration using three-level refinement, the properties are not well predicted at the spray tip.

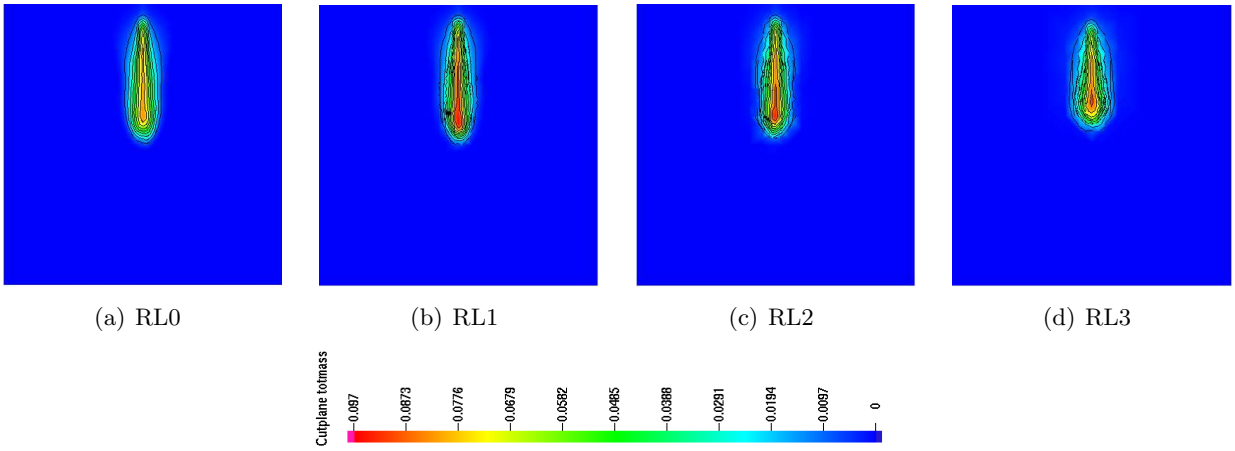

(a) RL0 (b) RL1 (c) RL2 (d) RL3

(e) mass fraction

Figure 5.35: Fuel vapor distributions predicted using different refinement levels at 0.8 ms after start of fuel injection (solid-cone spray)

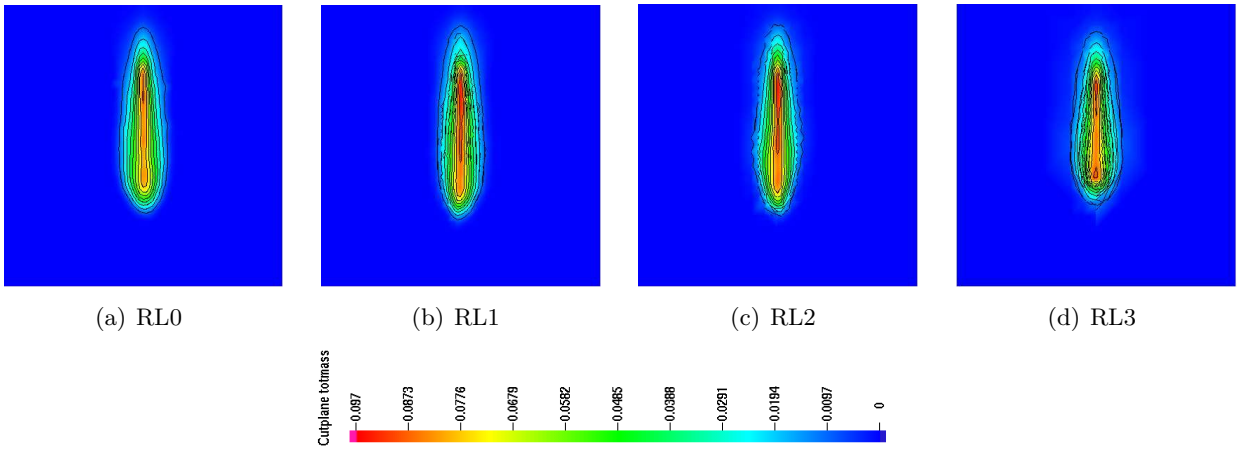

(a) RL0 (b) RL1 (c) RL2 (d) RL3

(e) mass fraction

Figure 5.36: Fuel vapor distributions predicted using different refinement levels at 1.4 ms after start of fuel injection (solid-cone spray)

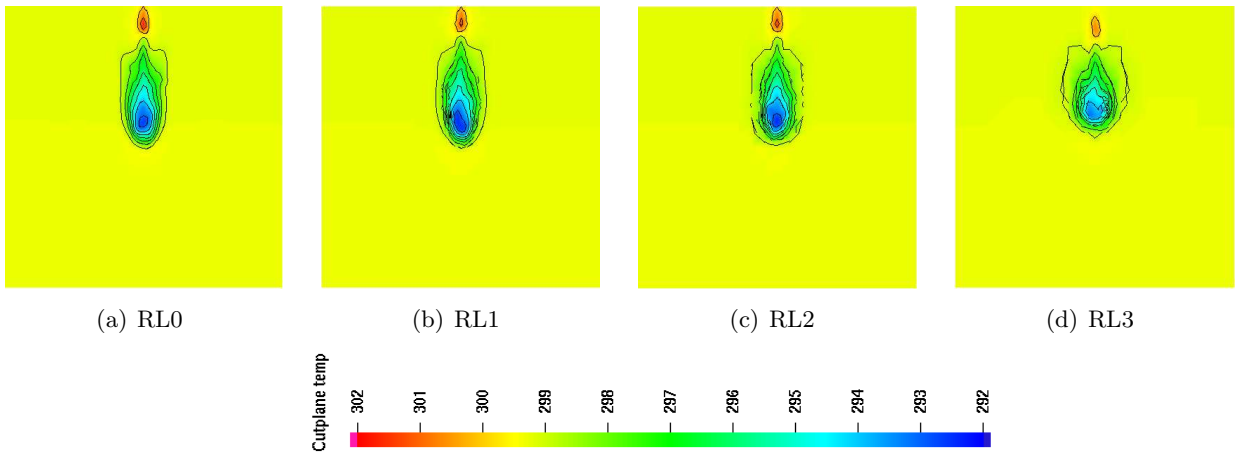

(a) RL0 (b) RL1 (c) RL2 (d) RL3

(e) temperature

Figure 5.37: Temperature contours predicted using different refinement levels at 0.8 ms after start of fuel injection (solid-cone spray)

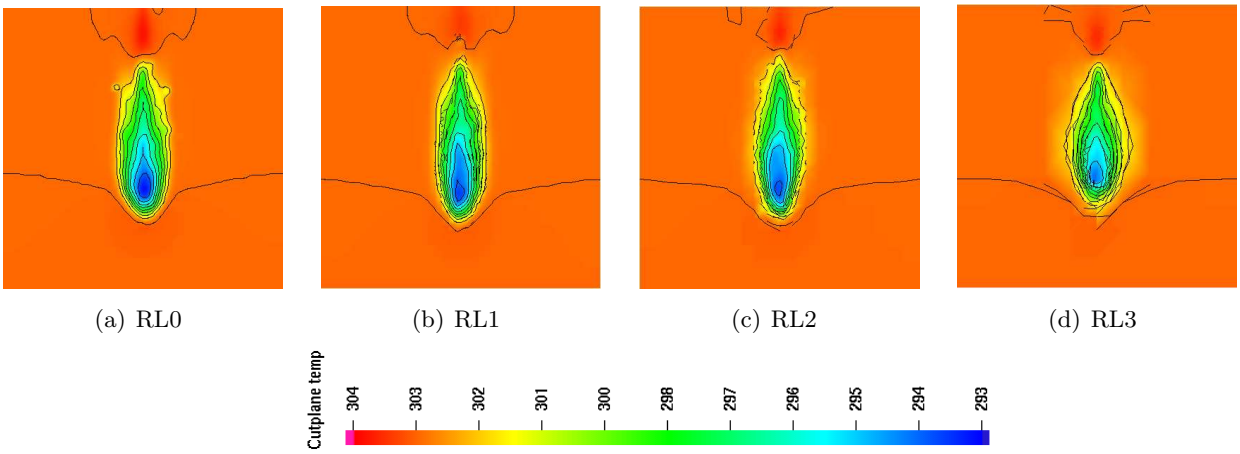

(a) RL0 (b) RL1 (c) RL2 (d) RL3

(e) temperature

Figure 5.38: Temperature contours predicted using different refinement levels at 1.4 ms after start of fuel injection (solid-cone spray)

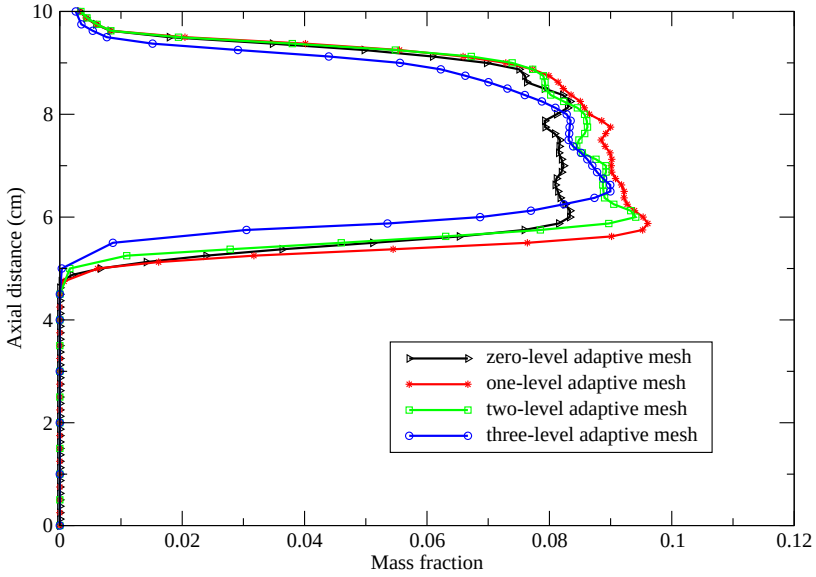

Figure 5.39: Mass fraction distribution along the spray axis predicted using different refinement level at 0.8 ms after start of injection (solid-cone spray)

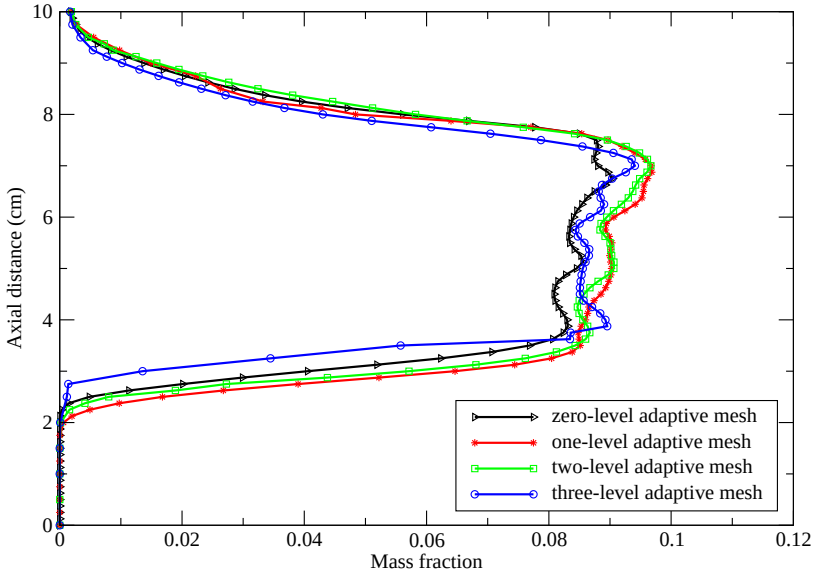

Figure 5.40: Mass fraction distribution along the spray axis predicted using different refinement level at 1.4 ms after start of injection (solid-cone spray)

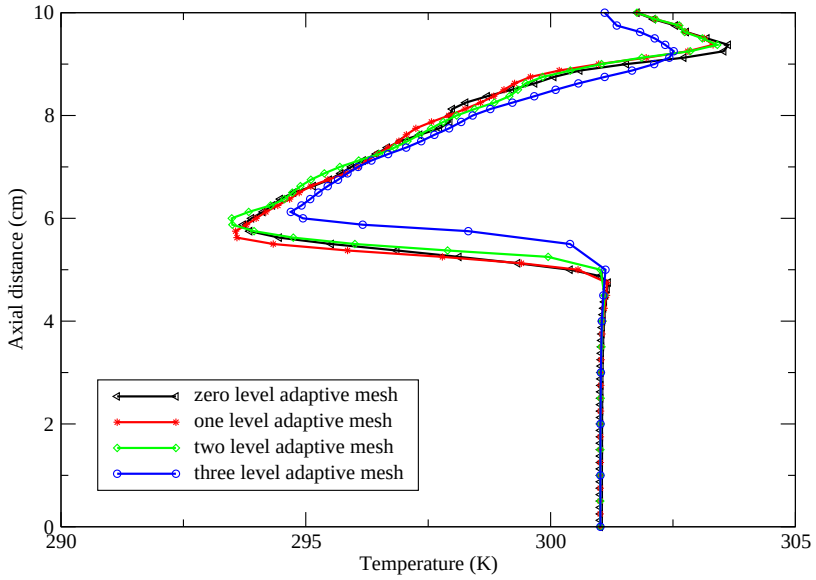

Figure 5.41: Temperature distribution along the spray axis predicted using different refinement level at 0.8 ms after start of injection (solid-cone spray)

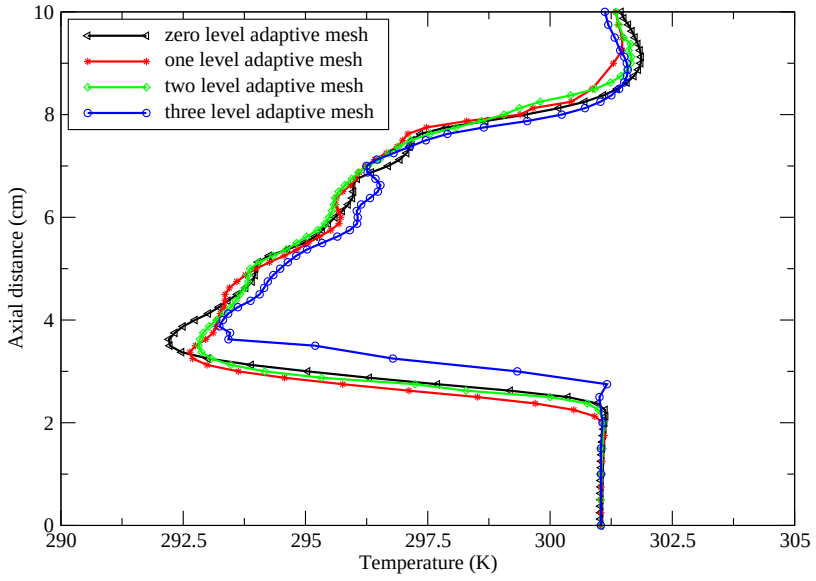

Figure 5.42: Temperature distribution along the spray axis predicted using different refinement level at 1.4 ms after start of injection (solid-cone spray)

5.2.5 AMR Algorithm Performance

To study the performance of this AMR algorithm for engine spray simulation, the computer time for mesh adaptation and other computations, total number of computational cells used in the simulation, and speed-up are investigated.

5.2.5.1 Computer Time

The algorithm basically consists of two parts: (1) KIVA-4 subroutines; and (2) the adaptation subroutines. First, the computer times for the two parts of the algorithm are separated and compared. The code was compiled and run on a single 2.8 GHz dual Intel Xeons processor. Results show that the adaptation part of the code consumed approximately 30% of the computer time and the spray and fluid dynamics computations consumes about 70% of the computer time. Figures 5.43, 5.44, and 5.45 show the computer time consumptions for the one-level, two-level, and three-level refinement for solid-cone spray simulations.

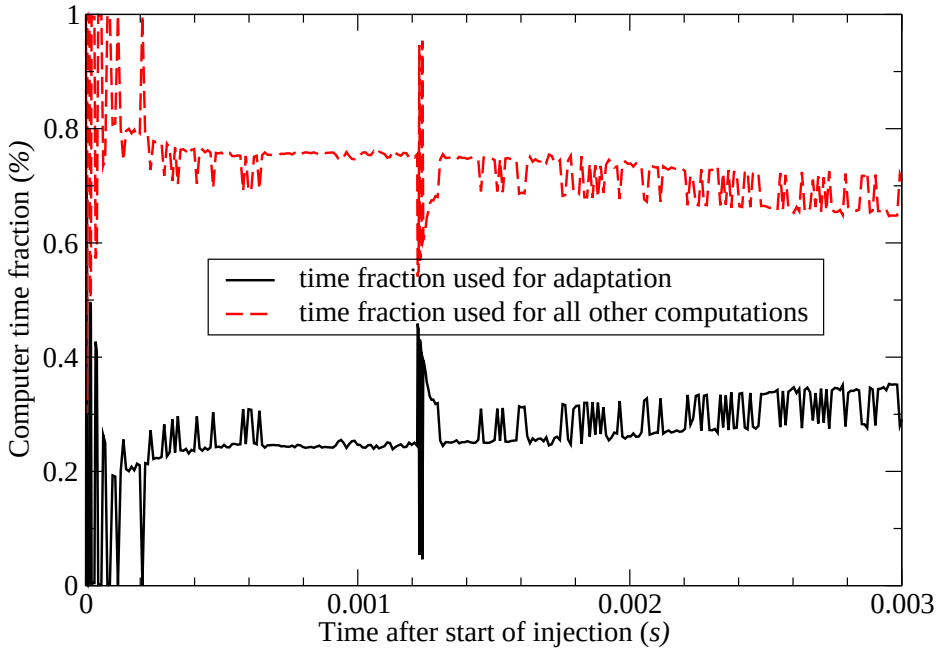

Figure 5.43: The fraction of computer time used for adaptation and all other computation at each time step (one level refinement solid-cone spray case)

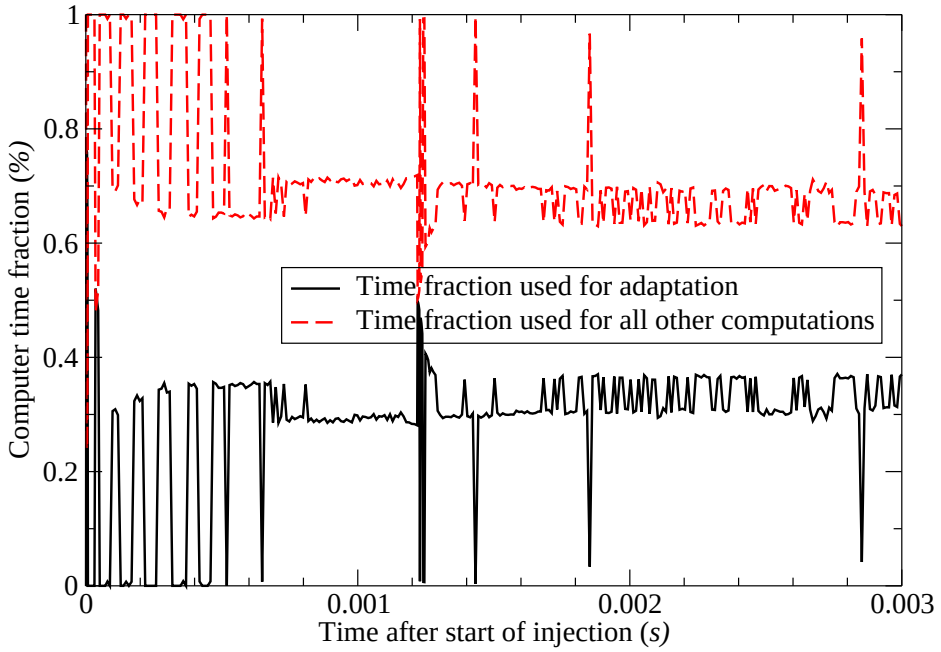

Figure 5.44: The fraction of computer time used for adaptation and all other computation at each time step (two level refinement solid-cone spray case)

5.2.5.2 Number of Computational Cells Used

For the solid-cone spray case, Figure 5.46 shows the ratio of the number of computational cells used in the AMR simulation to that of an equivalent, uniformly fine mesh (i.e., RL0 in Fig 5.26). The ratio increases with time, because more cells were added in the AMR mesh as the spray penetrates into the chamber during injection. For the one-level refinement case, the ratio is about 0.13 throughout the simulation. On average, the ratios for the two-level and three-level refinement cases are at 0.01-0.03. Because the total numbers of computational cells are only 13% (using RL1) to 1% (using RL3) of those using the uniformly fine mesh (RL0), this implies a factor of 7-100 savings in memory using the present mesh adaptation method.

5.2.5.3 Computational Efficiency

The advantage of using the adaptive algorithm is demonstrated by the reduction in computer time used. The computer time and the speed-up using a Pentium 2.8 GHz processor from the

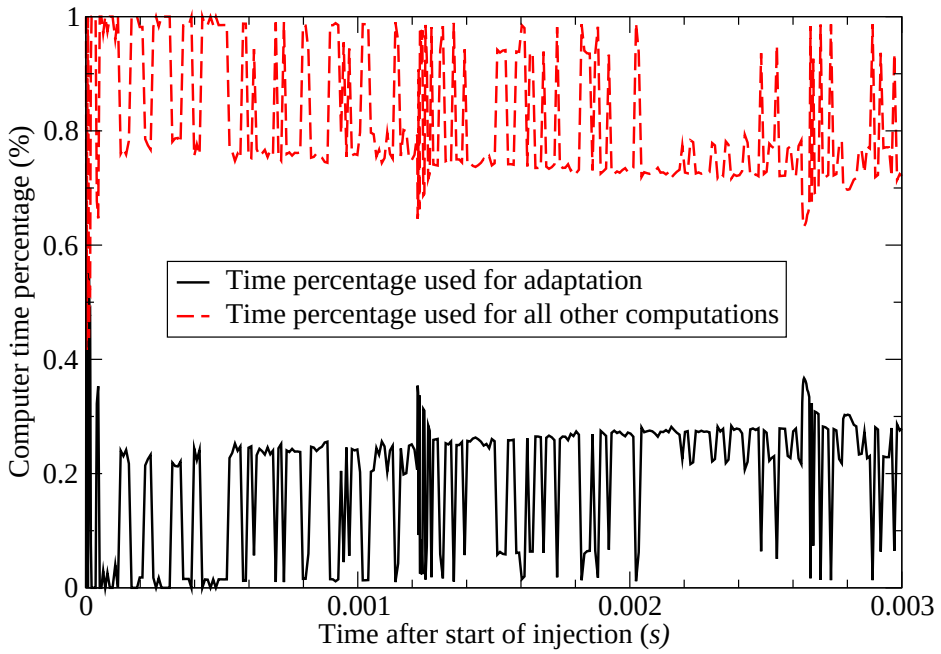

Figure 5.45: The fraction of computer time used for adaptation and all other computation at each time step (three level refinement solid-cone spray case)

start to 3.0 ms after injection are compared as shown in Tables 5.3 and 5.4 for the solid-cone and hollow-cone sprays, respectively. The speed-up is based on the computer time using the finest grid as defined in Eqn.(5.1). The present adaptive refinement method shows a significant time savings. As can be seen, the three-level adaptation can achieve a speed-up of 92 for the solid-cone spray and a speed-up of 46 for the hollow-cone spray. It is very computationally efficient and can benefit the analysis and optimization of the engine spray processes for new spray technique development.

Table 5.3: Comparison of the computer time and speed-up for the solid-cone spray simulation

Mesh	Refinement Level	Initial Grid Space (mm)	Computer Time (min)	Speed up
0L-AMR	RL0	1.25	1014	1
1L-AMR	RL1	2.50	146	7
2L-AMR	RL2	5.00	28	36
3L-AMR	RL3	10.0	11	92

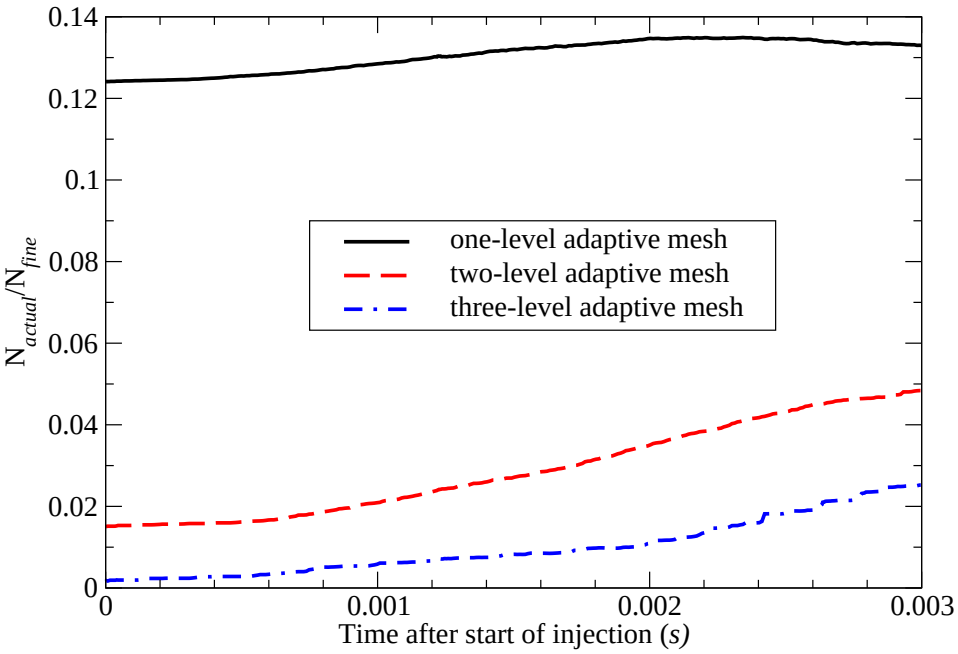

Figure 5.46: The ratio of actually used computational cells to the number of uniform grid cells for each time step (solid-cone spray case).

Table 5.4: Comparison of the computer time and speed-up for the hollow-cone spray simulation

Mesh	Refinement Level	Initial Grid Space (mm)	Computer Time (min)	Speed up
0L-AMR	RL0	1.25	1006	1
1L-AMR	RL1	2.50	200	5
2L-AMR	RL2	5.00	53	19
3L-AMR	RL3	10.0	22	46

5.3 Direct-Injection Engine Spray Simulation

5.3.1 Computational Conditions

The simulation of spray and mixture formation processes was also carried out using the present AMR method in a realistic direct-injection gasoline engine, as shown in Figure 5.47. The engine has a bore of 10 cm and a stroke of 9.5 cm. An O-type grid was used for simulation. In this study, a six-hole injector was simulated. The injection velocity was 142 m/s, and the injection started at 190 degrees after top-dead-center (ATDC). The injection duration was 36 crank angle degrees (CAD) with a total of 14.7 mg of fuel for an overall equivalence ratio of 0.3 for a part-load condition. The nozzle hole diameter and initial drop size were both 200 μm. The engine speed was 1500 rpm. The computation started at 180 ATDC with an initial temperature and pressure in the chamber of 400 K and 1 bar, respectively. The physical sub-models used are the same as previous engine case. A cell will be refined if the mass of liquid fuel exceeds 10^{-7} g.

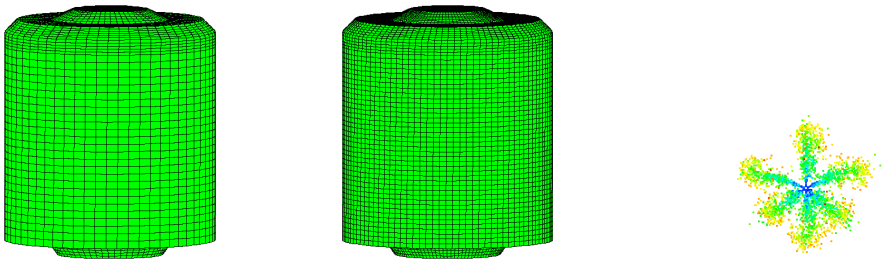

(a) AMR mesh (b) fine mesh (c) six-jet

Figure 5.47: Computational domain used for a DISI engine simulation: (a) baseline AMR mesh, and (b) fine mesh, and (c) six-jet spray arrangement.

5.3.2 Spray Structure and Equivalence Ratio

The predicted liquid spray patterns and equivalence ratio distributions were compared using three different meshes. The mesh density of the "fine mesh" (Fig. 5.47(b)) is 4 times that of the baseline coarse mesh (Fig. 5.47(a)), and the equivalent resolution of the "AMR mesh" is 8 times that of the baseline coarse mesh due to the isotropic cell division. Figure 5.48 shows liquid drop distributions colored by the radii of drops at 220 ATDC on three meshes. The

coarse mesh produced a limited spray penetration in the radial direction compared to the other two meshes. The fine mesh and the AMR mesh predicted similar liquid spray patterns. The penetrations using the AMR mesh are somewhat longer than those using the "fine mesh" in both the radial and axial directions due to the higher local mesh resolution of the AMR mesh.

Figure 5.49 shows the distributions of the equivalence ratio at 340 ATDC. The AMR mesh predicted a similar fuel vapor distribution to the "fine mesh." Results show that the current AMR scheme can provide improved spray simulations and the air-fuel mixing process in an engine with a moving boundary (i.e., piston).

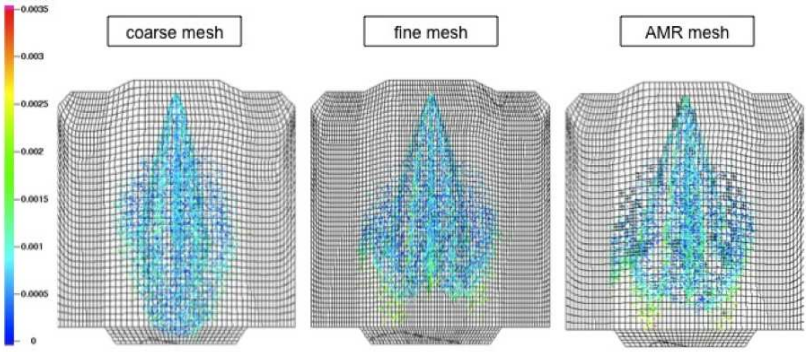

Figure 5.48: Distribution of the liquid droplets predicted on different meshes at 220 ATDC

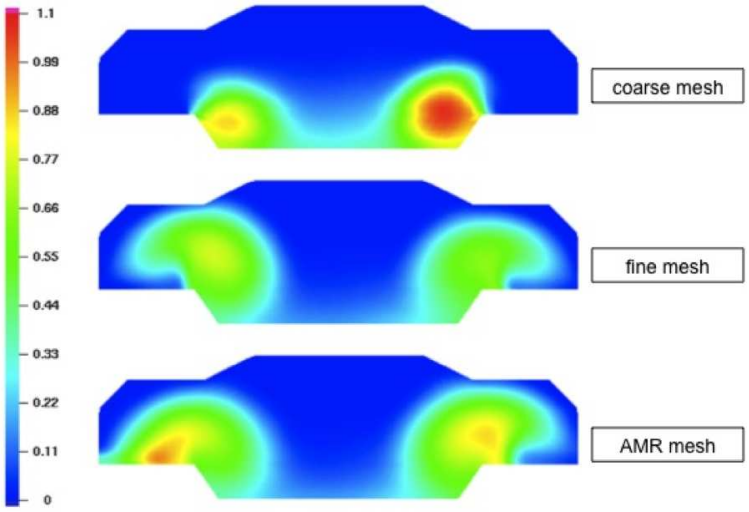

Figure 5.49: Equivalence ratio predicted on different meshes at 340 ATDC

5.4 Sensitivity Study

The total number of parcels is an important parameter for the spray simulation (Subramaniam et al., 1998). The influence of the total number of parcels used and spray sub-models on the adaptive mesh refinement is investigated here.

5.4.1 Influence of Variations of Total Number of Parcels on AMR

The study cases in Table 5.5 was performed on the grid with different input parameter ***tnparc*** values of 2×10^3, 5×10^3, 1×10^4, and 2×10^4, which control the number of spray parcels injected into the cylinder.

Table 5.5: Table of the number of parcels for sensitivity study

Cases	Evaporation Model	Collision Model	Break-up Model	**tnparc**
I	on	on	on	5000
II	on	on	on	10000
III	on	on	on	20000

5.4.1.1 Spray Structure

Figures 5.50 to 5.55 show the spray patterns at two different times, 0.8 ms and 1.4 ms after the start of fuel injection, for different total number of spray parcels (***tnparc***) cases. Overall, AMR performs similarly for different ***tnparc*** as for the case using 2000 ***tnparc***. The one-level and two-level adaptive calculations predict similar spray structure as the fine mesh. The three-level adaptive calculation somehow under-predicts the spray tip structure. The level of accuracy of predictions does not degenerate due to the number of the parcels.

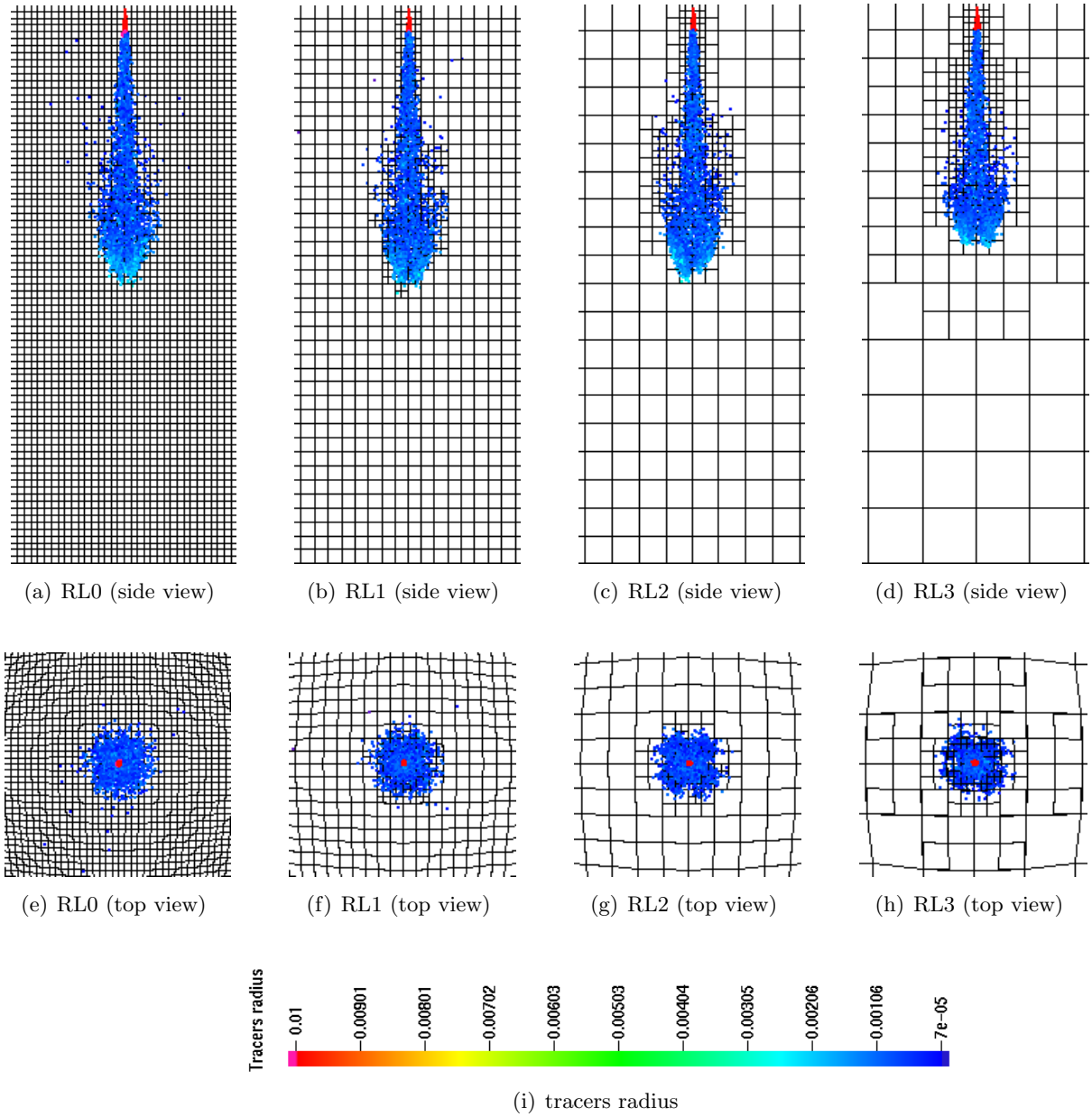

(a) RL0 (side view) (b) RL1 (side view) (c) RL2 (side view) (d) RL3 (side view)

(e) RL0 (top view) (f) RL1 (top view) (g) RL2 (top view) (h) RL3 (top view)

(i) tracers radius

Figure 5.50: Spray structure predicted using different meshes at 0.8 *ms* after start of injection for solid-cone spray (**tnparc**=5000)

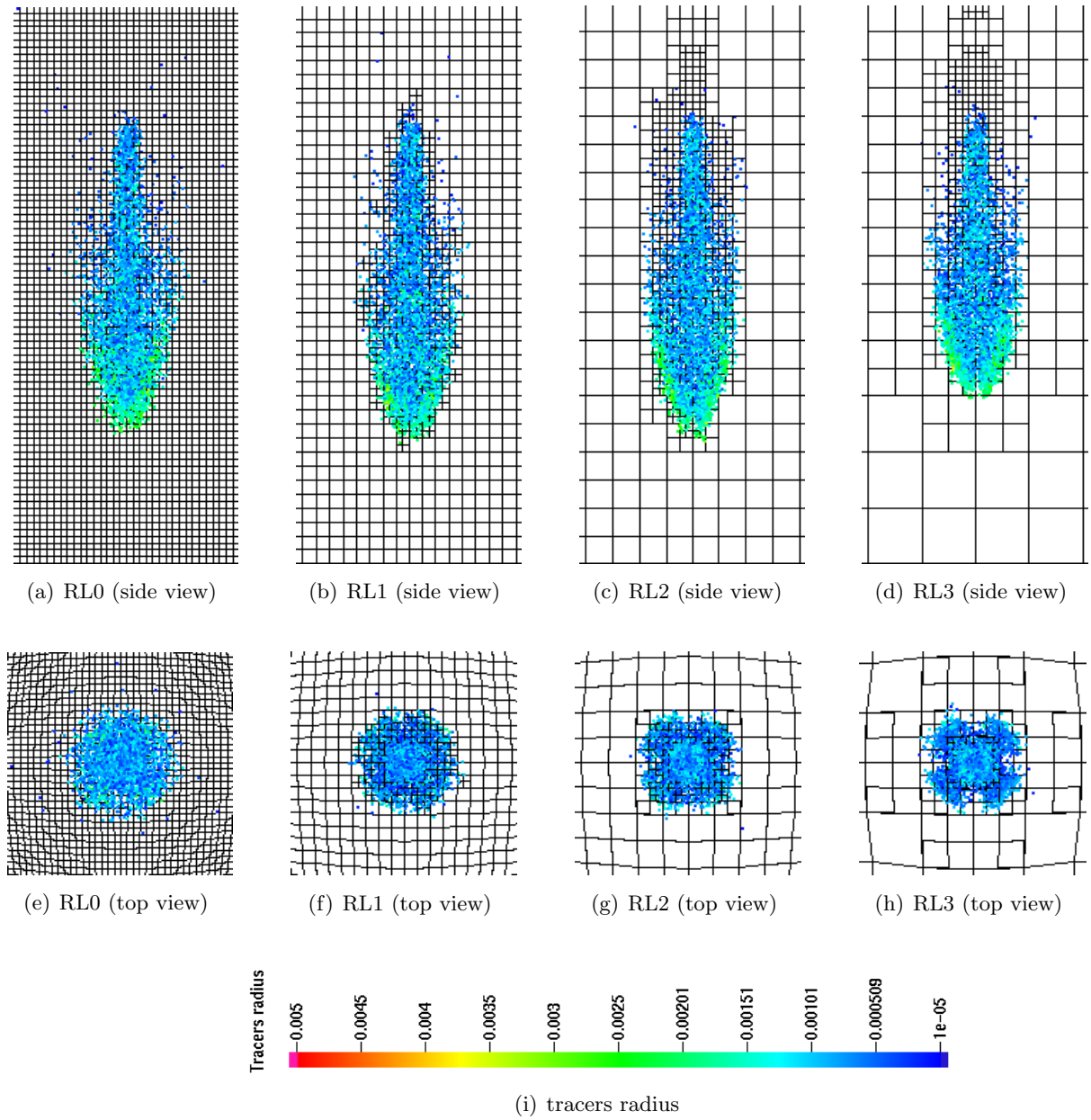

(a) RL0 (side view) (b) RL1 (side view) (c) RL2 (side view) (d) RL3 (side view)

(e) RL0 (top view) (f) RL1 (top view) (g) RL2 (top view) (h) RL3 (top view)

(i) tracers radius

Figure 5.51: Spray structure predicted using different meshes at 1.4 *ms* after start of injection for solid-cone spray (**tnparc**=5000)

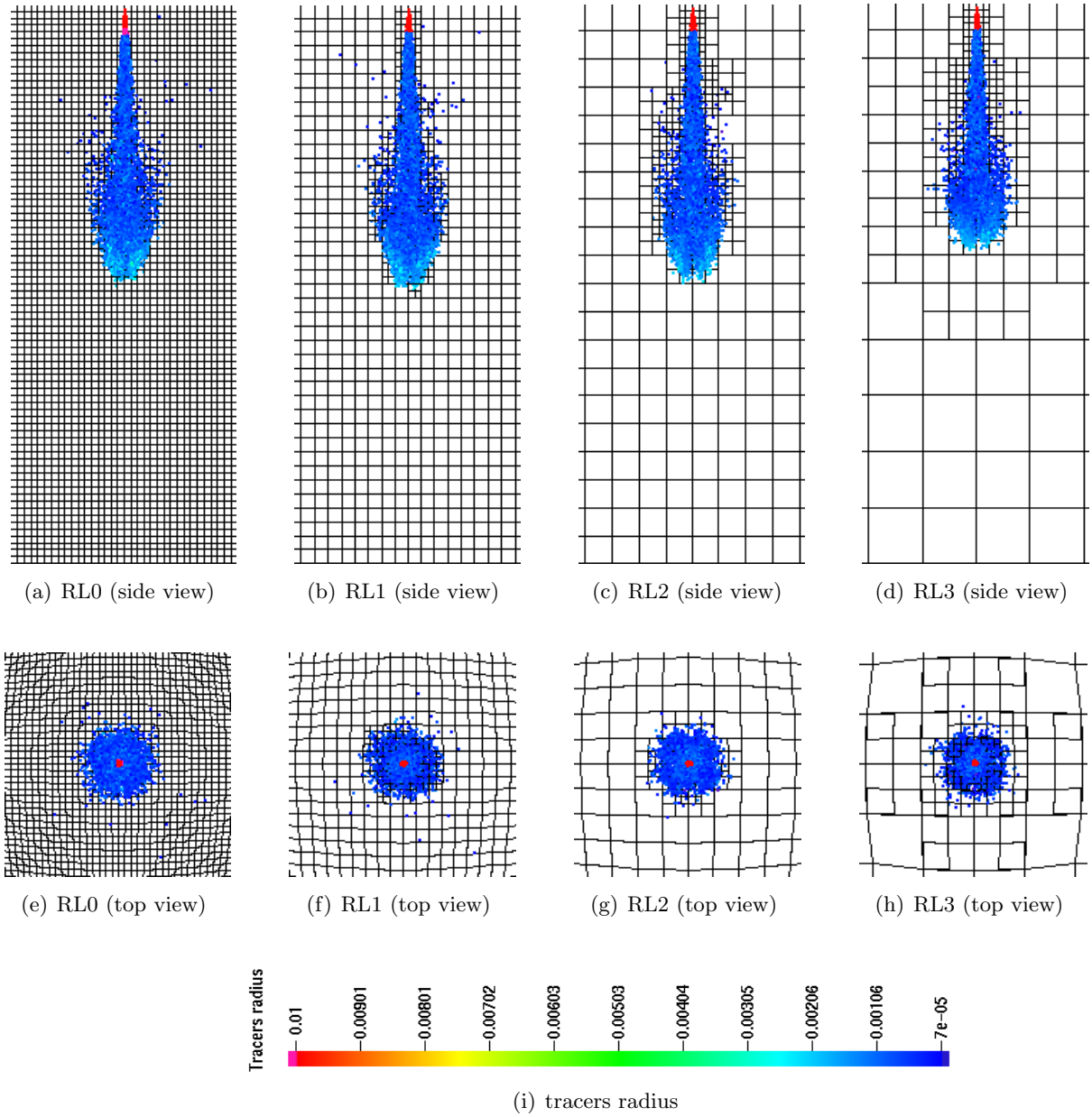

(a) RL0 (side view) (b) RL1 (side view) (c) RL2 (side view) (d) RL3 (side view)

(e) RL0 (top view) (f) RL1 (top view) (g) RL2 (top view) (h) RL3 (top view)

(i) tracers radius

Figure 5.52: Spray structure predicted using different meshes at 0.8 *ms* after start of injection for solid-cone spray (**tnparc**=10000)

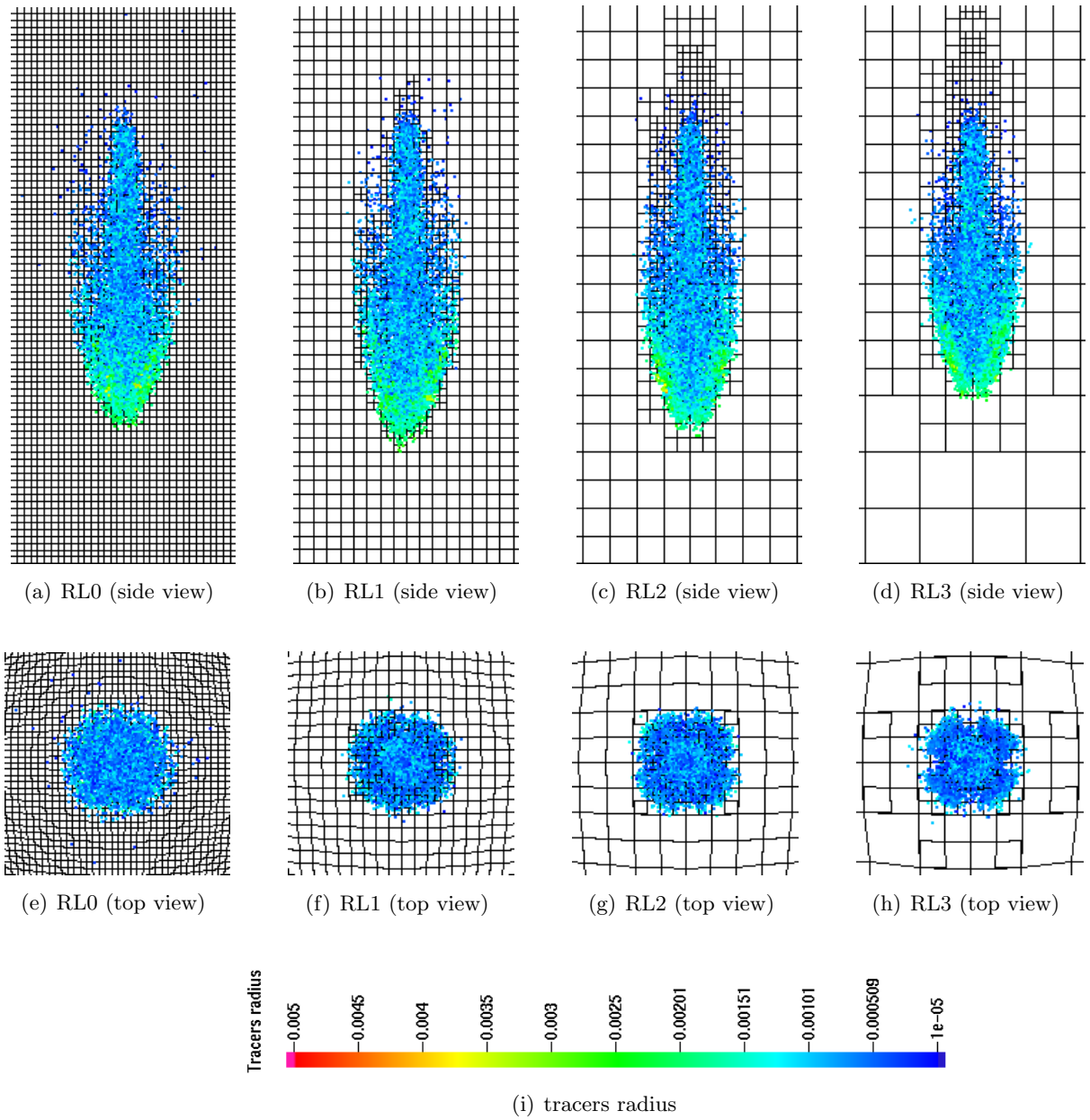

(a) RL0 (side view) (b) RL1 (side view) (c) RL2 (side view) (d) RL3 (side view)

(e) RL0 (top view) (f) RL1 (top view) (g) RL2 (top view) (h) RL3 (top view)

(i) tracers radius

Figure 5.53: Spray structure predicted using different meshes at 1.4 *ms* after start of injection for solid-cone spray (**tnparc**=10000)

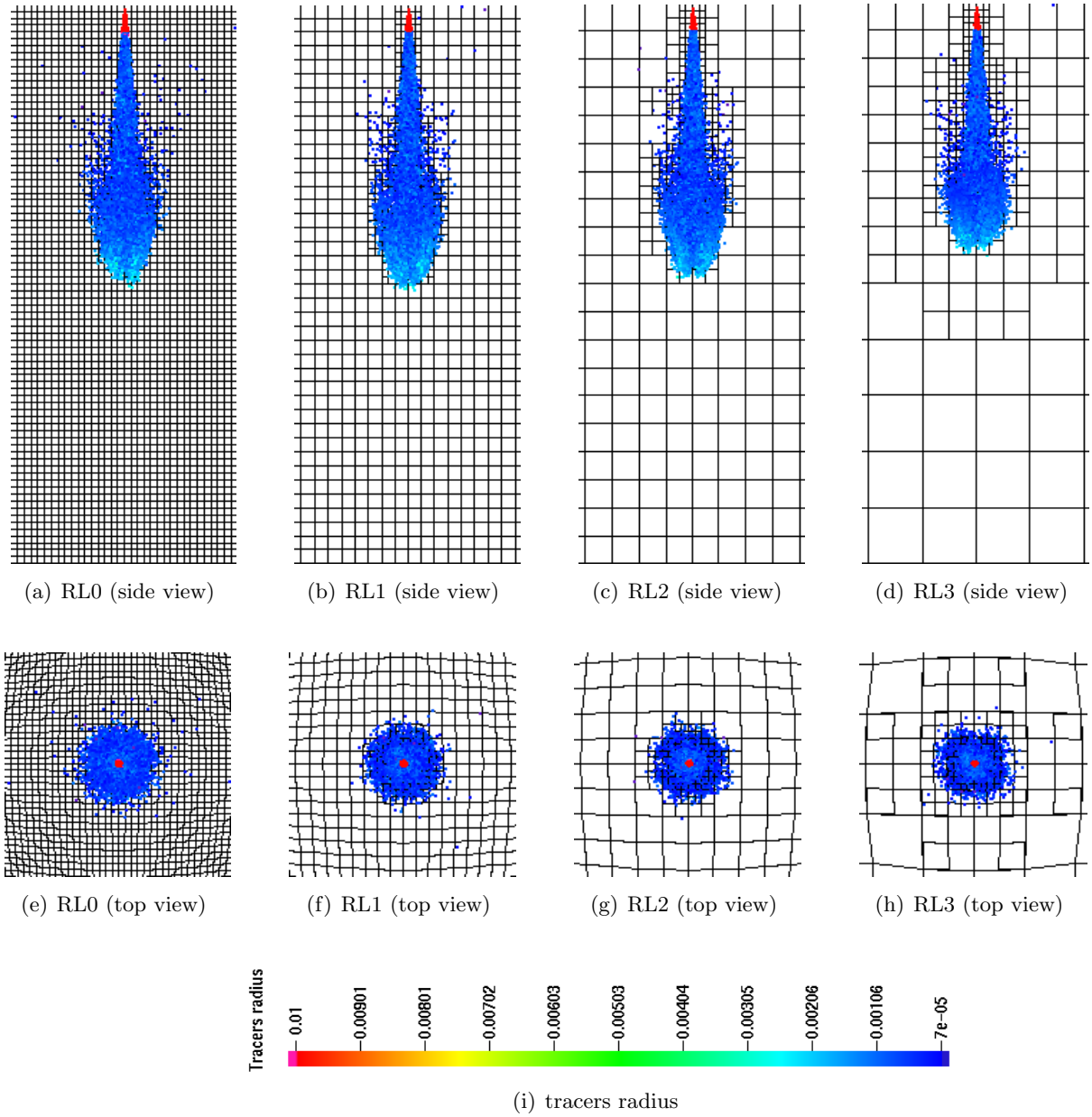

(a) RL0 (side view) (b) RL1 (side view) (c) RL2 (side view) (d) RL3 (side view)

(e) RL0 (top view) (f) RL1 (top view) (g) RL2 (top view) (h) RL3 (top view)

(i) tracers radius

Figure 5.54: Spray structure predicted using different meshes at 0.8 *ms* after start of injection for solid-cone spray (**tnparc**=20000)

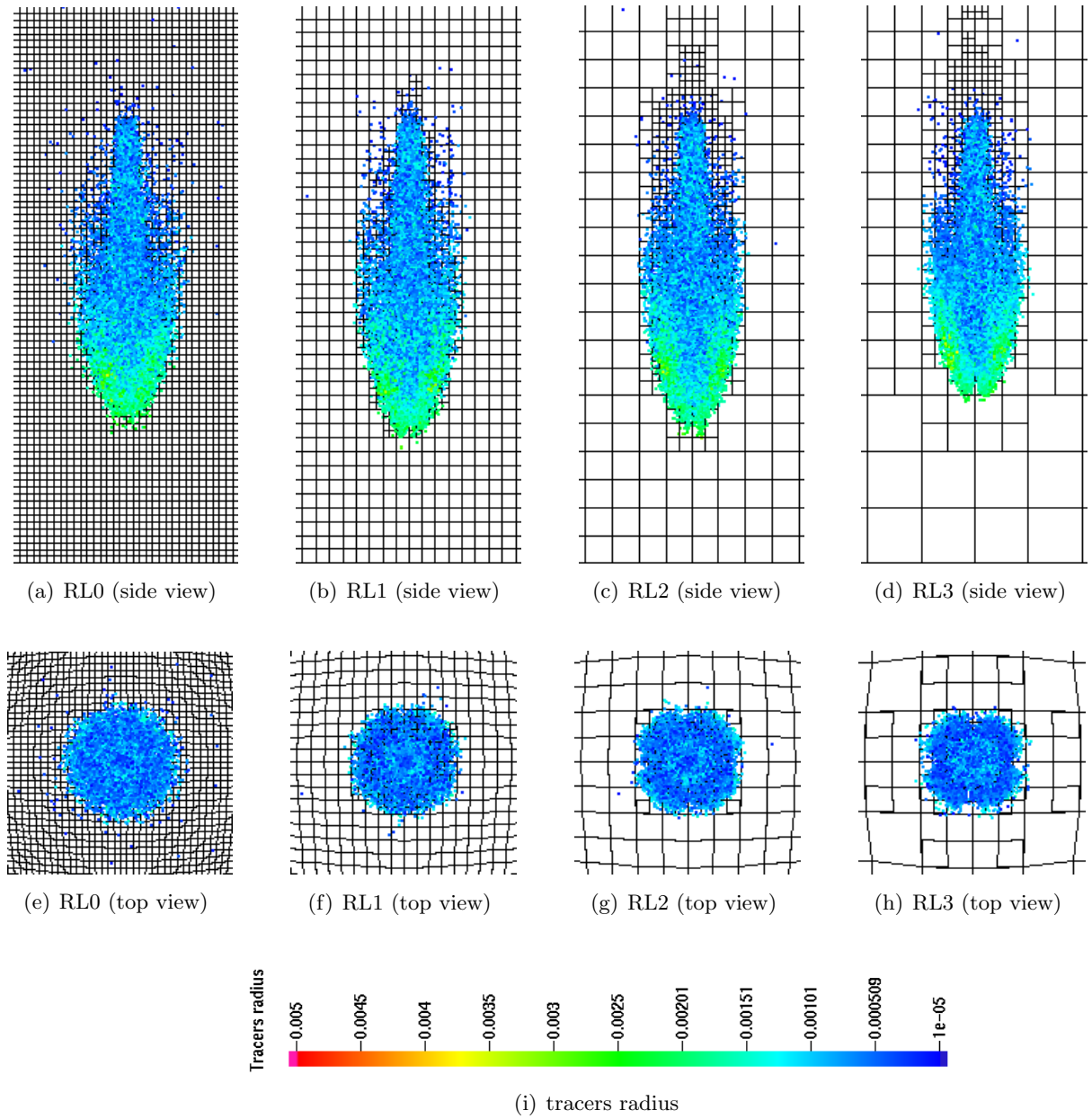

(a) RL0 (side view) (b) RL1 (side view) (c) RL2 (side view) (d) RL3 (side view)

(e) RL0 (top view) (f) RL1 (top view) (g) RL2 (top view) (h) RL3 (top view)

(i) tracers radius

Figure 5.55: Spray structure predicted using different meshes at 1.4 *ms* after start of injection for solid-cone spray (**tnparc**=20000)

5.4.1.2 Spray Penetration and SMD

The spray penetrations are shown in Figures 5.56 to 5.58. AMR predicts similar spray penetration variations on different meshes with the proper refinement level for different ***tnparc*** cases as the previous ***tnparc*** = 2000 cases. The one-level and two-level adaptive meshes predict similar spray tip penetration as the fine mesh. The three-level adaptive mesh under predicts the spray tip penetration.

The global SMD for different ***tnparc*** cases are shown in Figures 5.59 to 5.61. AMR gives similar SMD value comparison for different number of parcel cases.

Overall, AMR predicts the same level of accuracy for different number of parcels on different mesh with proper refinement level, in terms of spray structure, liquid spray tip penetration and SMD.

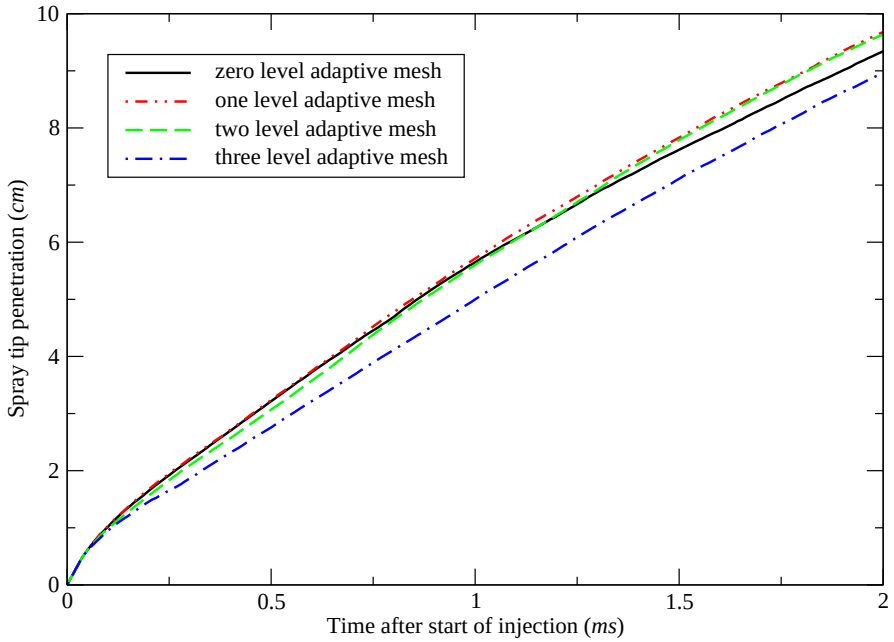

Figure 5.56: Liquid spray tip penetrations predicted using different mesh for solid-cone spray with **tnparc**=5000

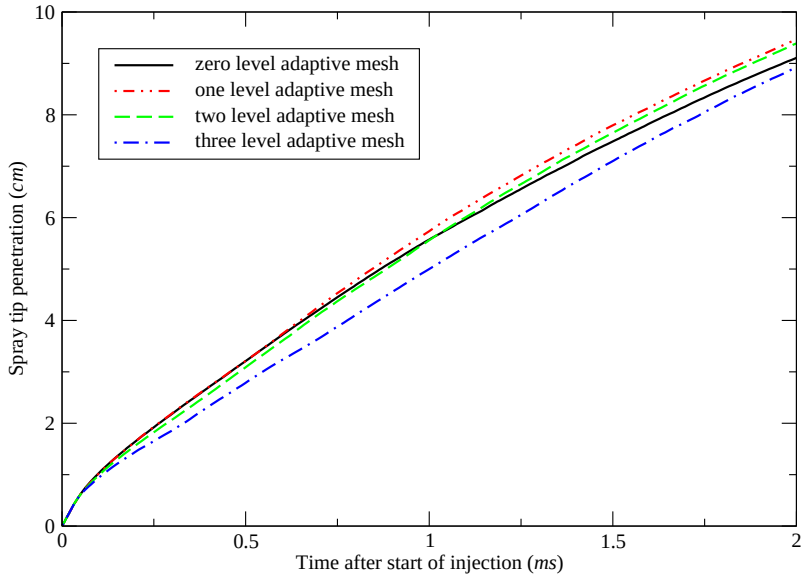

Figure 5.57: Liquid spray tip penetrations predicted using different mesh for solid-cone spray with **tnparc**=10000

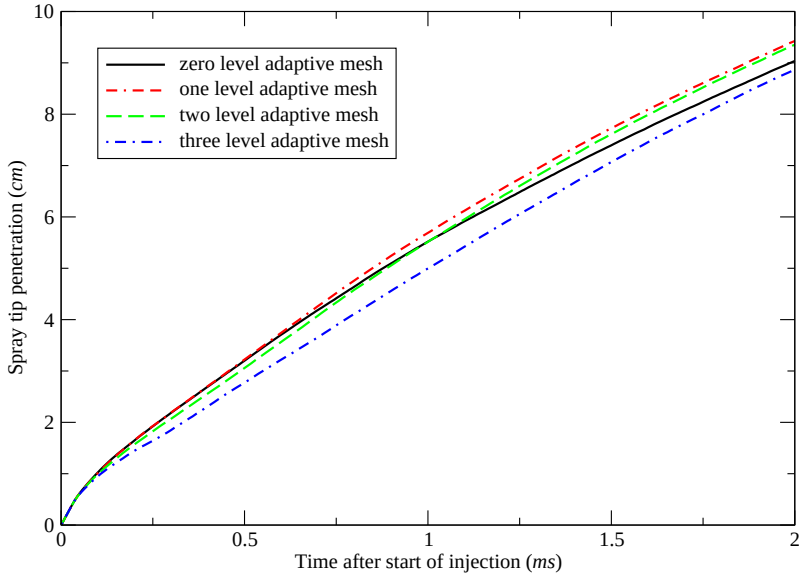

Figure 5.58: Liquid spray tip penetrations predicted using different mesh for solid-cone spray with **tnparc**=20000

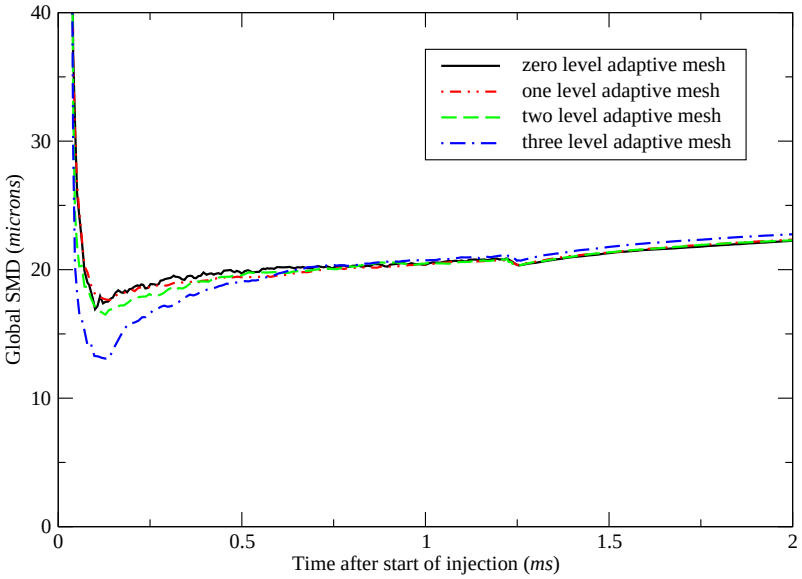

Figure 5.59: Global SMD predicted using different mesh for solid-cone spray with **tnparc**=5000

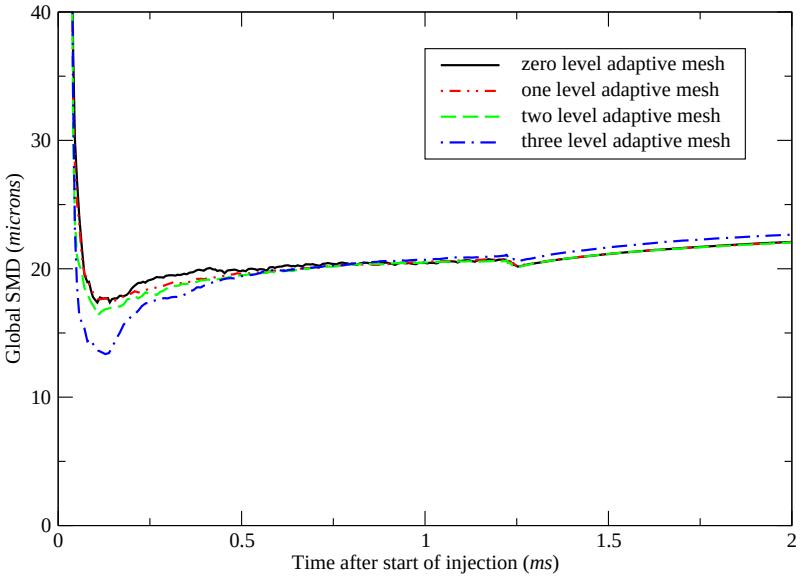

Figure 5.60: Global SMD predicted using different mesh for solid-cone spray with **tnparc**=10000

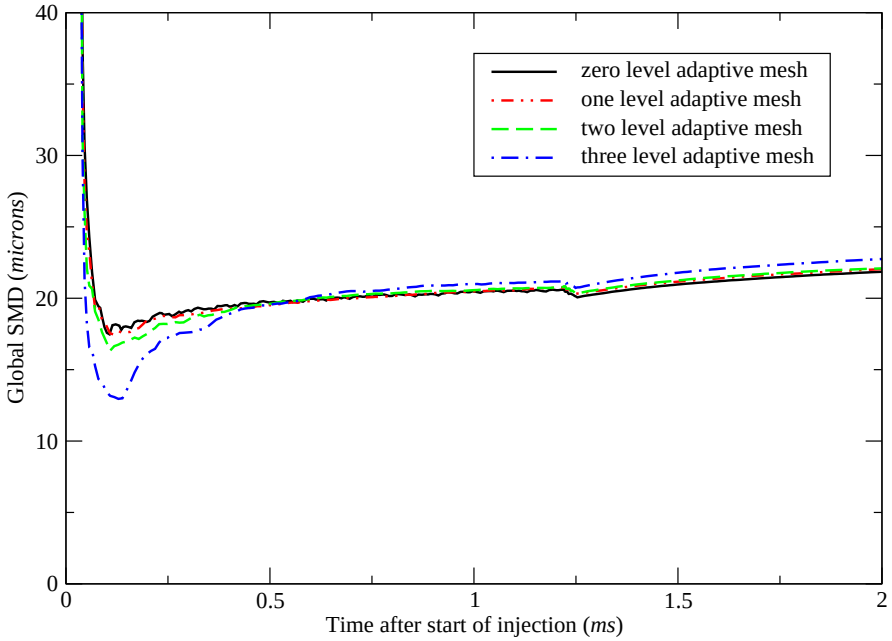

Figure 5.61: Global SMD predicted using different mesh for solid-cone spray with **tnparc**=20000

5.4.2 Influence of Different Spray Sub-models on AMR

To investigate the sensitivity of the adaptive mesh refinement method to the spray sub-models, AMR were tested with different spray sub-models combinations. All the studied cases are listed in Table 5.6. The predicted spray structure, spray tip penetration, and SMD are compared and discussed.

Table 5.6: Table of spray sub-model option for the sensitivity study

Cases	Evaporation Model	Collision Model	Break-up Model	**tnparc**
1	off	on	on	2000
2	off	off	on	2000
3	off	off	off	2000

5.4.2.1 Spray Structures

Figures 5.62 to 5.67 show the spray patterns at different time for different cases. Figures 5.62 and 5.63 show the spray structures at 0.8 ms and 1.4 ms of Case 1, in which the evaporation model were turned off. Results show that fine mesh and coarse meshes with appropriate refinement levels produce very similar spray penetrations. On the other hand, the drop distributions shown in topviews are somewhat different. The pattern predicted by three-level refinement shows a cross-shape structure.

Figures 5.64 and 5.65 present the snapshots of the predicted drop distributions of case 2 at 0.8 ms and 1.4 ms after start of fuel injection, respectively. Results are obtained using different adaptive levels on four different initial meshes. The drops are colored by their radii. It can be seen that similar spray penetration were predicted by the fine mesh and coarse meshes with proper refinement level. The topviews are also similar for the meshes. The pronounced cross-shape structure was improved. This, to some extend, indicates that the collision model is sensitive to grid resolution.

The snapshots of predicted drop distribution for Case 3 were plotted in Figures 5.66 and 5.67 for 0.4 ms and 0.8 ms after start of fuel injection, respectively. Results show that the fine mesh and coarse mesh with appropriate refinement levels produce very similar spray structure from both sideview and topview when all the spray sub-models are turned off. This indicates that the breakup and collision models are critical to grid-independency for spray simulation, which has been observed and studied by Abani et al. (2006); Schmidt et al. (2000); Stiesch (2003).

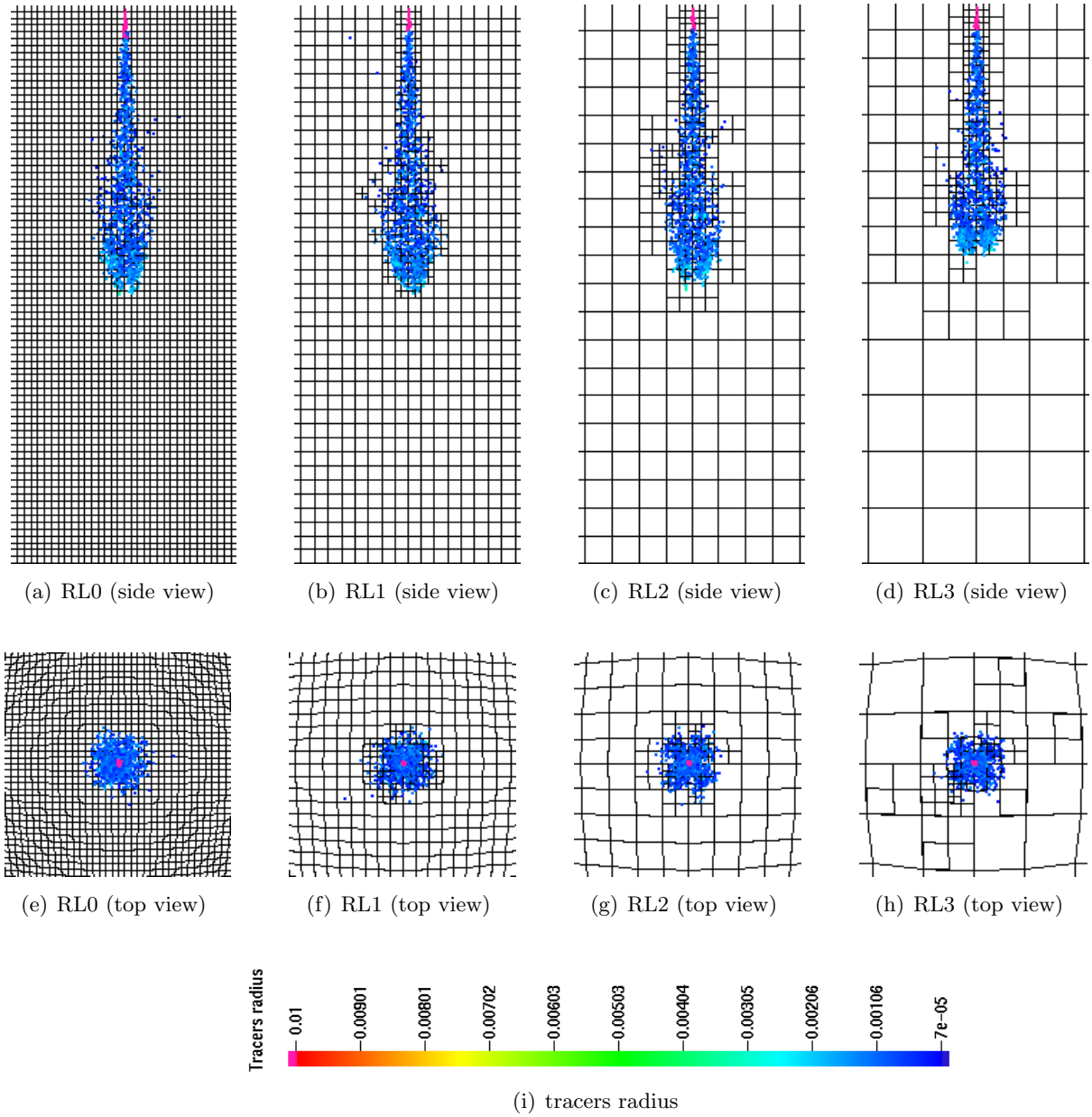

(a) RL0 (side view) (b) RL1 (side view) (c) RL2 (side view) (d) RL3 (side view)

(e) RL0 (top view) (f) RL1 (top view) (g) RL2 (top view) (h) RL3 (top view)

(i) tracers radius

Figure 5.62: Spray structure predicted using different meshes at 0.8 *ms* after start of injection for solid-cone spray (evaporation model off)

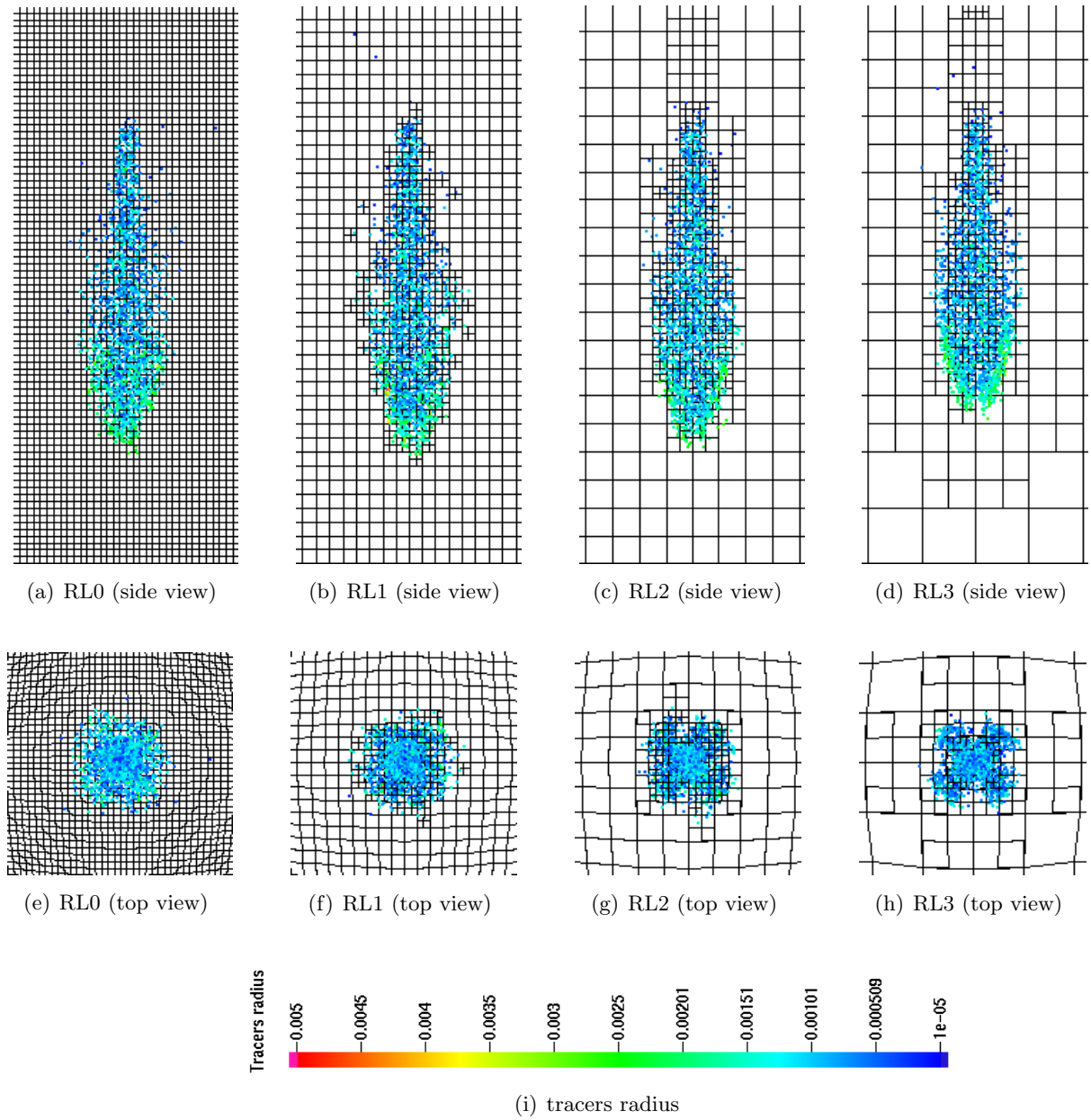

(a) RL0 (side view) (b) RL1 (side view) (c) RL2 (side view) (d) RL3 (side view)

(e) RL0 (top view) (f) RL1 (top view) (g) RL2 (top view) (h) RL3 (top view)

(i) tracers radius

Figure 5.63: Spray structure predicted using different meshes at 1.4 *ms* after start of injection for solid-cone spray (evaporation model off)

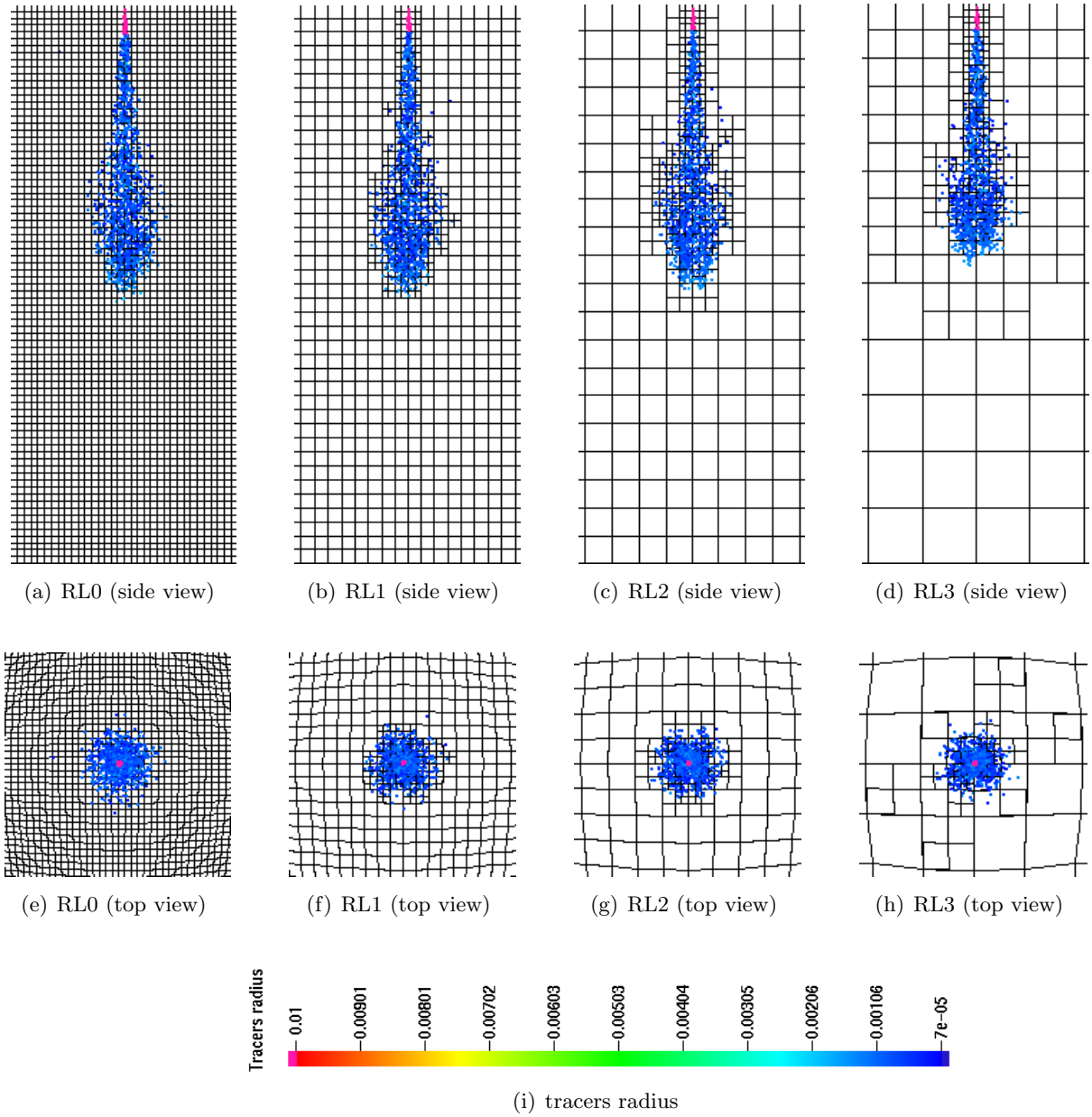

(a) RL0 (side view) (b) RL1 (side view) (c) RL2 (side view) (d) RL3 (side view)

(e) RL0 (top view) (f) RL1 (top view) (g) RL2 (top view) (h) RL3 (top view)

(i) tracers radius

Figure 5.64: Spray structure predicted using different meshes at 0.8 *ms* after start of injection for solid-cone spray (evaporation and collision model off)

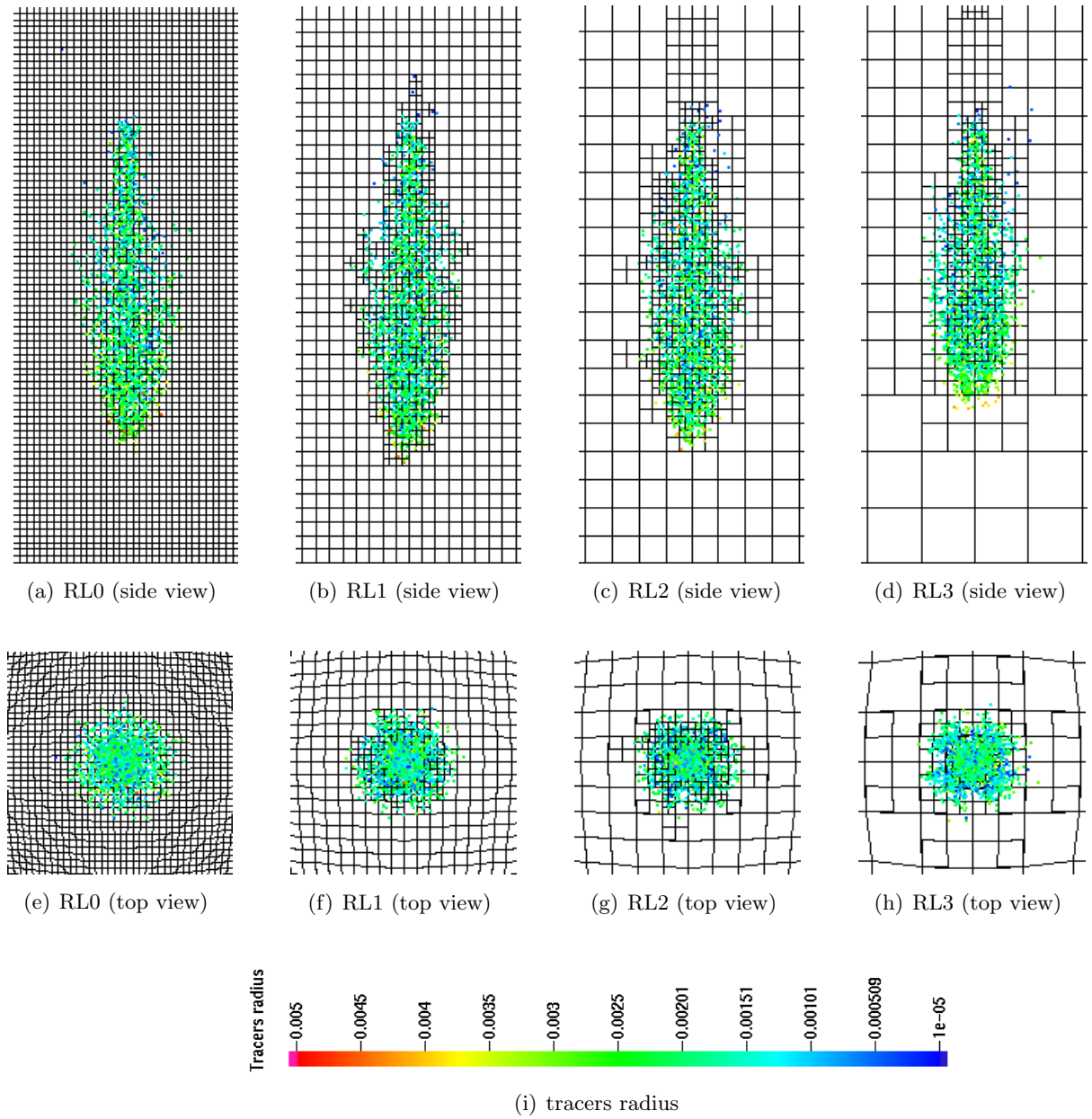

(a) RL0 (side view) (b) RL1 (side view) (c) RL2 (side view) (d) RL3 (side view)

(e) RL0 (top view) (f) RL1 (top view) (g) RL2 (top view) (h) RL3 (top view)

(i) tracers radius

Figure 5.65: Spray structure predicted using different meshes at 1.4 *ms* after start of injection for solid-cone spray (evaporation and collision model off)

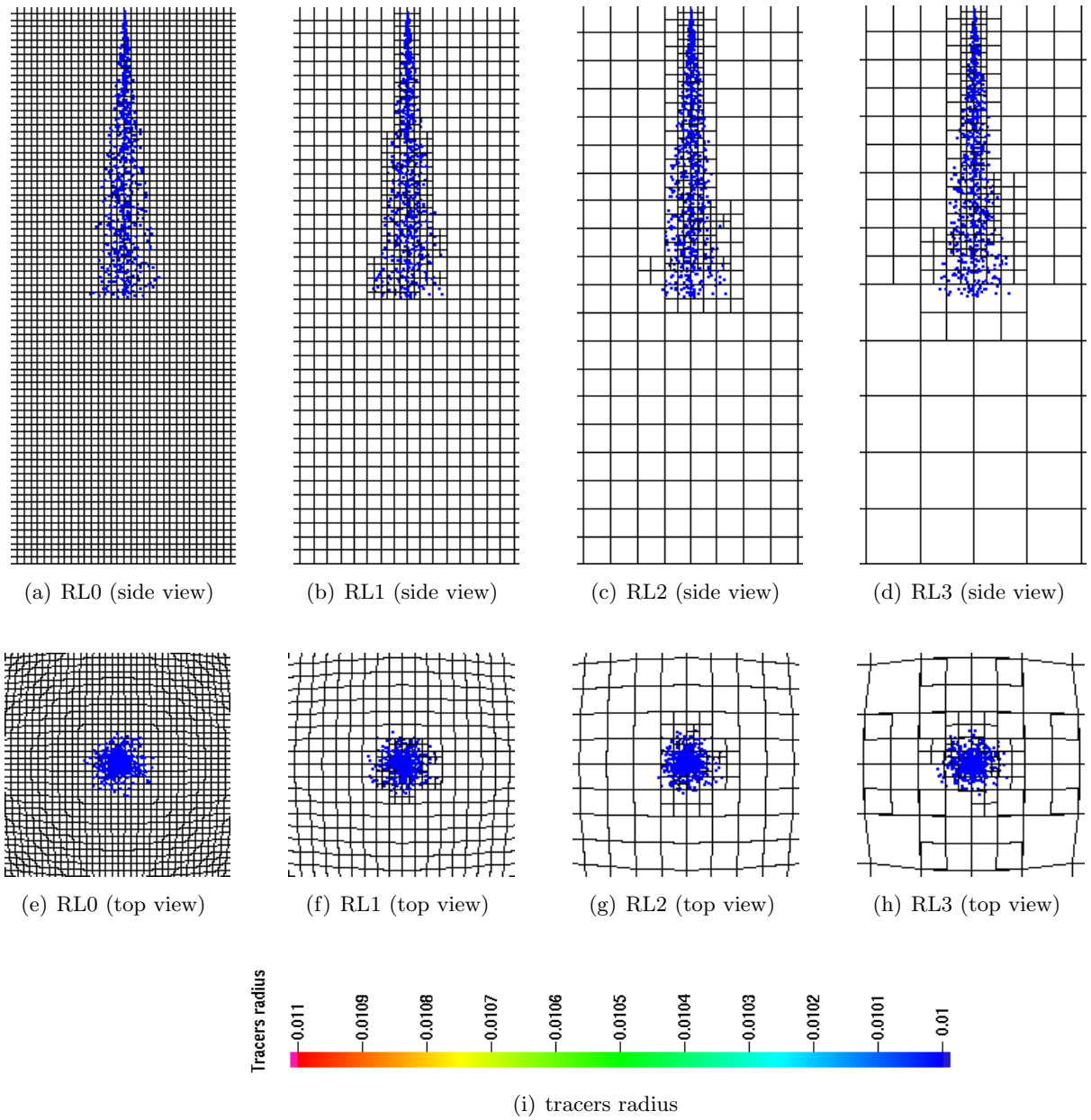

(a) RL0 (side view) (b) RL1 (side view) (c) RL2 (side view) (d) RL3 (side view)

(e) RL0 (top view) (f) RL1 (top view) (g) RL2 (top view) (h) RL3 (top view)

(i) tracers radius

Figure 5.66: Spray structure predicted using different meshes at 0.4 ms after start of injection for solid-cone spray (evaporation and collision and breakup model off)

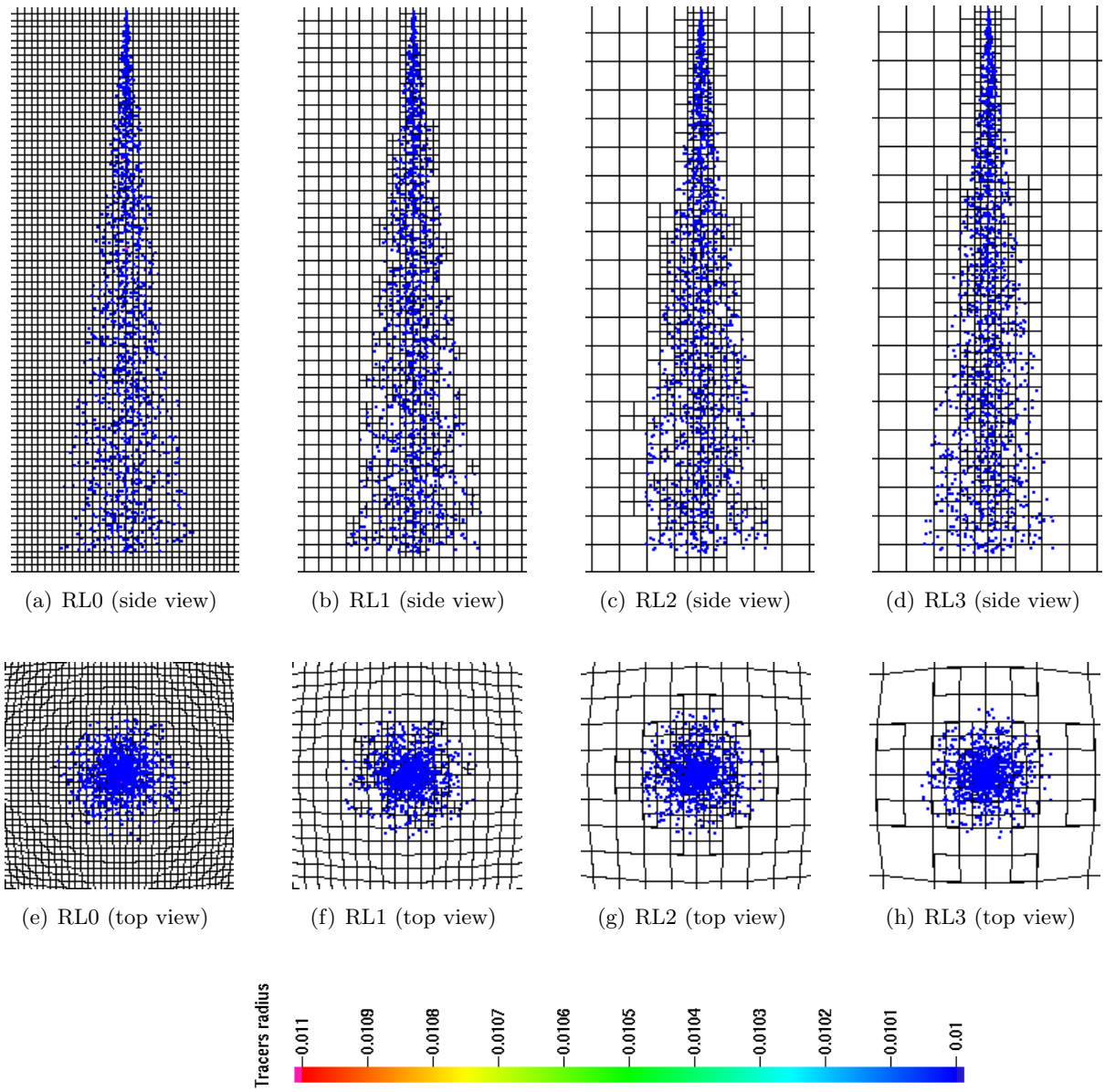

(a) RL0 (side view) (b) RL1 (side view) (c) RL2 (side view) (d) RL3 (side view)

(e) RL0 (top view) (f) RL1 (top view) (g) RL2 (top view) (h) RL3 (top view)

(i) tracers radius

Figure 5.67: Spray structure predited using different meshes at 0.8 *ms* after start of injection for solid-cone spray (evaporation and collision and breakup model off)

5.4.2.2 Spray Tip Penetration and SMD

The predicted spray tip penetrations are shown in Figures 5.68 to 5.70 for all cases. For Case 1 and Case 2, the liquid spray penetrations predicted on the fine mesh and AMR meshes agree well for one-level and two-level adaptations. The spray tip penetration predicted on three-level adaptive mesh shows a nearly constant discrepancy against the fine mesh shortly after the fuel injection. The liquid spray penetrations predicted on the fine mesh and coarse mesh using AMR agree well with each other for Case 3.

Figures 5.71 to 5.73 give the global SMD for all cases. Figure 5.71 shows the SMD revolution from start of fuel injection to 2.0 ms after start of fuel injection. Results are very similar to those in Figure 5.33. It shows good agreement between different mesh after 0.5 ms after fuel injection. The SMD became bigger than that in Figure 5.33 because the evaporation was not accounted for.

When all the spray sub-models are turned off, the liquid drops only have momentum exchange with gas. Their radii are constant for all cases as shown in Figure 5.73.

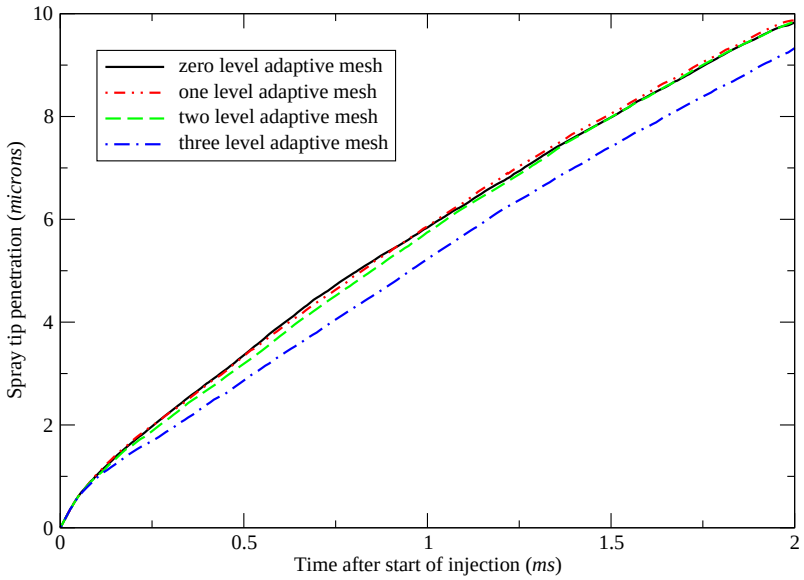

Figure 5.68: Spray tip penetrations predicted using different mesh for solid-cone spray with colide and breakup models

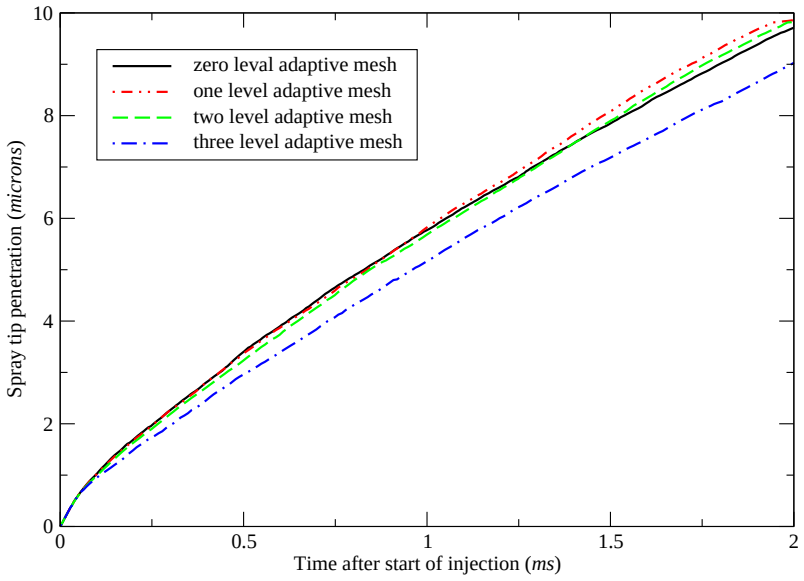

Figure 5.69: Spray tip penetrations predicted using different mesh for solid-cone spray with breakup models

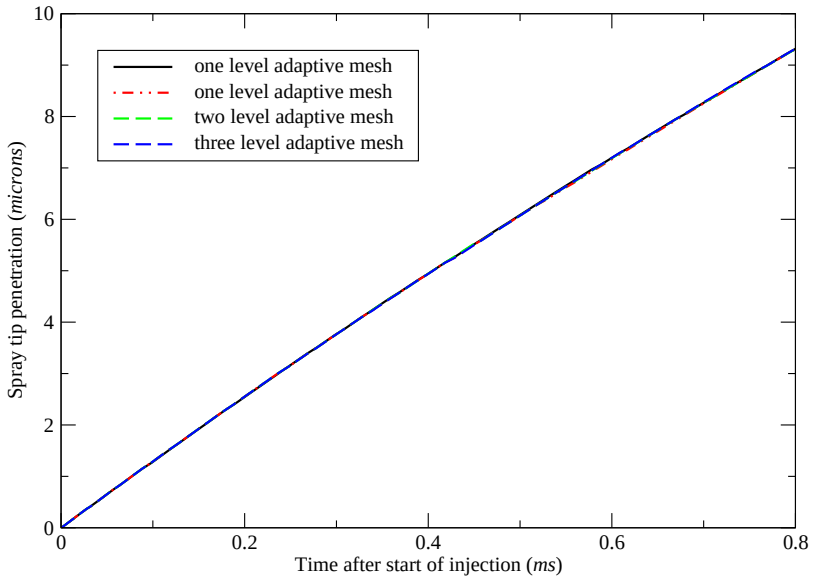

Figure 5.70: Spray tip penetrations predicted using different mesh for solid-cone spray without spray models

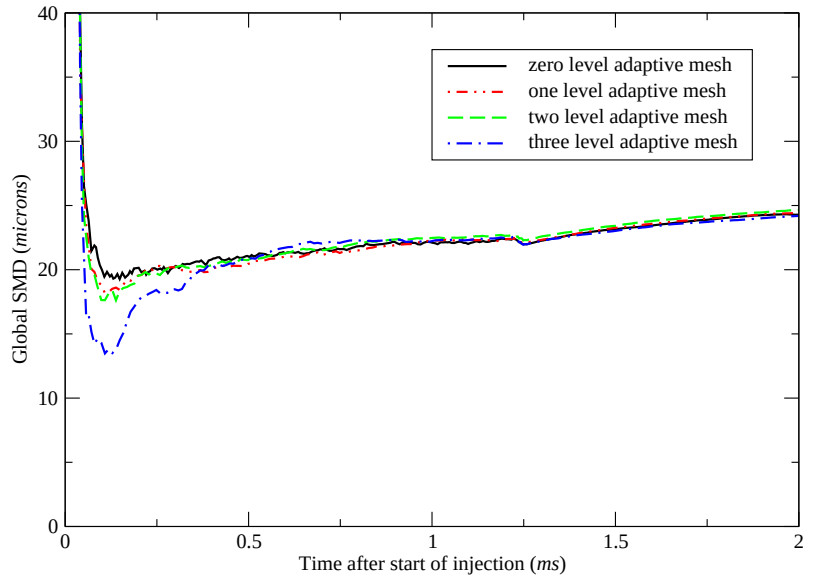

Figure 5.71: Global SMD predicted using different mesh for solid-cone spray with collide and breakup models

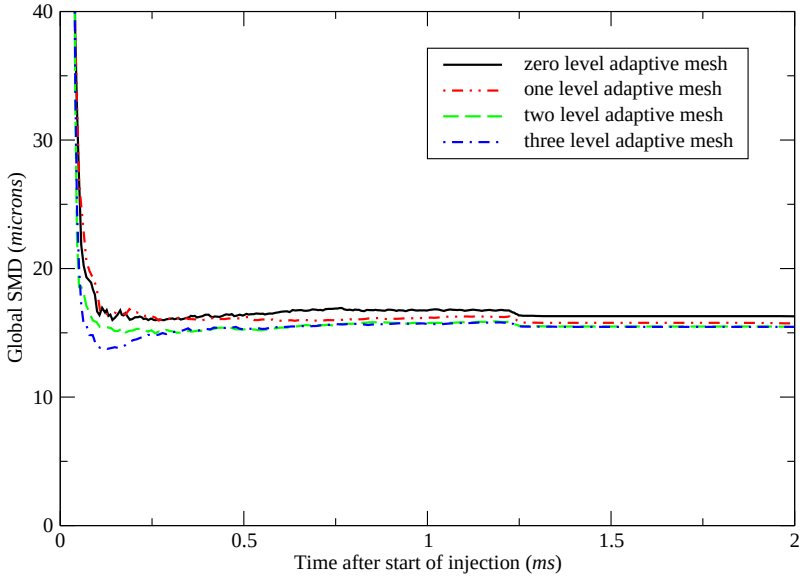

Figure 5.72: Global SMD predicted using different mesh for solid-cone spray with breakup models

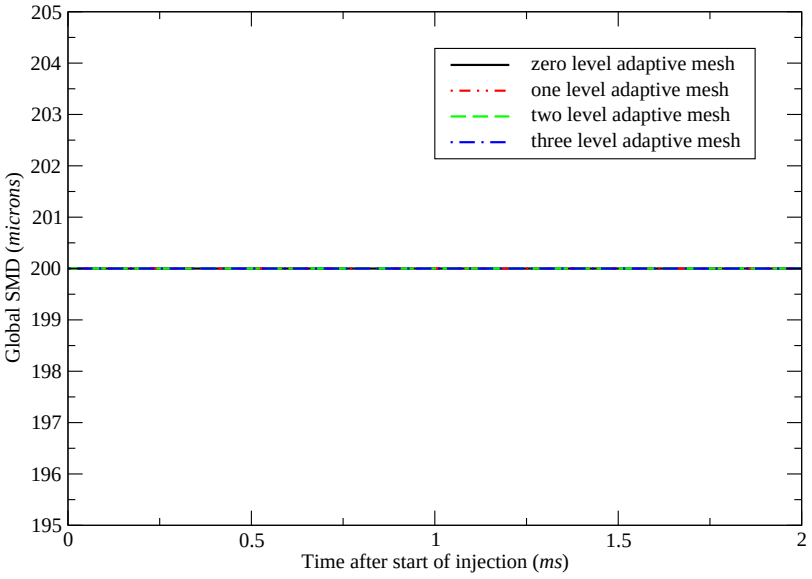

Figure 5.73: Global SMD predicted using different mesh for solid-cone spray without spray models

5.5 Refinement Criteria Study

The error indicator may have a major impact on the solution using mesh adaptation. Typically, the error indicator is not a true estimate of the error in the solution, rather, it is an indicator of high gradients in the flow-field that are assumed to be regions of high error. In most mesh adaptation techniques, the question of where to modify the grid resolution or the solution accuracy is addressed through the concept of error equidistribution. The principle of error equidistribution is strictly applied to the methods by r-refinement and the global remeshing techniques to redistribute grid points in the field optimally. The magnitude of the computed errors directly determines the grid spacing parameters in these method. In the methods based on h-refinement, however, error estimation practically serves a means to locate the grid elements experiencing large computational errors. The role of error estimation for h-refinement reduces to indication of computational errors induced by the dominant flow features. Many feature indicators in use are based on some physical flow quantities such as density, pressure, entropy, etc.

5.5.1 Error Indicator of Spray Characteristics

In the above results, the total mass of liquid droplets and fuel vapor has been used as a refinement criterion. The success of the refinement based on spray characteristics has been demonstrated in engine simulations. Here, further study of the refinement criterion will include the characteristics of dominant flow-field. In other words, the flow gradient will be part of the error estimators.

5.5.2 Error Indicator of Flow Field

The gradient indicator of the flow-filed was based on the work by Warren et al. (1991); Kallinderis et al. (1992); Cockburn et al. (1996). The undivided differences in the velocity magnitude is used as the criterion. The error indicator is equal to the difference in the velocity

across each cell multiplied by a length scale. It is defined as,

$$E = (\frac{L}{L_r})^{1/r}|\Delta q| \tag{5.3}$$

where L is a characteristic length for each cell, L_r is a reference length, and Δq is the difference in the velocity across the cell. The presence of the length scale in Eq.(5.3) means that the error indicator is reduced every time the cell is refined. The refinement criterion is weighted with a local cell size, so that as cells get refined to smaller and smaller size, they are weighted less and less.

In addition to parameter selection, a choice must be made of threshold levels for the detection parameters. A threshold value for the detection parameter Ψ is employed that is set by using the mean and standard deviation of the distribution of each parameter.

$$\Psi_{thre,refine} = \Psi_{mean} + \alpha\Psi_{std} \tag{5.4}$$

$$\Psi_{thre,coarsen} = \Psi_{mean} - \alpha\Psi_{std} \tag{5.5}$$

In the above equations, Ψ_{mean} and Ψ_{std} are the mean and standard deviation values of the detection parameter Ψ. If the detection parameter is above the threshold $\Psi_{thre,refine}$, the cell is flagged for refinement. Similarly, if the detection parameter is lower than the $\Psi_{thre,coarsen}$, then the cell is flagged for deletion. Here, α is a weighting factor that is empirically chosen.

5.5.3 Error Indicators Combining Spray and Flow Field Features

The combination of error estimators of spray and flow is studied in this part. Two parameters, which represent the characteristics of flow field, were chosen to serve as error indicators. They are turbulent kinetic energy and velocity magnitude. These error estimators were used associated with the spray indicator based on the total mass of liquid and fuel vapor which was used in early simulation. The computational mesh and simulation condition are already described in Section 5.2.1.

5.5.3.1 Fuel Vapor and Temperature

First, the mass fraction and temperature contours are compared. Figures 5.74 and 5.75 shows the mass fraction contours at 0.8 ms and 1.4 ms after start of fuel injection, respectively. In the figures, "fine mesh" represents the solution predicted on the fine mesh without mesh refinement. "liquid+vapor" represents the solution predicted on one-level adaptive mesh with the total mass of liquid drops and fuel vapor as the refinement criterion. "liquid+vapor & tke" represents the solution predicted on one-level adaptive mesh with the combination of total mass of liquid drops and fuel vapor and gradient of turbulent kinetic energy as the refinement criterion. "liquid+vapor & vel" represents the solution predicted on one-level adaptive mesh with the combination of total mass of liquid drops and fuel vapor and gradient of velocity magnitude as the refinement criterion. The improvement can be judged by the changes in contour color and shape when the combined refinement criteria were used. The temperature contours are plotted in Figures 5.76 and 5.77. The change of contour color and shape is also observed.

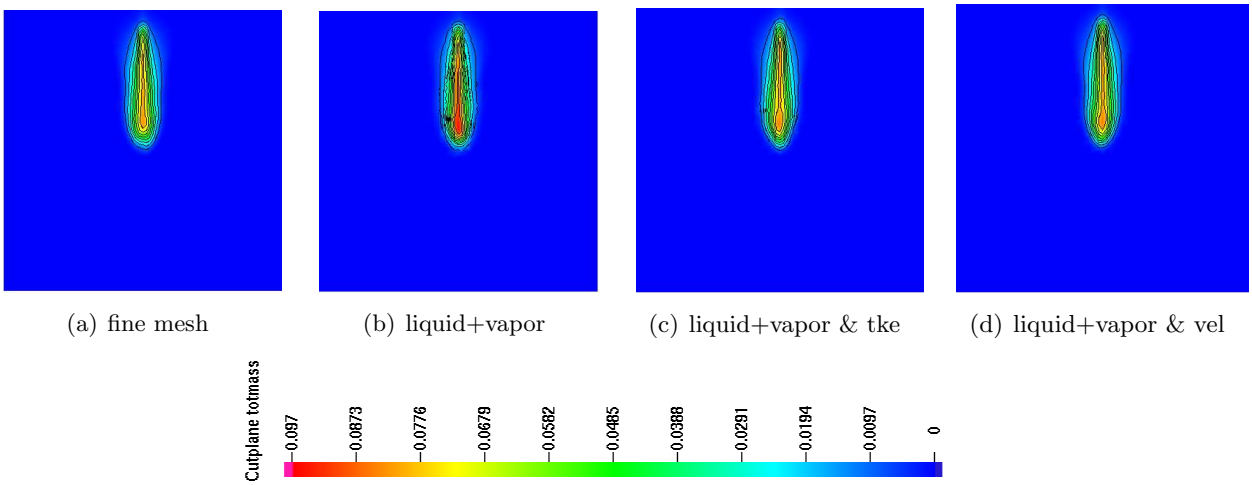

(a) fine mesh (b) liquid+vapor (c) liquid+vapor & tke (d) liquid+vapor & vel

(e) mass fraction

Figure 5.74: Comparison of fuel vapor distributions predicted using different refinement levels on one-level adaptive mesh with that predicted on fine mesh at 0.8 ms after start of fuel injection for solid-cone spray

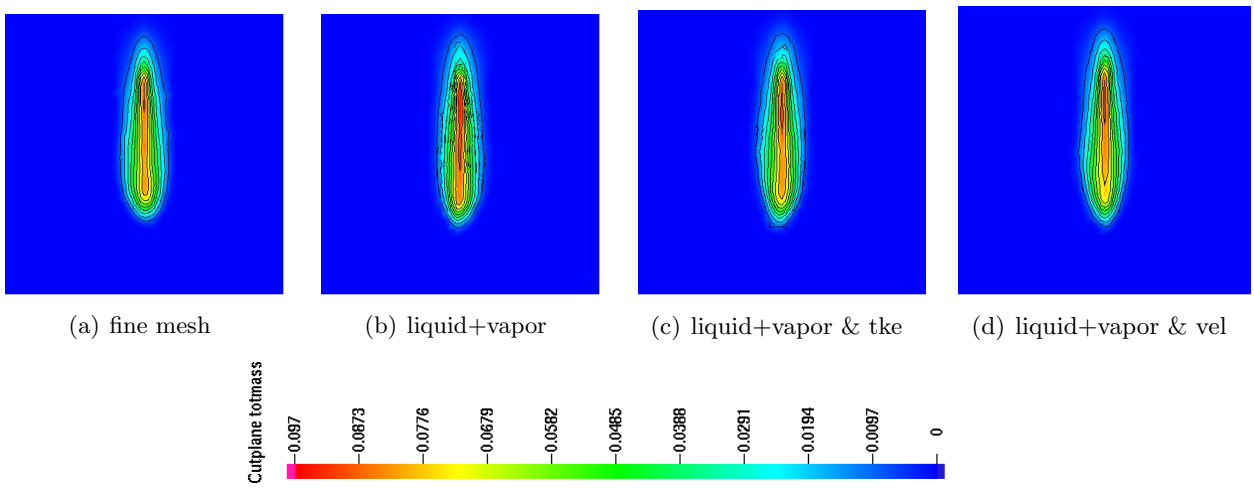

(a) fine mesh (b) liquid+vapor (c) liquid+vapor & tke (d) liquid+vapor & vel

(e) mass fraction

Figure 5.75: Comparison of fuel vapor distributions predicted using different refinement criteria on one-level adaptive mesh with that predicted on fine mesh at 1.4 ms after start of fuel injection for solid-cone spray

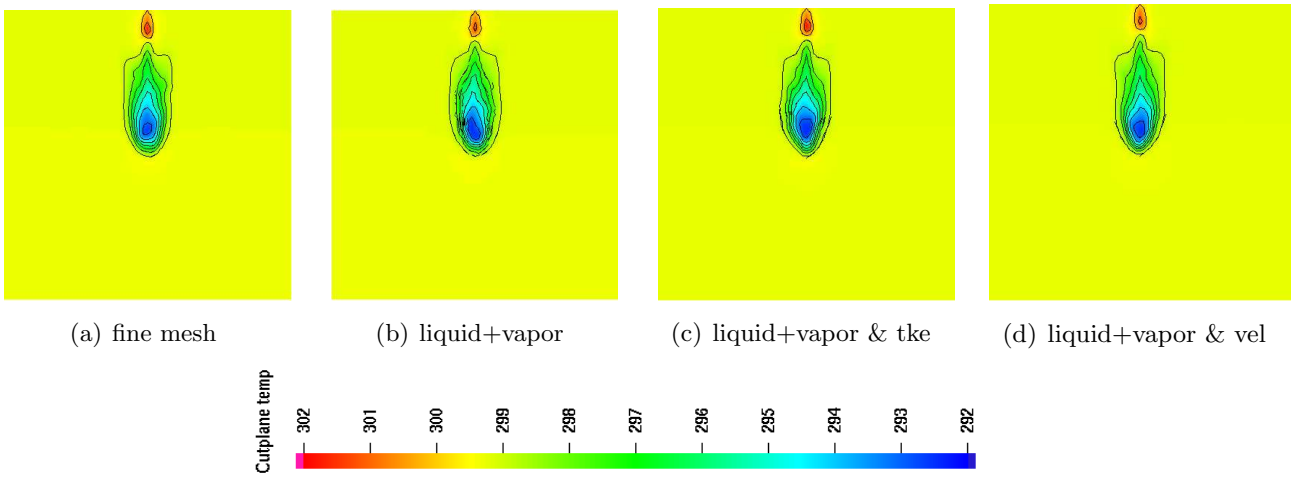

(a) fine mesh (b) liquid+vapor (c) liquid+vapor & tke (d) liquid+vapor & vel

(e) temperature (K)

Figure 5.76: Comparison of temperature distributions predicted using different refinement criteria on one-level adaptive mesh with that predicted on fine mesh at 0.8 ms after start of fuel injection for solid-cone spray

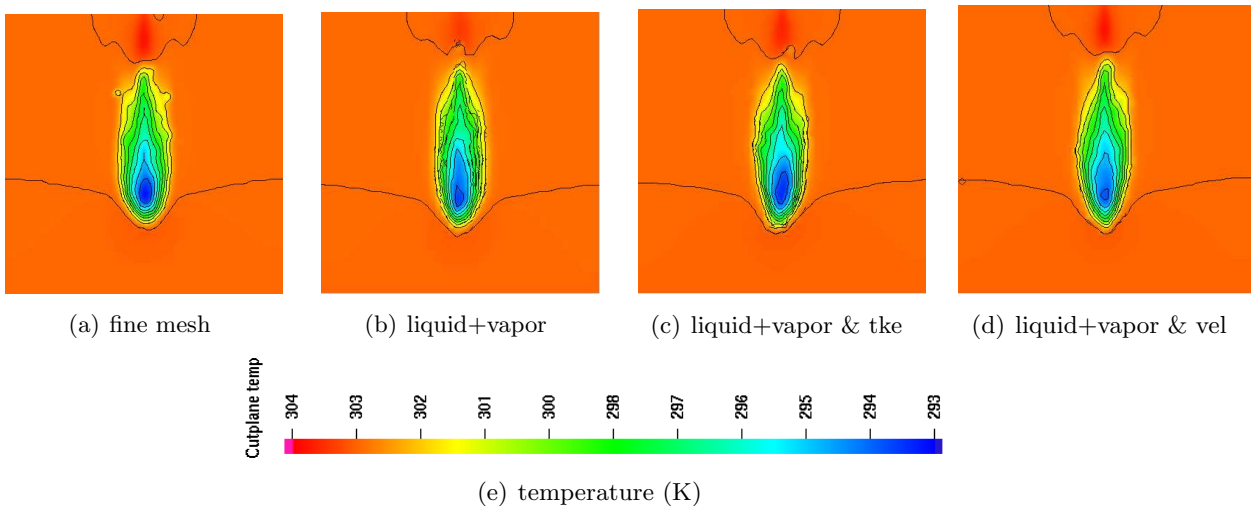

(a) fine mesh (b) liquid+vapor (c) liquid+vapor & tke (d) liquid+vapor & vel

(e) temperature (K)

Figure 5.77: Comparison of temperature distributions predicted using different refinement criteria on one-level adaptive mesh with that predicted on fine mesh at 1.4 ms after start of fuel injection for solid-cone spray

The quantitative comparisons are performed for mass fraction and temperature. The values of mass fraction and temperature at the center of the chamber in the axial direction are plot in Figures 5.78, 5.79, 5.80, and 5.81 at 0.8 ms and 1.4 ms after start of fuel injection. The results show the improvement when the error indicator of flow is accounted with the one of spray. Particularly for the mass fraction, the value is over-predicted with only spray indicator. However, the values predicted by a combined indicators agree well with that using the fine mesh (Figures 5.78 and 5.79). For temperature, a slight improvement is achieved. It seems the combination of the gradient of turbulent kinetic energy and spray results in better performance. Overall, the refinement criteria accounting for both spray and flow can achieve the same level accuracy as the fine mesh.

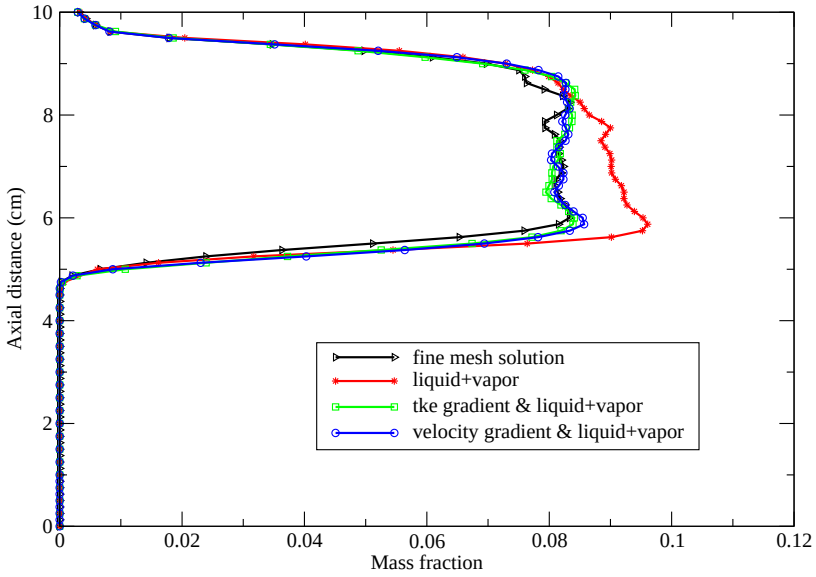

Figure 5.78: Comparison of axial mass fraction distributions predicted on one-level adaptive mesh by using different refinement criteria with that on fine mesh at 0.8 ms after start of injection for solid-cone spray

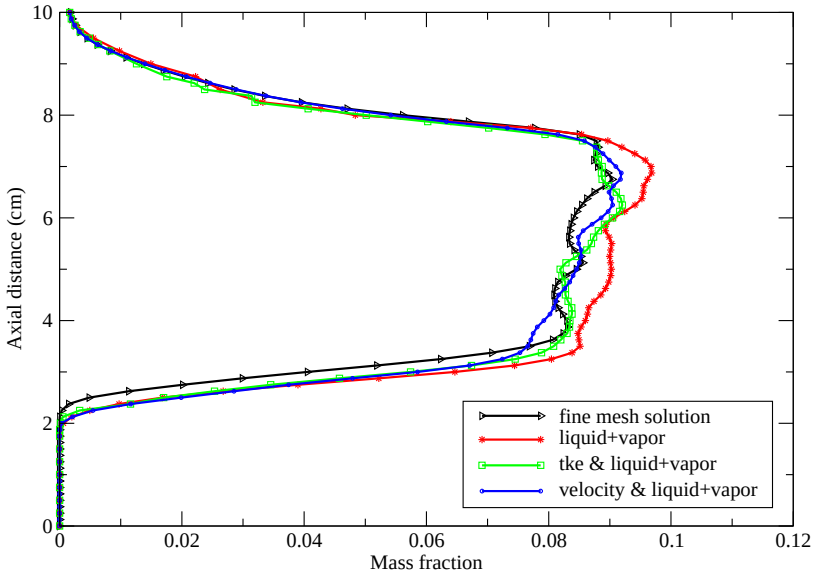

Figure 5.79: Comparison of axial mass fraction distributions predicted on one-level adaptive mesh by using different refinement criteria with that on fine mesh at 1.4 ms after start of injection for solid-cone spray

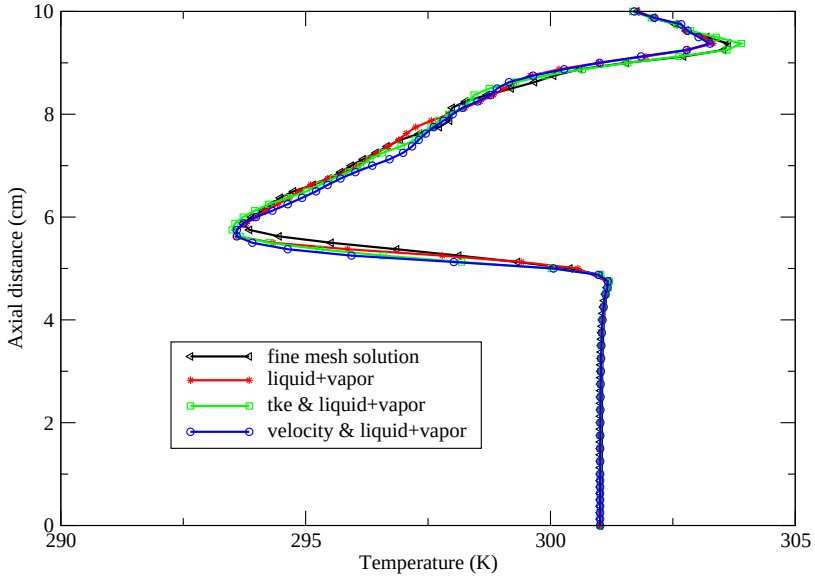

Figure 5.80: Comparison of axial temperature distributions predicted on one-level adaptive mesh by using different refinement criteria with that on fine mesh at 0.8 ms after start of injection for solid-cone spray

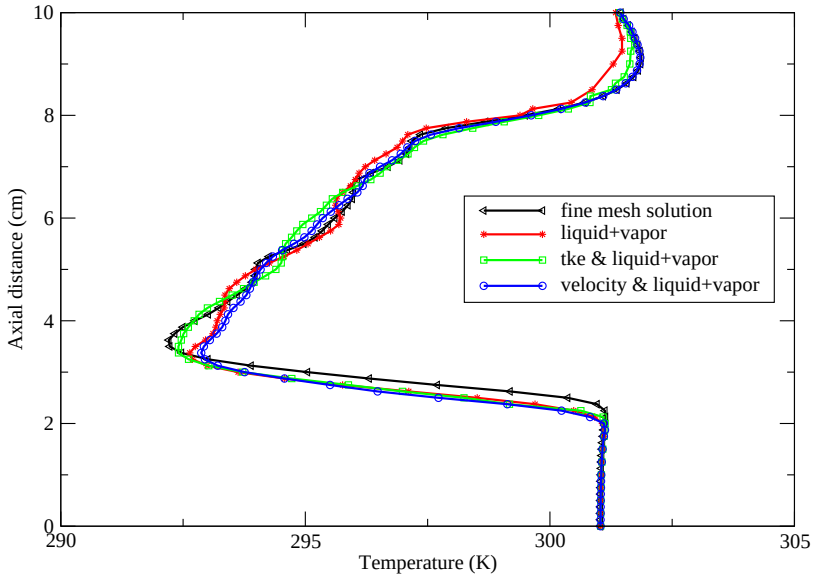

Figure 5.81: Comparison of axial temperature distributions predicted on one-level adaptive mesh by using different refinement criteria with that on fine mesh at 1.4 ms after start of injection for solid-cone spray

5.5.3.2 Spray Structures, Spray Tip penetration and SMD

Spray structures predicted by one-level adaptive mesh using different refinement criteria are compared with that predicted by the fine mesh in Figure 5.82 and 5.83 for 0.8 ms and 1.4 ms. It can be seen that all the spray structure are very similar from topview and sideview at different times. On can also find that more grid are refined near spray for the combined criteria simulation, which provide a smoother region across the fine grid to coarse grid. These contribute to the better resolution of the spray and flow around the spray, which is shown in the improvement of the mass fraction and temperature contours presented above.

The predicted spray tip penetrations by different refinement criteria on one-level adaptive mesh agree well with that predicted on fine mesh as shown in Figure 5.84. Different refinement criteria predicted similar SMD as the fine mesh, which can be seen in Figure 5.85.

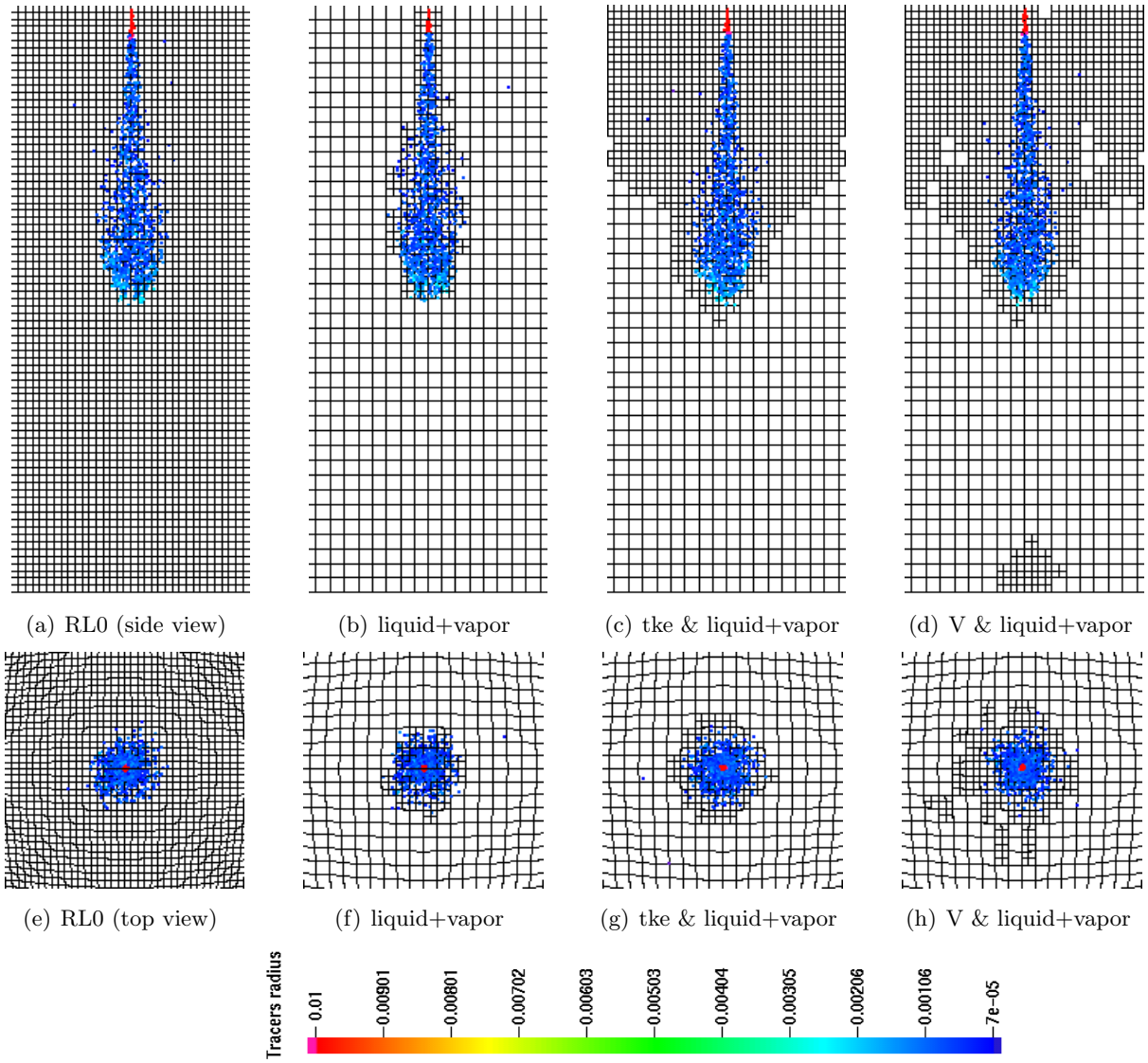

(a) RL0 (side view) (b) liquid+vapor (c) tke & liquid+vapor (d) V & liquid+vapor

(e) RL0 (top view) (f) liquid+vapor (g) tke & liquid+vapor (h) V & liquid+vapor

(i) tracers radius

Figure 5.82: Comparison of spray structures predicted using different refinement criteria on one-level adaptive mesh with that predicted on the fine mesh at 0.8 *ms* after start of injection for solid-cone spray

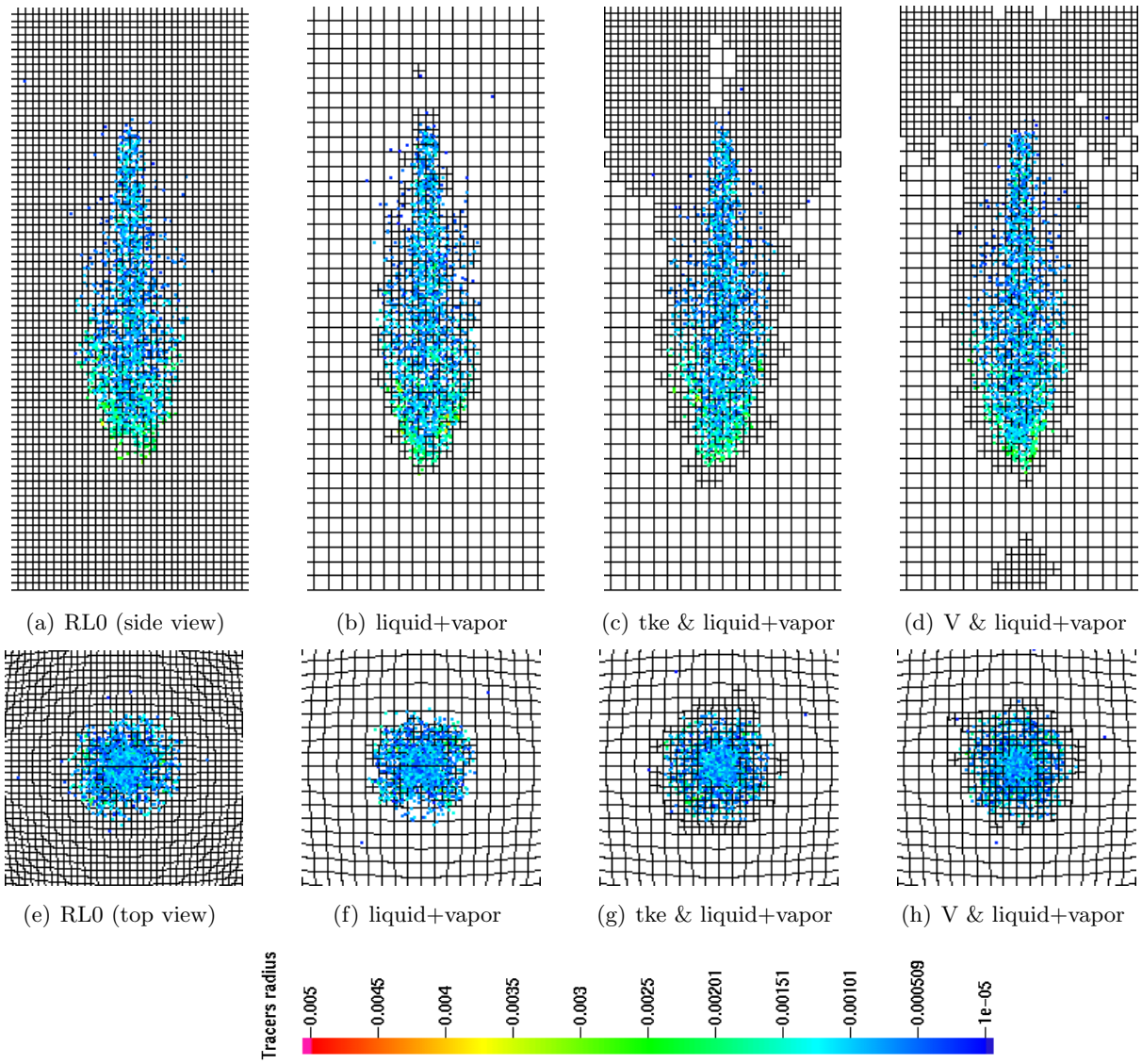

(a) RL0 (side view) (b) liquid+vapor (c) tke & liquid+vapor (d) V & liquid+vapor

(e) RL0 (top view) (f) liquid+vapor (g) tke & liquid+vapor (h) V & liquid+vapor

(i) tracers radius

Figure 5.83: Comparison of spray structures predicted using different refinement criteria on one-level adaptive mesh with that predicted on the fine mesh at 1.4 ms after start of injection for solid-cone spray

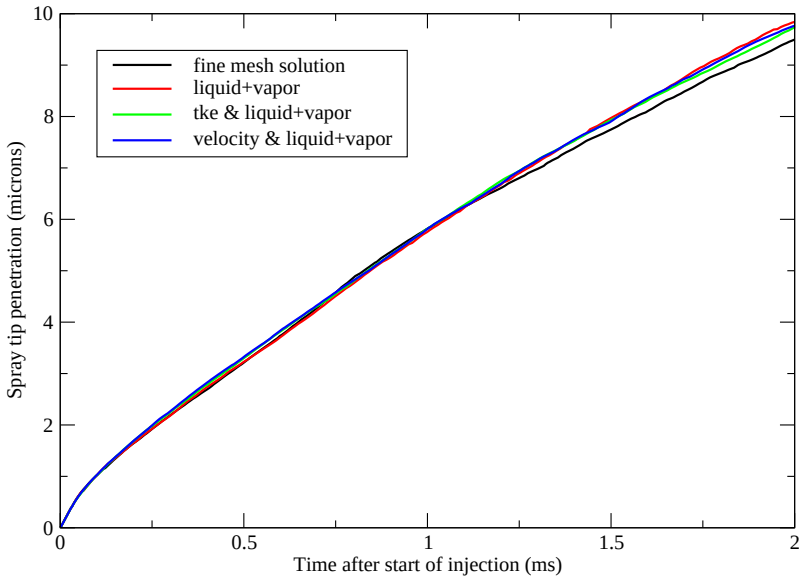

Figure 5.84: Comparison of spray tip penetrations predicted using different refinement criteria on one-level adaptive mesh with that predicted on the fine mesh for solid-cone spray

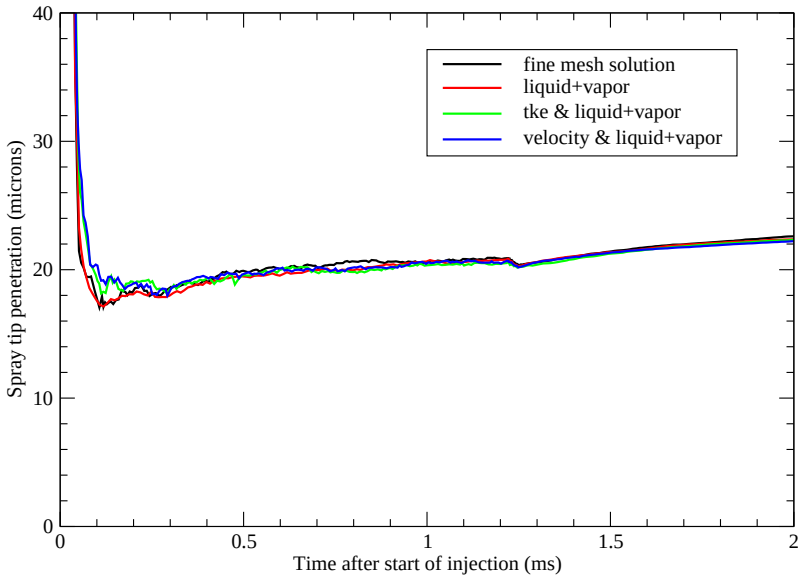

Figure 5.85: Comparison of global SMD predicted using different refinement criteria on one-level adaptive mesh with that predicted on the fine mesh for solid-cone spray

5.6 Summary

This study developed an adaptive mesh refinement scheme using the h-refinement method for the hexahedral meshes to improve the accuracy of spray simulations. The scheme was successfully implemented into an engine simulation code using unstructured mesh. It was demonstrated that the present methodology can achieve accurate numerical results by performing rigorous local mesh adaptation without the need of using a globally fine mesh. The tree-based data storage structure was developed to provide efficient storage. The treatment of the hanging nodes provides flexible and efficient data management for successive refinements. The present refinement/coarsening procedure is an automatic process controlled by the refinement criteria. This method can enhance engineering design and optimization of spray combustion systems. It can be used to study specific local phenomena (such as spray) with a high accuracy, and can also be used to perform extensive parametric studies efficiently. The presented sample results have clearly shown that accurate solutions can be generated automatically with substantially less computational time and cost.

The adaptive algorithm was tested for both solid-cone and hollow-cone spray simulations in a constant-volume chamber. The liquid spray structure, tip penetration, and global SMD were compared. The present refinement scheme can provide good levels of accuracy while significantly reducing the computer time. The solid-cone spray case can reach a speed-up of 92, and the hollow-cone spray case can reach a speed-up of 46 under the present conditions. The present methodology was also applied to simulate the air-fuel mixing in a direct-injection spark-ignition engine. Solution accuracy was improved by the adaptation of the mesh. It is demonstrated that the present scheme can be successfully used in simulating the mixture formation process in transient engine conditions.

Varying the total number of injected parcels (***tnparc***) was also studied. The results showed that AMR can produce the same level of accuracy as the fine mesh. In the meantime, AMR is not sensitive to the specific number of injected parcels. The influence of spray sub-models on AMR was also investigated. AMR achieved the same level of accuracy as the fine mesh with different sub-models. On the other hand, It was shown that collision and breakup models are

dependent on mesh resolution and orientation. When the refinement criterion accounts for the dominant flow features as well as spray characteristics, the solution accuracy was improved for both spray and flows.

CHAPTER 6. DIESEL ENGINE SPRAY COMBUSTION MODELING

This chapter presents results of diesel engine modeling. Various diesel spray atomization, autoignition, combustion, and soot and NOx emissions models were implemented into the staggered version of KIVA-4 (Kong et al., 1995; Patterson et al., 1998; Kong et al., 1999). The resulting KIVA-4 code was validated using experimental data obtained from a heavy-duty diesel engine. Note that this KIVA-4 code will be used as the platform for the further implementation of the conjugate heat transfer model to predict the temperature of the combustion chamber wall. To implement the conjugate heat transfer into code, first, modification was made to account for a non-uniform temperature distribution and run it with the uniform temperature profile specified in the input file.

6.1 Model Formulation

6.1.1 Kelvin-Helmholtz Spray Breakup Model

This so-called "wave" breakup model (also referred to as Kelvin-Helmholtz breakup model) is widely applied in modeling primary as well as secondary breakup of liquid drops. The wave model (Reitz, 1987) assumes that aerodynamic forces at a liquid-gas interface and the resulting surface waves are responsible for liquid atomization. Nozzle cavitation and flow turbulence effects are introduced through an initial disturbance level that is accounted for in model constants. The wave breakup model considers that the breakup of the injected liquid is due to the relative velocity between the gas and liquid phases. The instability induces the shearing-off of droplets from the liquid surface. A dispersion relation is fitted to obtain the wavelength and the frequency for the fastest growing wave on the surface. The expressions for the growth rate

Ω and wave length Λ are:

$$\frac{\Lambda}{a} = 9.02\frac{(1+0.45Z^{0.5})(1+0.4T^{0.7})}{(1+0.87We_g^{1.67})^0.6} \tag{6.1}$$

$$\Omega(\frac{\rho_l a^3}{\sigma})^{0.5} = \frac{0.34+0.38We_g^{1.5}}{(1+Z)(1+1.4T^{0.6})} \tag{6.2}$$

where We is the Weber number for the gas and defined as $We_g = \frac{\rho_g u_r^2 a}{\sigma}$ with u_r as the relative velocity between the liquid and the gas, and σ is the surface tension of the liquid. Z is the Ohnesorge number and defined as $Z = \frac{We_l^{0.5}}{Re_l}$ with the liquid Weber number $We_l = \frac{\rho_l u_r^2 a}{\sigma}$ and liquid Reynold number $Re_l = \frac{u_r a}{\nu_l}$. The Taylor number T is defined as $T = ZWe_g^{0.5}$.

The breakup time is expressed as

$$\tau = \frac{3.788 B_1 a}{\Omega\Lambda} \tag{6.3}$$

B_1 is a model constant that accounts for the difference in the drop breakup time due to unknown initial conditions for the drop. The recommended value for B_1 is 10 for diesel spray.

The drop size of the newly formed droplet, r, is assumed to be proportional to the wave length, unless the wavelength is large compared to the drop circumference. In the case of large wavelength, the droplet is assumed to forming from the liquid column near the nozzle and is allowed to have a radius larger than the nozzle for the initial breakaway from the liquid core of the spray. The resulting radius of the newly formed droplet is estimated by

$$r = \begin{cases} B_0\Lambda & (B_0\Lambda \le a) \\ min\begin{cases} (3\pi a^2 u_r/2\Omega) \\ (3a^2\Lambda/4)^{0.33} \end{cases} & (B_0\Lambda > a, once) \end{cases} \tag{6.4}$$

where B_0 is taken as 0.61.

The high injection pressure in diesel engines produces a very high drop velocity with respect to the surrounding gas. The high relative velocity results in large inertial forces acting on the drop which distort the drop into a disk shape. Further modifications to the wave breakup model were made by considering the effects of the distortion of a drop on its drag coefficient (Liu et al., 1993; Patterson et al., 1994; Kong et al., 1995). The drop drag coefficients is calculated by the

correlations:

$$\begin{cases} \frac{24}{Re_l}(1+\frac{1}{6}Re_l^{2/3}) & Re_l \leq 1000 \\ 0.424 & Re_l > 1000 \end{cases} \tag{6.5}$$

where $Re_l = \frac{2r_l\rho_l \cdot |\vec{u}_g - \vec{v}_l|}{\mu_l}$ is the Reynold number of the liquid drop. The above equations for the drag coefficients are valid for spherical particles. However, in engine spray the liquid droplets are typically distorted from their spherical shape due to the high injection velocity and this obviously has an effect on the drag coefficients. In fact, a distorted drop has a higher drag coefficient than a spherical drop. Liu et al. (1993) has consider the effect and applied the TAB model (O'Rourke et al., 1987) to determine the drop distortion parameter y.

$$\ddot{y} = \frac{2}{3}\frac{\rho_g}{\rho l}\frac{|\vec{u}-\vec{v}|^2}{r_l^2} - \frac{8\sigma}{\rho_l r_l^3}y - \frac{5\mu}{\rho_l r_l^2}\dot{y} \tag{6.6}$$

where ρ_l, σ, r_l, and μ are the droplet density, surface tension, radius, and viscosity, respectively. The distortion parameter y lies between the limits of a sphere ($y = 0$) and a disk ($y = 1$) which has a drag coefficient $C_D = 1.52$. Therefor, a simple expression for the drag coefficient that accounts for the effect of drop distortion is formulated as

$$C_D = C_{D,sphere}(1 + 2.632y). \tag{6.7}$$

6.1.2 Rayleigh-Taylor Breakup Model

The secondary breakup of liquid drops into even smaller droplets is primarily driven by aerodynamic forces on the frontal surface of the drops by the surrounding gas. The forces cause a distortion of the initially spherical droplet, which will eventually results in drop breakup when the surface tension is overcame by the deformation. In this study, the Kelvin-Helmholtz (KH) wave breakup model is combined with the Rayleigh-Taylor (RT) breakup model for secondary breakup (Patterson et al., 1998).

The theory of the RT model is based on the idea that the acceleration normal to the interface between two fluids of different densities can cause instabilities. For a liquid droplet decelerated by the drag force in a gas phase, the instabilities may be unstable at the trailing edge of the

droplet and thus can lead to breakup of drops into smaller droplets. The acceleration of a droplet is due to the drag force,

$$|\vec{a}| = \frac{3}{8} C_D \frac{\rho_g u_r^2}{\rho_l r} \tag{6.8}$$

where $\vec{a}$ is the droplet acceleration, u_r is the relative velocity between the droplet and the gas, and the r is the radius of the droplet. The frequency and wavelength of the fastest growing waves are,

$$\Omega = \sqrt{\frac{2|\vec{a}|}{3}} [\frac{|\vec{a}|(\rho_l - \rho_g)}{3\sigma}]^{1/4} \tag{6.9}$$

$$\lambda = 2\pi \sqrt{\frac{3\sigma}{|\vec{a}|(\rho_l - \rho_g)}} \tag{6.10}$$

The breakup time is found by taking the reciprocal of the frequency of the fastest growing wave. The droplet is only allowed to break up when the wavelength given by the above equation is smaller that the diameter of the parent drop. The size of the new child droplets is calculated in dependence of the RT-wavelength.

6.1.3 Shell Ignition Model

A widely used autoignition model in diesel engine simulation is the Shell model. It was originally developed by Halstead et al. (1977) in order to predict knock in spark-ignition engines, and it has been adjusted and applied to model diesel ignition (Kong et al., 1993, 1995). The Shell model uses a simplified reaction mechanism to simulate the autoignition process of hydrocarbon fuels. Eight generic reactions based on the degenerate branching characteristics

are formulated from five generic species. The eight reaction steps are specified as:

$$RH + O_2 \xrightarrow{k_q} 2R^* \tag{6.11a}$$

$$R^* \xrightarrow{k_p} R^* + P + Heat \tag{6.11b}$$

$$R^* \xrightarrow{f_1 k_p} R^* + B \tag{6.11c}$$

$$R^* \xrightarrow{f_4 k_p} R^* + Q \tag{6.11d}$$

$$R^* + Q \xrightarrow{f_2 k_p} R^* + B \tag{6.11e}$$

$$B \xrightarrow{k_b} 2R^* \tag{6.11f}$$

$$R^* \xrightarrow{f_3 k_p} termination \tag{6.11g}$$

$$2R^* \xrightarrow{k_t} termination \tag{6.11h}$$

where RH is indicates the hydrocarbon fuel, R^* is the radical formed from the fuel, B is the branching agent, Q is a labile intermediate species, and P denotes oxidized products such as CO, CO_2, and H_2O. The expressions for K_q, K_p, K_b, K_t, f_1, f_2, f_3, and f_4 are those given by Halstead et al. (1977). In addition, the local concentrations of O_2 and N_2 are needed to compute the reaction rates. The reaction (6.11b) represents the chain initiation, reactions (6.11c) to (6.11f) are chain propagation reactions, (6.11g) is the chain branching step, and (6.11h) and (6.11h) represent linear and quadratic terminations, respectively.

6.1.4 Combustion Model

The laminar-and-turbulent characteristic-time combustion model for spark-ignition engines (Abraham et al., 1977) was extended to model diesel combustion processes by Kong et al. (1995). The model was combined with the Shell ignition model to simulate the overall combustion process in a diesel engine. The criterion to combine the ignition and combustion model is to switch between the models at $1000K$. The ignition model was used whenever and wherever the temperature was lower than $1000K$ to simulate the low temperature chemistry. If the temperature is higher than $1000K$, the combustion model was activated for describing high temperature chemistry in diesel combustion.

With this model, the time rate of change of the partial density of species, due to conversion from one chemical species to another, is given by

$$\frac{dY_m}{dt} = -\frac{Y_m - Y_m^*}{\tau_c} \tag{6.12}$$

where Y_m is the mass fraction of species m, Y_m^* is the local and instantaneous thermodynamics equilibrium value of the mass fraction, and τ_c is the characteristic time for the achievement of such equilibrium. The characteristic time τ_c is assumed to be the same for seven species: fuel, O_2, N_2, CO_2, CO, H_2, and H_2O.

The characteristic time τ_c is the sum of a laminar timescale and a turbulent scale,

$$\tau_c = \tau_l + f\tau_t \tag{6.13}$$

The laminar timescale is derived from the correlated one-step reaction rate from a single droplet autoignition experiment (Bergeron et al., 1989),

$$Rate = A[C_{14}H_{30}]^{0.25}[O_2]^{1.5}exp(-E/RT) \tag{6.14}$$

where $A = 1.54\times10^{10}$ and $E = 77.3KJ/Mol$, considering that tetradecane is used. By equating this reaction rate to Eq.(6.1.4) and assuming an equilibrium state concentration of fuel equal to zero, the following laminar timescale is obtained,

$$\tau_l = A^{-1}[C_{14}H_{30}]^{0.75}[O_2]^{1.5}exp(-E/RT) \tag{6.15}$$

The turbulent timescale τ_t is proportional to the eddy turnover time

$$\tau_t = C_2k/\epsilon \tag{6.16}$$

The turbulent parameters, k and ϵ, are calculated from the $k-\epsilon$ models. The delay coefficient f was chosen to simulate the influence of turbulence on combustion after ignition has occurred and given by,

$$f = (1 - e^{-r})/0.632 \tag{6.17}$$

where r is the ration of the amount of products to that of total reactive species (except N_2):

$$r = \frac{Y_{CO_2} + Y_{H_2O} + Y_{CO} + Y_{H_2}}{1 - Y_{N_2}} \tag{6.18}$$

The parameter r indicates the completeness of the combustion in a specific region. Its value varies from 0 (no combustion yet) to 1 (complete consumption of fuel and oxygen). Accordingly, the delay coefficient f changes from 0 to 1 depending on the local conditions. In other words, the initiation of combustion relies on laminar chemistry; turbulence starts to have an influence only after combustion events have already been observed. Eventually, the combustion will be dominated by turbulent mixing effects in the regions of $\tau_l << \tau_t$. However, the laminar timescale is not negligible near the injector regions where the high injection velocity makes the turbulent timescale very small.

By using this combustion model, the chemical source term in the species continuity equation and the chemical heat release in the energy equation are computed.

6.1.5 Emission Model

The current modeling of nitric oxide production is described by the extended Zel'dovich mechanism (Patterson et al., 1994; Kong et al., 1995; Han et al., 1996). The extended Zel'dovich mechanism consists of the following equations (Bowman, 1975) as:

$$O + N_2 \longleftrightarrow NO + N \tag{6.19a}$$

$$N + O_2 \longleftrightarrow NO + O \tag{6.19b}$$

$$N + OH \longleftrightarrow NO + H \tag{6.19c}$$

The above equations are solved by assuming a steady state population of N and assuming the following reaction is in equilibrium

$$O + OH \longleftrightarrow O_2 + H \tag{6.20}$$

The extended Zel'dovich mechanism can be written as a single rate equation for NO as,

$$\frac{d}{dt}[NO] = 2k_{1f}[O][N_2]\{\frac{1 - [NO]^2/K_{12}[O_2][N_2]}{1 + k_{1b}[NO]/(k_{2f}[O_2] + k_{3f}[OH])}\} \tag{6.21}$$

where $K_{12} = (k_{11}/k_{1b})k_{2f}/k_{2b}$ and the subscripts 1, 2, and 3 refer to Eqns (6.19b), (6.19c), and (6.19c), respectively. N_2, O, O_2, and OH are assumed to in local thermodynamical equilibrium.

The rate constants are recommended by Bowman (1975) as:

$$k_{1f} = 7.6 \times 10^{13} exp[-38000/T] cm^3/(mol\ s) \tag{6.22a}$$

$$k_{1b} = 1.6 \times 10^{13} cm^3/(mol\ s)$$

$$k_{2f} = 6.4 \times 10^{9} exp[-3150/T] cm^3/(mol\ s) \tag{6.22b}$$

$$k_{2b} = 1.5 \times 10^{9} exp[-19500/T] cm^3/(mol\ s)$$

$$k_{3f} = 1.0 \times 10^{14} cm^3/(mol\ s) \tag{6.22c}$$

$$k_{3b} = 2.0 \times 10^{14} exp[-23650/T] cm^3/(mol\ s)$$

A two-step soot formation and oxidation model was used to predict soot emissions. The rate of change of soot mass is equal to the rate of formation less the rate of oxidation,

$$\frac{dM_{soot}}{dt} = \frac{dM_{formation}}{dt} - \frac{dM_{oxidation}}{dt} \tag{6.23}$$

The soot mass formation rate is given by (Hiroyasu et al., 1989)

$$\frac{dM_{formation}}{dt} = A_f M_{fv} P^{0.5} exp[-E_f/RT] \tag{6.24}$$

where M_{fv} is the fuel vapor mass, P is the pressure in bar, and $E_f = 125000(cal/mole)$ is the activation energy, and A_f is a model constant equal to 450. The Nagle and Strickland-Constable (Nagle et al., 1962) model is used for the soot oxidation rate

$$\frac{dM_{oxidation}}{dt} = \frac{MW_c}{\rho_s D_s} M_s R \tag{6.25}$$

where MW_c is the molecular weight of carbon (12 $g/mole$), ρ_s is the soot density (2 g/cm^3), and D_s is the soot diameter ($3 \times 10^{-6} cm$). The R term is the net reaction rate and is defined by

$$\frac{R}{12} = (\frac{k_A p_{O_2}}{1 + k_Z P_{O_2}})\chi + k_B p_{O_2}(1 - \chi) \tag{6.26}$$

where p_{O_2} is the partial pressure of oxygen in atm, and χ is the ratio of more reactive sites versus less reactive sites on the soot particle due to surface variation and it is given by

$$\chi = \frac{p_{O_2}}{p_{O_2} + (k_T/k_B)} \tag{6.27}$$

The rate constants used by the Nagle and Strickland-Constable in $(g - atm/sec - cm^2)$ are:

$$K_A = 20 \times exp(-30000/RT) \tag{6.28a}$$

$$K_B = 4.46 \times 10^3 \times exp(-15200/RT) \tag{6.28b}$$

$$K_T = 1.51 \times 10^5 \times exp(-97000/RT) \tag{6.28c}$$

$$K_Z = 21.3 \times exp(+4100/RT) \tag{6.28d}$$

6.2 Model Validations

Models are validated using experimental data from a Caterpillar diesel engine (3401 SCOTE). The specifications of this engine is listed in Table 6.1.

6.2.1 Simulation Conditions

The validation cases include different load conditions with different injection schemes, as listed in Table 6.2. The operating conditions include conventional diesel combustion (Choi et al., 1999) and PCCI-type (Premixed-Charge Compression Ignition) combustion with high exhaust gas recirculation (EGR) rates to produce a high amount of premixed burn (Klingbeil, 2002). When EGR is used, part of the exhaust gas is recirculated into the engine intake to displace part of the fresh air. Because CO_2 and H_2O in the exhaust have a higher specific heat (c_p) than O_2 and N_2, EGR can reduce combustion temperature and thus reduce NOx emissions. The EGR rate is defined as the ratio of CO_2 concentration in the engine intake to the CO_2 concentration in the exhaust. A total of 22 experimental cases were used for model validation. In the double injection conditions, 50% of the fuel was injected first, followed by 12 CAD dwell, then the rest of the fuel was injected. The computations used tetradecane ($C_{14}H_{30}$) as the diesel fuel surrogate due to their similar properties.

6.2.2 Cylinder Pressure and Heat Release Rate

A 60-*degree* sector mesh was used considering the symmetry of the six-hole injector. The computational grid is shown in Figure 6.1. The computed cylinder pressure history for all the

Table 6.1: Caterpillar engine specifications

Bore (mm)	137.6
Stroke (mm)	165.1
Connecting Rod Length (mm)	261.62
Displacement volume (L)	2.44
Compression ratio	15.1
Number of nozzle orificeXdiameter (mm)	6 X 0.259
Spray angle (from cylinder head) (degree)	27.5
Combustion chamber	Quiescent
Piston crown	Mexican hat
Inlet air pressure (kPa)	184
Inlet air temperature (K)	310
Intake valve closure (degree ATDC)	-147
Swirl ratio (nominal)	1.0

cases were compared with the measured data as shown in Figures 6.2 to 6.15.

The computed heat release rate data were also compared with experimental data as shown in Figures 6.16 to 6.25. Overall good levels of agreement are obtained and results indicated that the present diesel spray combustion models perform well in predicting diesel in-cylinder processes.

6.2.3 Engine Emission

The computed engine-out soot emission data with respect to the fuel injection timing are shown in Figures 6.26, 6.27, and 6.28. Measured emission data (Pierpont et al., 1995) are also given in the figures for comparison. It can be seen that the general trends of soot emissions with fuel injection timing are captured by the model.

6.3 Summary

The integrated models for diesel spray combustion have been validated under different engine loads and different injection timings in this study. For all the cases, the overall good levels of agreement are obtained between the prediction and measurement including engine

Table 6.2: Conditions of the validation cases for Caterpillar Engine

Engine load (%)	Injection pressure (MPa)	Engine speed (rpm)	SOI	EGR (%)
High load (75) Single injection	90	1600	-7 , -4, -1, +2, +5	0
High load (75) Double injection	90	1600	-7, -4, -1, +2, +5	0
Low load (25) Single injection	190	821	-10, -5, 0, +5	8
Low load (25) Single injection	190	821	-10, -5, 0, +5	27
Low load (25) Single injection	190	821	-10, -5, 0, +5	40

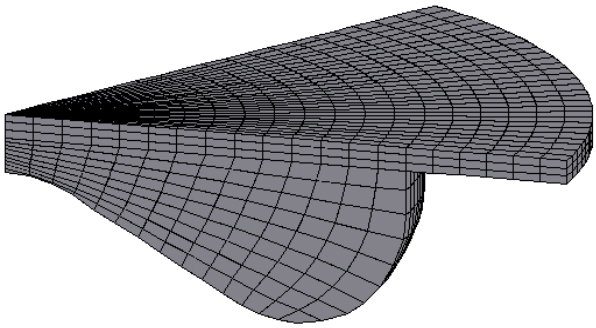

Figure 6.1: The computational sector mesh at TDC

in-cylinder pressure history, heat release rate, and soot emissions.

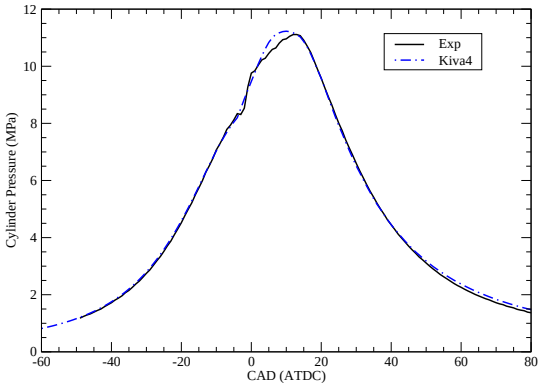

Figure 6.2: Comparison of cylinder pressure for high-load, single-injection cases for SOI = -7 ATDC

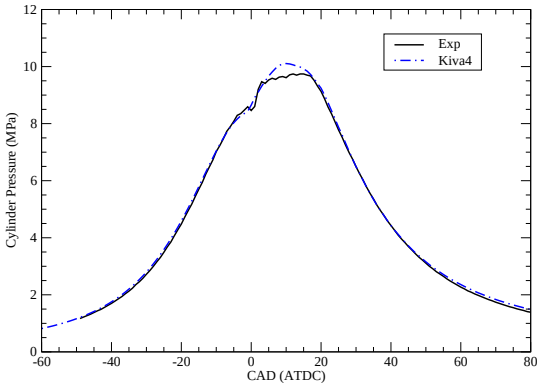

Figure 6.3: Comparison of cylinder pressure for high-load, single-injection cases for SOI = -4 ATDC

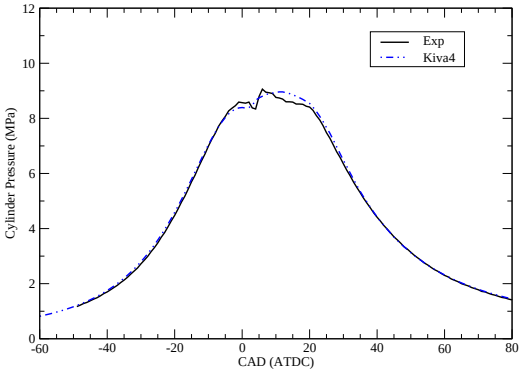

Figure 6.4: Comparison of cylinder pressure for high-load, single-injection cases for SOI = -1 ATDC

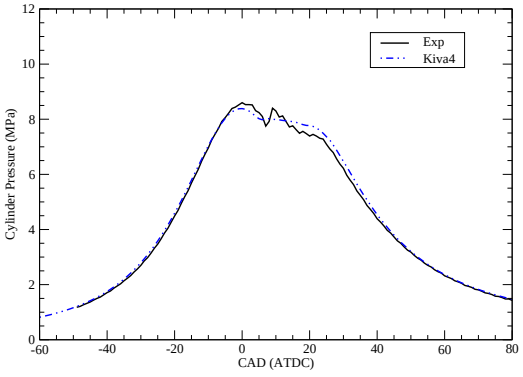

Figure 6.5: Comparison of cylinder pressure for high-load, single-injection cases for SOI = +2 ATDC

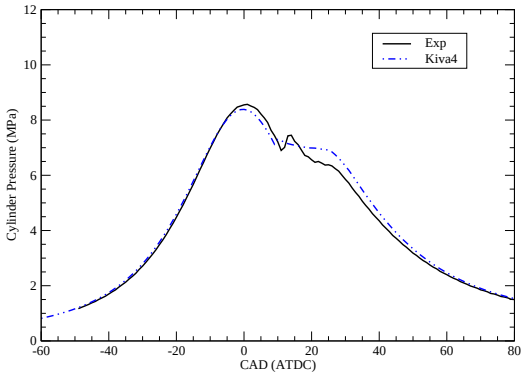

Figure 6.6: Comparison of cylinder pressure for high-load, single-injection cases for SOI = +5 ATDC

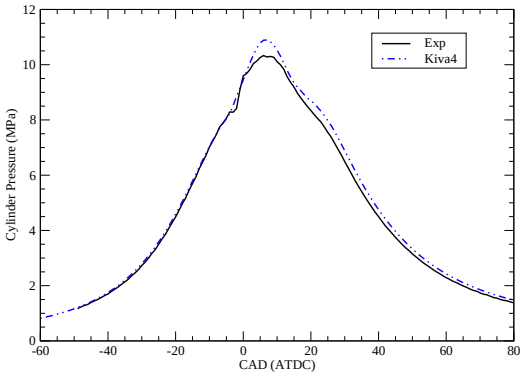

Figure 6.7: Comparison of cylinder pressure for high-load, double-injection cases for SOI = -7 ATDC

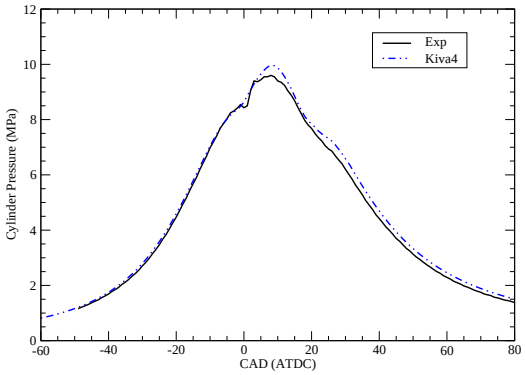

Figure 6.8: Comparison of cylinder pressure for high-load, double-injection cases for SOI = -4 ATDC

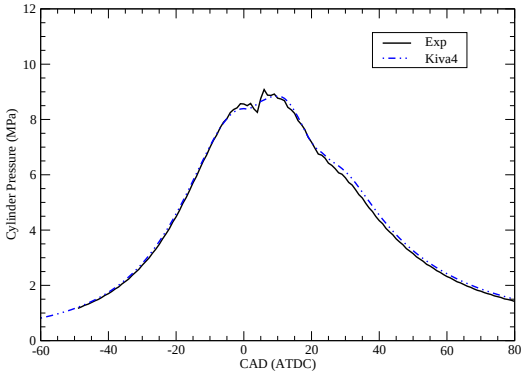

Figure 6.9: Comparison of cylinder pressure for high-load, double-injection cases for SOI = -1 ATDC

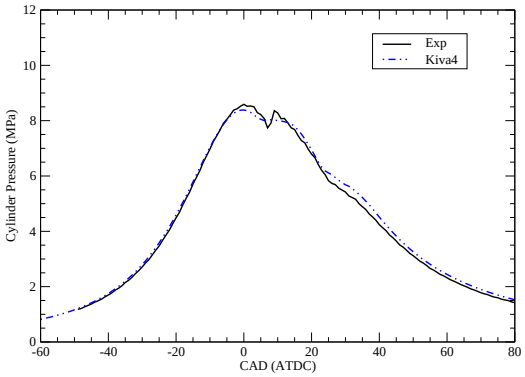

Figure 6.10: Comparison of cylinder pressure for high-load, double-injection cases for SOI = +2 ATDC

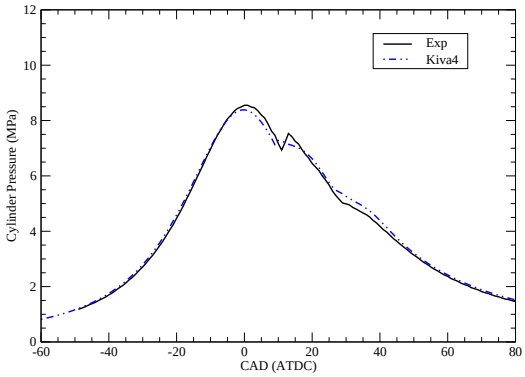

Figure 6.11: Comparison of cylinder pressure for high-load, double-injection cases for SOI = +5 ATDC

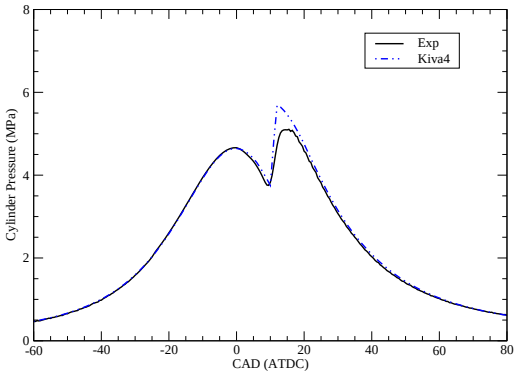

Figure 6.12: Comparisons of cylinder pressures for the selected low-load, PCCI case for SOI = +5 ATDC with EGR 8%

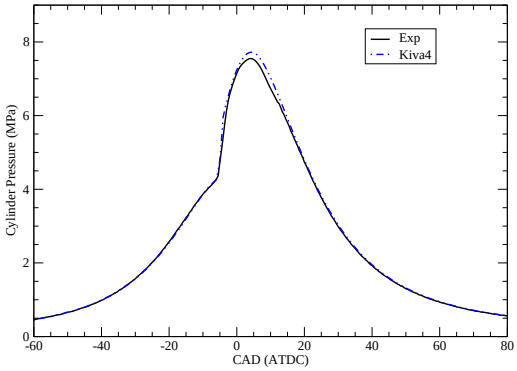

Figure 6.13: Comparisons of cylinder pressures for the selected low-load, PCCI case for SOI = -10 ATDC with EGR 8%

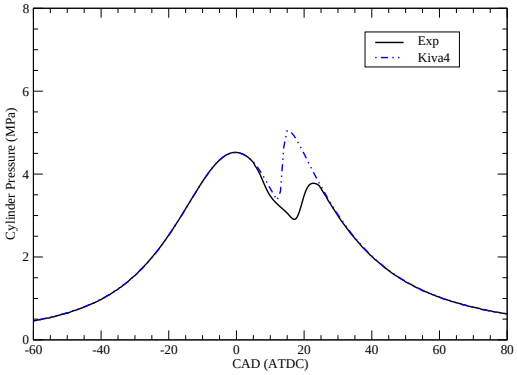

Figure 6.14: Comparisons of cylinder pressures for the selected low-load, PCCI case for SOI = +5 ATDC with EGR 40%

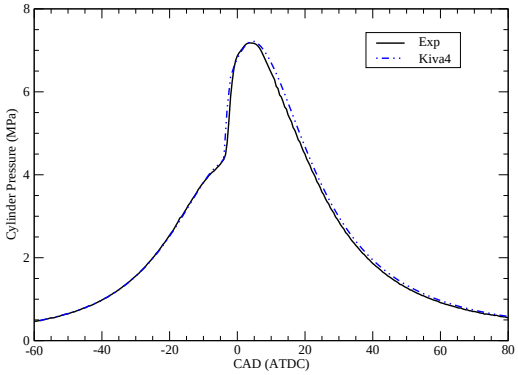

Figure 6.15: Comparisons of cylinder pressures for the selected low-load, PCCI case for SOI = -10 ATDC with EGR 40%

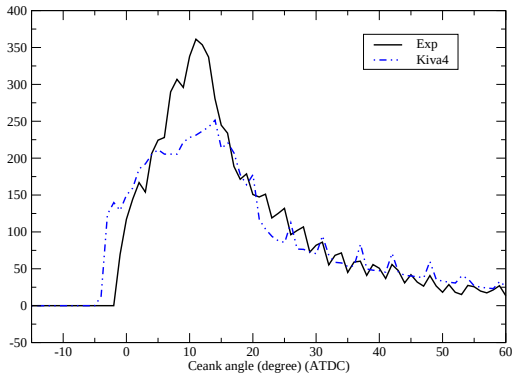

Figure 6.16: Comparisons of heat release rate for the high-load, single-injection with SOI = -7 ATDC case

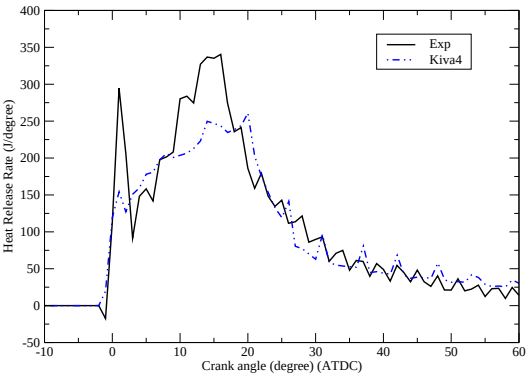

Figure 6.17: Comparisons of heat release rate for the high-load, single-injection with SOI = -4 ATDC case

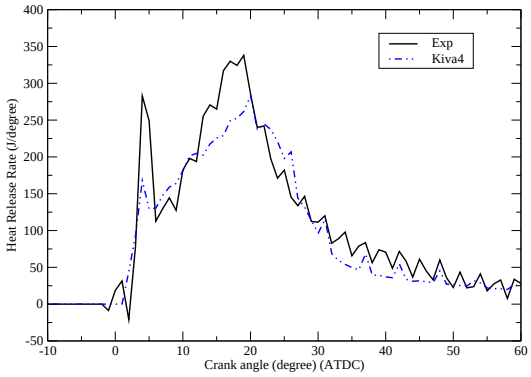

Figure 6.18: Comparisons of heat release rate for the high-load, single-injection with SOI = -1 ATDC case

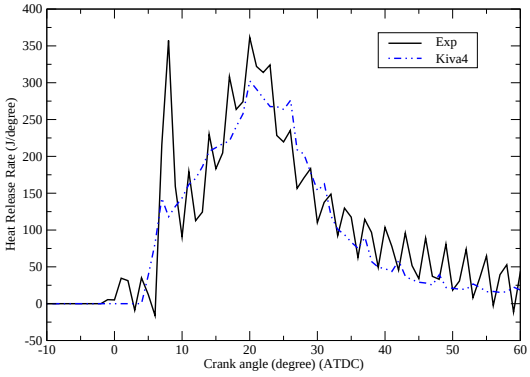

Figure 6.19: Comparisons of heat release rate for the high-load, single-injection with SOI = +2 ATDC case

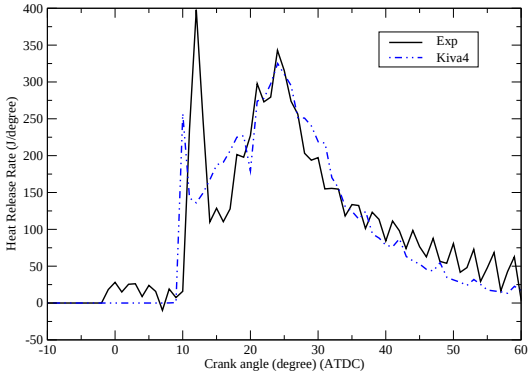

Figure 6.20: Comparisons of heat release rate for the high-load, single-injection with SOI = +5 ATDC case

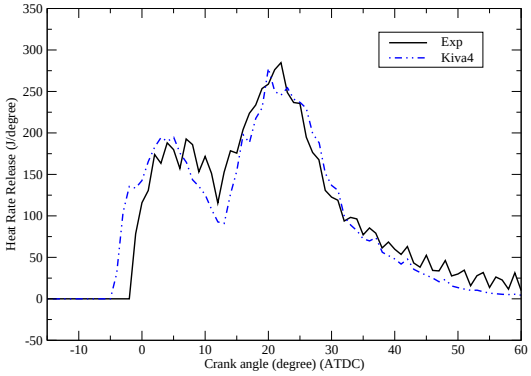

Figure 6.21: Comparisons of heat release rate for the high-load, double-injection with SOI = -7 ATDC case

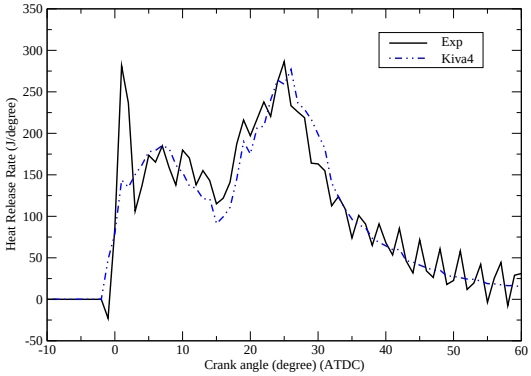

Figure 6.22: Comparisons of heat release rate for the high-load, double-injection with SOI = -4 ATDC case

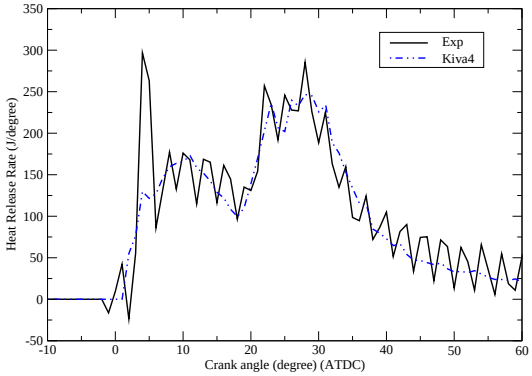

Figure 6.23: Comparisons of heat release rate for the high-load, double-injection with SOI = -1 ATDC case

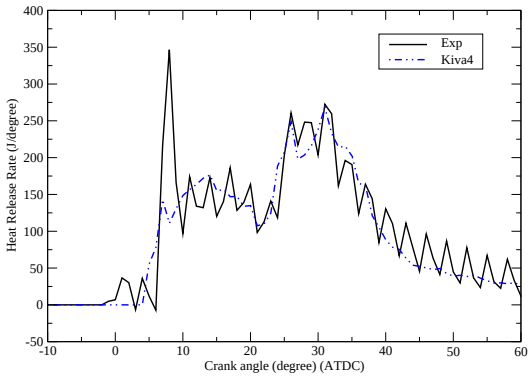

Figure 6.24: Comparisons of heat release rate for the high-load, double-injection with SOI = +2 ATDC case

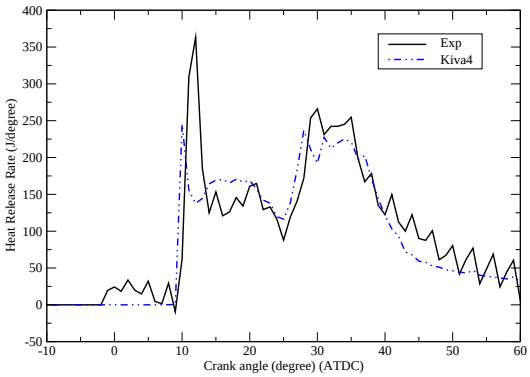

Figure 6.25: Comparisons of heat release rate for the high-load, double-injection with SOI = +5 ATDC case

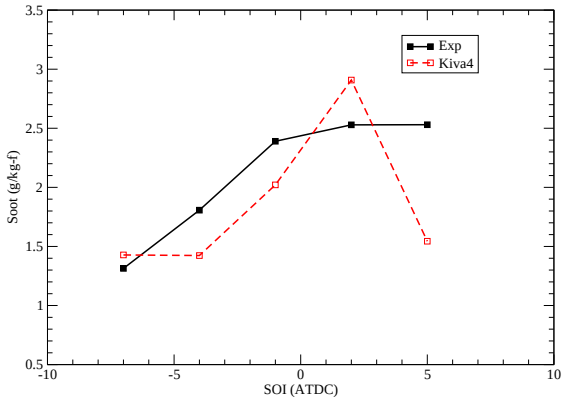

Figure 6.26: Comparisons of soot emissions with respect to start of injection timing for the high-load, single-injection cases

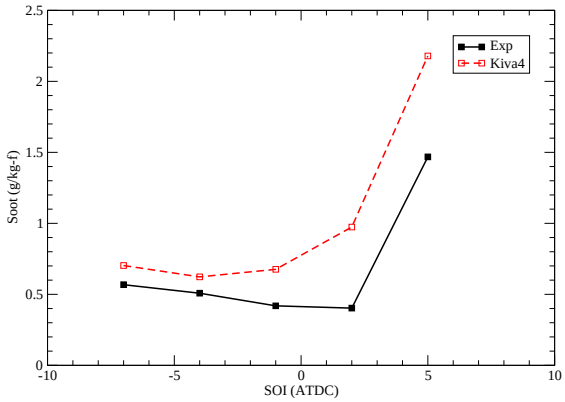

Figure 6.27: Comparisons of soot emissions with respect to start of injection timing for the high-load, double-injection cases

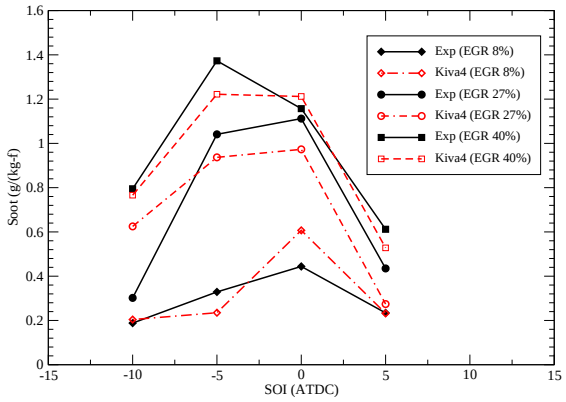

Figure 6.28: Comparison of soot emissions with respect to start of injection timing for the low-load, PCCI cases

CHAPTER 7. IMPLEMENTATION OF CONJUGATE HEAT TRANSFER MODEL

An understanding of the engine heat transfer mechanism is important because it influences engine performance, efficiency, exhaust emissions, and component thermal stresses. Engine heat transfer alone has been studied extensively by experiments and modeling. Heat transfer models are often incorporated in the computer code to calculate the heat flux from the combustion chamber to provide boundary conditions for combustion simulation (Woschni, 1967; Morel et al., 1985; Heywood, 1988; Wolff et al., 1997; Eiglmeier et al., 2001; Wiedenhoefer, 2002). However, heat transfer models that are coupled with in-cylinder models to predict surface temperature distributions are not common.

7.1 Wall Heat Transfer Modeling

The KIVA code can describe the chemically reactive flow with sprays and is extensively used for engine combustion simulation. It has the capability to calculate the flows in engine cylinders with arbitrarily shaped piston geometries, including the effects of turbulence and wall heat transfer. In the heat transfer model of the KIVA code (Amsden et al., 1989), the temperature of the chamber wall is a vital parameter for determining the magnitude of heat flux as shown in the following formula. Clearly, without an accurate representation for wall temperature, the heat flux levels may be not accurate.

$$\frac{J_w}{\rho u^* c_p (T - T_w)} = \begin{cases} 1/(Pr_l \frac{v}{u^*}) & (\zeta \le R_c) \\ 1/Pr[\frac{v}{u^*} + (\frac{Pr_l}{Pr} - 1)R_c^{1/2}] & (\zeta > R_c) \end{cases} \tag{7.1}$$

where T_w is the wall temperature, Pr_l is the Prandtl number of the laminar fluid, and $\zeta = \frac{\rho y v}{\mu_{air}(T)}$ is the Reynolds number based on the gas velocity relative the wall. R_c is equal to 114.

Generally, the combustion chamber of an internal combustion engine is formed by the cylinder wall, head, and piston. The temperature distributions are different for each surface. Typically the temperature of each surface is assumed to be a constant in the CFD code. This is not consistent with the actual situation occurring on the surface of the combustion chamber. An accurate temperature distribution is essential to obtain accurate wall heat flux, which, in turn, will affect combustion predictions near the wall.

7.2 Approach

The coupled calculation of the in-cylinder flow and wall heat transfer is a promising approach as both processes are strongly related. The coupled approach is achieved by maintaining a common temperature and local heat flux at the fluid-solid interface. The surface temperature varies with locations and thus the uniform temperature assumption is not needed.

7.3 Physical Criteria

Criteria are needed to describe the physical interaction (thermally) between the fluid and solid regions since both domains are modeled separately. The two physical conditions to be met are the continuity of heat flux across the fluid-solid interface and the common temperature on the interface. They are,

$$T_{fluid} = T_{solid} \tag{7.2a}$$

$$k_{fluid}\frac{\partial T}{\partial n}\Big|_{fluid} = k_{solid}\frac{\partial T}{\partial n}\Big|_{solid} \tag{7.2b}$$

The two conditions are imposed on each grid node along the interface as illustrated in Figures 7.1(a) and 7.1(b). The above figures define a pair of interfaces (one at the fluid boundary, the other at the solid boundary)

7.4 Governing Equations

The flow solver for in-cylinder flow was introduced in detail in Chapter 2. The physical process of heat conduction in solid medium is described by the heat conduction equation. The

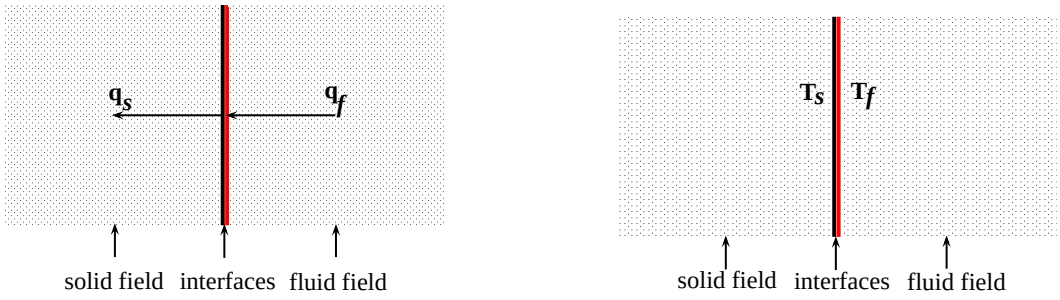

(a) heat flux (b) temperature

Figure 7.1: Continuity of heat flux (a) and temperature (b) at the fluid/solid interface

three-dimensional unsteady heat conduction equation without heat source has been written in integral form in Cartesian coordinates as

$$\frac{\partial}{\partial t}\int_{\Omega}\rho_s c_p T dV + \oint_{\partial\Omega} k\frac{\partial T}{\partial \hat{n}} dA = 0 \tag{7.3}$$

Here ρ_s is the density of solid body, c_p is the specific heat, and $\hat{n}$ is the outward unit vector of the control volume.

In the present work, the flow solver will be modified and extended to solve heat conduction equation for the solid domain. The objective is to implement the conjugate capability into the KIVA code with a minimum amount of modification to the code. Therefore, the fluid and solid regions are solved in basically the same manner, much like that described by Han et al. (2000) and Xue (2005) in Eulerian codes for internally cooled turbine blade. This manner makes the code consistent. The Navier-Stokes equations are also solved in the solid region. Hence, the following conditions are set: a constant density and zero velocity are used to satisfy the continuity and momentum equations, which leaves only a simplified form of the energy equation Eqn.(3.11) to be solved. This simplified energy equation is solved using the same method as in the gas flow regions with changes to the numerical parameters. The resulting energy equations in integral form is

$$\frac{D}{Dt}\int_{V}\rho I dV \quad = \quad \oint_{A} K\nabla T dA \tag{7.4}$$

In this case, the energy variable is basically as the internal energy component from the flow problem. This energy term may be expressed in terms of the specific heat of the solid and

temperature as

$$I = c_p T \tag{7.5}$$

7.5 Numerical Formulation

The numerical discretization of the above equation (Eq.7.4) can be obtained by simplifying Eqn.(3.46). In the solid region, Both pressure force and viscous dissipation terms are not needed. Hence, the numerical formulation for the solid region in the finite volume frame is as,

$$\rho \frac{I^{n+1} - I^n}{\Delta t} = \sum_f K_f^n \nabla [\Phi_D T^n + (1 - \Phi_D) T^{n+1}] \cdot A_f^n \tag{7.6}$$

Here, Φ_D is a variable implicitness parameter with a range of $(0 < \Phi_D < 1.0)$. The amount of implicitness is chosen, in part, to ensure numerical stability of the difference approximations to the individual terms in question. If stability is the only concern, fully-implicit schemes should be used, which means $\Phi_D = 0$. The computational efficiency can be obtained, on the other hand, by minimizing the amount of implicitness. The right-hand-side terms account the heat flux, which is solved using a method by first calculating geometric coefficients (Torres et al., 2006; Amsden et al., 1989). The detail is introduced in appendix.

7.6 Coupling Procedure for Unstructured Grid

At the interface, the coupling of the fluid and solid fields is needed for conjugate calculation. This is accomplished by balancing the local heat fluxes at the interface on both fluid and solid sides. Thus, a common wall temperature is produced at both sides at each iteration to serve as an internal thermal boundary condition for the coupling procedure. Similar approaches have been employed by several authors, such as Rigby et al. (2001) and Xue (2005).

7.6.1 General Procedure

The KIVA-4 code is based on unstructured, mixed-element grids (see Fig. 7.2), evaluation of the local heat flux based on the nodes on the interface is accomplished by an edge-weighted

averaging procedure, as shown in Figure 7.2. For a specific node, the following formula can be obtained,

$$\sum_{i=1}^{n} w_i k_f \frac{T_i - T_w}{\Delta n_i} = \sum_{j=1}^{m} w_j k_s \frac{T_w - T_j}{\Delta n_j} \tag{7.7}$$

where indices m and n are the numbers of adjacent edges that are connected to the interface nodes in the fluid and solid regions, respectively. i and j are the indices of the edges connected to the nodes in the fluid and solid regions, respectively. w_i and w_j are the associated edge weights, and k_f and k_s are the thermal conductivities of the fluid and solid, respectively. T_i and T_j are the off-face node temperature adjacent to the interfaces. T_w is the computed wall temperature at the interface node which is used to provide a thermal boundary condition for both the fluid and solid domains. During numerical calculation, the above equation is enforced iteratively at the fluid-solid interfaces.

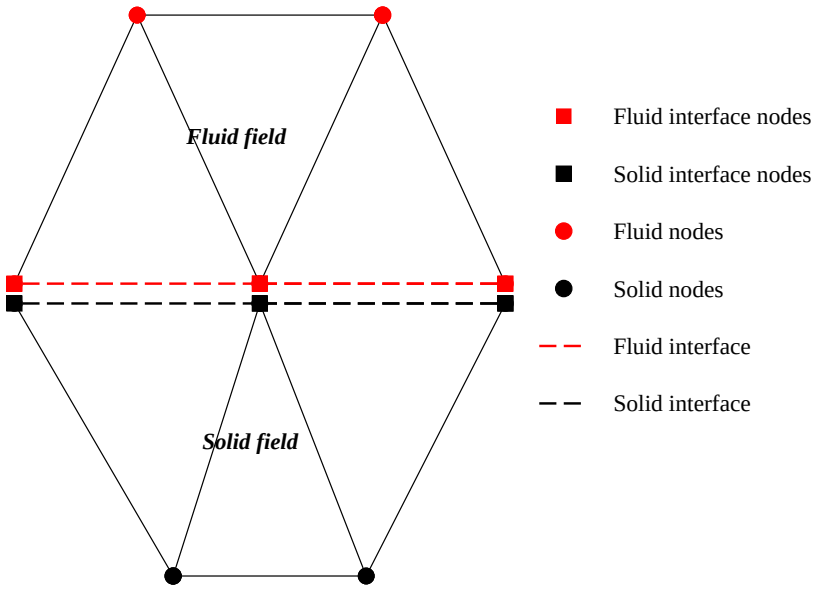

Figure 7.2: Schematic of the elements along the fluid-solid interface based on unstructured mesh in 2-D domain

7.6.2 Law-of-Wall Function

In KIVA, the wall function is used to determine the wall heat transfer due to the insufficient grid resolution in a typical engine simulation. Numerically, heat transfer is determined

by matching the computed temperatures at grid points closest to walls to the wall function. The wall heat flux J_w is given from Eq.(7.1) using the law-of-wall condition. A temperature wall function formulation was derived by Han et al. (1997) for the variable-density, turbulent flows typically found in engines. Here, only the temperature wall function and corresponding formulation of wall heat flux are given as

$$T^+ = 2.1ln(y) + 2.1G^+y^+ + 33.4G^+ + 2.5 \tag{7.8}$$

$$J_w = \frac{\rho c_p u^* T ln(T/T_w) - (2.1y^+ + 33.4)G\nu/u^*}{2.1ln(y^+) + 2.5} \tag{7.9}$$

Here, G represents the averaged chemical heat release. The chemical reaction rate slows significantly due to the interaction of the relatively cool combustion walls (Westbrook et al., 1981). Therefore, if the source term, G, can be ignored, the final form of wall heat transfer model in the KIVA simulation becomes

$$J_w = \frac{\rho c_p u^* T ln(T/T_w)}{2.1ln(y^+) + 2.5} \tag{7.10}$$

When matching the heat flux at the interface between the fluid and solid regions, one obtains,

$$J_w = K_f(\nabla T)_f) \cdot \mathbf{A}_f \tag{7.11}$$

The heat flux at the solid interface in Eq. (7.11) is calculated using geometric coefficients method and given as,

$$K_f(\nabla T)_f \cdot \mathbf{A}_f = K_f[a_c(T_c - T_w) + a_{e_{12}}(T_1 - T_2) + a_{e_{34}}(T_3 - T_4)](\mathbf{A}_f \cdot \hat{n}) \tag{7.12}$$

where, T_c is the cell-centered value of temperature of the cell next to the wall, T_w is temperature value of the wall surface, and T_i are the values of temperature on the face edges. $\hat{n}$ is the outward norm of the wall surface.

After substituting Eq. (7.12) into Eq. (7.11) and rearranging, the value of temperature T_w at the interface can be obtain

$$T_w = \frac{J_w - [K_f(a_cT_c + a_{e_{12}}(T_1 - T_2) + a_{e_{34}}(T_3 - T_4))(\mathbf{A}_f \cdot \hat{n})]}{-1.0K_f a_c} \tag{7.13}$$

this T_w is used to update the thermal boundary of both the fluid and solid interface.

7.7 Numerical Implementations

The implementation of the present approach basically includes solution procedure, grid topology, and interface matching.

7.7.1 Solution Procedure

For the conjugate implementation, modifications to the original KIVA code are required. First, a solid volume tag was added to flag the solid computational domain. The fluid domain is treated in the normal way, with the exception that an additional boundary condition is added to handle the fluid-solid interface. In the solid domain, the velocities are set to zero. The thermal conductivity can vary with temperature, but for the present work it is assumed constant.

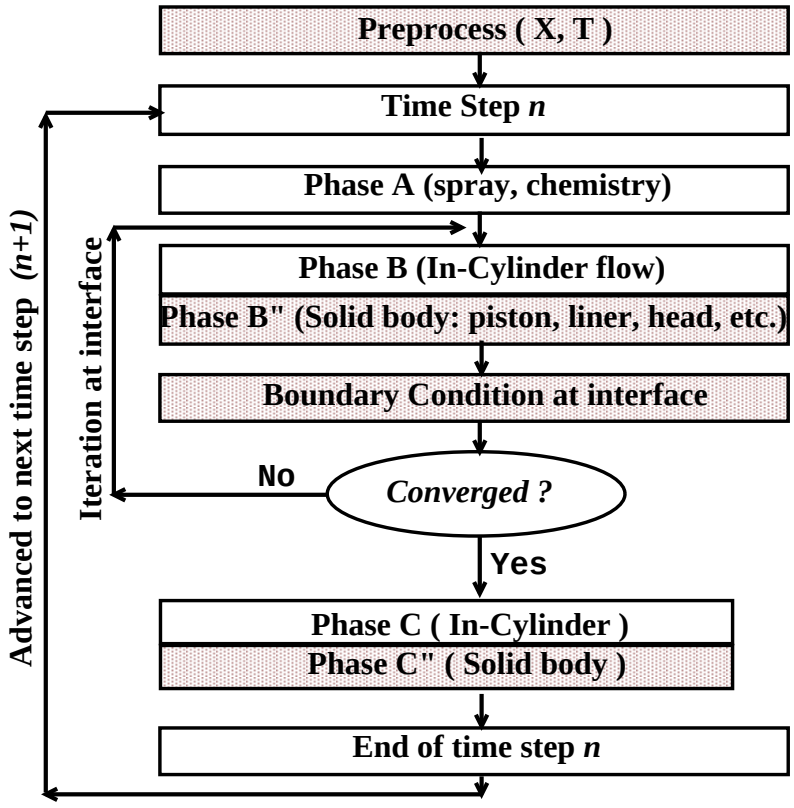

Figure 7.3: The solution procedure of the KIVA code with the conjugate heat transfer capability. The shadow boxes indicate the new parts added.

At the fluid-solid interface, the velocities are zero and turbulence quantities on the fluid side are handled as they are normally at any other wall. The key issue here is setting the temperature. It is required to impose a condition at the boundary such that the temperature and heat flux match at the interface. When the above boundary condition is imposed, it is assumed that all values internal to each domain are known. It is then possible to solve for the local wall temperature which will result in identical heat flux value from each side of the interface. Once the domain boundary values are set, the internal nodes are advanced. The procedure is repeated until convergence to steady state is achieved resulting in the matching of both temperature and heat flux at the fluid-solid interface. See Fig.7.3.

7.7.2 Domain Topology along Interfaces

The unstructured grid algorithm does not have the predictable connectivity of the structured grid, and all connectivities have to be built before they can be used. Figure (7.2) shows a pair of interfaces. Here, there are two assumptions: (1) there is no gap between interfaces, and (2) they are exactly matched at each node along the interface. Thus, the connectivity between the fluid interface and solid interface need to be built in order to perform the interaction between the fluid and solid domains during the computation.

7.7.3 Building the Connectivity between Interfaces

To perform the coupling of the fluid and the solid domains, the message has to be passed and stored to each side of the interface in some way, since there is no connectivity between the fluid-solid interface. The approach is that, in the preprocessing the identical mapping is built between the solid and fluid nodes on the interface. Based on the point-to-point match, it is to store the information of the neighbors of nodes on the fluid interface as the neighbors of the corresponding node on the solid interface, and to store the information of the neighbors of nodes on the solid interface as the neighbors of the corresponding node on the fluid interface. The information includes the temperature and other variables, which are updated at every iterative step.

CHAPTER 8. VALIDATION OF CONJUGATE HEAT TRANSFER MODEL

This chapter describes the validation of the new conjugate heat transfer model and its application in transient engine heat transfer study.

8.1 Validation of Heat Conduction Capability

The heat conduction modeling capability is a new addition to the present CFD code and requires validation before the model is used in conjunction with the flow solver. Simple test cases on three-dimensional grids will be used to demonstrate the conduction modeling capability. These test cases assumed constant thermophysical properties for the solid region. Also these tests have analytical solutions against which comparisons can be made.

8.1.1 Computational Domain and Boundary Conditions

This test case is an one-dimensional, transient conduction problem. This test case is an example problem taken from the textbook of Carslaw et al. (1959).

The computational geometry and mesh of a slab is shown in Figure 8.1 . This slab has a dimension of $3 \times 1 \times 1$ mm and the mesh resolution is $30 \times 10 \times 10$. The initial temperature is 0 K inside the domain. Both left and right walls are given an isothermal boundary condition. Front, back, top, and bottom walls are specified as adiabatic boundaries. The temperature is 300 K on the left and right walls all the time. The solid material has a thermal conductivity of 53.1 $W/(m * K)$, density of 7870 $kg/(m^3)$, and specific heat of 447 $J/(kg * K)$. The time step of 6.625×10^{-5} s is used for this simulation. The amount of implicitness is 0.5.

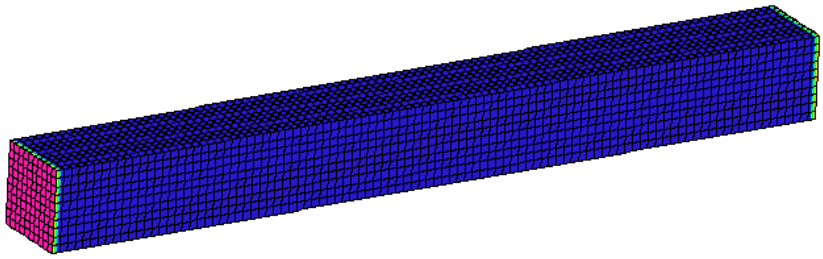

Figure 8.1: 3D computational mesh and initial temperature condition

8.1.2 Results and Analysis

The temperature along the center line were compared between the numerical solution and analytical solution as shown in Figure 8.2. Due to the symmetry, only one half of the slab was plotted in Figure 8.2. Here, the dimensionless parameters of time, length and temperature in plot are defined as

$$\begin{aligned} \mathbf{t} &= \frac{\alpha t}{l^2}, \\ \mathbf{x} &= \frac{x}{l} \\ \mathbf{T} &= \frac{T}{T_r} \end{aligned} \tag{8.1}$$

The values predicted are plotted in solid curves, and the analytical solution is plotted in circles. Different color represents values at different times. The numerical results agree well with the analytical solution at various times. The model predicted the transient heat diffusion accurately. The temperature contours at time 1.0 and 2.5 were shown in Figure 8.3. The heat diffusion is driven by the temperature gradient from the ends to the middle. The symmetric temperature distribution was observed in the plots. The temperature reaches a uniform distribution at time of 2.5 (see Fig. 8.3(c)).

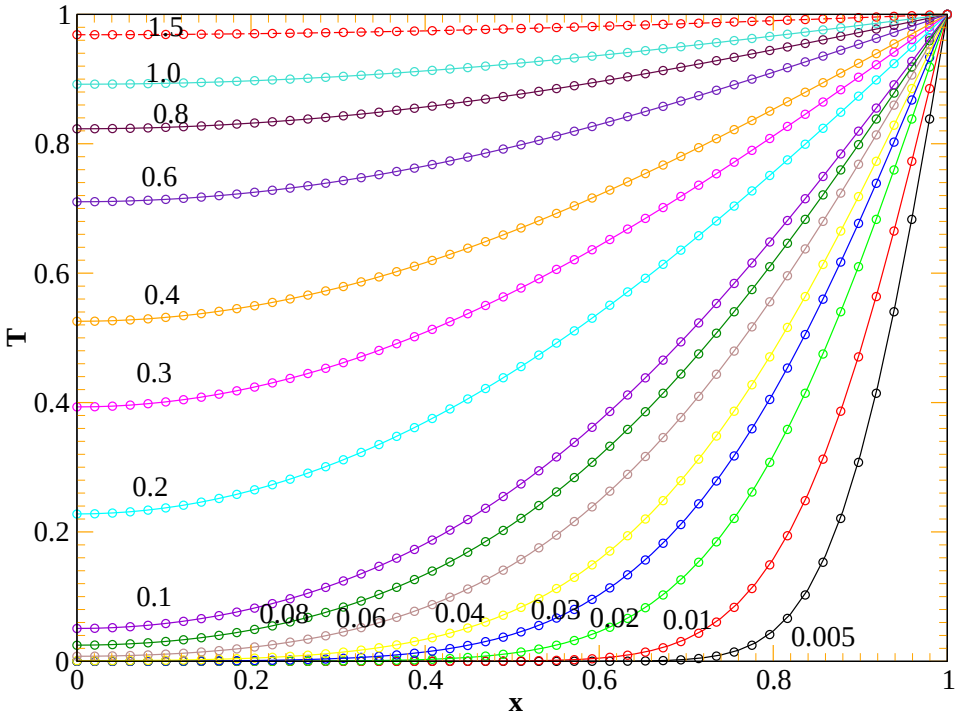

Figure 8.2: Comparison of the predicted temperature profile and analytical solutions. The solid lines are predicted and the circles are analytical solutions (Carslaw et al., 1959). The numbers on lines are non-dimensional time

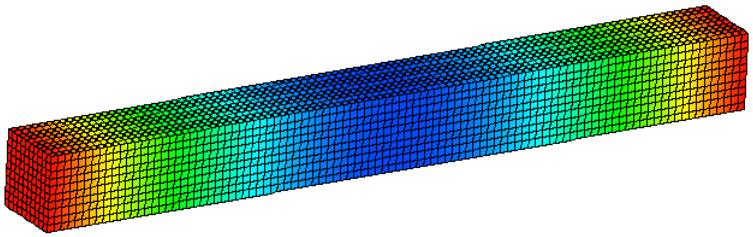

(a) Temperature contour at time 1.0

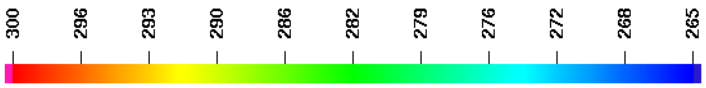

(b) scale

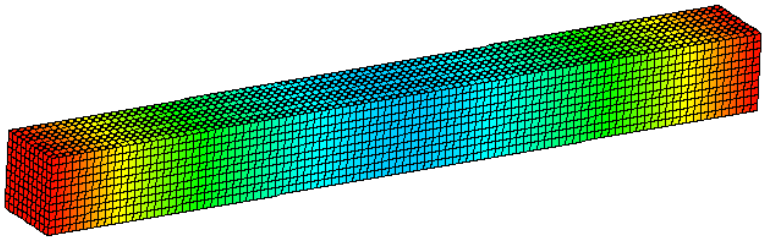

(c) Temperature contour at non-dimensional time 2.5

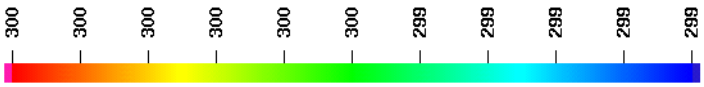

(d) scale

Figure 8.3: Temperature contour at non-dimensional time of 1.0 and 2.5 for the slab

8.2 Validation of Interface Procedure

The similar three-dimensional grid from the previous section is used to investigate the interface communication of the composite slab. The two key factors at the interface boundaries are the thermal diffusivities and the grid spacing on each side.

The thermal diffusivity is a measure of how rapidly thermal effects spread through a material. A composite slab is composed of at least two different materials, and consequently, at least two different diffusivities. This means that each part of component of the slab evolves at a different rate, depending on the diffusivity. The ratio of the respective diffusivities at a given boundary determines the physical behavior of the problem, moreover, it directly affects the numerical stability.

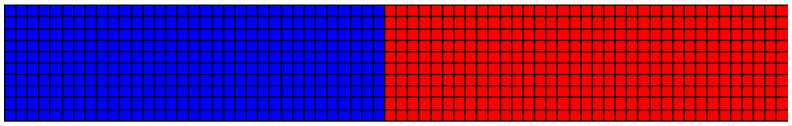

Figure 8.4: Computational domain and initial temperature conditions (zoomed view). Region 1 is on right and Region 2 is on the left.

8.2.1 Computational Domain and Boundary Conditions

Figure 8.4 shows the computational geometry and mesh. This composite slab consists of two regions. Each has a dimension of $30 \times 1 \times 1$ mm and a mesh size of $300 \times 10 \times 10$. Region 1 has a thermal conductivity of 53.1 $W/(m * K)$, density of 7870 $kg/(m^3)$, and specific heat of 447 $J/(kg * K)$. Region 2 has a thermal conductivity of 401 $W/(m * K)$, density of 8933 $kg/(m3)$, and specific heat of 385 $J/(kg * K)$. The initial temperature are 300 K and 0 K in region 1 and 2, respectively. Front, back, top, and bottom walls are adiabatic. The two regions are coupled at the interface without contact resistance. The time step is 2.325×10^{-6}, and the implicitness parameter is 0.5 for this simulation.

8.2.2 Results and Analysis

Figure 8.5 shows that the non-dimensional temperature ($T/300$) distribution against the dimensionless time along the center line at different times. The analytical solutions are also plotted as symbols. It can be seen that the curves and symbols overlap with each other. The numerical solutions agree well with the analytical solution at various times. The temperature is continuous across the interface. On the other hand, the slopes of curves are different at two sides. This is because that the thermal conductivity on the right is lower than the left. To obtain an equal heat flux at the interface, a higher temperature gradient is needed on the right. Figure 8.6 shows the temperature distribution at 0.2. A continuous temperature distribution is predicted at the interfaces.

8.3 Sinusoidal Temperature Variation at Boundary

A transient case is used to test the fluid-solid interface. The transient condition is initiated by a fluid boundary temperature that varies sinusoidally. The computational domain and mesh are shown in Figure 8.7. The left-hand side is the fluid domain with dimension of $10 \times 5 \times 5$ mm, and the solid domain on the right with dimension of $5 \times 5 \times 5$ mm.

The fluid and the solid wall are at a uniform initial temperature of 412 K. Then temperature at the left boundary of fluid begins varying with time with an amplitude of $100sin(\pi t)$.

The temperature variations of the fluid and solid sides at the interface are plotted in Figure 8.8. It shows the transient start-up and the ultimately periodic state of temperature. Since the periodic state has been reached with two computational cycles, results beyond the second cycle remain the same. This case qualitatively shows the present fluid-solid interface coupling works properly. The difference of variation magnitude between the fluid side and solid side is due to the large difference of the thermal conductivities of air and the solid material.

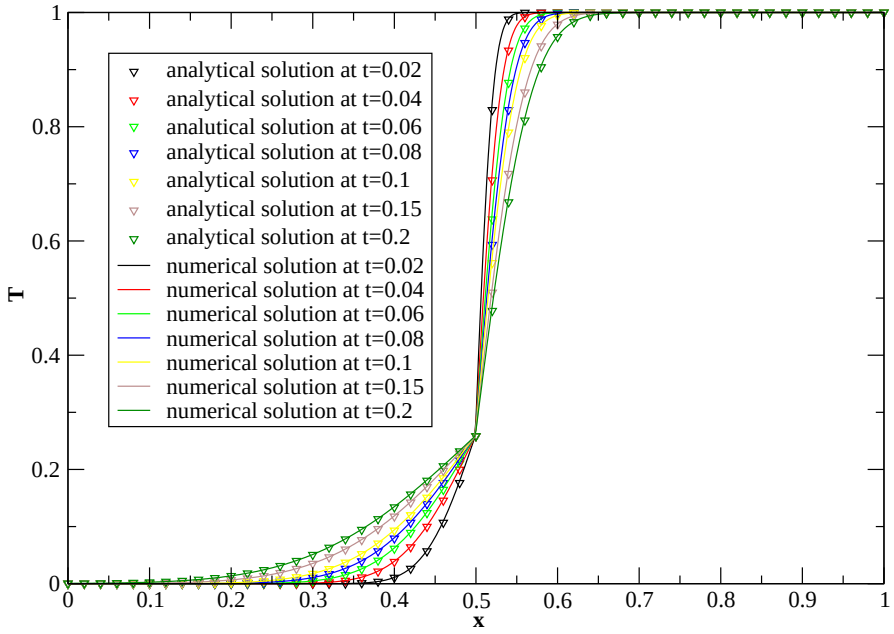

Figure 8.5: Comparison of the predicted temperature profile and analytical solutions (Carslaw et al., 1959) at various times

(a) zoomed view at interface

(b) Temperature contour of the composite slab

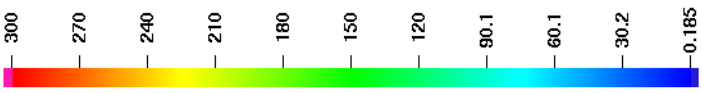

(c) scale

Figure 8.6: Temperature contour at time 2.5

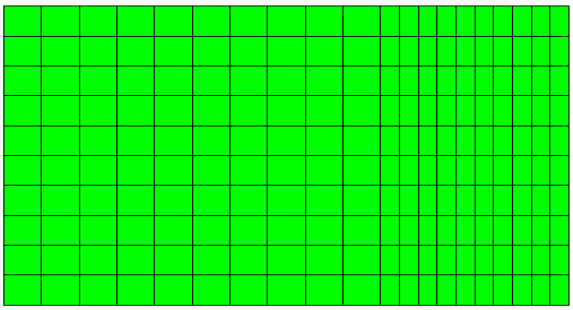

Figure 8.7: Computational domain and mesh

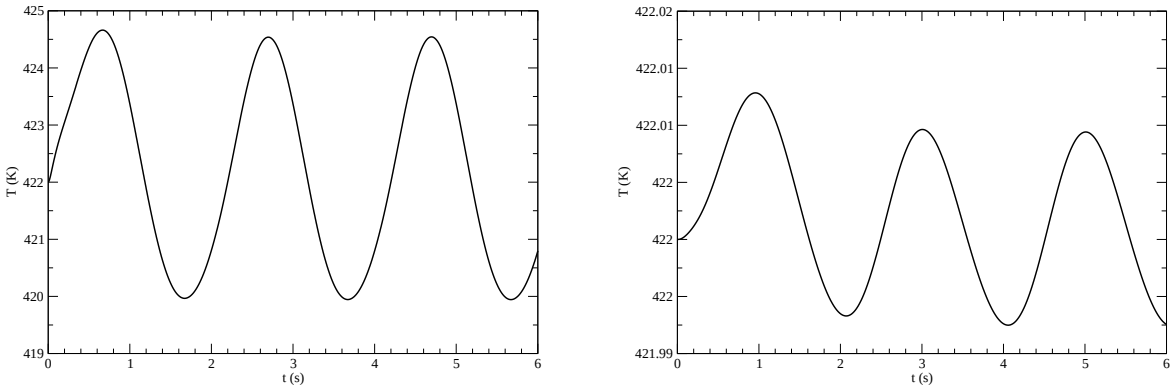

(a) fluid side

(b) solid side

Figure 8.8: Temperature variations of the fluid and solid at the interface

8.4 Application to Engine Simulation

The computational domain includes the combustion chamber, cylinder head and piston. The computational domain and mesh are shown in Figure 8.9. The chamber has a bore of 10 cm, stroke of 10 cm, and squish of 1.25 cm. The cylinder head is 1 cm high, and the piston is 1 cm thick. The grid size is 0.4 mm in the cylinder head and piston. The total number of grid cells is $28,800$. The engine speed is 1000 rpm. The compression ratio is 10. The material of the cylinder head and piston is cast iron with a density of $\rho = 7870 kg/m^3$, thermal conductivity of $k = 47.7 W/(m \cdot K)$, and specific heat of $c_p = 447 J/(kg \cdot K)$. The thermal boundary conditions are set as follows: The surface temperature of the top of the cylinder head is 412 K. The surface temperature of the bottom of the piston is 375 k. The calculation time step used is 1.0×10^{-5} s.

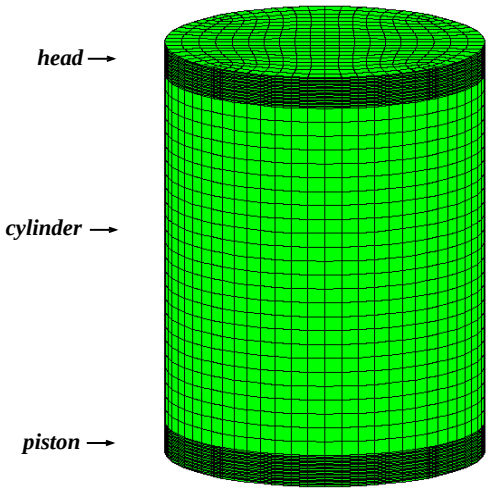

Figure 8.9: Computational domain and mesh for the engine geometry

Figure 8.10 shows the convergence history of the surface temperature of cylinder head and piston for the engine simulation. The simulation starts from the uniform wall temperature of $T = 422$ K initially. It takes about 300 simulation cycle to reach the convergent state. This simulation takes 20 days on a workstation. Figure 8.11 gives the transient temperature variation at different depths into the cylinder head surface and piston surface, respectively. It can be seen that when the depth exceeds a thin layer, an obvious transient temperature

variation can hardly be seen. The results agree with the conclusions of Morel et al. (1985) and Liu et al. (1998).

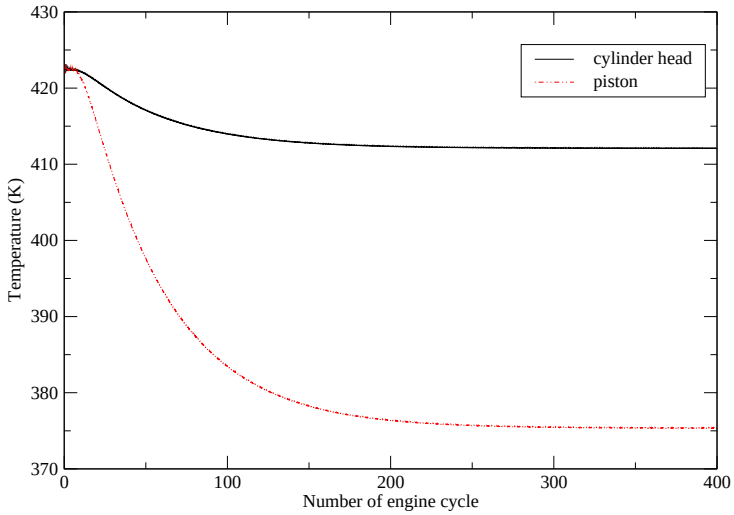

Figure 8.10: Convergence history of the engine simulation against engine cycle

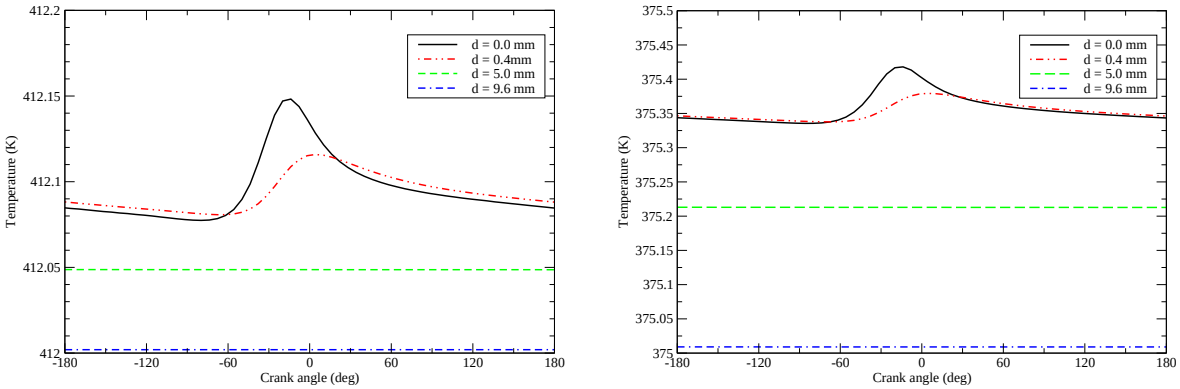

(a) cylinder head (b) piston

Figure 8.11: Predicted temperature variations at different depths into the wall of the head and piston.

8.5 Diesel Engine Simulation with Spray

An engine geometry with diesel-like conditions is studied using the conjugate heat transfer model. A similar operating condition to that of the Caterpillar diesel engine (3401 SCOTE)

in Chapter 6 is simulated. The engine is operated at high load with engine speed of 1600 rpm with single nozzle injection. The intake valve is closed at -147 $ATDC$ and the exhaust valve is opened at 135 $ATDC$. The fuel ($C_{14}H_{30}$) is injected from the center of the cylinder head with high pressure and high speed. The fuel injection starts from -9 $ATDC$ with a duration of 19.6 CAD.

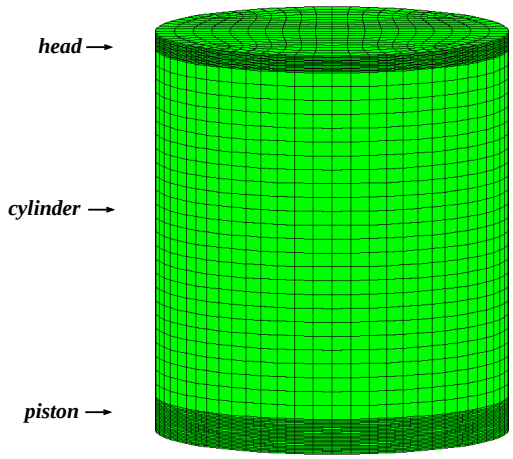

Figure 8.12: Computational domain and mesh for the diesel engine geometry

The cylinder geometry and computational mesh are shown in Figure 8.12. The engine bore and stroke are 10 cm and 9.4 cm, respectively. The compression ratio is 16. The gas has an initial temperature of 361 K and pressure of 2.082 bar. The cylinder head and piston are 0.5 cm and 1.0 cm thick, respectively. The material of the cylinder head and piston is cast iron, which has density of $7870 kg/m^3$, specific heat of $447 J/(kg \cdot K)$, and thermal conductivity of $47.7 W/(m \cdot K)$. Regarding the temperature boundary conditions for the cylinder heat and piston, the wall temperature at the bottom surface of the piston and at the top surface of the head are 375 K and 361 K, respectively. The temperature is 361 K on the cylinder wall. The grid size inside the cylinder is 5 mm. The grid is fine in the solid wall, which has a grid size of 0.3 mm in the axial direction.

In the present simulation, first, 30 engine cycles was run to warm up the engine to attain

a pseudo steady-state for surface temperature. Then one additional engine cycle simulation was performed from intake valve closure (IVC) to exhaust valve open (EVO) with spray but without combustion. The calculation time step used is 5.0×10^{-6} s. The liquid spray is plotted with fuel vapor at different CAD in Figure 8.13. It shows liquid fuel impinges on the piston surface. Figure 8.14 shows the predicted temperature history at two locations in the cylinder head and piston, respectively. The locations are selected at the center of the interface between the head/piston and cylinder. Results show that all the temperature peaks occur within a range from -10 to 20 ATDC. This is coincident with the fuel injection phase.

Because the fuel is injected into the cylinder with very high speed, most of the fuel is vaporized before 20 ATDC. The mass fraction of fuel vapor is shown in Figure 8.15 at 20 $ATDC$. It can be seen that locally high mass fraction of fuel vapor appears on the piston surface. The temperature contours are shown in Figure 8.16 at 20 ATDC. Figure 8.16(a) shows the temperature of a vertical cut-plane along the spray axis. The blue color represents the temperature distribution in the cylinder head. A black line identifies the border between the piston and cylinder. A high temperature region indicated by red color can be observed at the piston surface from both the sideview (Figure 8.16(a)) and topview (Figure 8.16(b)). The horizontal plane in Figure 8.16(b) is located at 0.4 mm below the piston surface. A non-uniform temperature distribution is predicted inside the piston due to the impingement of fuel spray. The hot spot region in the piston exists near the high fuel vapor region shown in Figure 8.15. Although liquid fuel absorbs energy from surrounding gas during the evaporation process, the gas temperature (Figure 8.17) is still higher than the piston surface. Also, the injected fuel brings high momentum into the surrounding gas and favors high gas flow turbulence as shown in Figure 8.18, which then enhances the heat transfer rate in these regions. Thus, this contributes to the local high temperature spots as shown in Figure 8.16.

Results demonstrates that the current conjugate heat transfer model can predict a more realistic non-uniform temperature distribution on the wall due to the fuel spray through simultaneous calculations of convection heat transfer of the in-cylinder fluid and heat conduction in the cylinder head and piston. Note that the present study only simulates non-combustion

spray and the temperature variation on the piston surface is not significant. Future studies can be performed for combustion conditions and significant variations of the piston surface temperature is expected.

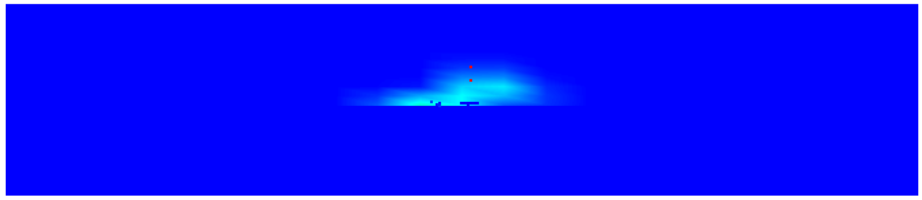

(a) -5 ATDC

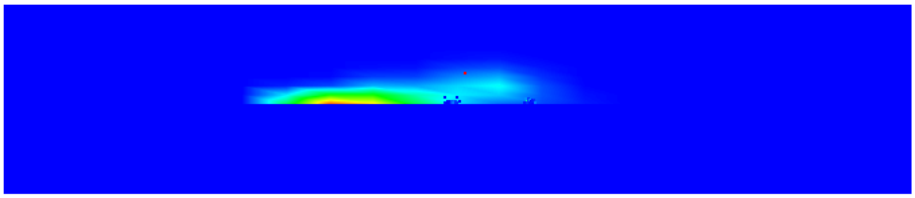

(b) TDC

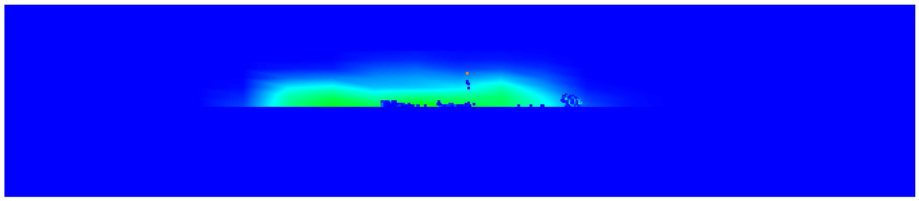

(c) +5 ATDC

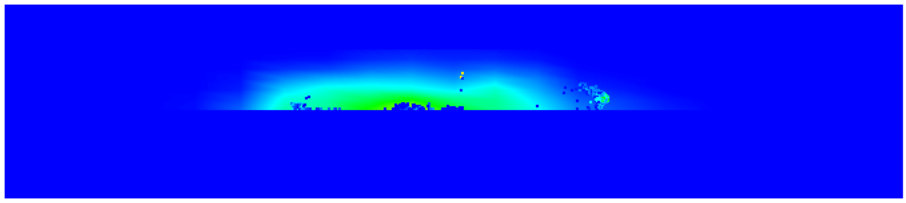

(d) +10 ATDC

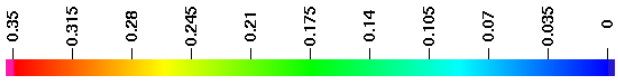

(e) mass fraction scale

Figure 8.13: Spray drops and mass fraction of fuel vapor

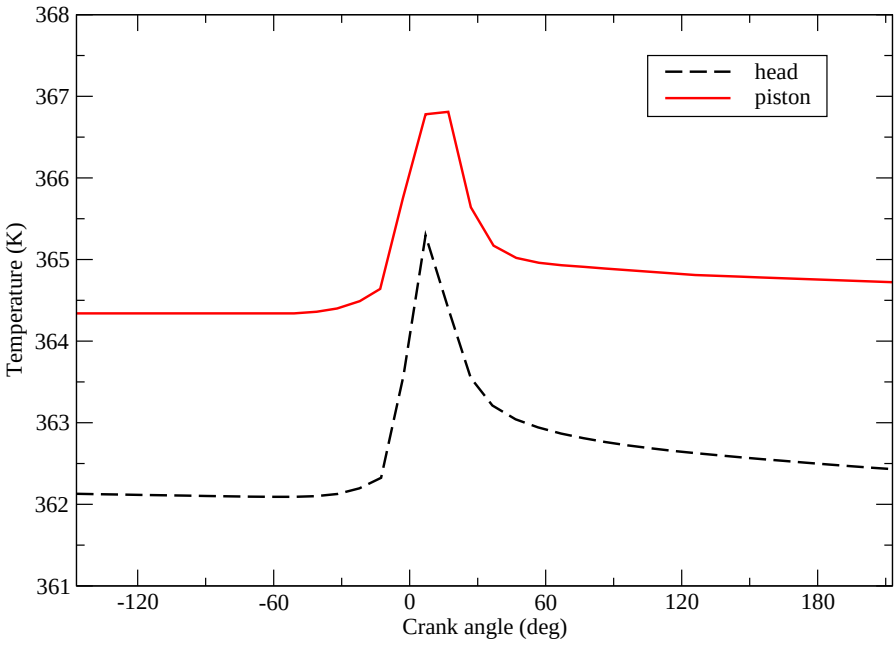

Figure 8.14: Predicted temperature variation at the center of piston and cylinder head surfaces for the diesel engine case

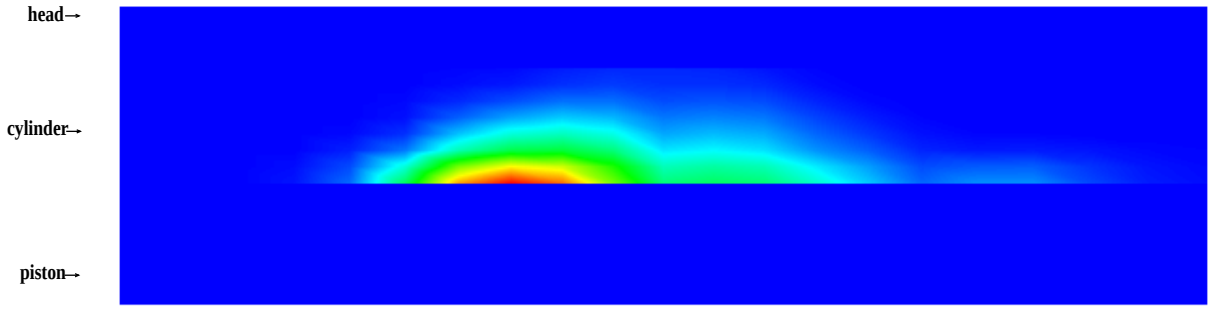

(a) fuel vapor mass fraction

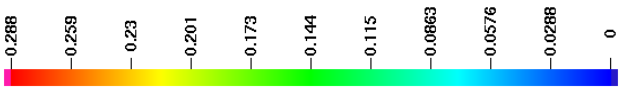

(b) scale

Figure 8.15: Predicted mass fraction of fuel vapor at 20 ATDC for the diesel engine case

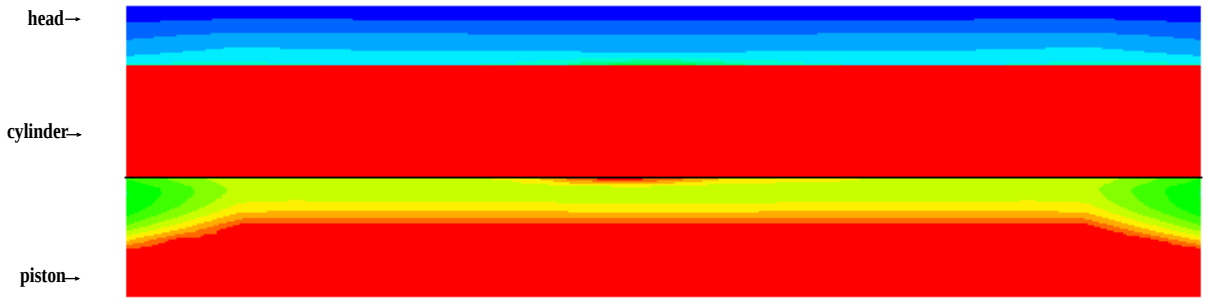

(a) side view

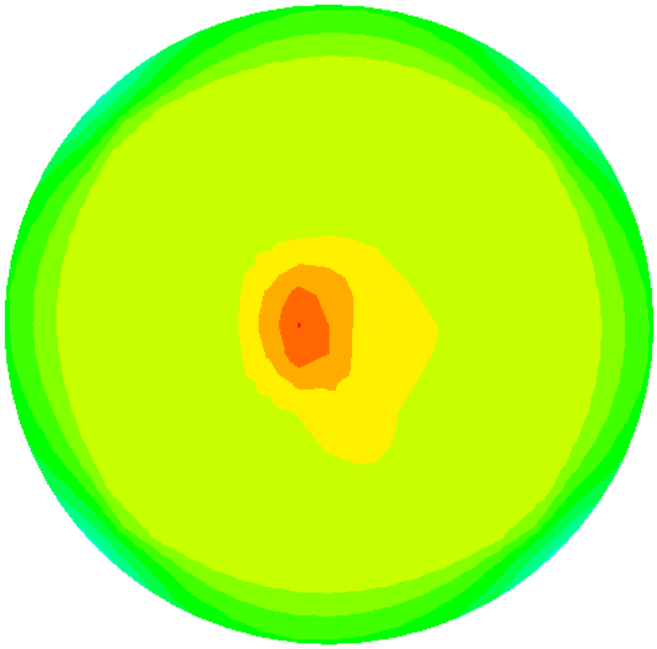

(b) top view

(c) temperature scale

Figure 8.16: Predicted temperature at 20 ATDC at: (a) vertical cut-plane in axial direction, (b) horizontal cut-plane at 0.4 mm inside the piston

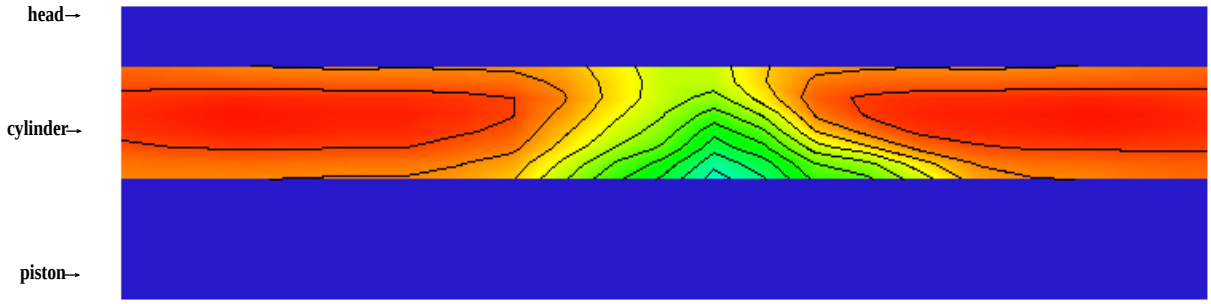

(a) temperature

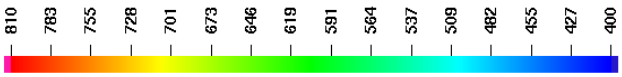

(b) scale

Figure 8.17: Predicted gas temperature at 20 ATDC for the diesel engine case

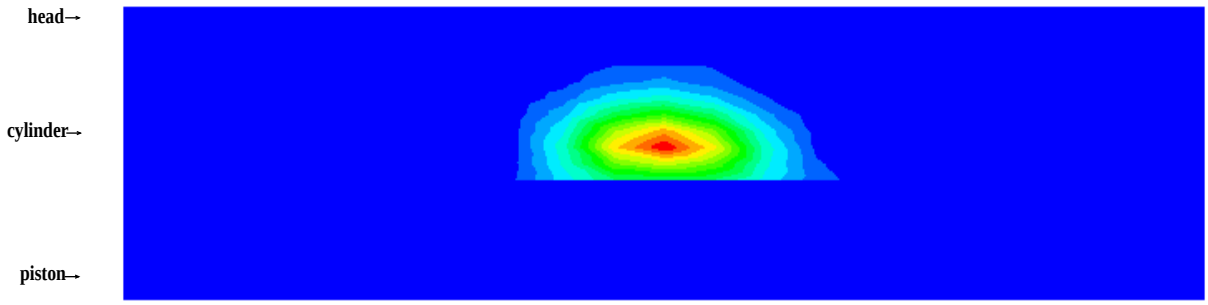

(a) turbulent kinetic energy

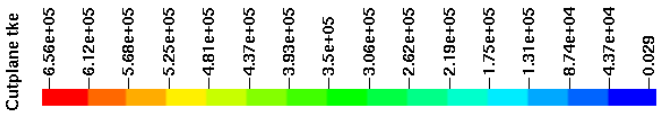

(b) scale

Figure 8.18: Predicted turbulent kinetic energy at 20 ATDC for the diesel engine case

CHAPTER 9. CONCLUSIONS AND RECOMMENDATION

9.1 Conclusions

This study developed an adaptive mesh refinement scheme using the h-refinement method for the hexahedral mesh to improve the accuracy of spray simulations. The scheme was successfully implemented into an engine simulation code using unstructured mesh. It was demonstrated that the present methodology can achieve accurate numerical results by performing rigorous local mesh adaptation without the need of using a globally fine mesh. The tree-based data storage structure was developed to provide efficient storage. The treatment of the hanging nodes provides flexible and efficient data management for successive refinements. The present refinement/coarsening procedure is an automatic process controlled by the refinement criteria. This method can enhance engineering design and optimization of spray combustion systems. It can be used to study specific local phenomena (such as spray) with a high accuracy, and can also be used to perform extensive parametric studies efficiently.

The adaptive algorithm was tested for both solid-cone and hollow-cone spray simulations in a constant-volume chamber. The liquid spray structure, tip penetration, and global SMD were compared. The present refinement scheme can provide good levels of accuracy while significantly reducing the computer time. The solid-cone spray case can reach a speed-up of 92, and the hollow-cone spray case can reach a speed-up of 46 under the present conditions. The present methodology was also applied to simulate the air-fuel mixing in a direct-injection spark-ignition engine. Solution accuracy was improved by the adaptation of the mesh. It is demonstrated that the present scheme can be successfully used in simulating the mixture formation process in transient engine conditions.

The second part of this dissertation studied the wall heat transfer modeling for engine

simulation. First, the integrated models for diesel spray combustion were validated under different engine loads and different injection timings using a heavy-duty diesel engine. For all the cases, the overall good levels of agreement were obtained between the predictions and measurements including the engine in-cylinder pressure history, heat release rate, and soot emissions.

A fully-coupled conjugate heat transfer model was successfully implemented into the CFD code for transient engine simulation. Essentially, all of the discretization and convergence techniques that have been used in in-cylinder flow were extended to the solid region. A numerical procedure for simultaneous calculation of convective heat transfer in fluid and heat conduction in solid was developed and tested. This approach extended the capability of an existing CFD code to conjugate heat transfer prediction. The methodology was consistent with the finite-volume method, as it was based on conservation principles. Heat conduction modeling was validated against analytical solutions based on a slab. The conjugate heat transfer prediction of a composite slab was compared with the exact solution and results demonstrated the successful handing of the conjugate boundary condition. The simulation of a diesel engine also demonstrated that this approach could predict the spatial temperature variation on the wall due to fuel spray.

9.2 Recommendation

The conjugate heat transfer calculation required a longer computer time than the traditional in-cylinder engine simulation alone. Parallel computing or appropriate numerical techniques can be investigated to accelerate the simulation. Additionally, the conjugate heat transfer model can be integrated with spray and combustion sub-models to improve the prediction of in-cylinder events such as spray wall impingement, wall film dynamics, combustions, and emissions. Effects of wall temperature on exhaust emissions can be evaluated by considering the spatial temperature variation. Temperature distributions on the combustion chamber surface can be used to explore the thermal stress of the piston under different operating conditions to characterize the local hot spots on the piston surface for engine durability study.

APPENDIX A. GEOMETRIC COEFFICIENTS

The term of form $\sum_f (\nabla Q)_f \cdot \mathbf{A}_f$ is computed by first calculating the geometric coefficients a_c, $a_{e_{12}}$ and $a_{e_{34}}$ using

$$a_c(\mathbf{x}_{c_n} - \mathbf{x}_c) + a_{e_{12}}(\mathbf{x}_1 - \mathbf{x}_2) + a_{e_{34}}(\mathbf{x}_3 - \mathbf{x}_4) = \mathbf{A}_f \tag{A.1}$$

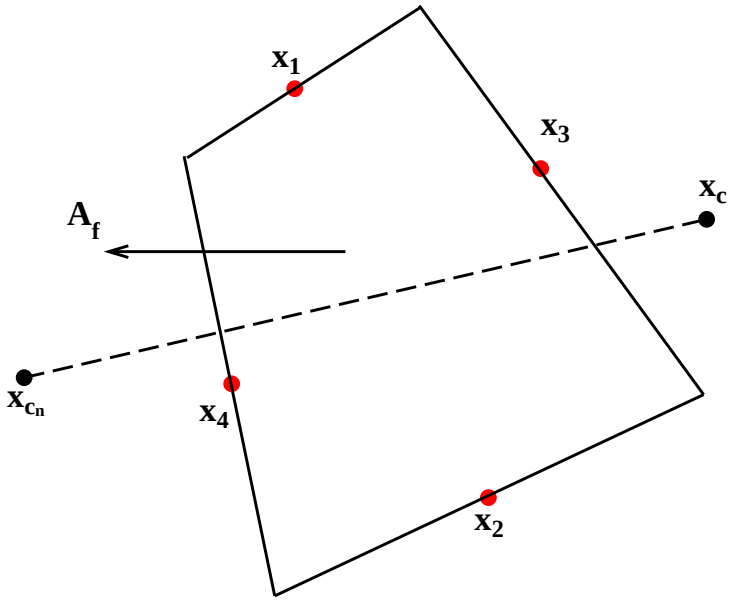

Figure A.1: The six points and edge conventions for calculation of geometric coefficients on cell face f

Eqn. (A.1) is a 3×3 linear system, which is solved using Cramer's rule. The finite-difference approximation to $(\nabla Q)_f \cdot \mathbf{A}_f$ is obtained by dotting both sides of Eq. (A.1) with $(\nabla Q)_f$ and ignoring terms of second and higher order in the cell dimensions. Then $(\nabla Q)_f \cdot \mathbf{A}_f$ is computed

using

$$a_c(Q_{c_n} - Q_c) + a_{e_{12}}(Q_1 - Q_2) + a_{e_{34}}(Q_3 - Q4) = (\nabla Q)_f \cdot \mathbf{A}_f \tag{A.2}$$

where Q_c is the cell-center value of Q, Q_{c_n} is the cell-center value of the neighboring cell across the face, and Q_i are the values of Q on the face edges, respectively. The Q_i are calculated by averaging all cells that share the edge.

Bibliography

Abani, N., Munnannur, A., and Reitz, R. D. (2006). Reduction of Numerical Parameter Dependencies in Diesel Spray Models. *19th Annual Conference on Liquid Atomization and Spray Systems*.

Abraham, J., Bracco, F. V. and Reitz, R. D. (1985). Comparisons of Computed and Measured Premixed Charge Engine Combustion. *Combust. Flame*, 60:309-322.

Abraham, J. (1997). What of Adequate Resolution in the Numerical Computationas of Transient Jets ? . *SAE-970051*.

Aftosmis, M. J. (1994). Upwind Method for Simulation of Viscous Flow on Adaptively Refined Meshes. *AIAA J.*, 32:375-392.

Aftosmis, M. J. (1997). Solution Adaptive Cartesian Grid Methods for Aerodynamic Flows with Complex Geometries. *Lecture notes for 28th Computational Fluid Dynamics Lecture Series*.

Aftosmis, M. J., Berger, M. J. and Adomavicius, G. (2000). A Parallel multilevel Method for Adaptively Refined Cartesian Grids with Embedded Boundaries. *AIAA-2000-0808* .

Aftosmis, M. J., Berger and M. J. (2002). Multilevel Error Estimation and Adaptive h-Refinement for Cartesian Meshes with Embedded Boundaries. *AIAA-2002-0863* .

Amsden, A. A., O'Rourke, P. J. and Butler, T D. (1989). KIVA-II: A Computer Program for Chemically Reactive Flows with Sprays. *Technical Report LA-11560-MS*.

Amsden, A. A. (1997). KIVA-3V: A Block-Structured KIVA Program for Engines with Vertical or Canted Valves. *Technical Report LA-13313-MS*.

Anderson, R. W., Pember, R. B., and Elliott, N. S. (2004). An Arbitrary Lagrangian-Eulerian Method with Adaptive Mesh Refinement for the Solutions of the Euler equations. *J. Comp. Phys.*, 199:586-617.

Anderson, W. K. and Bonhaus, D. L. (1994). An Implicit Upwind Algorithm for Computing Turbulent Flows on Unstructured Grids. *Computers and Fluids*, 23:1-21.

Aneja, R., and Abraham, J. (1998). How Far Dose the Liquid Penetration in Diesel Engine: Computed Results vs. Measurements. *Combustion Sci. Technol.*, 138:233-255.

Assanis, D. N. and Badillo, E. (1987). Transient Heat Conduction in Low-Heat-Rejection Engine Combustion Chambers. *SAE Technical Paper 870156*.

Assanis, D. N. and Badillo, E. (1988). Transient Analysis of Piston-Liner Heat Transfer in Low-Heat-Rejection Diesel Engines. *SAE Technical Paper 880189*.

Beard, P., Duclos, J. M., Habchi, C., Bruneaux, G., Mokaddem, K. and Baritaud, T. (2000). Extension of Lagrangian-Eulerian Spray Modeling: Application to High Pressure Evapotating Diesel Spray. *SAE-2000-01-1893*.

Beard, P., Colin, O., and Miche, M. (2003). Improved Modeling of DI Diesel Engines using Sub-grid Descriptions of Spray and Combustion. *SAE-2003-01-0008*.

Belardini, P., Bertoli, C., Ciajolo, A., D'Anna, A. and Delgiacomo, N. (1992). Three-Dimensional Calculations of D.I. Diesel Engine Combustion and Comparison with Incylinder Sampling Valve Data. *SAE Technical Paper 922225*.

Berger, M. J. and Oliger, J. (1984). Adaptive Mesh Refinement for Hyperbolic Partial Differential Equations. *J. Comp. Phy.*, 53:484–512.

Berger, M. J. and Colella, P. (1989). Local Adaptive Mesh Refinement for Shock Hydrodynamics. *J. Comp. Phy.*, 82:64–84.

Bergeron, C. A. and Hallett, W. L. H. (1989). Ignition Characteristic of Liquid Hydrocarbon Fuels as Single Droplet. *Canadian J. of Chem. Eng*, 67:142-149.

Bowman, C. T. (1975). Kinetics of Pollutant Formation and Destruction in Combustion. *Prog. Energy Combust. Sci.*,1:33-45.

Carslaw, H. S. and Jaeger, J. C. (1959). Conduction of Heat in Solids. *Clarendon Press*, Oxford.

Chang, S., and Haworth, D. C. (1997). Adaptive Grid Refienment using Cell-Level and Global Imbalances. *Int. J. Num. Meth. Fluids*, 24:375-392.

Choi, C. Y. and Reitz, R. D. (1999). An Experimental Study on the Effects of Oxygenated Fuel Blends and Multiple Injection Strategies on D.I. Diesel Engine Emissions. *FUEL*, 78/11:1303-1317.

Carslaw, B. and Gremaud, P. A. (1996). Error Estimators for Finite Element Methods for Scalar Conservation Laws. *SIAM J. Numer. Anal*, 33:522-554.

Coirier, W. J. (1994). An Adaptively-Refined, Cartesian, Cell-Based Scheme for the Euler and Navier-Stokes Equations. *NASA Technical Memorandum*, 106754.

Culham, J. R. and Yovanovich, M. M. (1993). Conjugate Heat Transfer from a Raised Isothermal Heat Source Attached to a vertical Board. *Ninth IEEE SEMITHERM Symposium*.

Dukowicz, J. K. (1980) . A Particle-Fluid Numerical Model for Liquid Sprays. *J. of Comp. Phys.* , 35:229-253.

Eiglmeier, C., Lettmann, H., Stiesch, G. and Merker G. P.(2001) . A Detailed Phenomenological Model for Wall Heat Transfer Prediction in Diesel Engines. *SAE Technical Paper 2001-01-3265*.

Gupta, H. C. and Bracco, F. V. (1978). Numerical Computations of Two-Dimensional Unsteady Sprays for Application to Engines. *AIAA J.*, 16:1053-1061.

Halstead, M., Kirsh, L. and Quinn, C. (1977). The Autoignition of Hydrocarbon Fuels at high Temperatures and Pressures-Fitting of a Mathematical Model. *Combust. Flame*, 30:45-60.

Han, Z., and Reitz, R D. (1998). Turbulence Modeling of Internal Combustion Engines Using RNG $k-\epsilon$ Models. *Combustion Sci. Technol.*, 106:267-295.

Han, Z., Uludogan, A., Hampson, G. J., and Reitz, R. D. (1996). Mechanism of Soot and NOx Emission Reduction Using Multiple-Injection in a Diesel Engine. *SAE Technical Paper 960633*.

Han, Z. and Reitz, R. D. (1997). A Temperature Wall Function Formulation for Variable-Density Turbulent Flows with Application to Engine Convective Heat Transfer Modleing. *Int. J. Heat Mass Transfer*, 40:613-625.

Han, Z., Dennis, B. and Dulikravich G. (2000). Simultaneous Prediction of External Flow-Field and Temperature in Internally cooled 3-D Turbine Blade Material. *IGTI paper 2000-GT-253*.

Hay, A. and Visonneau, M. (2007). Adaptive Finite-Volume Solution of Complex Turbulent Flows. *Computers and Fluids*, 36:1347-1363.

Heywood, J. B. (1988). Internal Combustion Engine Fundamentals. *McGraw-Hill*, New York, NY.

Hieber, S. (2001). An Investigation of the Mesh Dependence of the Stochastic Droplet applied to Dense Liquid Sprays. *MS Thesis*, Michigan Tech. Univ..

Hiroyasu, H. and Nishida, K. (1989). Simplified Three-Dimensional Modeling of Mixture Formation and Combustion in a D.I. Diesel Engine. *SAE Technical Paper 890269*.

Hou, S. and Schmidt, D. P. (2006). Adaptive Collision Meshing and Satellite Droplet Formation in Spray Simulations. *Int. J. of Multiphase Flow*, 32:935-956.

Hunt, J. D. (2004). An Adaptive 3D Cartesian Approach for the Parallel Computation of Inviscid Flow About Static and Dynamic Configurations. *PhD Thesis*, The University of Michigan.

Hyams, D. G. (2000). An Investigation of Parallel Implicit Solution Algorithm for Incompressible Flows on Unstructured Topologies. *PhD Thesis*, Mississippi State University.

Kallinderis, Y. G., and Baron, J. R. (1989). Adaptive Methods for a New Navier-Stokes Algorithm. *AIAA J.*, 27:37-43.

Kallinderis, Y. G., and Baron, J. R. (1992). A New Adaptive Algorithm for Turbulent Flows. *Computers & Fluids.*,21(1):37-43.

Klingbeil, A. E. (2002). Particulate and NOx Reduction in a Heavy-Duty Diesel Engine Using High Levels of Exhausts Gas Recirculation and Very Early Start of Injection. *MS Thesis*, University of Wisconsin-Madison.

Kong, S. C. and Reitz, R. D. (1993). Multidimensional Modeling of Diesel Ignition and Combustion Using a Multistep Kinetics Model. *ASME Paper 93-ICE-22.*

Kong, S. C., Han, Z. and Reitz, R. D. (1995). The Development and Application of a Diesel Ignition and Combustion Model for Multidimensional Engine Simulation. *SAE Technical Paper 950278.*

Kong, S. C., Senecal, P. K. and Reitz, R. D. (1999). Developments in Spray Modeling in Diesel and Direct-Injection Gasoline Engines. *Oil and Gas Science and Technology - Rev. IFP*, 197-204.

Launder, B. E. and Spalding, D. B. (1974). The Numerical Computation of Turbulent Flows",. *Comput. Methods Appl. Mech. Eng.*, 3: 269-289.

Lippert, A. M., Chang, S., Are, S. and Schmidt, D. P. (2005). Mesh Independence and Adaptive Mesh Refinement for Advanced Engine Spray Simulations. *SAE-2005-01-0207.*

Liu, A. B. and Mather, D. and Reitz, R. D. (1993). Modeling the Effects of Drop Drag and Breakup on Fuel Sprays. *SAE Technical Paper 930072.*

Liu, Y. and Reitz, R. D. (1998) Modeling of Heat Conduction within Chamber Walls for Multidimensional Internal Combustion Engine Simulations. *Int. J. Heat Mass Transfer*, 41:859-869.

Mavriplis, D. J. (1990). Accurate Multigrid Solution of the Euler Equations on Unstructured and Adaptive Meshes. *AIAA J.*, 28:213-221.

Mavriplis, D. J. and Gosman, A. D. (2000). Adaptive Meshing Techniques for Viscous Flow Calculations on Mixed Element Unstructured Meshes. *Int. J. Num. Meth. Fluids*, 34:93-111.

Morel, T. and Keribar, R. (1985). A Model for Predicting Spatially and Time Resolved Convective Heat Transfer in Bowl-in Piston Combustion Chamber. *SAE Technical Paper 850204*.

Muzaferiia, S. and Gosman, A. D. (1997). Fineite-Volume CFD Procedure and Adaptive Error Control Strategy for Grids of Arbitrary Topology. *J. of Comp. Phys.*, 138:766-787.

Nomura, Y., Miyagawa, H., Fujikawa, T., Tomoda, T., Kubota, M. and Abe, S. (2001). Numerical Study of Mixture Formulation and Combustion Processes in a Direct Injection Gasoline Engine with Fan-Shaped Spray. *SAE-2001-01-0738*.

Nuutinen, M., Kaario, O. and Larmi, M. (2008). Conjugate Heat Transfer in CI Engine CFD Simulations. *SAE Technical Paper 2008-01-0973*.

Nagle, J. and Strickland-Constable, R. F. (1962). Oxidation of Carbon Between 1000-2000 C. *Pro. of the Fifth Carbon Conf, Volume 1, Pergammon Press*,154.

O'Rourke, P. J. (1981). Collective Drop Effects on Vaporizing Liquid Sprays. *PhD Thesis*, Princeton Univ..

O'Rourke P. J. and Amsden, A. A. (1986). Implementation of a Conjugate Residual Iteration on the KIVA Computer Program. *Technical Report*, LA-10849-MS.

O'Rourke, P. J. and Amsden, A. A. (1987). The TAB Method for Numerical Calculation of Spray Droplet Breakup. *SAE Technical Paper 872089*.

O'Rourke, P. J. and Sahota, M. S. (1998). A Variable Explicit/Implicit Numerical Method for Calculating Advection on Unstructured Meshes. *J. Comp. Phy.*, 143:312–345.

Pierpont, D. A., Montgomery, D. T. and Reitz, R. D. (1995). Reducing Particulate and NOx Using Multiple Injections and EGR in a D.I. Diesel. *SAE Technical Paper 950217*.

Pizadeh, S. Z. (1999). An Adaptive Unstructured Grid Method by Grid Subdivision, Local Remeshing and Grid Movement. *AIAA-99-3255*.

Patterson, M. A., Kong, S. C., Hampson, G. J. and Reitz, R. D. (1994). Modeling the Effects of Fuel Injection Characteristics on Diesel Engine Soot and NOx Emissions. *SAE Technical Paper 940523*.

Patterson, M. A. and Reitz, R. D. (1998). Modeling the Effects of Fuel Spray Characteristics on Diesel Engine Combustion and Emission. *SAE Technical Paper 980131*.

Ramshaw, J. D., O'Rourke, P. J., and Stein, L. R. (1985). Pressure Gradient Scaling Method for Fluid Flow with Nearly Uniform Pressure. *J. Comput. Phys.*, 58: 361.

Reitz, R. D., and Diwakar, R. (1987). Structure of High Pressure Fuel Sprays. *SAE Technical Paper 870598*.

Reitz, R. D. (1987). Modeling Atomization Processes in High-Pressure Vaporizing Sprays. *Atomization and Spray Technology*, 3: 309-337.

Rhie, C. M., and Chow, W. L. (1983). Numerical Study of the TurbulentFlow Past an Airfoil with Trailing Edge Separation. *AIAA J.*, 21: 1525-1532.

Rigby, D. L. and Lepicovsky, J. (2001). Conjugate Heat Transfer Analysis of Internally Cooled Configurations. *ASME Paper 01-GT-0405*.

Schmidt, D. P. and Rutland, C. J. (2000). A New Droplet Collision Algorithm. *J. of Comp. Phys.*, 164:62-80.

Schmidt, D. P., and Senecal, P. K. (2002). Improving the Numerical Accuracy of Spray Simulations. *SAE-2002-01-1113*.

Schubert, C., Wimmer, A and Chmela, F. (2005). Advanced Heat Transfer Model for CI Engines. *SAE Technical Paper 2005-01-0695*.

Stalsberg-Zarling, K., Feigl, K. and Tanner, F. X. (2004). Momentum Coupling by Means of Lagrange Polynomials in the CFD Simulation of High-Velocity Dense Sprays. *SAE-2004-01-0535*.

Stiesch, G. (2003). Modeling Engine Spray and Combustion Processes. *Springer*.

Subramaniam, S. and O'Rourke, P. J. (1998). Numerical Convergence of the KIVA-3 Code for Sprays and its Implications for Modeling. *LAUR Report, 1998-5465*.

Tiainen, J., Kallio, I., Leino, A. and Turunen, R. (2004). Heat Transfer Study of a High Power Density Diesel Engine. *SAE Technical Paper 2004-01-2962*.

Torres, D. J. and Trujillo, M. F.(2006). KIVA-4: An Unstructured ALE Code for Compressible Gas Flow with Sprays. *J. of Comp. Phys.*, 219:943-975.

Torres, D. J. and Xue Q. (2006). Private Communication.

Torres, D. J. (2007). Collocated KIVA-4. *17th International Multidimensional Engine Modeling User's Group Meeting at the SAE Congress*.

Tsui, Y. and Pan, Y. (2006). A Pressure-Correction Method for Incompressible Flows Using Unstructured Meshes. *Numerical Heat Transfer, Part B*, 49:43–65.

Urip, E. (2006). The KIVA Code with Conjugate Heat Transfer Model for IC Engine Simulation. *PhD Thesis*, Michigan Tech. Univ..

Wang, Z. J. (2000). A Fast Nested Multi-Grid Viscous Flow Solver for Adaptive Cartisan/Quad Grids. *Int. J. Num. Meth. Fluids*, 33:657-680.

Wang, Z. J. and Chen, R. F. (2002). Anisotropic Solution-Adaptive Viscous Cartesian Grid Method for Turbulent Flow Simulation. *AIAA J.*, 40:1969-1978.

Warren, G. P. and Anderson, W. K. and Thomas, J. L. and Krist, S. L. (1991). Grid Convergence for Adaptive Methods. *AIAA-91-1592, AIAA 10th Computational Fluid Dynamics Conference.*.

Wendroff, B. (2005). Cell-Centered lagrangian: Adaptive Mesh Refinement and High-Order Method in 1D. *Technical Report, LAUR-05-7863*.

Westbrook, C. K., Adamczyk, A. A. and Lavoie G. A. (1981). A Numerical Study of Laminar Flame Wall Quenching. *Combust. and Flame*, Vol. 40, 81-99.

Wiedenhoefer, J. F. and Reitz, R. D. (2000). Modeling the Effect of EGR and Multiple Injection Schemes on I.C. Engine Component Temperatures. *Numerical Heat Transfer, Part A*, 37:673-694.

Wiedenhoefer, J. F. (2002). A Computational Investigation on the Effects of Radiation and Wall Heat Transfer on Diesel Engine Performance. *PhD Thesis*, University of Wisconsin - Madison.

Wiedenhoefer, J. F. and Reitz, R. D. (2003). A Multidimensional Radiation Model for Diesel Engine Simulation with Comparison to Experiment. *Numerical Heat Transfer, Part A*, 44:665-682.

Wolff, A., Aou;ouchos, K. and Mueller, R. (1997). Computational Investigation of Unsteady Heat Flux Though an IC Engine Wall Including Soot Layer Dynamics. *SAE Technical Paper 970063*.

Woschni, R. (1967). A Universally Applicable Equation for the Instantaneous Heat Transfer Coefficient in the Internal Combustion Engine. *SAE Technical Paper 670931*.

Xin, J., Shih, S. and Itano, E. (2003) Integratin of 3D Combustion Simulations and Conjugate Heat Transfer Analysis to Quantitatively Evaluate Component Temperatures. *SAE Technical Paper 2003-01-3128*.

Xue, Q. (2005). Development of Conjugate Heat Transfer Capability to an Unstructured Flow Solver - U^2NCLE. *MS Thesis* , Mississippi State University.

Yakhot, V., Orszag, S. A., Thangam, S., Gatski, T. B. and Speziale, C. G. (1992). Development of Turbulence Models for Shear Flows by a Double Expansion Technique. *Phys. Fluids A* , Vol:4, No.7, pp.1510-1520.